Single-Photon Counting Lidar For Long-Range Three-Dimensional Imaging

Thesis submitted for the degree Doctor of Engineering

Agata M. Pawlikowska, MSc

Heriot-Watt University
School of Engineering and Physical Sciences

September 2016

Abstract

Single-photon time-of-flight (ToF) distance ranging lidar is a candidate technology for high-resolution depth imaging for use, for example, from airborne platforms. This approach enables low average power pulsed laser sources to be used while allowing imaging from significantly longer target ranges compared to analogue imaging. The recent availability of Geiger-mode (Gm) arrays has revolutionised photon-counting lidar as they provide single-photon full-frame data in short acquisition times.

This thesis presents work on the opto-mechanical design, tolerance analysis and performance evaluation of a re-configurable single-photon counting lidar which can accommodate either a single-element single-photon avalanche photodiode (SPAD) or a 32 × 32 Gm-array. By incorporating an inter-changeable lens, the two configurations were designed to provide identical pixel resolution for both the single-pixel system and the Gm-array configurations in order to permit a performance comparison to be conducted. This is the first time that such a comparison has been reported and the lidar is one of the earliest to assess the performance of a short-wave infra-red (SWIR) Gm-array. Both detection configurations used InGaAs/InP SPAD detectors and operated at a wavelength of 1550 nm. The main benefits of operating within the SWIR band include reduced solar background, lower atmospheric loss, improved covertness, as well as improved laser eye-safety thresholds. The system estimates target range by measuring the ToF using time-correlated single-photon counting (TCSPC) and was used to produce high-resolution three-dimensional images of targets at between 800 m and 10.5 km range. The single-element system has the potential to provide improved depth resolution over the array due to a smaller timing jitter but requires longer acquisition times due to the need for two-dimensional scanning. The acquisition time of the array configuration can be up to three orders of magnitude faster than the single-element configuration but requires significantly higher average laser power levels.

The Gm-array provided a simultaneous estimation of angle-of-arrival and intensity fluctuations from which a comparable strength of atmospheric turbulence could be measured. This demonstrated that Gm-arrays provide a new way of high-speed turbulence measurement with time intervals much shorter than those offered by existing scintillometers.

To Mum and Dad

ACADEMIC REGISTRY

Research Thesis Submission

Name*:*	Agata Pawlikowska		
School/PGI:	School of Engineering and Physical Sciences		
Version: *(i.e. First, Resubmission, Final)*	Final submission	Degree Sought	Engineering Doctorate in Optics and Photonics Technologies

Declaration

In accordance with the appropriate regulations I hereby submit my thesis and I declare that:

1) the thesis embodies the results of my own work and has been composed by myself
2) where appropriate, I have made acknowledgement of the work of others and have made reference to work carried out in collaboration with other persons
3) the thesis is the correct version of the thesis for submission and is the same version as any electronic versions submitted*.
4) my thesis for the award referred to, deposited in the Heriot-Watt University Library, should be made available for loan or photocopying and be available via the Institutional Repository, subject to such conditions as the Librarian may require
5) I understand that as a student of the University I am required to abide by the Regulations of the University and to conform to its discipline.

* *Please note that it is the responsibility of the candidate to ensure that the correct version of the thesis is submitted.*

Signature of Candidate*:*		Date:	

Submission

Submitted By *(name in capitals):*	
Signature of Individual Submitting:	
Date Submitted:	

For Completion in the Student Service Centre (SSC)

Received in the SSC by (name in capitals):			
Method of Submission (Handed in to SSC; posted through internal/external mail):			
E-thesis Submitted (mandatory for final theses)			
Signature:		Date:	

Acknowledgements

This work would have not been accomplished without the input, help and hard work of a large team of people. First of all, I'd like to thank my academic supervisor, Prof. Gerald Buller, for his guidance, expertise, his never ending support, for being a source of motivation, encouragement and for having my back when things were really difficult.

This project would have not been possible without the effort of Prof. Robert Lamb of Selex ES who was the driving force behind it and who gave me the opportunity to get involved in this work. Big thanks should go to Rob for his guidance, advice, patience and support throughout this long process.

Thanks to my industrial supervisor Roger Pilkington for his time, support and advice, especially for coming in at weekends during the period of trials, for helping me to get equipment and making all the arrangements required to facilitate this work.

Massive thanks should go to Dr. Karen Jane Gordon for all the support she provided, for her eagerness to share knowledge, for being my mentor in the initial phase of the project and most of all, for her friendship which helped me to stay strong and tackle all the challenges along the way.

A big thank you to the Selex ES team who welcomed me in the group: Iain Clark, Jim Henderson, Mike McPartlin, Dr. Peter Sinclair, Dr. Phil Hiskett, Jeremy Copley, Phil Oakley, Fiona Beath, Michaela Clarke, Dr. Peter Findlay, Ryan O'Donnel and Dr. Gez Wong. These individuals were a huge source of support throughout the duration of this EngD project and beyond. Thanks to Norman Watson for being my office neighbour; for his calming influence, laid back attitude, all the advice, discussions about quantum physics and his (unsuccessful) attempts to teach me how to speak proper English. Also, thanks should go to David Cowan for reviewing some chapters of this thesis.

I would also like to thank members of the Single-Photon Group at Heriot-Watt University whose support and friendship have been priceless: Dr. Aongus McCarthy, Aurora Maccarone, Dr. Ross Donaldson, Dr. Robert Collins, Dr. Peter Vines, Dr. Ximing Ren, Dr. Nathan Gemmel, Dr. Silvia Butera, Dr. Giuseppe Intermitte and Dr. Ryan Warburton. Special thanks should go to Dr. Robert Collins for his useful advice and help with GuideTech programming and timing electronics.

Thanks to Selex ES employees: Michael Dugan for working with me on the mechanical design, Dr. Stephen Harding for all his advice on laser safety, Naomi Mitchison for her work on electrical wiring of the safety enclosure, Chris Davies for overlooking the design phase, many tips on how to use ZEMAX and for many useful optical design insights and to Bill McNaught for providing equipment in the roof laboratory when needed.

Thanks go to my EngD mentor Dr. Brian Flemming for offering his support, understanding and guidance throughout this process.

Many thanks to apprentices Jamie Natta and Dillon Finesy for the amazing job they did helping me out with trials and for sacrificing their weekends standing for hours in the cold, wind and rain.

Thanks should also go to Dr. Justin Richardson for his support, advice and for introducing me to single-photon detectors. Without his encouragement I have most likely become a “microbubble” expert.

Finally, I want to thank my mum and dad for always being there for me, especially when I needed it most, and my friends: Sandy Vadher, Gabrielle Thomas, Marcus Ardron, Gabriella Moericke, Lisa Glen, Ewa and Rob Cox, Kathleen Prophet, Nipa Begum and last but not least, Linda Monteith.

Contents

List of Publications

Conference Proceedings

- A.M. Pawlikowska, R.M. Pilkington, K.J. Gordon, P.A. Hiskett, G.S. Buller and R.A. Lamb, *"Long-Range 3D Single-Photon Imaging Lidar"*, Proc. SPIE 925007 (2014)
- K.J. Gordon, P.A. Hiskett, R.M. Pilkington, J. Copley, A. Pawlikowska, R.A Lamb, *"New Trends in Integrated Imaging Lidar", OSA* Advanced Solid-State Lasers (2013)

Recently Submitted Conference Proceedings

- R.A. Lamb, A.M. Pawlikowska, R.M. Pilkington, *"Measurement of Cn^2 Using a Single-Photon Avalanche Diode and a Geiger-Mode Array",* SPIE Commercial + Scientific Sensing and Imaging, Baltimore, April (2016)

Journals and Conference Proceedings in Preparation

- A.M. Pawlikowska, R.M. Pilkington, P. Sinclair, G.S. Buller, R.A. Lamb, *"Atmospheric Turbulence Analysis at 1550 nm Wavelength using InGaAs/InP Single Photon Avalanche Diode Detectors",* Rev. Sci. Instrum.
- A.M. Pawlikowska, G.S. Buller, R.A. Lamb, *"Long-Range 3D Imaging Lidar with Single Element and Geiger-Mode Array Detectors"*, Opt. Express

Conference Presentations

- A.M. Pawlikowska, *"Long-Range 3D Single-Photon Imaging Lidar",* SPIE Defence + Security, Amsterdam (2014)
- A.M. Pawlikowska, *"Long-Range 3D Single-Photon Imaging Lidar"*, EngD Conference in Optics and Photonics, Edinburgh (2014)
- A.M. Pawlikowska, *"Long-Range 3D Single-Photon Imaging Lidar"*, EngD Conference in Optics and Photonics, Edinburgh (2013)

Posters

- A.M. Pawlikowska, P.A. Hiskett, R.A. Lamb and G.S. Buller, *"Long-Range 3D Single-Photon Imaging Lidar"*, EngD Conference in Optics and Photonics, Edinburgh (2012)

Glossary of Abbreviations

ADC	Analogue-to-Digital Converter
APD	Avalanche Photodiode
CAD	Computer Aided Design
CCD	Charge-Coupled Device
CFD	Constant Fraction Discriminator
CMOS	Complementary-Metal-Oxide Semiconductor
cps	Counts per second
CW	Continuous Wave
DARPA	Defense Advanced Research Projects Agency
DAQ	Data Acquisition Devices
DCR	Dark Count Rate
DOE	Diffractive Optical Elements
Er/Yb	Erbium/Ytterbium
ESA	European Space Agency
FFT	Fast Fourier Transform
FPA	Focal Plane Array
FPGA	Field Programmable Gate Array
FWHM	Full Width Half Maximum
FoV	Field of View
Ge	Germanium
Gm	Geiger-Mode
GUI	Graphical User Interface
HD	Hyperfocal Distance
He-Ne	Helium-Neon
InGaAs	Indium Gallium Arsenide
InP	Indium Phosphide

IRF	Instrumental Response Function
LIDAR	Light Detection and Ranging
LWIR	Long-Wave Infrared
MEMS	Micro-Electro-Mechanical Systems
MCA	Multi-Channel Analyser
MIT	Massachusetts Institute of Technology
MPD	Micro Photon Devices
MWIR	Mid-Wave Infrared
NASA	National Aeronautics and Space Administration
ND	Neutral Density
Nd:YAG	Neodymium-Doped Yttrium Aluminium Garnet
NI	National Instruments
PCI	Peripheral Component Interconnect
PMT	Photo-Multiplier Tube
POP	Physical Optics Propagation
PPG	Pulse Pattern Generator
PSF	Point Spread Function
PXI	PCI eXtensions for Instrumentation
RJMCMC	Reversible Jump Markov Chain Monte Carlo
SBR	Signal-to-Background Ratio
SE	Single-Element
SLM	Spatial Light Modulator
SLR	Satellite Laser Ranging
SPDE	Single-Photon Detection Efficiency
Si	Silicon
SNR	Signal-to-Noise Ratio
SPAD	Single-Photon Avalanche Diode

SWIR	Short-Wave Infrared
TAC	Time-to-Amplitude Converter
TCSPC	Time-Correlated Single-Photon Counting
TDC	Time-to-Digital Converter
TEC	Thermo-Electric Cooler
TEM	Transverse Electromagnetic Mode
TTL	Transistor-Transistor Logic
ToF	Time-of-Flight
UAV	Unmanned Aerial Vehicle
VLWIR	Very Long-Wave Infrared

Chapter 1
Introduction

In recent years there has been increasing interest in the development of lidar for long-range three-dimensional imaging for a number of remote sensing applications. One reason for this is the recent availability of Geiger-mode (Gm) arrays which provide full frame data acquisition of low light levels. The technology has also found applications in airborne surveillance where long-range target identification through turbulence presents an engineering challenge [1]. Specifically, strong attention is being focused on developing a wide range of applications such as wide field-of-view (FoV) airborne surveillance sensors and long-range target recognition and identification sensors. Although each application will have specific requirements influencing the design and the choice of components, it is clear that there is a need for systems which can provide three-dimensional, high-resolution imaging over long ranges, ability of night-time imaging, covertness, eye-safety and ease of implementation with airborne platforms, unmanned aerial vehicles (UAVs) and satellites. This imposes limits on system weight, size and volume and requires low-power laser sources and sensitive detectors [2][3].

Single-photon ranging lidar is a candidate technology that potentially meets the specification of an airborne depth imager. In contrast to analogue detection the timing resolution of single-photon detection is not limited by the duration or rise time of the voltage pulse and is only affected by the variance in the rise time of the detector, or timing jitter. Single-photon detection can therefore provide timing error up to an order of magnitude better than that of an analogue detector, leading to significantly improved depth resolution. In addition, the high sensitivity of single-photon detectors allows lower power laser sources to be used and permits time-of-flight data to be measured from significantly longer ranges. The possibility of using weaker sources means that single-photon lidar systems can be smaller, lighter and consume less power which is essential for integration into airborne platforms.

Distance ranging lidar uses time-correlated single-photon counting (TCSPC) which is a repetitively pulsed statistical sampling technique that has been available since 1960's which records the time-of-arrival of photons reflected from a target and logs this against the time of emission of a laser pulse [4][5][6] . The TCSPC distance ranging approach

has a number of advantages over analogue detection techniques including improved depth resolution [7][8][9]. The improved depth resolution allows identification of closely separated targets while the advantage of shot-noise limited detection of single-photon returns means that the system can be used with a greater signal-to-noise ratio which is critical in long-distance ranging applications [10].

Recent development of two-dimensional arrays of single-photon detectors allows one to record images [11]. In this case the scene of interest is flood-illuminated and imaged onto an array, so that each pixel measures the round-trip time of transmitted photons scattered from the corresponding point in the scene [12][13]. This eliminates the need for two-dimensional scanning mechanisms and simplifies the opto-mechanical design.

This thesis is concerned with the design and evaluation of a reconfigurable transceiver system used for single-photon distance ranging which can operate with a single-element scanned detector and a Geiger-mode (Gm) array. The system was designed to provide a matching angular resolution per pixel for both types of detectors and thus allows a performance comparison to be made between these detector configurations. The comparison includes an assessment of data acquisition time, depth and spatial resolution, spatial coverage, laser power requirements, data transfer speed, system size, weight and cost. In addition, the thesis provides an initial assessment of the use of photon counting to investigate atmospheric turbulence and proposes single-photon detection as a potential candidate technology for measuring parameters characterising atmospheric turbulence.

1.1 Thesis Structure

The thesis is structured such that Chapter 2 presents an introduction to lidar distance ranging techniques and a description of TCSPC, single-photon detectors, photon-counting statistics and a review of the current state of single-photon lidar systems and Gm-array technology.

Chapter 3 presents the design tolerance analysis of a re-configurable transceiver single-photon counting ranging system which can accommodate either a single-element single-photon avalanche diode (SPAD) detector operating in a scanning mode or a 32 × 32 array of SPAD detectors operating in a non-scanning mode. Both the single-element detector and Gm-array systems can be re-configured to operate in a bi-static or a mono-

static configurations. The chapter describes the operational and design requirements for remote sensing of objects at very long ranges (up to ~ 10 km).

In Chapter 4 measurements along with the analysis performed with the lidar system operating in the bi-static scanning configuration with the single-element detector are presented. Details on the transmitter design, timing electronics scheme, the alignment and setup of the system used in experiments are described. In addition, theoretical modelling of the system losses is described and evaluated against the real-life measurement along the instrumental response function of the system and an assessment of imaging through a semi-transparent sheet of netting.

Chapter 5 describes experimental results acquired with the transceiver configured in a mono-static mode with a scanned single-element detector. Details of the transmitter design, timing electronics and backscatter mitigation with an electrical gating approach are presented. A surface-to-surface test resolution is described where the data analysed using a least-squares fit peak finder applied to the data and a cross-correlation with normalised instrumental response function technique are compared. In addition, depth images of different types of objects such as buildings, an electricity pylon, foliage and terrain acquired over distances between 800 m and 10.5 km are presented. These target types present different scales of shape, size and range profile which provide tests of both spatial and range resolution at various ranges.

Chapter 6 presents the experimental results acquired with the Gm-array operating in a bi-static mode. An instrumental response function (IRF) was measured. Its full width at half maximum (FWHM) was equivalent to a depth resolution of 15 cm and matched that measured with the scanned single-element detector operating in a bi-static configuration. In addition, a comparison between the single-element and Gm-array configurations is presented in terms of system performance parameters, design parameters and cost.

Chapter 7 introduces properties of the Earth's atmosphere and describes laser beam propagation through turbulence. The work presented in this chapter experimentally determines parameters characterising optical turbulence with a new approach using single-photon lidar data obtained from sets of measurements performed over ranges of 5.6 km and 9.5 km with a single-element detector and a Gm-array. The results obtained were used to analyse the effect of background noise on the scintillation index, σ_I^2.

Finally, this chapter introduces a comparative method of estimating the refractive index structure parameter, C_n^2.

In Chapter 8 the conclusions drawn from the work contained within this thesis are given and the possibility of improving the performance of the system in terms of opto-mechanical design, theoretical modelling, testing, image processing, system integration and performance parameters are discussed.

References

[1] Committee on Developments in Detector Technologies; National Research Council, "*Seeing Photons: Progress and Limits of Visible and Infrared Sensor Arrays"*, The National Academy Press (2010)

[2] A. McCarthy, R.J. Collins, N.J. Krichel, V. Fernandez, A.M. Wallace and G.S. Buller, *"Long-Range Time-of-Flight Scanning Sensor Based on High-Speed Time-Correlated Single-Photon Counting",* Appl. Opt., 48, 32 (2009)

[3] M.A. Albota, B.F. Aull, D.G. Fouche, R.M. Heinrichs, D.G. Kocher, R.M. Marino, J. Mooney, N.R. Newbury, M.E. O'Brien, B.E. Player, B.C. Willard, J.J. Zayhowski, *"Three-dimensional Imaging Laser Radars With Geiger-Mode Avalanche Photodiode Arrays*", Linc. Lab. J., 13, 2 (2002)

[4] R.H. Hadfield, *"Single-Photon Detectors for Optical Quantum Information Applications*", Nat. Photonics, 3, 12, 696-705 (2009)

[5] A. McCarthy, X. Ren, A.D. Frera, N.R. Gemmel, N.J. Krichel, C. Scarcella, A. Ruggeri, A. Tosi, G.S. Buller, *"Kilometer-Range Depth Imaging at 1550 nm Wavelength Using an InGaAs/InP Single-Photon Avalanche Diode Detector",* Opt. Express, 21, 19, 22098-22113 (2013)

[6] W. Becker, "*Advanced Time-Correlated Single-Photon Counting Techniques"*, Springer (2005)

[7] G.S. Buller, R.J. Collins*, "Single-Photon Generation and Detection"*, Meas. Sci. Technol., 21, 012002 (2010)

[8] G.S. Buller, N.J. Krichel, A. MCarthy, N.R. Gemmel, M.G. Tanner, C.M. Natarajan, X. Ren, R.H. Hadfield, *"Kilometer Range Depth Imaging Using Time-Correlated Single-Photon Counting",* Proc. SPIE, 8155, 81551l-1 (2011)

[9] S. Pellegrini, G.S. Buller, J.M. Smith, A.M. Wallace and S. Cova, "*Laser-Based Distance Measurement Using Picosecond Resolution Time-Correlated single-Photon Counting"*, Meas. Sci. Technol., 11, 712-716 (2000)

[10] J.J. Degnan, "*Photon-Counting Multikilohertz Microlaser Altimeters for Airborne and Spaceborne Topographic Measurements"*, J. Geodyn. 34(3): 503-549 (2002)

[11] M.A. Itzler, M. Entwistle, M. Owens, K. Patel, X. Jiang, K. Slomkowski, S. Rangwala, "*Comparison of 32 x 128 and 32 x 32 Geiger-Mode APD FPAs for Single-Photon 3D LADAR Imaging"*, Proc. SPIE, Vol. 8033, 8033G-1 (2011)

[12] B.F. Aull, A.H. Loomis, D.J. Young, R.M. Heinrichs, B.J. Felton, P.J. Daniels, D.J. Landers, "*Geiger-Mode Avalanche Photodiodes for Three-Dimensional Imaging"*, Linc. Lab. J., 13, 2 (2002)

[13] R. Marino, W.R. Davis Jr., *"Jigsaw: A Foliage-Penetrating 3D Imaging Laser Radar System"*, Linc. Lab. J., 15, 1 (2005)

Chapter 2

Time-of-Flight Single-Photon Counting Lidar

2.1 Introduction

This chapter provides an introduction to detection techniques used in distance ranging lidar where detection approaches are classified into coherent and direct detection schemes. The coherent detection is categorised into homodyne and heterodyne detection and the direct detection techniques are divided into analogue detection and Geiger-mode (Gm) detection. The chapter also includes a discussion on long-distance ranging lidar, describing its basic principles, layout and possible configurations.

Single-photon time-of-flight lidar, the benefits and motivation for use, as well as a description of relevant instrumentation are discussed. This is followed by a review of some of the most commonly-used single-photon detectors and performance metrics of single-photon avalanche photodiodes (SPADs). Photon statistics, governed by Poisson distribution, is also introduced.

Finally, an overview of state-of-the-art single-photon lidar systems is presented. The reviewed systems comprise of cutting-edge single-element and multi-element detectors and incorporate different scanning mechanisms which include galvanometer scanning mirrors, dual-wedge scanners and rotating diffractive optical elements capable of producing multiple beams on the transmission path.

2.2 Introduction to Lidar

Lidar (light detection and ranging) is an optical remote sensing technology which detects scattered light to find range and/or other information about distant objects [1]. Use of lidar precedes the invention of the laser when in 1938 pulses of light generated by electric sparks were used for the first time to measure the height of the cloud base [2]. The term lidar was first introduced in 1953 by Middleton and Spilhouse and ever since then the progress in this area has been strongly connected with the advancement in electro-optics; in particular the invention of the laser in the 1960's and advances in optical detection techniques [3] [4].

The variety of interaction processes between the laser radiation with atoms and molecules involve a range of physical processes which allowed a wide range of variables such as temperature, pressure, humidity and chemical constituents of the atmosphere to be measured. Initially lidar techniques were primarily used as a research tool in atmospheric and earth sciences [5]. However, with the development of sub-nanosecond pulsed lasers and precise timing electronics, lidar expanded its capabilities to time-of-flight (ToF) range measurements paving its way to high-resolution three-dimensional imaging of remote objects. The shorter wavelength of operation offered by laser sources gives advantages on improved beam directionality and spatial resolution of imaged objects with comparison to that achieved by state-of-the art radars. Due to the increased spatial resolution of images, ToF lidar opened up a new avenue for three-dimensional imaging offering possibilities of improvement in many areas such as security, surveillance, cultural heritage preservation, terrain mapping and virtual reality [3].

2.3 Classification of Lidar Range Detection Techniques

Lidar range detection techniques can be characterised by the type of illumination: amplitude-modulation, frequency-modulation and pulsed or by the detection technique: coherent and direct [6] [7] [8] [9]. As shown in Figure 2.1 coherent detection can be classified into homodyne and heterodyne detection while the direct detection can be grouped into analogue and Gm detection [10].

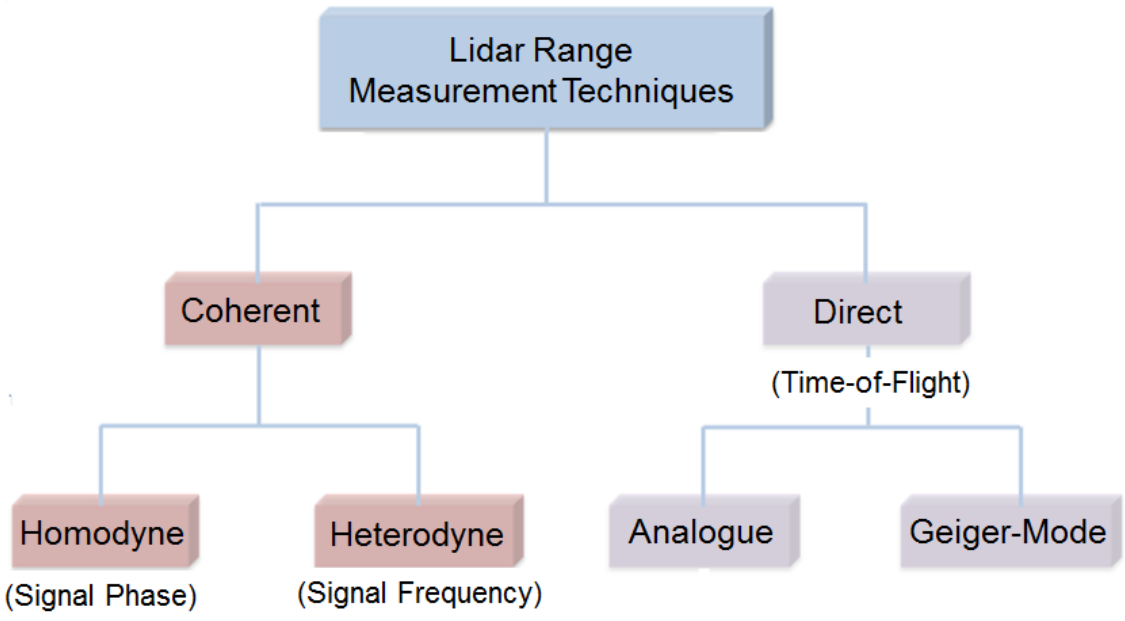

Figure 2.1. Classification of lidar range detection techniques.

Coherent detection is concerned with measuring the phase or frequency delay between the transmitted and the detected signal from which range to a target can be indirectly determined [11]. Direct detection determines range by measuring ToF of a pulse [9].

2.3.1 Coherent Detection

Coherent systems rely on the detection of a signal phase or frequency. The input signal is mixed with a reference signal from a local oscillator and the combined signal is then detected [10]. In *heterodyne* detection (Figure 2.2), the incoming (carrier) signal represented by

$$E_c(t) = A_c \cos(\omega_c t + \phi_c) \qquad \textit{Eq. 2.1}$$

where A_c, ω_c and ϕ_c represent the amplitude, angular frequency and phase of the signal respectively, is mixed with one from a local oscillator given by [10]

$$E_0(t) = A_0 \cos(\omega_0 t + \phi_0) \qquad \textit{Eq. 2.2}$$

where A_0, ω_0 and ϕ_0 represent the amplitude, angular frequency and phase of the local oscillator respectively and ω_0 is chosen to be slightly different than the ω_c [10]. The signal output of the detector, O_{det}, can be then expressed by

$$O_{\text{det}} = PA_cA_0 \cos[(\omega_c - \omega_0)t + (\phi_c - \phi_0)] \qquad \textit{Eq. 2.3}$$

where P is responsivity of the detector. Heterodyne detection allows the difference between the ω_0 and the ω_c to be measured [10]. If the frequency of the local oscillator in a system shown in Figure 2.2 is increased at a known constant ramp rate, Δf, with a ramp period, t_m, (Figure 2.3) and the frequency difference measured on the detector is $\Delta\omega=\omega_c - \omega_0$, then the round trip time of the object signal, t, is [9]

$$t = \frac{\Delta\omega t_m}{\Delta f} \qquad \textit{Eq. 2.4}$$

The range between the object and the reference beam splitter, R, is proportional to $\Delta\omega$ [9]. Since the speed of light, c, is known and the round trip time, t, is given by

$$t = \frac{2R}{c} \qquad \textit{Eq. 2.5}$$

then the range, R, can be calculated from [9].

$$R = \frac{\Delta\omega t_m}{2\Delta f} \qquad \textit{Eq. 2.6}$$

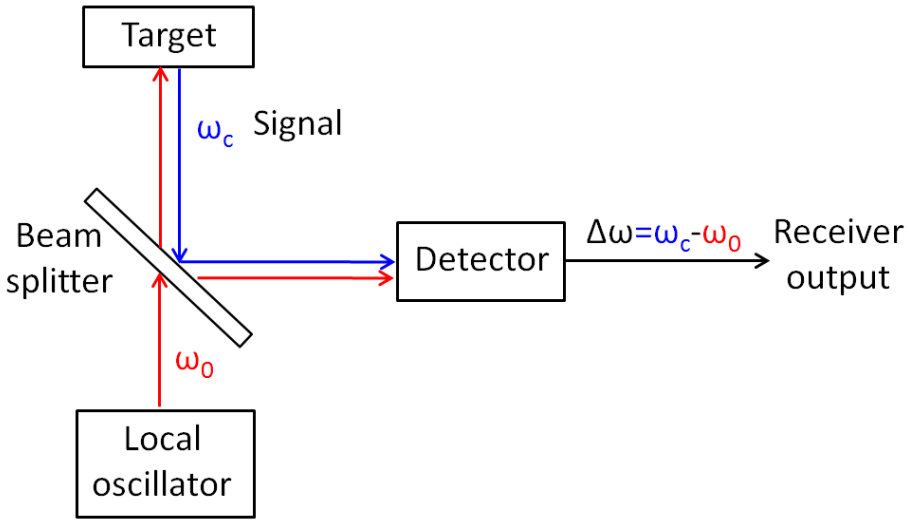

Figure 2.2. Schematic diagram of a heterodyne detection receiver. The incoming signal of frequency ω_c is mixed with a signal from a local oscillator of frequency ω_0 using a beam splitter. The frequency difference between signals, $\Delta\omega = \omega_c - \omega_0$, is recorded by a detector [10].

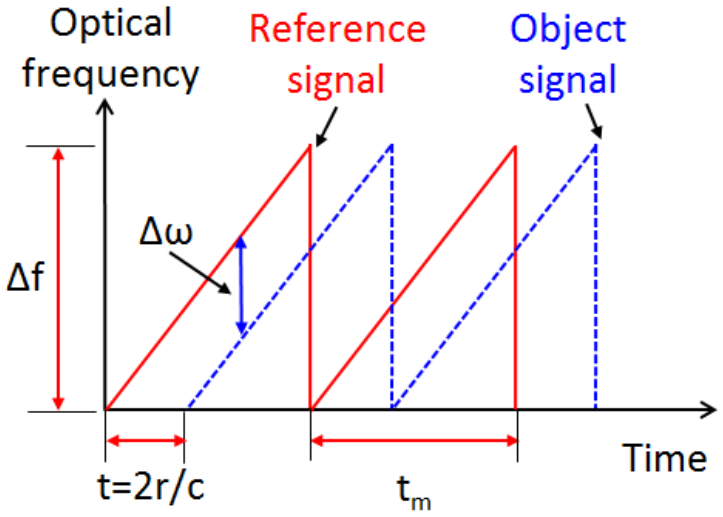

Figure 2.3. Instantaneous optical frequencies versus time for the object and reference (local oscillator) signals for a linear frequency ramp [9].

In *homodyne* detection the carrier frequency, ω_c, is set such that it matches the frequency of the local oscillator ω_0. O_{det}, can be represented by [10]

$$O_{\text{det}} = PA_c A_0 \cos[(\phi_c - \phi_0)] \qquad \textit{Eq. 2.7}$$

In this case, range to the target, R, is proportional to $\Delta\phi$ represented by the phase difference between the target signal, ϕ_c, and the reference signal, ϕ_0 and is given by [9]

$$R = \frac{1}{2} c \frac{\Delta\phi}{2\pi} \omega_0 \qquad \textit{Eq. 2.8}$$

Homodyne detection components tend to be difficult to align with comparison to heterodyne detection and is suitable in applications where complex alignment is not an issue [3][10].

2.3.2 Direct (Time-of-Flight) Detection

Direct detection is concerned with measuring the power of the signal directly on the surface the detector [10]. In direct detection, the signal output on the detector is given by

$$O_{\text{det}} = PA_c^{\,2}\left\langle \cos^2(\omega_c t + \phi_c)\right\rangle = \frac{RA_c^{\,2}}{2} \qquad \textit{Eq. 2.9}$$

where angle brackets indicate an average taken over a complete period of the function inside. Eq. 2.9 indicates that in direct detection only the signal irradiance - proportional to the square of the amplitude - can be measured [10].

Direct *time-of-flight* (ToF) ranging relies on the measurement of the round-trip time required by a pulse of light to travel from the light source to the target and back onto a detector. The first ToF ranging system was set up in the 19th century and was used to estimate the speed of light [3].

A typical setup that measures ToF is shown in Figure 2.4. It consists of several components:

- Modulated light source, typically in a form of a pulsed laser;
- Collecting lens which gathers the light scattered from the target and focuses it onto a photodetector;
- Time-resolving photo-sensor which measures the ToF of the laser pulse;
- Sensor interface which reads out the data stream from the sensor [3].

In ToF measurements the detector starts a highly accurate stopwatch synchronously with the emitted laser pulse [3]. The pulse emitted from the transmitter starts the clock while the pulse scattered from a target, which is then collected by the receiver optics and recorded by a detector, stops it.

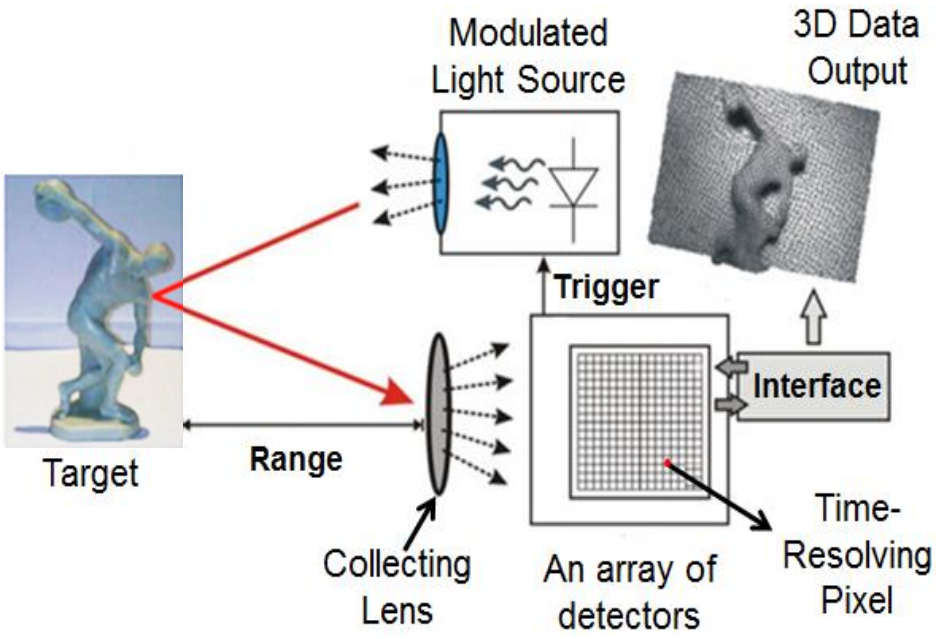

Figure 2.4. Typical time-of-flight (ToF) measuring system. It consists of a modulated light source, a collecting lens, an array of time-resolving photo-detectors and a sensor interface [3].

The time difference between the emitted laser pulse and the recorded detection event, called ToF, t_{TOF}, is then calculated with respect to a stable time reference. Since the velocity of light, c, is known, the range to the target, R, can be determined from

$$R = \frac{ct_{TOF}}{2} \qquad \textit{Eq. 2.10}$$

2.3.2.1 Transceiver Configurations in Time-of-Flight Lidar Systems

Two possible configurations for the transmitter and the receiver (collectively referred to as a transceiver) of a distance ranging lidar are possible: a bi-static configuration and a mono-static configuration. As can be seen in Figure 2.5(a), the transmitted beam can have a parallel and displaced axis to that of the receiver; this is a *bi-static configuration* while the *mono-static configuration* (Figure 2.5(b)) has a common optical axis for the transmitter and the receiver.

Both arrangements have their advantages and drawbacks. The mono-static configuration requires an additional component, such as a beam splitter or an annular mirror, which allows the laser beam to access the optical receiver. The mono-static arrangement can contribute to additional losses to the signal due to the optical component required to separate the transmitted and collected beams and generates internal backscatter from optical components inside of the system due to the laser. The

main benefit of such a setup is its compactness. In addition, when scanned single-element detector is used, illumination to the region which is equivalent to the field-of-view (FoV) of the detector, not to the entire scene, is provided. This decreases the level of required laser power and provides improved eye-safety while allowing smaller and more cost-effective laser sources.

Since the bi-static configuration transmits the beam along a different path to the receiver, it does not take the advantage of the scanning mechanism which points at the detector FoV. Therefore, all regions of interest at the scene need to be illuminated simultaneously which increases power requirements of the illuminating source. On the other hand, this arrangement eliminates the issue of backscatter.

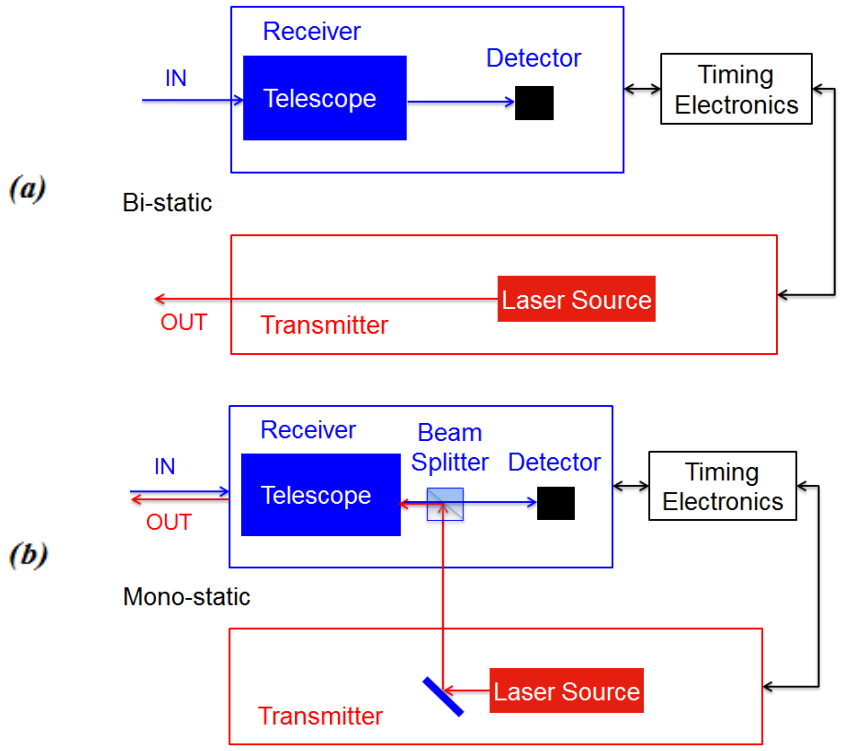

Figure 2.5. Schematic diagram illustrating two possible lidar configurations: (a) bi-static, where the laser beam is transmitted along an axis parallel and displaced from that of the receiver, (b) mono-static configuration which has a common optical axis for the transmitter and the receiver.

2.3.2.2 Analogue and Geiger-Mode Detection

Time-of-flight lidar systems can be divided into analogue or Geiger mode (single-photon) approaches. In the analogue lidar system, typically avalanche photodiodes (APDs) operating in linear amplification mode are used. On the other hand, SPADs are often used as detectors in single-photon lidar systems. More detailed information about

the operation of APDs is given in section 2.9.2. In this section, only basic differences between the linear multiplication and Geiger-mode APD detection are outlined.

In linear multiplication mode, a constant reverse bias is applied to the APD where the photocurrent generated due to the absorption of light is internally amplified and the level of signal output is proportional to the level of illumination it receives. Hence linear multiplication APDs can read signal amplitude [12].

In *Geiger-mode (Gm)*, the reverse bias is held above the avalanche breakdown point, so that if an incident single-photon creates an electron-hole pair, then a self-sustaining photocurrent can be triggered (see section 2.9.2). In this active state the diode produces a fast electrical pulse in response to the detection of a single photon [13], however, it cannot distinguish between a single-photon or two, or more, photons arriving at the same time since it is a purely triggering detector. In this mode the signal can either be detected ("1") or undetected ("0"); this discrete detection scheme can eliminate read-out noise [14]. A Gm device records whether a photon was detected in a given time window [13] and the number of detectable photons or photoelectrons shows a statistical variation which is limited by shot noise [3]. The time resolution of a single-photon lidar system also depends on the number of photons returned from the target; each photon event is an independent measurement of time and distance, meaning that the uncertainty of the distance measurement can be much less than the timing jitter of the system.

2.4 Coherent vs. Direct Detection

Heterodyne detection has been known to have advantages over direct detection: it can operate with signals which are close to the shot noise limit and - by varying the frequency of the local oscillator - the receiver can tune in to any signal frequency of interest provided that it is within the tuning range of the local oscillator. It therefore provides a possible solution to the problem of separating individual signals from the group of signals when different wavelengths are used. Although coherent detection allows a relative speed between the target and the measuring system to be calculated from the phase-shift (Doppler effect), it involves a considerable increase in system complexity, and hence cost, over direct detection systems [10].

Linear mode APDs are characterised by the multiplication gain which in turn has statistical variations leading to excess noise [13]. In this context, Gm detection is a direct detection technique which is capable of operating close to the shot noise limit.

Exploiting Gm detection can be a useful approach to improving the sensitivity of lidar applications; this is discussed in further sections.

2.5 Challenges to Existing Technologies

In recent years there has been an increasing interest in collecting three-dimensional data for the purpose of mapping and weather observations as well as in understanding, assessing and forecasting national security [15]. Specifically, strong attention is being focused on developing a wide range of applications such as:

1) Continuous, wide FoV surveillance sensors. An important aspect of this type of sensor is the potential to provide a user with detailed information about what occurred in a particular situation, such as a terrorist attack;
2) Inexpensive airborne sensors. Inexpensive, small systems mounted on lightweight drones to obtain high resolution images of the target which can be used for dangerous tasks such as explosive removal;
3) Missile warning systems. Used primarily for aircraft defence, this type of sensor requires high resolution to allow discrimination of a missile from the background clutter;
4) See-and-avoid sensors. One important application for this type of a system is to allow drones to fly under visible flight rules. For visual flight rules an aircraft is supposed to operate under guidelines of National Aviation authorities and be able to identify another aircraft and manoeuvre to avoid it as well as a pilot;
5) Infrared search and track systems. A sensor that requires high resolution to discriminate against clutter;
6) Inexpensive terrestrial based sensors. Such systems are required to support small, unmanned ground robots to obtain high resolution maps of surfaces that can be used for applications in hazardous tasks, such as removal of explosives;
7) Ground-based targeting sensors. Tanks frequently require targeting sensors that can operate over kilometre range with high spatial and depth resolution. Atmospheric turbulence can be problematic along a ground path and therefore high-speed correcting algorithms are desirable in such systems;

8) Satellite platforms. These types of systems are designed for a specific satellite mission - either space-borne or inter-planetary - and require high resolution imaging over hundreds of kilometres [15].

The requirement for such systems is primarily driven by government intelligence and defence agencies to be used as a support tool for tactical military missions. On the other hand, European Space Agency (ESA), National Aeronautics and Space Administration (NASA), National Oceanic and Atmospheric Administration, Defense Advanced Research Projects Agency (DARPA) have a strong interested in using a wide range of satellite sensors for a variety of missions.

Although each application will have specific requirements influencing the design and the choice of specific components, it is clear that there is a need for systems that can provide:

- Three-dimensional, high resolution imaging over long ranges;
- Capability of night-time imaging;
- Ease of implementation and integration with air platforms, unmanned aerial vehicles (UAVs) and satellites;
- Compensations for atmospheric turbulence.

The above requirements impose limits on a system's weight, size, and volume and demand highly sensitive detectors and low-power sources.

Conventional, commercially available distance ranging lidar systems incorporating analogue detection have higher noise and limited sensitivity when compared to coherent and Gm detection techniques. This directly translates into lower depth resolution and a requirement for a higher laser power. As discussed earlier, coherent systems often require a level of complexity greater than direct detection approaches. Hence a strong candidate with the potential to meet these challenging requirements is the emerging technology of Gm distance ranging lidar. It offers high sensitivity, high spatial and temporal resolution, kilometre range of operation, eye-safety, covertness and reduced mass and volume.

The following sections discuss the principles of single-photon lidar and time-correlated single-photon counting and provide a review of state-of-the-art single-photon imaging technology.

2.6 Single-Photon Counting Lidar

The first photon-counting lidar was developed in early 70's at the University of Texas McDonald Observatory after an optical retro-reflector was placed on the lunar surface during the Apollo 15 mission. The system was used to measure the Moon-Earth distance with centimetre accuracy using ground-based photo-multiplier cathode tubes (PMTs) [16].

The motivation behind incorporating single-photon detection in range measurements is driven by a desire to use the few available scattered photons in the most efficient way [17]. Single-photon counting lidar systems allow low-power optical sources to be used and enable the ToF to be acquired from significantly longer ranges. Theoretically, such a system requires only one detected photon to provide a range measurement as opposed to hundreds or thousands of photons in a pulse required by a conventional analogue system [18]. In practice, however, single-photon detectors are heavily susceptible to noise and even an isolated false photon event due to dark counts can cause error in the range measurement. This issue needs to be taken into consideration when designing single-photon imaging systems.

In contrast to analogue detection the timing resolution of single-photon detection is not limited by the duration or rise time of the voltage pulse [19]. It is, however, affected by the variance in the rise-time of the detector (the temporal jitter), and the number of returns measured. The jitter depends on a number of factors, including the quality of the timing electronics used, the laser pulse duration and the transit time fluctuations in the detector [20]. As a consequence, single-photon detection can provide timing errors of an order of magnitude better than that of an analogue detector significantly improving depth resolution [19].

The possibility of using weaker sources in distance ranging lidar systems can be translated into systems that are smaller, lighter and consume less power, even when operating over long distances [18]. The combined effect of all of the above factors makes a single-photon lidar a suitable candidate for long-range air/space-borne applications that require high depth resolution.

The recent availability of Gm-arrays allows complete images to be taken without scanning. This extends the advantages of single-photon counting lidar to three-

dimensional imaging lidar providing high range resolution with low average laser power.

2.7 Time-Correlated Single-Photon Counting

Since its development in the 1960's single-photon counting has mainly been used to record fluorescence decays. The technique provided excellent time-resolution and single-photon sensitivity and was ideal for measurements of fluorescence decays of materials with low photo-structural damage thresholds, typically biological samples. However, the limited throughput of the timing chain meant that detection rates were very low, typically 10's kilo counts per second (kcps), resulting in very long acquisition times. In the last twenty years timing electronics have made huge progress allowing higher data throughput. Significant advances in laser technology and increasingly powerful computer processors have made time-correlated single-photon counting (TCSPC) a realistic option in a range of picosecond optical measurements scenarios. Currently, the TCSPC technique is used in single-molecule spectroscopy, fluorescence correlation spectroscopy, optical tomography, quantum key distribution (QKD) and ToF lidar; the timing resolution, count rates and spectral coverage have improved considerably over the past 20 years [19].

TCSPC is a statistical sampling technique where the photon arrival time is measured relative to the time of laser pulse emission or a stable clock. In optical range finding, a target is illuminated by a high pulse repetition rate laser source. When a photon scattered from the target is detected, its time-of-arrival is measured with respect to the previously emitted laser pulse using a time interval analyser synchronised with a stable timing reference. The collection of time-stamps from multiple returns allows a histogram of the statistical distribution of photon arrival times to be generated [19].

2.7.1 Basic Principles of TCSPC for Distance Ranging

Figure 2.6 shows a typical TCSPC ToF ranging system. A laser pulse emitted by a high pulse repetition rate laser source triggers the timing electronics to start a clock. The pulse travels to a target from which it is reflected or scattered back to the system and detected by a single-photon avalanche diode (SPAD) which triggers the timing electronics to stop the clock. The time difference between the start and stop signals indicates the ToF which is then stored in the memory of timing electronics. The

counting process is typically repeated between 10^3 – 10^6 times for a fixed point of the scene [21].

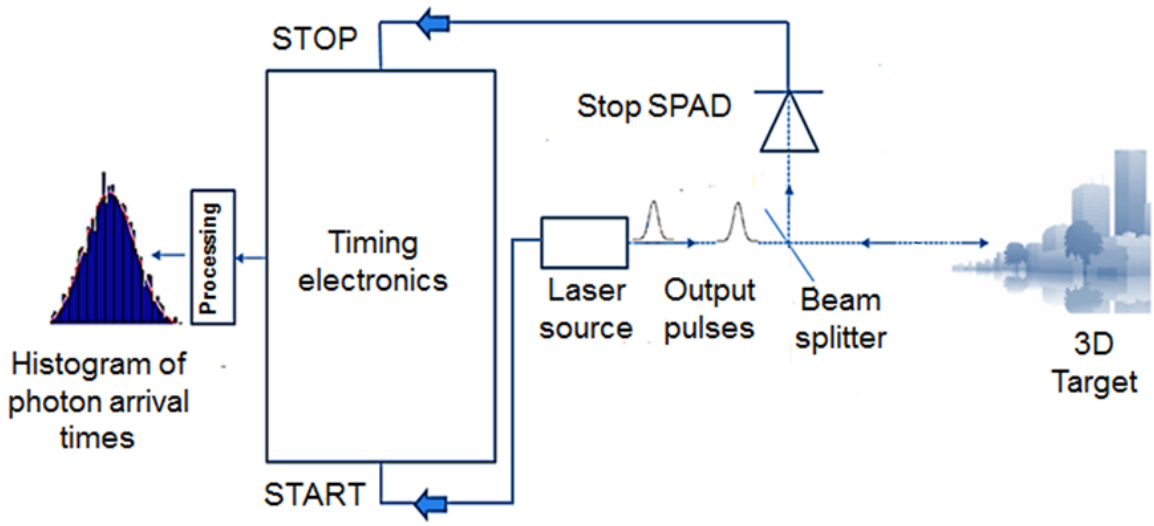

Figure 2.6. Schematic diagram of a typical ToF ranging system. The system consists of timing electronics, a pulsed laser source which, in a forward-mode, starts the counting process and a SPAD detector which stops the time counting process.

The number of required repetitons of the timing measurement depends on a variety of intrinsic and extrinsic factors such as: laser pulse power, detection efficiency of the detector, range to target, atmospheric conditions, target reflectivity and the aperture size of the collecting system. The distribution of photon arrival times is represented in a histogram the peak of which indicates the most likely ToF to the target used to calculate the range.

The TCSPC technique is ideal for low-light level sensing where the probability of a detected photon return is low [22]. If a returned pulse contains more than one photon, then the SPAD is not able to detect a second photon due to detector dead-time [21]. If the rate of photon return is a large enough fraction of the pulse rate, then this can have the effect of preferentially detecting photons at the leading edge of the pulse and distorting the distribution of photon arrival times [22]. This is known as *pulse pile-up* and it affects the timing accuracy of the measured signal [22] [21]. To avoid pulse pile-up, the intensity of the detected signal must be no higher than that necessary to detect at a detector count rate ≤ 5 % photons per pulse [19].

2.7.1 TCSPC Instrumentation

As shown in Figure 2.7, a typical photon counter consists of a pulse generator, a source, a detector, a constant fraction discriminator (CFD), time to amplitude converter (TAC), analogue to digital converter (ADC) and multi-channel analyser (MCA). The pulse generator produces a series of synchronous pulses which simultaneously trigger the source and the "start CFD" [23]. A pulse from the "start CFD" is routed to the timing electronics which is generally in the form of a TAC. The circuitry of the TAC starts the timing sequence, usually by charging a capacitor [19].

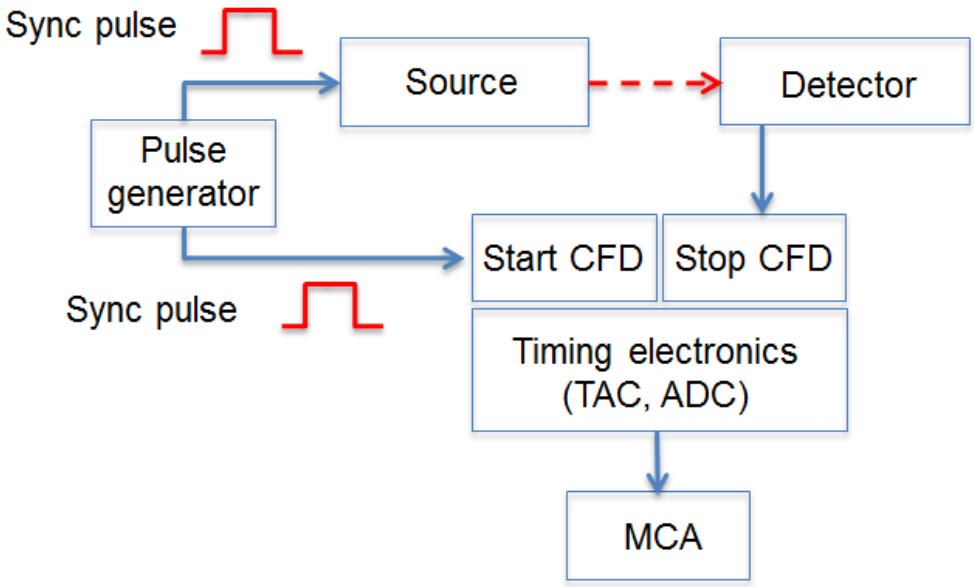

Figure 2.7. Schematic diagram of instrumentation used in single-photon counting. It consists of a pulse generator, a source, a detector, a constant fraction discriminator (CFD), time-to-amplitude converter (TAC), analogue-to-digital converter (ADC) and multi-channel analyser (MCA) [19].

The output from the source is detected by the detector, typically in the form of a photomultiplier tube or a SPAD which, on detection of a photon, releases an electrical pulse to trigger the CFD to stop the timing process. This is known as *forward start-stop mode* of operation. The stochastic nature of the avalanche process in the detector can cause pulse height timing jitter. The role of the CFD is to remove any height variation by triggering on a constant fraction of the pulse height. The role of the TAC is to measure the true difference between the start and stop signals. If no stop pulse is detected by the TAC during the time range set by the user, the TAC resets ready for the next signal. The TAC range refers to the maximum time that the TAC can take to charge, defining the maximum value of measureable time difference [19].

The ADC translates the output analogue voltage to a digital value which is then transferred to the MCA. The MCA typically contains up to 2^{12} channels which correspond to the number of time intervals within the TAC range – this defines the timing resolution (or bin width) which can be of the order of few picoseconds [19]. A count is stored in the MCA in the channel corresponding to the time difference generated by the ADC. This process is then repeated until a histogram of time differences is built up.

In reality, when taking range measurements, there are multiple periods in which no photon is detected. For high repetition rates of a light source such as 50 - 100 MHz it would be impossible for the TAC to start and stop continuously at every 10 – 20 ns. To overcome this limitation it is possible for the TAC to be initiated not by each pulse that is released from the source but only by each detected pulse [19]. The TAC is then stopped by the next pulse released by the source. This mode of operation is known as a *reverse start-stop mode* and allows the TAC to operate at repetition rates driven by the number of photon detection events, which is considerably lower than that of the source repetition rate.

A successor of the TAC and the ADC is a time-to-digital converter (TDC) which converts time domain information directly into a digital representation. Digital building blocks take advantage of reduced device geometries in terms of area, power consumption, switching speed and allows complex and more flexible signal processing [24]. Time measurements presented later in this thesis were acquired using TDC based time interval analysers (TIAs) such as HydraHarp and GuideTech [25] [26].

2.8 Analogue vs. Photon-Counting Detection

In analogue detection the detected signal can be considered to be a response function superimposed on the shot noise of the photons. In photon-counting detection the signal originates from individual photons. The analogue technique is based on direct signal digitising where the analogue detector waveform is first digitised in short time intervals and then accumulated over a number of signal periods to average over noise. The problem with this technique occurs at low intensities. In this regime the signal-to-noise ratio (SNR) significantly decreases. This suggests that analogue recording is better suited to signals of high intensity. In photon counting each pulse detected by a detector represents the detection of an individual photon. In this case it is the number of

detected photons rather than the amplitude of the signal that determines the intensity of the light at the detector [19].

Photon-counting differs significantly from analogue detection in a number of important respects which are discussed below.

In photon counting, the timing jitter depends on the variance of the rise-time of the detected pulse, which depends on a number of factors described in section 2.9.2.2. In many cases, photon-counting will yield a better timing resolution in comparison with the analogue technique.

The random nature of the multiplication process at the detector causes amplitude jitter in the voltage pulse of the detector. This is called *gain noise* and it contributes to the noise in analogue detection [19]. In single-photon detection the gain noise should have no impact on the measurements because all photons are counted with the same weight [19].

The sampling rate is the rate at which the analogue signal is digitised. Analogue detection sample rates above a few GHz are typically inefficient, inaccurate, or extremely expensive. Photon-counting allows the photon arrival time to be determined with a resolution equal to that of a channel which is of the order of few picoseconds yielding a sample rate equivalent to more than 1 THz [19].

When it comes to the *acquisition time*, it is believed that analogue techniques are faster than photon counting. Photon counting is usually considered as a technique capable of providing excellent timing resolution at the expense of extremely long acquisition times. Photon counters are limited by the detector dead-time, timing jitter of counting electronics, low pulse repetition rates and high attenuation of scattered signal. In contrast, analogue detection techniques are capable of working at very short acquisition times [19].

2.9 Single-Photon Detectors

Single-photon detectors must be capable of high signal amplification with a very low noise level. In addition, the reset time between each detected photon must be short in order to maximise the operating count rate [27]. The most common single-photon detectors are PMTs and semiconductor devices [3].

2.9.1 Photoemissive Detection

When radiation with a wavelength less than a critical value is incident on a metal surface, electrons are found to be emitted. This is called the photoelectric or photoemissive effect. When a photon of energy *hv* enters the metal it may be absorbed transferring its energy to an electron [10]. If the electron is able to overcome the potential barrier, it may escape, creating a photoelectric emission.

PMTs are photoemissive detectors capable of single-photon detection when used in conjunction with an electron multiplying stage.

2.9.1.1 Photomultiplier Tubes

A schematic diagram of a PMT is shown in Figure 2.8, it consists of a high vacuum glass envelope, several positively charged electrodes called dynodes and an anode [28].

As a consequence of the photoelectric effect incident photons release electrons from the surface of a cathode. A focusing electrode accelerates the electrons towards the electron multiplier (dynode) where it has a sufficient kinetic energy to eject a number of secondary electrons from the dynode. These secondary electrons are then accelerated to a second dynode which is held at a higher potential and where further multiplication takes place. The dynodes are kept at progressively higher voltages with respect to the cathode, with a typical difference between adjacent dynodes of 100 V. As we go down the dynode chain, an increasing number of electrons collide with subsequent dynodes; further electrons are ejected and eventually collected by the last anode. As the multiplied electrons hit the anode, the accumulation of charge results in a sharp current pulse indicating that a photon has been detected [29].

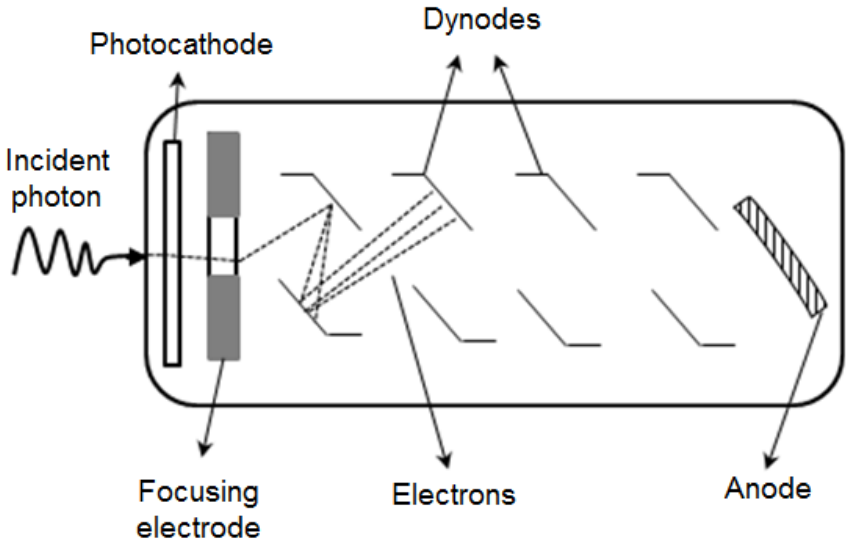

Figure 2.8. Schematic diagram of a "dynode chain" photomultiplier tube (PMT) showing the process of electron multiplication from each dynode [28].

PMTs exhibit high internal gains from 10^4 to 10^7. In comparison with semiconductor detectors PMTs offer much larger area of detection, and are more suitable for use with extended optical sources. However, they come in much larger packages and provide low single-photon detection efficiency, particularly at longer wavelengths. Typically, the timing jitter is of the order 1 ns due to transit time spread of the multiplied electrons making PMTs less suitable for single-photon ToF ranging applications [27] [28].

2.9.2 Avalanche Photodiodes

APDs consist of a p-n junction which is formed by two semiconductor crystals; one of which contains a dopant contributing to an excess of holes in the material (p-type) and the other one containing a dopant creating an excess of carriers (n-type). A diagram of the structure of the p-n junction is shown in Figure 2.9. At the interface between the two materials electrons from the n-region diffuse into the p-region. As electrons diffuse, they leave positively charged ions (donors). Likewise, holes from the p-type zone near the p-n interface diffuse into the n-type region leaving behind fixed ions with negative charge (acceptors). Therefore, the region near the p-n interface, referred to as a depletion region, becomes charged and an electric field is formed across it [30].

When the n-doped material in the p-n junction is connected to a positive terminal of a battery and the p-doped material is connected to its negative terminal (reverse bias), and the voltage is sufficiently high, then a drifting electron can gain enough kinetic energy to excite another electron to the conduction band, creating an electron-hole

pair [28] [30]. This effect is called *impact ionisation* and can also occur for holes drifting in an electric field. If the voltage is sufficiently high, then each created electron-hole pair can then create a new pair, as can the original primary carrier, thus creating an avalanche of carriers – this is referred to as *avalanche breakdown* [30]. The voltage threshold that triggers the self-sustaining avalanche is called the *breakdown voltage*. *Excess bias* is a term describing the magnitude by which the voltage applied to a SPAD exceeds the breakdown value and determines the magnitude of the electric field across the device and hence, its performance [23].

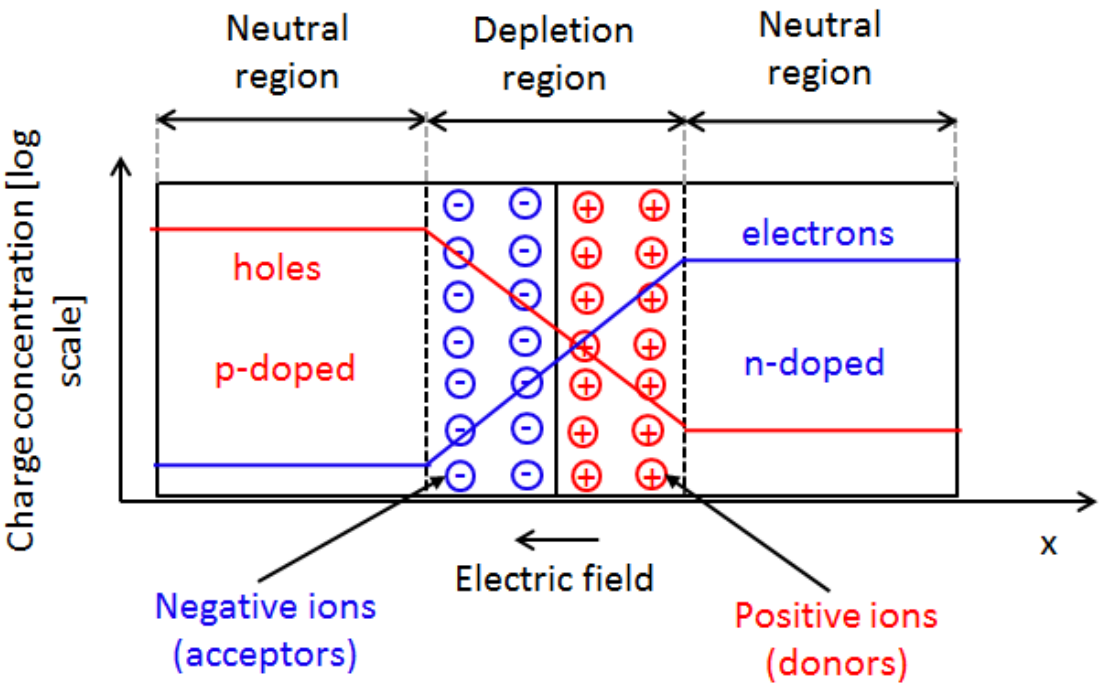

Figure 2.9. A p-n junction in thermal equilibrium under no external bias. A depletion region is created at the interface between the p-type and n-type material. The holes in the p-doped material recombine with the electrons in the n-type material creating positive ions (donors). The electrons in the n-doped material recombine with the holes in the p-type material creating negative ions (acceptors) [28].

The multiplication factor for electrons and holes varies for different semiconductor materials and the electric field magnitude. The type of carrier that is typically injected depends on *the impact ionisation coefficient* for electrons, α_e, and holes, α_h, in a material. The impact ionisation coefficients define the number of ionising collisions per unit distance and depend upon the electric field and the material. In silicon (Si), the $\alpha_e > \alpha_h$, therefore the injection of electrons is preferred whereas in germanium (Ge), the $\alpha_h > \alpha_e$, which requires the injection of holes [23].

Figure 2.10 shows the cross-sectional structure of an example reach-through silicon (Si) APD. The absorption region, where the energy of a photon is absorbed, is made of a

thick layer of un-doped or lightly doped semiconductor (π) grown in between the p and n-type material. This design ensures that an electron is injected into the region of high electric field of the predominantly electron multiplying structure. By making the layer sufficiently thick, the design also ensures that almost all the incident photons are absorbed within the depletion region [28].

A photon that is absorbed within the π region creates an electron-hole pair. The hole travels toward the negative terminal of the contact while the electron travels in the direction of the positive terminal. In the multiplication region, where the electric field is high, the electron gains enough energy from the field between collisions to excite another electron from the valence band into the conduction band, creating an additional electron-hole pair [31]. These new carriers can also create new electron-hole pairs [30] [31]. If the electric field applied across the APD is above the avalanche breakdown voltage, then a single photon generated carrier can induce a self-sustaining avalanche [28].

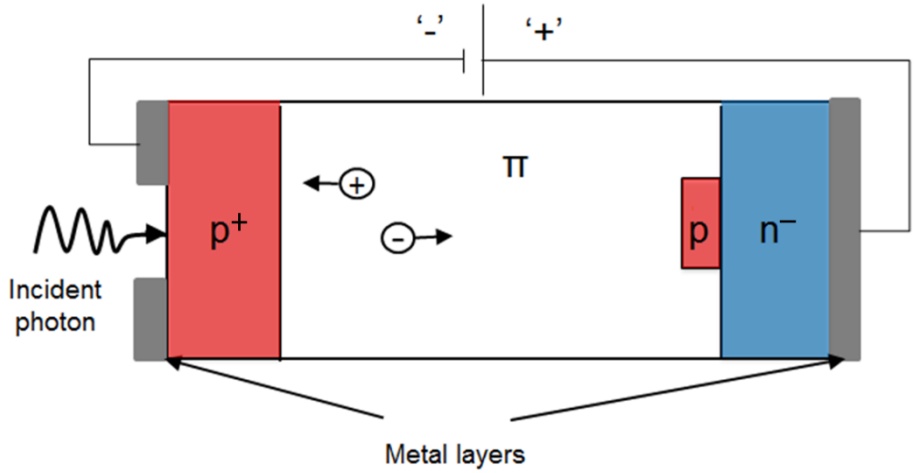

Figure 2.10. Cross-sectional structure of a reach-through Si avalanche photodiode (APD) [28].

In an electric field which is higher than the breakdown voltage, a single electron or hole can initiate a self-sustaining current which is readily detectable by an external circuit. This mode of APD operation is referred to as *Geiger-mode* and the device is called a single-photon avalanche diode (SPAD) [13]. In order for the device to detect more photons it is necessary to reset the detector through the process of *quenching* which is described in section 2.9.2.1 [28].

2.9.2.1 Quenching

Quenching is a process of detecting and stopping an avalanche and is followed by resetting the bias conditions to bring the SPAD back to its original quiescent state [32]. During this reset process, the detector cannot detect photons, and the duration of this process is called the detector *dead-time* [32].

Quenching requires a number of steps to be undertaken in the following sequence: detection of the level of avalanche current, generation of an electrical signal that is closely time-correlated to the detected avalanche current, reduction of the voltage below the breakdown level and finally, restoration of the voltage to the operating level [28].

There are three forms of quenching applied to detectors: passive, active and gated [28]. *Passive quenching* is the most elementary approach adding a quench resistor in series with the SPAD. When a photon is detected by a SPAD, it is followed by the avalanche breakdown event and the fast build-up of a current related to the bias voltage. Prior to the avalanche, most of the voltage is dropped across the non-conducting SPAD, however during the avalanche most of the bias becomes dropped across the resistor [32]. As a consequence of this, the bias voltage across the SPAD device drops below the breakdown voltage, effectively turning the detector off and quenching the avalanche. Passive quenching is simple to implement but the long voltage recovery time limits the operating frequency. Reducing the detector dead-time is essential for applications demanding high photon count rate. Other approaches like active quenching offer the potential of lower dead-time than passive quenching [23].

In *active quenching*, a circuit is used to sense a steep increase in the avalanche current through a resistor and provides a digital output pulse synchronous with the photon arrival time. Subsequently, the bias voltage is reduced to below the breakdown voltage. The device then quickly recovers the bias to above the breakdown value, ready to detect another photon. The dead-time can be of the order of few nanoseconds allowing photon detection at a rate of hundreds of MHz [28].

The circuits described above operate in the so-called *free running mode*. This way, outside the dead-time, the SPAD is always ready to detect photons. In the case of time-of-flight ranging, the signal from a target can only occur in a well-defined timing interval after each transmitted laser pulse. It is therefore convenient to enable the detector only during those particular time intervals. This type of quenching is called

gating and relies on keeping the bias voltage below the breakdown voltage and increasing it to the desired level for a well-defined interval that coincides with the expected photon arrival [33]. The gate-on period, called the *gate width* is typically between 10 ns to 1 μs.

2.9.2.2 SPAD Performance Indicators

The primary role of a detector in a single-photon counting system is to efficiently detect single photon arrivals with a high degree of temporal precision. The degree of effectiveness to which the detector performs this role is determined by a set of performance parameters such as photon dark count rate, detection efficiency and timing jitter [32].

Dark counts are events that trigger the avalanche without the absorption of any incident photons and occur as a result of three phenomena:

1) Thermal excitation of carriers into the conduction band due to current leakage [23];
2) Release of trapped carriers from defects in the material, also known as *afterpulsing*, which occurs during the device breakdown when the large flow of charge through the device causes trap centres to fill [23]. Carrier trap centres are associated with defect states caused by the presence of impurities or lattice imperfections. Any such defect state can act as a recombination centre if it is able to trap a carrier of one type and subsequently capture a carrier of the opposite type, thereby enabling them to recombine [10]. The majority of trapped carriers are released during the quenching process. However, if the device is returned above the breakdown voltage before all the traps have emptied then the released carriers can cause another avalanche long after the initial avalanche event, contributing to the overall detector dark count rate. High quality crystals, such as silicon, can be grown relatively free of defects hence, there is a reduced probability of afterpulsing in this material;
3) Band-gap tunnelling occurs when an electron tunnels from the valence band to the conduction band and it is independent of the trigger rate [23]. Quantum mechanics predicts that there is a low probability that a particle will travel through a potential barrier by "borrowing" energy from its surroundings.

At higher excess bias levels dark counts become more problematic. The increase in electric field increases the probability of thermally generated carriers drifting into the multiplication region as well as tunnelling. Higher fields and thus larger avalanche

currents result in more traps to be filled which causes afterpulsing. Temperature can also have negative effects on dark counts. At higher temperatures there is an increase of thermally excited carriers and the probability of tunnelling also rises [23]. In the case of long trap times, operating in a gated mode can be beneficial because most of the traps can be emptied during the hold-off time which decreases the probability of dark counts due to afterpulsing.

Single-photon detection efficiency (SPDE) is the probability that an incident photon will trigger a self-sustaining avalanche and is defined as

$$SPDE = P_A \times P_T \qquad \textit{Eq. 2.11}$$

where P_A is the probability of a photon being absorbed and the generated carrier being swept into the multiplication region of a SPAD and P_T is the probability that a carrier, once inside the multiplication region, will trigger an avalanche [23]. *SPDE* can be calculated from the following

$$SPDE = \frac{N_{MP}}{N_{IP}} \qquad \textit{Eq. 2.12}$$

where N_{MP} refers to a number of measured photon events per unit of time and N_{IP} is a number of incident photons per unit of time [23]. Experimentally, N_{MP}, is found by measuring the power of an incident beam. Given that the wavelength of the incident beam and the energy of a photon are known, then the number of incident photons can be calculated. N_{IP} can be found by subtracting the average level of measured dark counts from the total number of recorded photon events.

High excess bias which creates high electric fields has a positive effect on single-photon detection efficiency, D_E, because it increases the trigger probability. As the temperature increases the band gap of the material tends to narrow which can increase the probability of absorption. In addition, the probability of a carrier drifting into the high electric field region increases, increasing the P_A [23].

When photons are incident on a SPAD, and originate from a source with very short pulse duration and with well-defined repetition rate, the temporal position of the resulting avalanche breakdown pulse has a statistical variation. This effect is called *timing jitter* of the detector.

The timing jitter of a SPAD detector is affected by the following three factors:

1) Avalanche build-up time. The rate over which the avalanche spreads from the seed point to the active region is proportional to the voltage. This means that for higher values of excess bias the avalanche spreads more quickly which in turn decreases the build-up time;
2) The position where the photon is absorbed. The position of photon absorption and carrier generation in the absorption layer depends on the absorption coefficient. A carrier generated by a photon absorbed outside the depletion region takes longer to drift into the multiplication region compared to carriers absorbed within the depletion region. This difference can be hundreds of picoseconds;
3) The stochastic nature of the multiplication process. Because the multiplication process is random, there is a variation in the build-up time of the avalanche current. This causes timing jitter between the beginning of the avalanche pulse and the time when it has reached a large enough value to trigger timing electronics [23]. An increase in the electric field across the multiplication layer results in a decrease of the timing jitter.

2.9.2.1 Silicon SPADs

Silicon SPADs (Si-SPADs) are sensitive to wavelengths throughout the visible spectrum up to a wavelength of approximately 1.1 μm corresponding to the silicon bandgap energy [15]. In a thick junction geometry, they exhibit a detection efficiency of ~70% at a peak wavelength of ~ 700 nm [23]. Si-SPADS can be divided into two main geometries: thin and thick junction. The thin junction device is characterised by a thin depletion region of a few μm whereas for the thick junction device the depletion region is extended to a few tens of μm [28]. The cross-sections of a thin junction Si-SPAD are shown in Figure 2.11. A reduction in the depletion region thickness improves the timing jitter. However, it also causes a reduction in detection efficiency as photons cannot be absorbed as effectively within the depletion region [23].

Typically, thin junction devices have 20 ps timing jitter full width half maximum (FWHM) whereas thick junction devices, shown in Figure 2.12, generate a timing jitter of the order of several hundred picoseconds. Thick junction Si-SPADs generally have the highest detection efficiency at visible wavelengths [27].

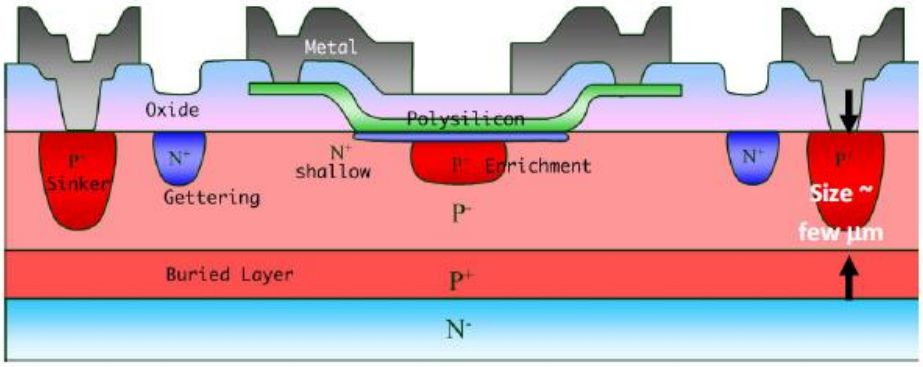

Figure 2.11. Cross-section of a structure of a thin junction Si-SPAD [27].

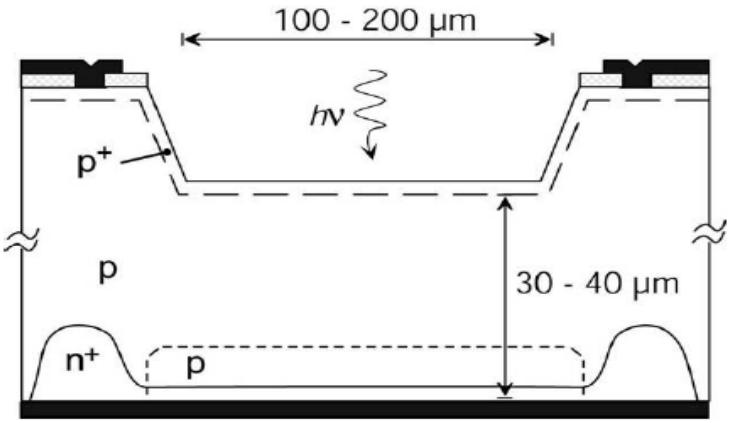

Figure 2.12. Cross-section of a structure of a thick junction Si-SPAD [27].

There has been an interest in producing Si-SPADS using a standard Complementary Metal-Oxide-Semiconductor (CMOS) technology. A great advantage of CMOS SPADs is that they have the ability to integrate into a complete imaging system, including pixel control electronics, addressing and control circuitry, analogue-to-digital conversion, and even some signal processing, into a single chip that has relatively simple digital interfacing requirements and does not require the user to design analogue read-out electronics [15]. Low cost and ease of fabrication means two-dimensional arrays of SPADs can now be made to produce focal plane arrays.

Single-element Si-SPAD detectors are available commercially from Perkin Elmer Optoelectronics [34] and Micro Photon Devices (MPD) [35]. Arrays of Si-SPADs are also commercially available from MPD [36] [37].

2.9.2.2 InGaAs/InP SPADs

InGaAs/InP SPADs work beyond the silicon cut-off wavelength and offer high quantum efficiency between 1.3 µm to 1.55 µm. Operating at those wavelengths can be

beneficial for lidar applications because of increased eye safety thresholds and reduced solar background irradiance.

A cross-section of a typical InGaAs/InP SPAD structure with a plot of electric field profile across different layers of the device is shown in Figure 2.13. The absorption of a photon occurs in the InGaAs layer. This region is not suitable for multiplication; a narrow band-gap present in this layer would contribute to band-to-band tunnelling at electric field values much lower than that required to instigate impact ionisation [27]. A photo-generated hole created in the absorption region must pass into the InP layer where it undergoes avalanche multiplication via impact ionisation [28]. In order for the hole to pass from the narrow band-gap InGaAs layer to the wide-band InP layer, the hole needs to overcome the valence band discontinuity between the hetero-interface. To facilitate this transition and avoid the possibility of recombination, an InGaAsP layer, with a band-gap intermediate to that of the InGaAs and InP layer is grown in between the two materials [38].

An InGaAs/InP SPAD can be easily integrated with single-photon counting electronics. In this configuration a gated quenching circuit can be modulated by a gated pulse generator which determines the frequency and duration of a gate. During the gate activation period the SPAD is biased above the breakdown voltage, ready for the detection of a single-photon. After the initiation of an avalanche the bias is reduced to below the breakdown voltage until the next gate window [38].

InGaAs/InP SPADs are commercially available from MPD in Peltier-cooled packages [39].

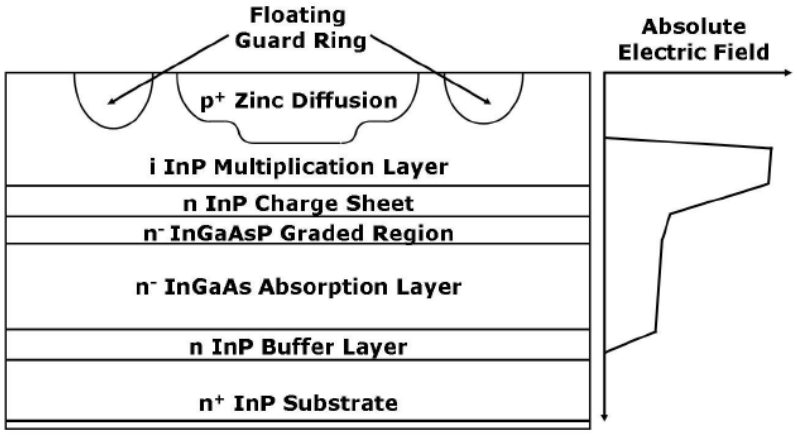

Figure 2.13. Cross-section of an InGaAs/InP SPAD structure and a plot of absolute electric field profile across different layers of the device [28].

2.9.2.1 Princeton Lightwave InGaAs/InP 32 × 32 Array

In [40] [41] [42] the authors reported on the development of a camera that uses a two-dimensional array of InGaAs/InP-based Gm-SPADs capable of detecting single photons at shortwave infrared with high quantum efficiency and low dark count rates. Each pixel of the array was hybridised to CMOS read-out circuitry enabling independent ToF measurements for each of the pixels at a maximum frame rate of 186 kHz. Micro-lens arrays were assembled on the front layer of the camera and enable a fill factor of 75 % [40].

The camera is available to operate in two spectral regions: 920 nm - 1140 nm (fabricated using an InGaAsP absorber) and 920 nm - 1620 nm (fabricated using an InGaAs absorber). The first generation of these focal planes were available in a 32 × 32 detector format, composed of 100 µm pixel pitch. However, the more recent generation has been extended to a format of 128 × 32 pixels with a pixel pitch reduced to 50 µm [43].

A schematic cross-section of the sensor design is shown Figure 2.14. It consists of a chip stack with integrated circuit, the SPAD array and the array of micro-lenses attached to a ceramic interposer. The SPAD was bonded to a custom CMOS integrated circuit providing a frame read-out time of ~ 3.33 µs (~ 186 kHz). Each pixel contains an independent counter providing independent time-stamps with bin resolution of 250 ps and detection efficiency of 18 % to 22 % at 1550 nm wavelength (for bias voltage of 73 V and excess bias of 3.3 V). The camera operates in a gated mode with gate range setting between 5 ns and 2 µs and timing jitter between 350 ps to 500 ps and is supplied with a comprehensive, Graphical User Interface (GUI) driven control interface [44].

Optical-cross talk is a common problem that occurs in array detectors. It refers to a process where the avalanche current generates photons due to hot carrier luminescence (~ 1 photon per 10^6 avalanche carriers). The luminescence - induced photon can then be detected by the neighbouring pixel. To minimise the probability of this cross-talk, isolation trenches were etched along pixel boundaries [44].

Fill factor of an image sensor describes the ratio between the pixel light sensitive area to its total area. In SPAD arrays, a monolithic process involves a partition of a pixel into detector and circuit sections thus limiting the fill factor. Effective fill factor of the Gm-array for broad illumination is ~ 9 %. However, when a microlens array – which

converges light from the whole area of a pixel onto a photo-sensitive area – is used, fill factor of ~ 75 % is achieved [44].

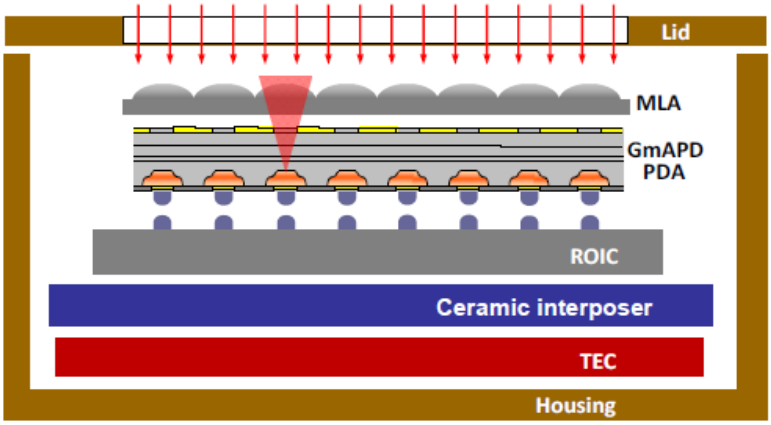

Figure 2.14. Cross-section of the Geiger-mode APD design of the focal plane array. It consists of the chip stack with integrated circuit, an APD array and a microlens array attached to a ceramic interposer and cooled by a thermoelectric cooler (TEC) in a sealed housing [44].

Figure 2.15(a) shows a 32 × 32 InGaAs/InP SPAD sensor and Figure 2.15(b) shows an integrated camera module of dimensions 10 × 10 × 8 cm.

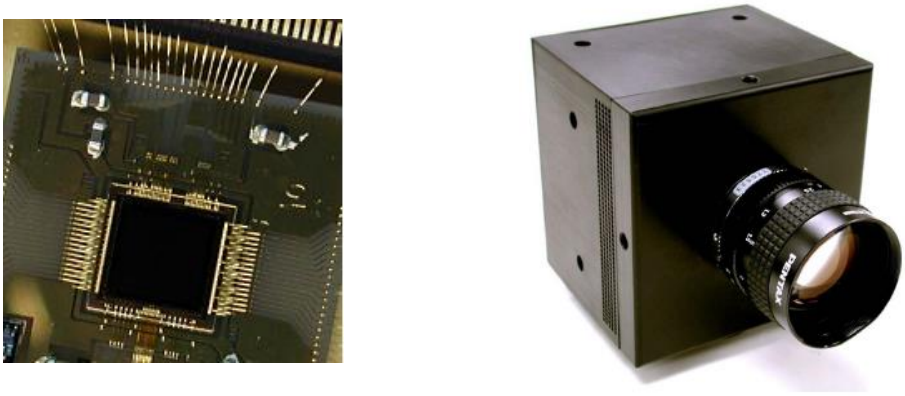

Figure 2.15. A photograph of (a) a 32 × 32 InGaAs/InP SPAD sensor, (b) an integrated camera module of dimensions 10 × 10 × 8 cm [43].

2.10 Photon Statistics

2.10.1 Poisson Probability on n-Photons in the Pulse

Assuming that there is a source generating photons at a mean rate known to be n photons in a specified interval, then the statistics of the Poisson distribution defines the probability P_N of N photons being received in a randomly selected interval of the same specified length as [23].

$$P_N = \frac{n^N e^{-n}}{N!} \qquad \textit{Eq. 2.13}$$

For example the probability of receiving 1 photon when the mean rate is known to be 5 is ~ 0.034. The probability distributions for a number of *n* values are shown in Figure 2.16.

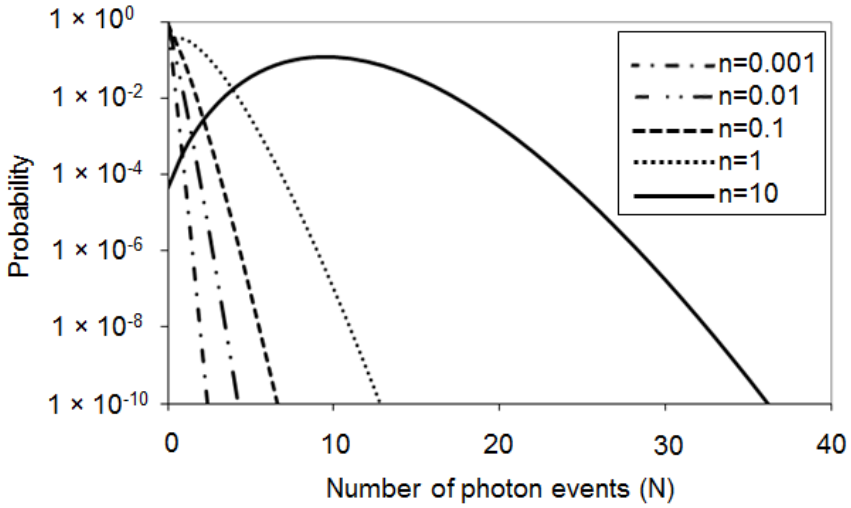

Figure 2.16. Graph showing the probability P_N for N photons being received for an average number of photons in a pulse varying between n = 0.001 and n = 10.

2.10.1 Probability of i-th Photon Being Detected

If a pulse containing two or three photons reaches the single-photon detector then only the first detected photon is registered since only one avalanche breakdown can be recorded within each time period *T*. Therefore, the probability of detecting a photon at the front of the pulse is higher than the probability of detecting a photon at the back end of the pulse. The probability of detecting the first photon is equivalent to the detection efficiency of the sensor, while the probability of detecting each subsequent photon is subject to the first photon not being detected [23]. The probability P_i of detecting *i*-th photon in a pulse is given by

$$P_i = P_{(i-1)} \times (1 - D_E) \qquad \textit{Eq. 2.14}$$

where D_E is the single-photon detection efficiency of the SPAD detector [23]. The probability of a detection of *i*-th photon in a pulse is plotted and shown in Figure 2.17 for D_E values between 0.001 and 0.99.

Figure 2.17 shows that the probability of detecting photons at the trailing edge of a pulse is low when the detection efficiency of a device, D_E, is high (pile-up effect is

more likely to occur). For low detection efficiency, D_E, the likelihood of detecting a photon is approximately uniform across the pulse.

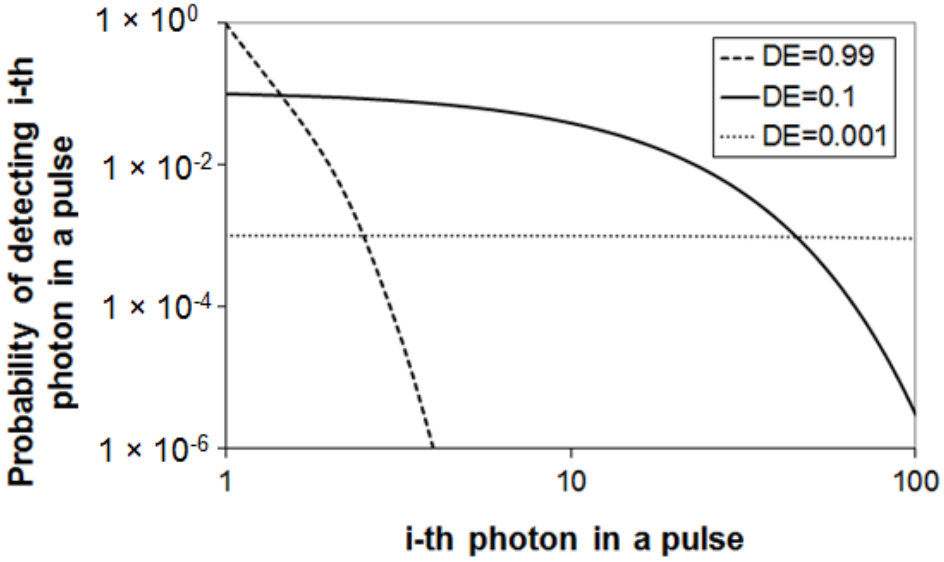

Figure 2.17. Plot showing probability of detecting the i-th photon in a pulse for detection efficiency D_E between 0.001 to 0.99.

2.10.2 Photo-Count Probability

Summing the probabilities of detecting each subsequent photon in a pulse defines the probability of a count, P_c [23]

$$P_c = \sum_{i=1}^{N} P_i \qquad \textit{Eq. 2.15}$$

Figure 2.18 shows a graph of probability of a photo-count depending on the number of photons in a pulse, N_p.

The overall probability of a SPAD registering a count, P_{rc} is given by [23]

$$P_{rc} = \sum_{N=1}^{N\max} (P_N \times P_C) \qquad \textit{Eq. 2.16}$$

Figure 2.19 shows a plot of probability of recording a photo-count, $P_{rc,}$ by a SPAD operating at a detection efficiency, D_E = 0.22 against the attenuated laser pulse energy between 0.1 nJ to 20 µJ.

The graph shows that the probability of recording a count increases linearly to about 0.6 µJ and above that it is constant at nearly 1.

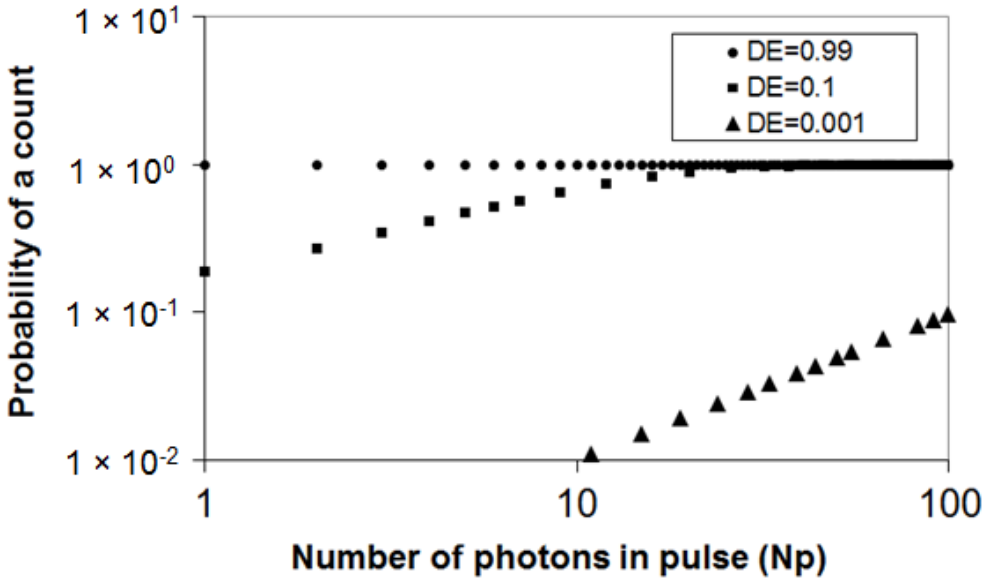

Figure 2.18. Graph showing probability of detecting a photo-count versus the number of photons in a pulse, Np, for detection efficiency D_E between 0.001 to 0.99.

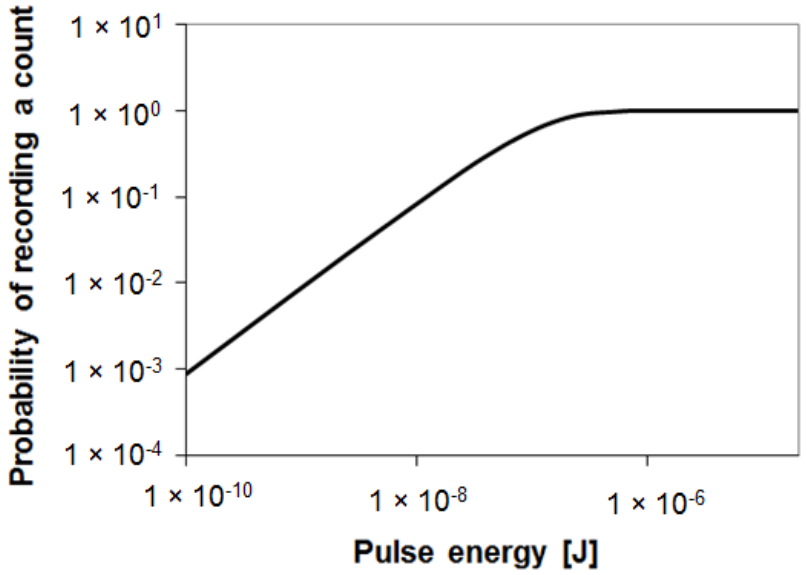

Figure 2.19. Probability P_{rc} of recording a photo-count by a SPAD operating at a detection efficiency D_E = 0.22 against the attenuated pulse energy at 1550 nm.

2.10.3 Histogram Generation

During a depth measurement the return photons are recorded by a detector and time-tagged by timing electronics. The time of arrival of each photon is recorded with a resolution depending on the width of a time bin (see section 4.9) and is represented in a histogram [19]. As shown in Figure 2.20, the histogram can give an accurate

representation of a waveform of the repetitive signal of an optical pulse scattered from a target [19].

The histogram represents statistical variations in photon arrival times. These variations account for the shape of the optical pulse, the timing jitter of a detector and the response of the timing electronics. As discussed earlier, the timing jitter of a detector is primarily caused by the avalanche build-up time and the position where the photon is absorbed within the device. In addition, the shape of the histogram from a TCSPC system containing a SPAD detector can be affected by photons absorbed outside the detector depletion region contributing to a slow diffusion tail in the timing response, leading to an asymmetric temporal profile [19]. The response of the timing apparatus depends on the timing jitter between the laser trigger and the rising edge of the detector avalanche pulse and the laser pulse duration [19]. Typically, the timing jitter of detector tends to have the most significant contribution to the overall time response.

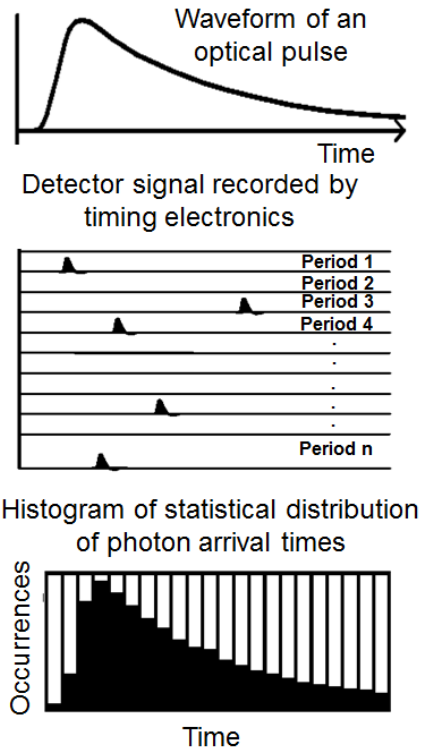

Figure 2.20. Figure illustrating the principle of histogram generation in single-photon counting [19].

2.10.4 Signal-to-Noise Ratio in TCSPC

In any type of counting problem, the probability distribution of a given number of random events occurring in a fixed interval of time - assuming that these events occur independently - is represented by a *Poisson distribution* [45]. The count rate recorded

over an interval represents an estimate of the mean count rate. The probability of observing any specific number of counts is described by a Poisson probability function with a mean μ and variance $\sigma^2 = \mu$. The variance σ^2 equals the number of photon counts, N_T, recorded by a detector during the acquisition time. The uncertainty, or standard deviation, in the number of counts is proportional to the square root of the variance. The variance, σ_i, corresponds to the *SNR* of the single-photon counting technique recorded in the absence of background counts [46].

$$\sigma_i = SNR = \sqrt{N_T} \qquad \textit{Eq. 2.17}$$

Figure 2.21 shows the ratio of standard deviation, $\sqrt{N_T}$, to number of photon counts, N_T, versus the number of photon counts and indicates that by increasing the measurement time and hence the number of detected photon counts it is possible to decrease the ratio of standard deviation to mean count rate and therefore increase the accuracy of the measurement [46]. The experimenter must decide on the acceptable level of uncertainty that can provide the best result.

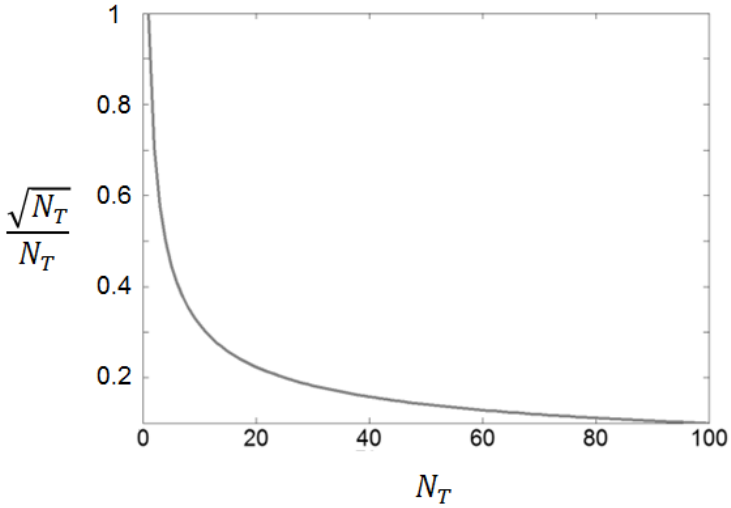

Figure 2.21. The ratio of standard deviation, $\sqrt{N_T}$, to number of photon counts, N_T, versus the number of photon counts.

In real experiments, both ambient light and dark counts generate background noise. This creates temporally uncorrelated events in a histogram. The *SNR* defined earlier in Eq. 2.17 does not include background counts. In order to find experimental signal-to-noise ratio, SNR_E, it is necessary to take into account the noise which can be defined as the ratio between the maximum peak height and the background level. If N_T denotes counts that correspond to the total number of counts at the peak intensity and N_B refers to counts that correspond to background intensity, then the *SBR* can be expressed by Eq. 2.18 [47].

$$SBR = \frac{N_T}{N_B} \qquad \textit{Eq. 2.18}$$

The SNR_E can be then defined as [47]

$$SNR_E = \frac{N_T}{\sqrt{N_T + N_B}} \qquad \textit{Eq. 2.19}$$

Eq. 2.19 shows that the value of SNR_E is close to the SNR only when SBR is very high, i.e. when $N_B << N_T$ [47].

2.10.5 Time Resolution vs. Number of Photon Events

In [47] Pellegrini et al. experimentally determined the effect of the varying number of photon counts, N_T, on time resolution of a ToF ranging TCSPC system. In the experiment 20 sets of range measurements between a reference surface and a static target were taken (all having the same distance between the reference and the target and the same number of counts, N_T). This was repeated seven times for different values of N_T in the range of 10 to 10^6. The distance between the target and the reference surface was then calculated for each value of N_T. The standard deviation of the distance calculated for the 20 independent measurements indicates the accuracy of the depth resolution of the system for various values of N_T. The resulting plot of time resolution versus the total integrated number of photon events, N_T, is shown in Figure 2.22.

Simulated standard deviation of the measured distance - with parameters and number of data sets matching to those taken during experiments - is also plotted in Figure 2.22 . In this case the uncertainty in the calculated distance, σ_{Dist}, is given by

$$\sigma_{Dist} = \frac{\sigma_{Jitter}}{\sqrt{N_T}} \qquad \textit{Eq. 2.20}$$

where σ_{Jitter} is the mean timing jitter of the whole TCSPC system in each measurement [47].

According to the results of this study a resolution of 3 mm can be achieved with only 10 scattered photons from the target when an overall instrumental response of ~ 34 ps is used [47].

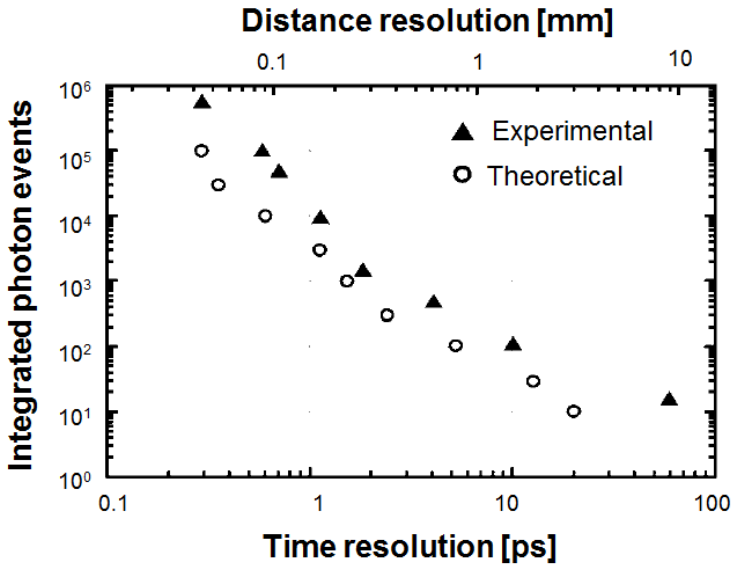

Figure 2.22. Number of photon counts, N_T, versus distance and time resolution. Both the experimental and theoretical results are shown [47].

2.10.6 Instrumental Response Function

The maximum sensitivity at which a photon-counting system is capable of operating at is called the *instrumental response function* (IRF) [46]. An example of instrumental response function for a single-photon counting setup measured with a Si-SPAD detector is shown in Figure 2.23.

The shape of the instrumental response is represented by a convolution between the temporal width of an optical pulse, the time response of the detector and the response of the timing apparatus [46]. The FWHM of the instrumental response of the system shown is ~ 300 ps.

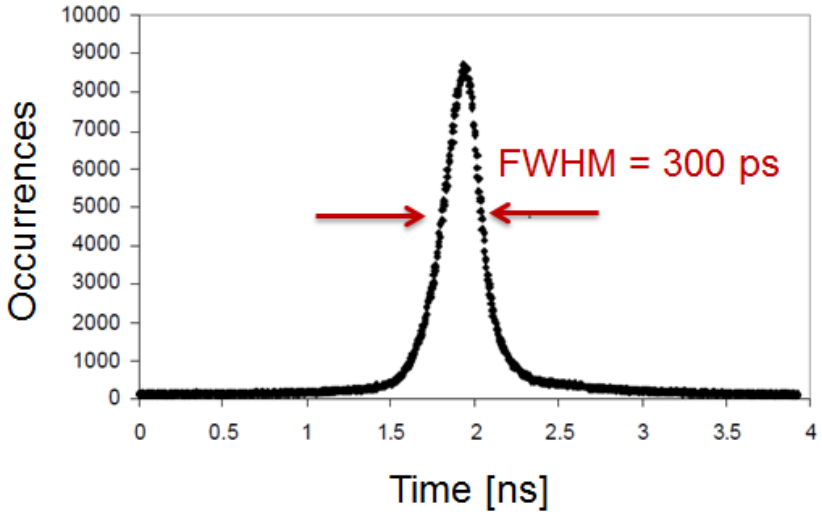

Figure 2.23. An example of an instrumental response function of FWHM = 300 ps measured with a Si-SPAD detector [23].

2.10.7 Summary of Photon Statistics

Total number of counts imposes a limit on the precision with which a location of the peak can be determined. As indicated by Eq. 2.17, by increasing the number of detected counts the ratio of standard deviation to mean count rate can be increased which in turn increases the depth resolution of the measurement. In photon-counting a large number of events must be accumulated to achieve a standard deviation of less than 1%.

In single-photon lidar, the ToF of each individual photon is measured and represented in a histogram in order to determine the range to an object. The number of events counted over the duration of the measurement exhibits statistical fluctuations described by the Poisson probability distribution. These fluctuations limit the precision to which the location of a peak - and therefore the range to a target - can be calculated. A simple technique for locating the position of a peak is the least squares fit described in section 4.13.1.1. In section 5.8.2.1 a cross-correlation technique is also described.

2.11 Range Ambiguity

Taking ToF measurements with a periodic illumination range-finder can introduce range ambiguity. As shown in Figure 2.24, when multiple pulses are in transit between a transmitter, a target and a receiver, it cannot be distinguished which laser pulse was detected. Assuming the range return time is greater than the repetition period of the laser source, the return signal, *Rx*, could be caused by any previously transmitted laser pulse, *Tx* [48] [49].

In a periodic illumination range-finder, the minimum distance that can be unambiguously determined, d_{rep}, is that distance which allows only one optical pulse in transit at one time [50]. For a repetition rate, f_{rep}, this corresponds to

$$d_{rep} = \frac{c}{2 f_{rep}} \qquad \textit{Eq. 2.21}$$

Hence, a repetition rate f_{rep} = 125 kHz, which was used in experiments described in this thesis, limits the range which could be unambiguously determined to 1.2 km. A reduction of the repetition rate, without any other changes in the system configuration, will increase the required data acquisition time [50]. In principle, arbitrarily long unambiguous distances can be achieved using random pattern techniques. In this technique, one key metric of the emitted signal undergoes a random or pseudo-random

modulation. Correlation of the return signal to a time-shifted version of the input modulation is used to calculate the unambiguous target range [50].

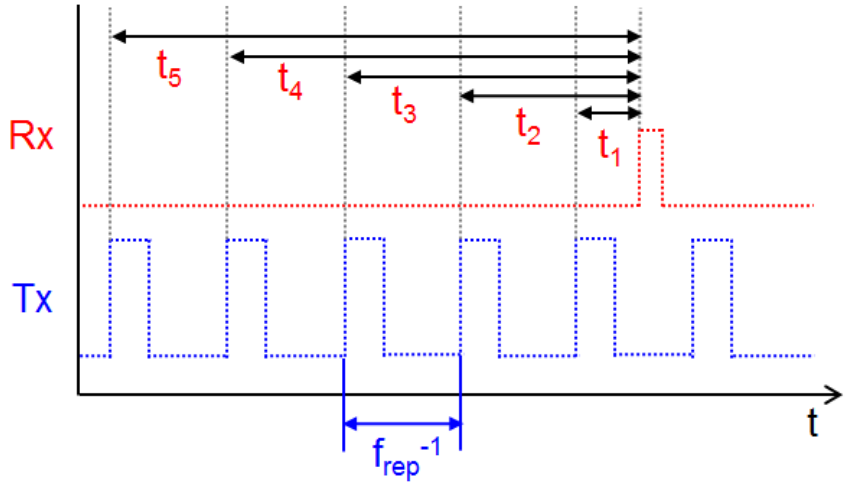

Figure 2.24. Range ambiguity in a periodic illumination ToF range-finder.

2.12 Review of Time-of-Flight Single-Photon Distance Ranging Systems

A broad range of ToF ranging systems that use single-photon detection have been described in scientific literature. The design and choice of components of each system is shaped by the specific application. Design features of these systems vary in terms of wavelength of operation, transceiver configuration, size, weight, volume, pulse repetition rate, power and the number of beams of the laser source, parameters of the receiving optics, scanning mechanism, acquisition time, choice of timing electronics and the number of detector pixels (single-element or array of multiple detectors). These features determine the limits on spatial and temporal resolution, FoV, maximum and minimum range of operation and the characteristics of targets that can be imaged.

The vast majority of developmental work for single-photon distance ranging has been undertaken by researchers from the NASA Goddard Institute for Space Studies, Massachusetts Institute of Technology (MIT) Lincoln Laboratories, Swedish Defence Agency, Heriot-Watt University and Princeton Lightwave Inc.

2.12.1 Satellite Laser Ranging

Satellite range finding was first successfully demonstrated in 1964 by the NASA Goddard Space Flight Center and achieved 2 - 3 m resolution compared to the 50 m or

more provided by radar at that time [17]. This improvement in resolution represented a significant step-change in capability for the precise determination of satellite orbits.

Satellite laser ranging (SLR) measured a round-trip time of an optical pulse transmitted from Earth to a passive retro-reflector mounted on an orbiting satellite. The source used in the initial experiment was a 1064 nm wavelength Nd:YAG laser operating at a repetition rate of 20 Hz and emitting few hundred picoseconds duration pulses of 100 mJ energy. The laser beam was directed towards the satellite using a positioner with 5 arcsec pointing accuracy. The signal reflected from the retro-reflector was then collected by the ground-based telescope and detected by a PMT. The ToF was measured using a time interval analyser with 70 ps resolution [51].

Currently there are about 23 available Earth-based SLR systems with retro-reflectors mounted on satellites orbiting Earth at distances between 960 km and 20,000 km. Their role is primarily concerned with facilitating orbit calibration and measurements of Earth's gravity and rotation characteristics [51].

2.12.2 NASA Instruments for Inter-planetary and Planetary Measurements

Severe limitations on the size, weight and power are placed on the payloads of spacecraft which prevent powerful lasers and larger aperture telescopes from being used. Since inter-planetary distances can reach up to several million kilometres, there is much to be gained in minimising the power requirements and the size of a laser source, consequently single-photon detection has become a prime candidate for optical measurements and communication approaches.

NASA Goddard Space Center have developed several photon-counting instruments for inter-planetary measurements [52] [53] [54]. This section focuses on an Inter-planetary Laser Transponder (ILT) used for distance ranging between an Earth-based terminal and a Mars lander [52].

As illustrated in Figure 2.25, an ILT comprises two terminals: terminal TE, located on Earth and terminal TM, located on a Mars lander; each containing an independent transceiver. A pulse emitted from TE is detected by TM which then generates a response pulse subsequently detected by TE. Both terminals independently send laser pulses to each other at a known pulse repetition rate. The TE time-stamps the

transmission of its own pulses as well as the time-of-arrival of pulses emitted from the TM and vice versa. The transmission and arrival times measured at each terminal are then communicated to and paired at an Earth-based processor which then calculates a range between two terminals.

The ILT used at both ends used a low power Q-switched micro-laser source operating a 2 kHz repetition rate, at wavelength of 532 nm of sub-nanosecond pulse width and produced 135 µJ per pulse. The system used a refractive telescope of ~ 15 cm aperture diameter and a PMT detector [52].

The transponder was mounted on a Mars-lander breadboard. It demonstrated decimetre accuracy measurements of an Earth-Mars distance [52]. The use of single-photon detection allowed much lower signal levels to be detected relative to conventional detection methods. As a result, it greatly benefitted inter-planetary studies allowing for high resolution range measurements. Applications to extra-terrestrial sciences included mapping of other planets, moons, asteroids and comets within the solar system [54].

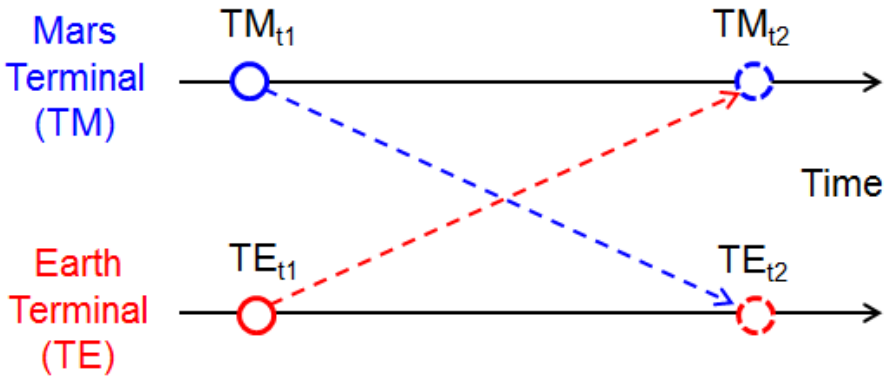

Figure 2.25. Timing diagram for an inter-planetary laser transponder [53].

2.12.3 Single-Element Scanning Ranging Systems

2.12.3.1 Galvanometer Ground-Based Scanning Lidar

In [55] McCarthy et al. reported on the development of a scanning ToF depth sensor. The system incorporated a single-element ungated detector module, a pulsed laser diode and a pair of galvanometer scanning mirrors. The transceiver was configured in a mono-static mode where the mirrors were used to scan the both the outgoing laser beam and the return beam to produce a three-dimensional image. The laser transmitted

picosecond pulses of < 30 pJ per pulse, and exhibited a low probability of photon return per pulse, thus reducing the likelihood of pulse pile-up.

A schematic diagram of the system is shown in Figure 2.26. An objective lens of aperture 70 mm in diameter was used to direct the outgoing laser beam to the target and to collect scattered photons from the scene. The FoV of the region of interest was scanned by the computer-controlled galvanometer scanning mirrors and the image of the scene was delivered to the fibre detector via the imaging optics. The scanning mirrors steered the beam in a stop-and-stare mode using a raster pattern. The detector fibre core diameter of 5 μm combined with the system focal length of 200 mm provided spatial resolution of 70 mm at 1 km [55].

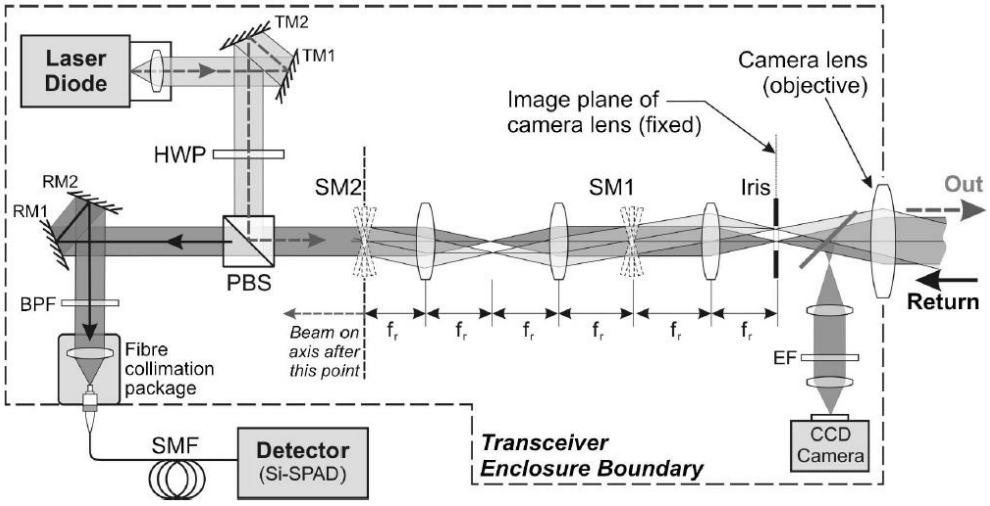

Figure 2.26. Optical layout of the single-element galvanometer scanning system [55].

The optical system assembly had dimensions ~ 275 × 275 × 170 mm. The imager was used in a series of experiments reported in [22] [56] [57] and [58], using laser wavelengths between 842 nm and 1560 nm and either a Si-SPAD or InGaAs/InP SPAD detector. It allowed high-resolution three-dimensional images of targets located at ranges between 330 m and 4500 m to be generated.

Figure 2.27 shows depth images a life-sized mannequin from a standoff distance of 910 m. The images contain 30 × 80 pixels covering area of 75 × 200 cm in the target plane [22].

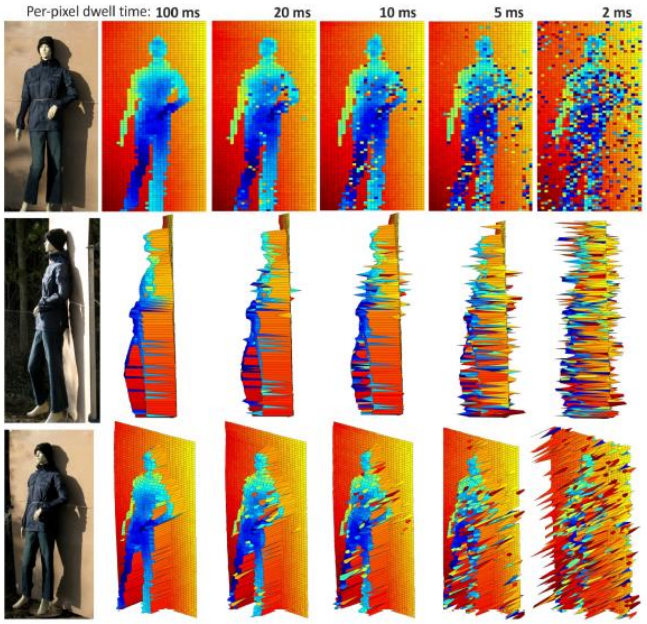

Figure 2.27. Depth images (30 × 80 pixels) of a life-sized mannequin from a standoff distance of 910 m using InGaAs/InP detector at a wavelength of 1560 nm. Pixel-to-pixel spacing is ~ 25 mm [57].

2.12.4 Single-Element Non Scanning Ranging Systems

2.12.4.1 Multiple Wavelength Time-of-Flight Sensor

The use of multiple wavelengths in single-photon depth imaging allows a broad range of subjects to be studied such as: the wavelength dependence on temporal resolution, simultaneous multichannel data acqusition, multi-wavelength laser beam propagation through atmosphere, the wavelength dependence on speckle formation and the wavelength dependence on target reflectivity [59] [60].

A schematic diagram of a multiple-wavelength ToF system developed at Heriot-Watt University is shown in Figure 2.28. It consisted of six pulsed diode lasers operating at the following wavelengths: 630 nm, 686 nm, 780 nm, 841 nm, 911 nm, 975 nm mounted around the circumference of the telescope aperture, a laser driver sequencer used to trigger the six lasers in a sequence, a fibre alignment translation stage and a reflective Schmidt-Cassegrain telescope.

The optical system comprised a commercially available Schmidt-Cassegrain telescope and three main assemblies: an optical routing module, an output assembly and a collection assembly. The optical routing module was based on a diffraction grating approach which was used to spatially separate the six wavelengths of the return signal and route each wavelength to a dedicated single-photon detector. The output assembly

consisted of a support ring on which six pulsed diode lasers were mounted around the circumference of the telescope aperture. The collection assembly was used for attaching and positioning a collection fibre and camera in the image plane of the telescope [59].

A laser driver sequencer triggered the six lasers independently and in sequence, hence each laser operated at a pulse repetition rate of $1/6^{th}$ of the trigger rate. The pulses from each of the six lasers were reflected from the target back to the telescope aperture which focused the collected light onto the fibre. The collected signal was then transmitted to the optical routing module where they were separated into their individual wavelengths and detected by six individual Si-SPADs via optical fibre patch-cords.

The system proved the feasibility of ToF ranging over distances between 200 m to 17 km and investigated SNR properties of various targets [60]. The ability of the system to extract useful multi-spectral depth information about different targets at a depth resolution of 10 cm was demonstrated toward the aim of target identification [59].

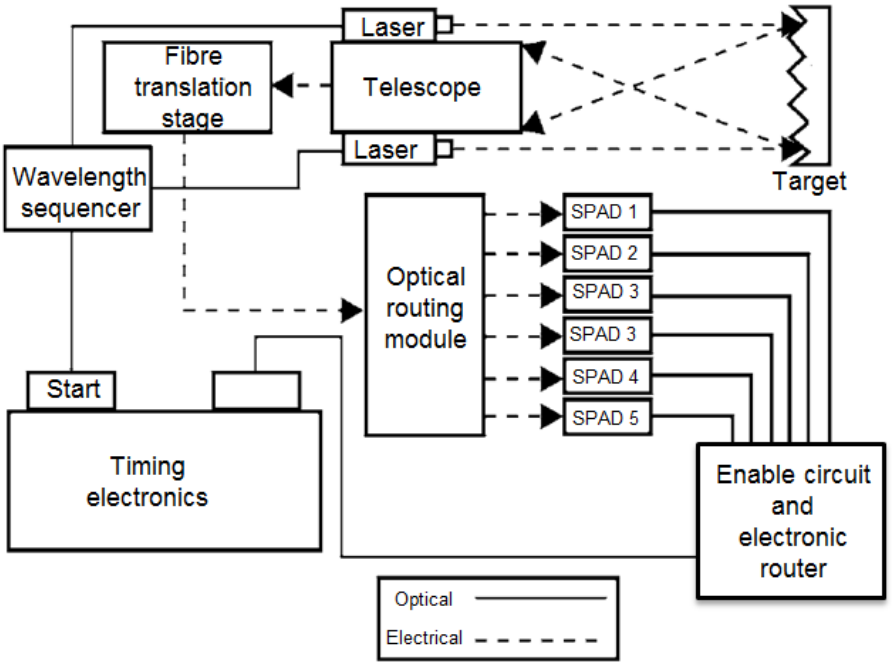

Figure 2.28. Schematic of the multiple-wavelength ToF sensor illustrating the integration of a telescope, an optical routing module, a multi-wavelength sequencer, a fibre translation stage, the enabling circuit and the router [59].

2.12.5 Multiple-Element Ranging Systems

Single-element detectors require a scanning mechanism in order to take images. This requires high pulse repetition rate of a laser source, high scan rates and fast processors;

otherwise an increase in the overall image acquisition time can be expected. An alternative to using a single-element detector is to use a one or two-dimensional array of detectors where individual detector pixels are arranged periodically with either the quench and timing circuitry positioned adjacent to each detector or beneath the array of detectors. In the latter case the array is bump-bonded to the layer containing the circuitry. Using an array of detectors offers fast acquisition and read-out times from multiple pixels simultaneously. This however, requires wide FoV optics which is often more complex and expensive when compared with the optics required by single-element detectors. Examples of array detectors include inexpensive and commercially available segmented anode PMTs and more expensive but less technically mature SPADs [61] [62].

2.12.5.1 Jigsaw Foliage-Penetrating Dual-Wedge Scanning Lidar

DARPA have developed a programme aimed at delivering a high-resolution three-dimensional imaging lidar which incorporates a Si-SPAD Gm-array. The system was designed for use in airborne platforms to image and identify military ground vehicles under camouflage or foliage [63].

A 532 nm wavelength laser beam consisting of 32 × 32 beams produced by a diffractive optical element (DOE) was directed onto a target along the optical axis of the receiver. The signal was collected by a 750 mm aperture objective lens and directed onto a detector via a dual wedge prism scanner, a set of optical lenses and a duplexer mirror [63]. The prism scanner contained two counter-rotating prisms which scanned the FoV in a rosette pattern. The duplexer mirror contained an aperture through which the transmit signal was directed out of the system.

The detector used in the system was a 32 × 32 Si-SPAD of 500 ps timing jitter. The system provided depth resolution of 400 mm and covered a FoV of 20 m diameter over a distance of 150 m. Because the number of detector pixels was not sufficient to cover the FoV with the required resolution, a beam scanning mechanism was used. The diffractive optical element provided high efficiency of the transmitted laser power while minimising background flux and false-alarm rates [63].

The lidar system was integrated into a helicopter flight-test platform and demonstrated day and night-time three-dimensional imaging of camouflaged objects. Figure 2.29(a)

shows a photograph of a tank with camouflage and foliage while Figure 2.29(b) shows the three-dimensional image of the tank uncovered from under the camouflage [63].

(a) *(b)*

Figure 2.29. (a) Photograph of a tank under a camouflage. (b) Three-dimensional map of a tank imaged with the Jigsaw system over 150 m uncovered from under the camouflage [63].

2.12.5.2 10 × 10 Hundred Beam Airborne Lidar

In [18] Sigma Space Corporation reported on the development of an airborne hundred-beam lidar system. The system was small enough to fit in a miniature UAV and used a laser of 1064 nm wavelength operating at a repetition rate of 22 kHz with a pulse energy of 11 µJ and duration of 700 ps [18].

The system operated in a mono-static mode and consisted of an optical transceiver and supporting electronics. The transceiver fitted in a volume of 1/3rd of a cubic metre and included a laser, a refractive telescope with a 750 mm telescope aperture diameter, relay optics and a 1000 mm aperture external prism scanner. A diffractive optical element (DOE) was used to spatially separate the transmitted laser beam into a uniform array of 10 × 10 Gaussian beams which were then collected by a 10 × 10 array of GaAsP PMTs [18].

The scanner was driven by two ring motors allowing the two prisms to independently rotate at speeds up to 25 Hz [64]. The movement of the prisms was synchronised to laser pulses allowing the laser beam to be projected precisely at the same angle on each frame. In addition, the scan pattern was tailored to the velocity of the host aircraft to provide an optimal coverage of the imaged area [18].

The lidar system was tested at an altitude of 1 km. At this altitude the diffracted laser beam illuminated a 1.5 × 1.5 m area on the ground, creating the beam-to-beam distance

of 15 × 15 cm. Thus, each pixel monitored a 15 × 15 cm area on the ground. The individual images were then mosaicked together, taking into account the aircraft motion and the movement of the scanner, and provided three-dimensional images of scanned objects [18]. Figure 2.30(b) shows a three-dimensional image of a building, shown in Figure 2.30(a), acquired over 1 km range.

(a)

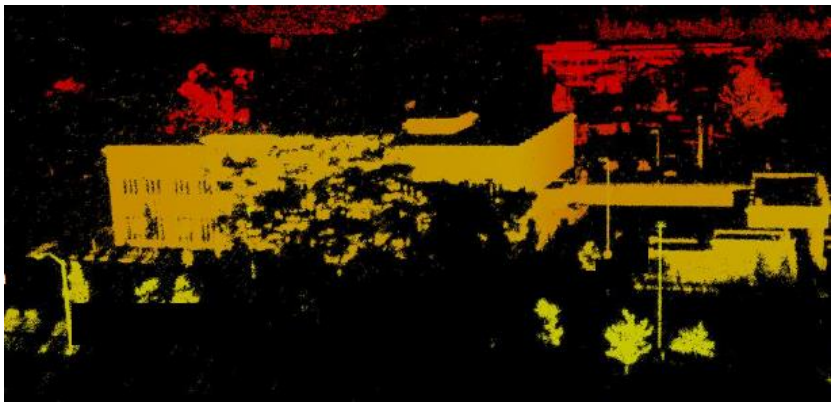

(b)

Figure 2.30. (a) A photograph of the imaged building, (b) three-dimensional image of the building taken by the lidar system [18].

NASA has stated that the single-photon lidar can be scaled to orbital altitudes and achieve high spatial resolution in applications such as topographic scanning of planets and moons in the solar system. Their most recent study indicated that scanning photon-counting lidars have the potential to be used in mapping the surfaces of Jupiter's three primary moons: Calisto, Ganymede and Europa from a 100 km orbit [64].

2.13 Conclusions

Using the TCSPC technique in lidar systems has been shown to have potential for widespread applications. The high sensitivity of the technique allows imaging at low light levels; this means that weak signals can be detected from longer ranges or that

lower power lasers can be used with reduced size, weight, and volume and power requirements. In addition, the use of a single-photon approach may also permit smaller aperture collection optics which will also reduce payload. All these advantages may facilitate use on air-platforms, satellites and space-crafts. Photon-counting image sensors capable of determining signal arrival times with picosecond or sub-nanosecond resolution are becoming increasingly important in many applications, particularly, for high-resolution three-dimensional space and air-borne imaging applications. This is because of their potential to meet a broad and complex range of requirements.

Some of the challenges of the single-photon approach include the high sensitivity of single-photon detectors which creates issues with background detection. Most previously built systems used a combination of spectral and spatial filtering to reduce the likelihood of detection of the solar background, as well as the inherent time-gating technique and use of a statistical determination of the most probable time-of-arrival.

With the TCSPC technique, depth information cannot be accurately determined from a single-shot optical pulse and therefore a number of detected photon events are required for each depth measurement, usually necessitating high repetition rate sources. Higher repetition rates in turn mean that there are many pulses in transit on a round-trip path between the imaging system and the target. This causes a range ambiguity where the absolute distance to targets cannot be uniquely determined, and hence more sophisticated techniques are required such as the use of pseudo-random sources and pattern recognition [50].

The development of arrayed detectors, capable of a simultaneous ToF read-out from thousands of pixels, eliminates the necessity for incorporating expensive, heavy and bulky scanning mechanisms and minimise acquisition times. The process of developing an integrated array of detectors is significantly more challenging than the fabrication of an individual detector, leading to detector arrays being considerably more expensive than single-element detectors. However, when making design choices between a single-element and array SPADs many questions regarding the performance trade-offs between a single-element detector and a Gm-array need to be answered. Significant progress has been made in research and development of photon-counting systems over the past twenty years. Systems differ in design characteristics such as wavelength, FoV, transceiver configuration (bi-static/mono-static) as well the transceiver configuration.

References

[1] S. Karp, L.B. Stotts, "*Fundamentals of Electro-Optic Systems Design: Communications, Lidar and Imaging"*, Cambridge University Press (2015)

[2] R.M. Measures, "*Laser Remote Sensing"*, John Wiley and Sons (1984)

[3] P. Saitz, A. J.P. Theuwissen, "*Single-Photon Imaging"*, Springer (2011)

[4] T.H. Maiman, *"Stimulated Optical Radiation in Ruby*", Nature, 187 (4736), 493-497 (1960)

[5] K. Weitkamp, "*Lidar, Range-Resolved Optical Remote Sensing of the Atmosphere"*, Springer (2005)

[6] R.A. Jarvis, *"A Perspective on Range Finding Techniques for Computer Vision",* IEEE Trans. Pattern anal. Mach. Intell., 5 (2). 122-139 (1983)

[7] P.A. Forrester, K.F. Hulme, *"Laser Rangefinders",* Opt. Quant. Electron., 13 (4), 259-293 (1981)

[8] R.D. Richmond, S.C. Cain, *"Direct-Detection LADAR Systems"*, SPIE (2010)

[9] M.C. Amman, T. Bosh, M. Lescure, R. Mylylla, M. Rioux, *"Laser Ranging: a Critical Review of Usual Techniques for Distance Measurement",* Opt. Eng., 13 (1), 10-19 (2001)

[10] J. Wilson, J. Hawkes, *"Optoelectronics",* Prentice and Hall (1998)

[11] S. Karp, L.B. Stotts, "*Fundamentals of Electro-Optic Systems Design: Communications, Lidar and Imaging"*, Cambridge University Press (2015)

[12] G.M. Williams, *"GHz-Rate Single-Photon Sensitive Linear Mode APD Receivers",* Proc. SPIE, 7222, 72221L-1 (2009)

[13] B.F. Aull, A.H. Loomis, D.J. Young, R.M. Heinrichs, B.J. Felton, P.J. Daniels, D. J. Landers, "*Geiger-Mode Avalanche Photodiodes for Three-Dimensional Imaging"*, Linc. Lab. J., 13, 2 (2002)

[14] K. Kolb, "*Signal-to-Noise Ratio of Geiger-mode Avalanche Photodiode Single-Photon Counting Detectors"*, Proc. SPIE, 58, 8, 0091-3286 (2014)

[15] Committee on Developments in Detector Technologies; National Research Council, "*Seeing Photons: Progress and Limits of Visible and Infrared Sensor Arrays"*, The National Academy Press (2010)

[16] E. C. Silverberg, "*Operation and Performance of a Lunar Laser-Ranging Station"*, Appl. Opt., 13, pp.565-573 (1974)

[17] J.J. Degnan, "*Thirty Years of Satellite Laser Ranging"*, Keynote Speech, Proc. Of the 9th Intern. Workshop on Laser Ranging Instrumentation, Australia (1994)

[18] J.J. Degnan, "*Scanning, Hundred Beam Photon-Counting Airborne 3D Imaging Lidar"*, IEEE Trans. Geosci. Remote Sens. (2011)

[19] W. Becker, "*Advanced Time-Correlated Single-Photon Counting Techniques"*, Springer (2005)

[20] G.S. Buller, A.M. Wallace, *"Ranging and Three dimensional Imaging Using Time-Correlated Single-Photon Counting and Point-by-Point Acquisition",* IEEE J. Sel. Top. Quantum Electron., 13,.4 (2007)

[21] A.M. Wallace, R.C. Sung, G.S. Buller, R.D. Harkins, R.E. Warburton, R.A. Lamb, *"Detecting And Characterising Returns in a Pulsed Ladar System",* IEEE Proc. Vis. Image Signal Process., 153, 160-172 (2006)

[22] A. McCarthy, X. Ren, A.D. Frera, N.R. Gemmel, N.J. Krichel, C. Scarcella, A. Ruggeri, A. Tosi, G.S. Buller, *"Kilometer-Range Depth Imaging at 1550 nm Wavelength Using an InGaAs/InP Single-Photon Avalanche Diode Detector",* Opt. Express, 21, 19, pp. 22098-22113 (2013)

[23] A.Y. Loudon, P.A. Hiskett, G.S. Buller, R.T. Carline, D.C. Herbert, W.Y. Leong, J.G. Rarity, *"Enhancement of the Infrared Detection Efficiency in Si Photon Counting Avalanche Photodiode using SiGe Absorbing Layers"*, Opt. Lett., 27, 219–221, (2002)

[24] S. Henzler, *"Time-to-Digital Converters"*, Spriner (2010)

[25] https://www.picoquant.com/products/category/tcspc-and-time-tagging-modules/hydraharp-400-multichannel-picosecond-event-timer-tcspc-module#documents

[26] http://www.guidetech.com/gt668pci-40ps.html

[27] R.E. Warburton, A. McCarthy, A.M. Wallace, S. Hernandez–Marin, R.H. Hadfield, S.W. Nam, G.S. Buller, *"Sub-Centimeter Depth Resolution Using a Single–Photon Counting Time–of–Flight Laser Ranging System at 1550 nm Wavelength"*, Opt. Lett., 32 (15), 2266–2268 (2007)

[28] G.S. Buller, R.J. Collins*, "Single-Photon Generation and Detection"*, Meas. Sci. Technol., 21, 012002 (2010)

[29] A. Yariv, P. Yeh, "*Photonics: Optical Electronics in Modern Communications"*, Oxford University Press (2007)

[30] J. R. Hook, H.E. Hall, "*Solid State Physics"*, John Wiley and Sons (1991)

[31] J. Singh, *"Semiconductor Optoelectronics",* Electrical Engineering Series (1995)

[32] S. Cova, M. Ghioni, A. Lacaita, C. Samori, F. Zappa, *"Avalanche Photodiodes and Quenching Circuits for Single-Photon Detection",* App. Opt., 25, 12, 1956-1976 (1996)

[33] A. Galliovani, I. Rech, M. Ghioni, "*Progress in Quenching Circuits for Single Photon Avalanche Diodes"*, IEEE Trans. Nucl. Sci., 57, 6 (2010)

[34] http://www.optics.rochester.edu/workgroups/lukishova/QuantumOpticsLab/homepage/apd_spcm_aqr.PDF

[35] A. Giudice, M. Ghioni, R. Biasi, F. Zappa, S. Cova, P. Maccagnanni, A. Gulinatti, *"High-Rate Photon Counting and Picosecond Timing with Silicon-SPAD Based Compact Detector Modules",* J. Mod. Opt. , 94, 2-3 (2007)

[36] F. Guerrieri, S. Tisa, A. Tosi, and F. Zappa, ***"****Two-Dimensional SPAD Imaging Camera for Photon Counting****",*** IEEE J. Photonics, 2, 5, pp. 759–774 (2010)

[37] http://www.micro-photon-devices.com/Products/Photon-Counters/SPC2

[38] P.A. Hiskett, G.S. Buller, A. Y. Loudon, J. M. Smith, I. Gontijo, A. C. Walker, P.D. Townsend and M. J. Robertson*, "Performance and Design of InGaAs/InP Photodiodes for Single-Photon Counting at 1.55 μm"*, App. Opt., 39, 36 (2000)

[39] A. Tosi, A. Della Frera, A. Bahgat Shehata and C. Scarcella, "*Fully Programmable Single-Photon Detection Module for InGaAs/InP Single Photon Avalanche Diodes with Clean and Sub-Nanosecond Gating Transitions"*, Rev. Sci. Instrum. 83, 013104 (2012)

[40] M.A. Itzler, M. Entwistle, M. Owens, K. Patel, X. Jiang, K. Slomkowski, S. Rangwala, "*Comparison of 32 x 128 and 32 x 32 Geiger-Mode APD FPAs for Single-Photon 3D LADAR Imaging"*, Proc. SPIE, 8033, 8033G-1 (2011)

[41] M.A. Itzler, U. Krishnamachari, Q. Chau, X. Jiang, M. Entwistle, M. Owens, K. Slomkowski, *"Statistical Analysis of Dark Count Rate in Geiger-Mode APD FPAs",* Proc. SPIE, 9250, 925003-1 (2014)

[42] M.A. Itzler, X. Jiang, M. Entwistle, K. Slomkowski, M. Owens, A.Tosi, F. Acerbi, F. Zappa, and S. Cova, *"Advances in InGaAsP-Based Avalanche Diode Single Photon Detectors*", J. Mod. Opt., 58, 3–4, 174 – 200 (2011)

[43] http://www.princetonlightwave.com/

[44] M.A. Itzler, M. Entwistle, M. Owens, K. Patel, X. Jiang, K. Slomkowski, S. Rangwala, "*Geiger-Mode Avalanche Photodiode Focal Plane Arrays for 3D Lidar Imaging"*, Imaging and App. Opt., OSA Technical Digest (2011)

[45] P. Seitz, A. J.P. Theuwissen, "*Single Photon Imaging"*, Springer Series in Optical Sciences (2011)

[46] D.V. O'Connor, D. Phillips, "*Time-Correlated Single-Photon Counting"*, Academic Press (1984)

[47] S. Pellegrini, G. S. Buller, J.M. Smith, A.M. Wallace and S. Cova, "*Laser-Based Distance Measurement Using Picosecond Resolution Time-Correlated single-Photon Counting"*, Meas. Sci. Technol., 11, 712-716 (2000)

[48] N.J. Krichel, A. McCarthy, R.J. Collins, G.S. Buller, *"Anti-aliasing techniques in photon-counting depth imaging using GHz clock rates",* Proc. SPIE, 7681, 768108-1 (2010)

[49] P.A. Hiskett, C.S. Parry, A. McCarthy, G.S. Buller, " *A Photon-Counting Time-of-Flight Ranging Technique Developed for the Avoidance of Range Ambiguity at Gigahertz Clock Rates",* Opt. Express, 16, 18, 13685 (2008)

[50] N. Krichel, A. McCarthy, G.S. Buller, *"Resolving Range Ambiguity in a Photon Counting Depth Imager Operating at Kilometer Distances",* Opt. Express, 18, 9, 9192 (2010)

[51] E. Vermaat, J.J. Degnan, P.J. Dunn, R. Noomen, A.T. Sinclair, "*Satellite Laser Ranging, Status and Impact for Wegner*, J. Geodyn., 25, 3/4, 195-212 (1998)

[52] J.J. Degnan, "*Unified Approach to Photon-Counting Microlaser Ranger Transponders and Altimeters"*, Surv. in Geophys., 22, 431-447 (2002)

[53] J.J. Degnan, "*Asynchrounous Laser Transponders for Precise Inter-planetary Ranging and Time Transfer"*, J. Geodynamics 34, 551-594 (2002)

[54] J.J. Degnan, "*Photon-Counting Multikilohertz Microlaser Altimeters for Airborne and Spaceborne Topographic Measurements"*, J. Geodyn., 34(3): 503-549 (2002)

[55] A. McCarthy, R.J. Collins, N.J. Krichel, V. Fernandez, A.M. Wallace and G.S. Buller, *"Long-Range Time-of-Flight Scanning Sensor Based on High-Speed Time-Correlated Single-Photon Counting",* Appl. Opt., 48, 32 (2009)

[56] G.S. Buller, N.J. Krichel, A. McCarthy, N.R. Gemmel, M.G. Tanner, C.M. Natarajan, X. Ren, R.H. Hadfield*, "Kilometer Range Depth Imaging Using Time-Correlated Single-Photon Counting*, Proc. SPIE, 8155 (2011)

[57] A. McCarthy, N.J. Krichel, N.R. Gemmel, X. Ren, M.G. Tanner, S.N. Dorenbos, V. Zwiller, R.H. Hadfield, G.S. Buller, "*Kilometre-Range, High-Resolution Depth Imaging Using 1560 nm Wavelength Single-Photon Detector"*, Opt. Exp., 21(7), 89-8915 (2013)

[58] G.S. Buller, N.J. Krichel, A. McCarthy, N.R. Gemmel, M.G Tanner, C.M. Natarajan, X. Ren, R.H. Hadfield, *"Kilometer Range Depth Imaging Using Time-Correlated Single-Photon Counting",* Proc. SPIE, 8155, 81551l-1 (2011)

[59] G.S. Buller, R.D. Harkins, A. McCarthy, P.A. Hiskett, G.R. MacKinnon, G.R. Smith, R. Sung, A.M. Wallace, R.A. Lamb, K.D. Ridley and J.G. Rarity, "*Multiple Wavelength Time-of-Flight Sensor Based on Time-Correlated Single-Photon Counting"*, Rev. Sci. Instrum.,76, 083112 (2005)

[60] A.M. Wallace, G.S. Buller, R.C.W. Sung, R.D. Harkins, A. McCarthy, S. Hernandez–Marin, G.J. Gibson and R.A. Lamb, *"Multi–Spectral Laser Detection and Ranging for Range Profiling and Surface Characterization"*, J. Opt. A: Pure Appl. Opt., 7, S438–S444 (2005)

[61] P.A. Hiskett, R.A. Lamb, "*Design Considerations for High-Altitude Altimetry and Lidar Systems Incorporating Single-Photon Avalanche Diode Detectors"*, Proc. SPIE, 8033 (2011)

[62] J.J. Degnan, "*A Conceptual Design for a Spaceborne 2D Imaging Lidar"*, E&I, 119, 4, pp.99-106 (2002)

[63] R.M. Marino, W.R. Davis Jr., "*Jigsaw: A Foliage-Penetrating 3D Imaging Laser Radar System"*, Linc. Lab. J., 15, 1 (2005)

[64] J.J. Degnan, R. Machan, "*Inflight Performance of a Second Generation Photon Counting 3D Imaging Lidar"*, Proc. SPIE, 6950, 695007 (2008)

Chapter 3
Re-Configurable Transceiver Design

3.1 Introduction

This chapter describes the design of a re-configurable lidar system which can accommodate either a single-element SPAD detector operating in a scanning mode or a 32 × 32 array of SPAD detectors (Gm-array) operating in a non-scanning mode. By incorporating an inter-changeable lens, the system is designed to have an identical angular resolution for each pixel in the Gm-array as the single-element detector in the alternative configuration. In addition, both the array and the single-element detector options can be re-configured to operate in a bi-static and a mono-static configuration. This flexibility results from the design of the optical system and the associated opto-mechanics of the module which allows the choice of detector and configuration. In all configurations the system employs a ToF approach in conjunction with the time-correlated single-photon counting (TCSPC) to produce three-dimensional images of different targets at ranges up to ten kilometres. This chapter describes operational and design requirements for a defence application of interest to Selex ES. The existing theoretical and technological constraints as well as the system architecture and optical design of the transceiver are also discussed.

Tolerance analysis of the receiver optics and its effect on the mechanical design as well as a brief description of a safety enclosure are also discussed. These safety considerations are typical of the design and operational constraints that the proof-of-principle demonstrator equipment must comply with in an engineering and manufacturing arrangement. Finally, robust transceiver alignment procedures are briefly discussed.

3.2 Background

One of the aims of Selex ES is to work with Heriot-Watt University to develop a state-of-the art three-dimensional active imager which can be used in air-to-ground targeting, surveillance and recognition. This involves the design, construction, alignment and testing of a proof-of-principle demonstrator lidar system the aperture

diameter of which does not exceed that of an airborne pointing, steering and stabilisation system with an optical aperture of 30.5 cm (see Figure 3.1) [1].

Figure 3.1. Titan 385ES multi-sensor turret of maximum optical aperture of 30.5 cm [1].

The design of the proof-of-principle demonstrator is driven by the requirement to integrate multiple sub-systems including a laser transmitter, an optical receiver, transmission fibres, filters, a scanning mechanism, detectors, electrical hardware, timing electronics and data processing algorithms in order to meet the following requirements:

- Kilometre range three-dimensional imaging with spatial and depth resolution ≤ 30 cm at 10 km;
- Single-photon detection for low emission power and sensitive detection;
- Wavelength within the short-wave infra-red wavelength (SWIR) such as 1550 nm for improved eye-safety thresholds;
- Single-element SPAD detector (25 μm active area pixel diameter) operating in a scanning mode and an array of 32 × 32 SPAD detectors (100 μm active area pixel diameter each) operating in a non-scanning mode;
- Matching angular resolution per single detector pixel for the two types of detectors;
- Ability of monitoring the FoV in the visible spectrum bore-sighted to the SWIR wavelength.

Advantages of operating in SWIR wave-band include the availability of low-loss atmospheric windows in this spectral region of the electromagnetic spectrum, covertness, decreased solar background, maturity of SWIR optics technology, the availability of high-power pulsed optical fibre lasers and SPAD detectors operating in

this spectral range as well as the improved laser eye-safety thresholds [2]. Eye-safety is an extremely important consideration for any deployed lidar. Wavelengths above 1400 nm are primarily absorbed by the cornea and lens, leading to burns and cataracts as in the worst case scenarios, whereas the photo-sensitive retina - which is critical in the detection of light - tends not to be significantly affected by the radiation in this region of the spectrum.

The requirement for spatial and range resolution is driven by the need for the detection of people and recognition of vehicles over distances up to 10 km. Based on *Johnson's criteria*, the criteria for target detection, recognition and identification corresponding to 50 % of discrimination probability, are shown in Table 3.1 [3]. Target detection indicates a reasonable probability that a recorded "blob" is the object being sought, target recognition allows for a discrimination of an object class (human, tank, tree, house) while target identification enables an object type to be discriminated (M1A, T-62 or T-72 tank) [3].

Target type	**Vehicle**	**Person**
Target critical size [m]	6.5	1.1
Number of pixels required for detection	2	
Spatial resolution required for detection [m]	3.250	0.550
Number of pixels required for recognition	8	
Spatial resolution required for recognition [m]	0.812	0.137
Number of pixels required for identification	12	
Spatial resolution required for identification [m]	0.542	0.092

Table 3.1. Johnson's criteria for target detection, recognition and identification [3]

The matching pixel angular resolution between the single-element detector and the Gm-array allows a direct comparison between the performance of a scanned and non-scanned (flood-illumination) single-photon counting lidar system which is also of significant interest to the defence industry.

In the following sections the limitations on resolution are discussed together with the system focal length and its impact on the size of the system.

3.3 Design Limitations

The spatial resolution of an optical system is typically limited by factors such as lens aberrations or component misalignment. However, there is a fundamental maximum in the resolution of any optical system which is due to diffraction; an Airy disk of diameter *q* (see Eq. 3.1) is the first minimum of best focused spot that an aberration-free lens with circular aperture of diameter, *D*, and of focal length, *f*, produces and is given by [4].

$$q = \frac{2.44\lambda f}{D} \qquad \textit{Eq. 3.1}$$

As illustrated in Figure 3.2, the focal length, *f*, required for an optical system to provide a specific value of spatial resolution, *S*, is defined by the diameter of a detector pixel, *d*, and the range to a target, *R*, and can be expressed as follows

$$f = \frac{dR}{S} \qquad \textit{Eq. 3.2}$$

By combining Eq. 3.1 and Eq. 3.2 the limit on the maximum spatial resolution, *S*, achievable by an optical system is given by

$$S = \frac{2.44\lambda dR}{qD} \qquad \textit{Eq. 3.3}$$

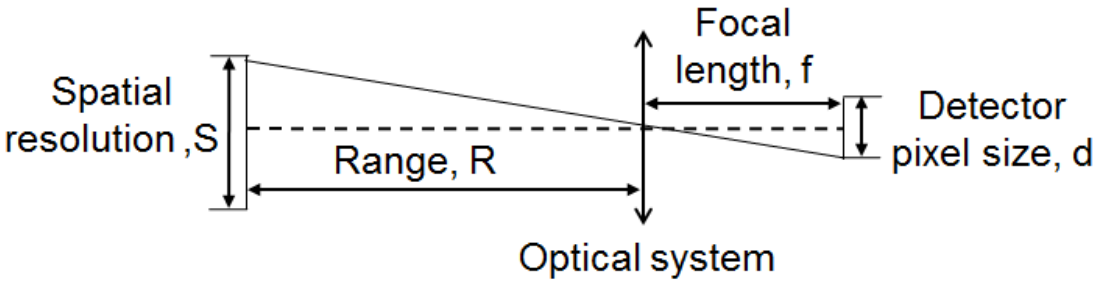

Figure 3.2. Diagram representing the relationship between focal length, f, detector pixel diameter, d, and spatial resolution, S, that can be achieved over a range, R.

In the absence of optical aberrations the diameter of the Airy disk, *q*, imposes a limit on spatial resolution. Given that the diameter of the Airy disk is within the pixel size, *d*, then the pixel size determines the spatial resolution of the image.

By assuming that the Airy disk diameter, *q*, is equal to 66 % of the detector diameter, *d*, the relationship between the spatial resolution, *S*, and range, *R*, is plotted for an aperture diameter of an optical system, *D*, equal to 10 cm, 20 cm and 30 cm. This is shown in Figure 3.3 and demonstrates that at a range of *R* = 10 km the diffraction limit allows spatial resolution, *S*, of up to *S* = 57 cm, *S* = 29 cm and *S* = 19 cm to be achieved for apertures of *D* = 10 cm, *D* = 20 cm and *D* = 30 cm respectively.

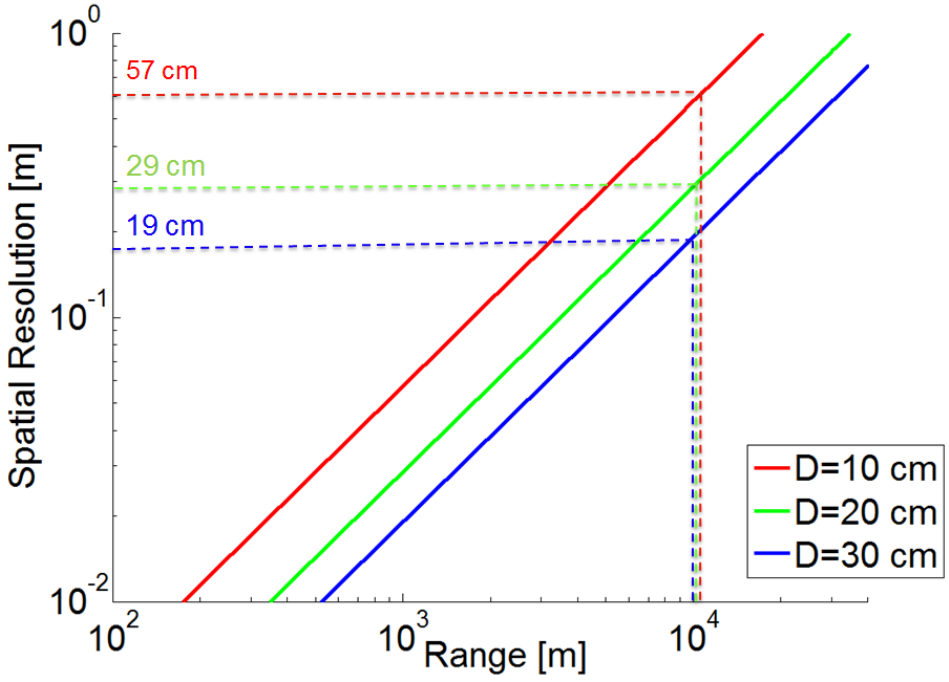

Figure 3.3. Plot showing the relationship between spatial resolution, S, and range, R, for an Airy disk diameter, q, equal to 66 % of the detector diameter, d, and three different aperture diameters of an imaging system: D = 10 cm, D = 20 cm, D = 30 cm for λ=1550 nm.

Optical systems with very long focal lengths are typically more bulky than short focal length systems unless path-folding elements such as mirrors or de-magnifying telescopes are used. Additional elements increase the system complexity, cost and weight. This can be particularly problematic for airborne lidar systems which are required to fit within the strict constraints on volume and weight. Hence, short focal length systems are generally preferred. Eq. 3.2 indicates that the focal length of the imaging system is driven by the diameter of the detector pixel. Figure 3.4 shows the dependence determined between the focal length, *f*, and detector pixel diameter, *d*, calculated for a range, *R* = 10 km and spatial resolution, *S* = 30 cm using Eq. 3.2. Current InGaAs/InP SPAD technology provides single-element and array detectors with effective pixel diameters varying between 25 µm and 100 µm, requiring focal

lengths between 0.83 m to 3.30 m in order to provide diffraction limited performance. Thus progress in the area of SPAD pixel miniaturisation will have a direct impact on the miniaturisation of photon-counting lidar sensors.

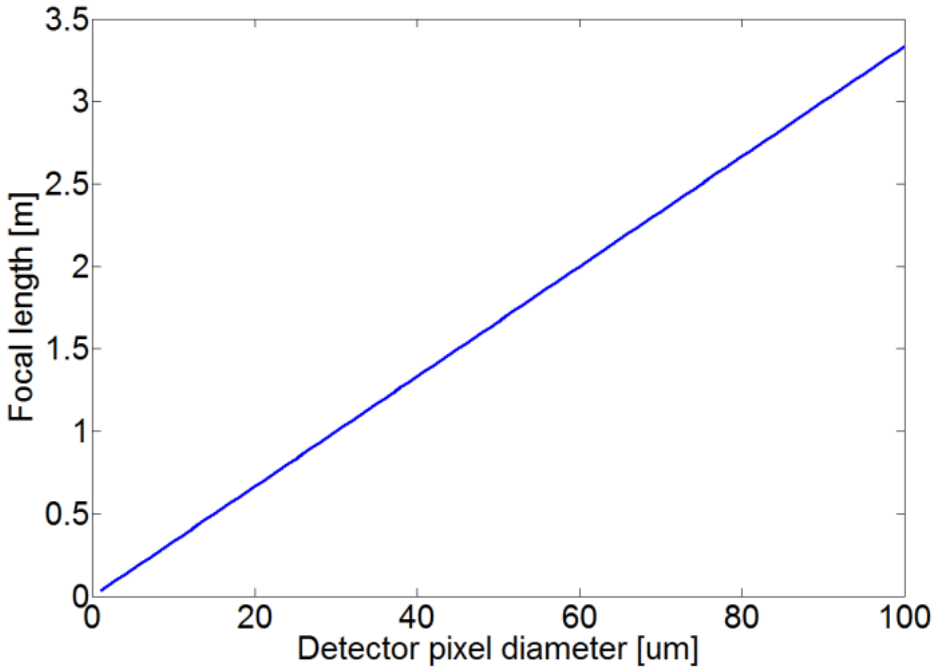

Figure 3.4. Plot showing the relationship between the pixel diameter, d, and the focal length of an optical system, f, for a range of 10 km and spatial resolution of S = 30 cm.

According to the most recent prognosis from Princeton Lightwave Ltd the pixel diameter of their InGaAs/InP SPADs detector arrays is expected to reach 30 – 40 µm in 2018/2019 and in 2022 it is expected be further reduced to 17 µm [5]. A 17 µm diameter pixel would allow focal lengths below 50 cm as compared to nearly 3.5 m for a 100 µm pixel, and would reduce the volume, weight and the cost of an airborne single-photon lidar.

3.4 Optical Design and Specifications of the Receiver

Optical design can be defined as the process of modelling the performance of an optical system and selecting parameters that meet a set of performance requirements and constraints, including manufacturing and cost limitations that are commensurate with a function or application [6].

ZEMAX design software was used to design the lidar system. This is a comprehensive, industry standard software package used for optical design of complex systems.

In order to meet the requirements listed in section 3.2, the optical system needs to provide identical FoV and resolution per pixel when operating in a scanning mode using a single-element SPAD of 25 µm active area and when operating in a non-scanning mode using a Gm-array of 100 µm active area. This effectively requires two separate optical systems with different specifications. The simplest way of achieving this is to design a system that shares all optical components apart from the lens that focuses the beam onto the detector. This lens can be inter-changed depending on the detector used.

Figure 3.5 illustrates the difference in FoV between a single-element system operating in a scanning mode and an array system operating in a non-scanning mode. As shown in Figure 3.5(a) the array allows data from multiple pixels to be captured simultaneously and therefore the entire FoV_{Array} can be imaged without employing the scanning mirrors. As shown in Figure 3.5(b) the single-pixel detector only allows the signal from the FoV_{Pixel} to be registered, hence the scanning mirrors are required to extend the FoV_{Pixel} to $FoV_{Scanner}$ which is equivalent to that of the FoV_{Array}. In this case 32 horizontal and 32 vertical scanner steps are needed with each angular step equal to the FoV of a single detector pixel, FoV_{Pixel}.

In a practical system which is representative of a prototype the project cost is an important factor. Thus the availability of commercial components is an important point in the choice of system parameters. Before defining optical specifications for each of the two optical systems it is essential to establish whether commercial components are available to meet the requirements of the system.

The following equipment was identified to meet the requirements and was subsequently used in the design:

- Schmidt Cassegrain Telescope: commercially available from Celestron, model C-GEM, focal length f = 2032 mm, aperture diameter 203 mm, a secondary mirror obstruction of 33 % of the aperture diameter, coated for the visible spectrum [7].
- Annular mirror with a clear diameter equal to 45 mm, and a hollow aperture diameter of φ = 9 mm, coated for a wavelength of 1545 nm;
- Breadboard of dimensions 90 × 60 cm. The breadboard can be attached to a safety-approved tripod available on-site to provide *x*, *y*, *z* positioning towards targets of interest.

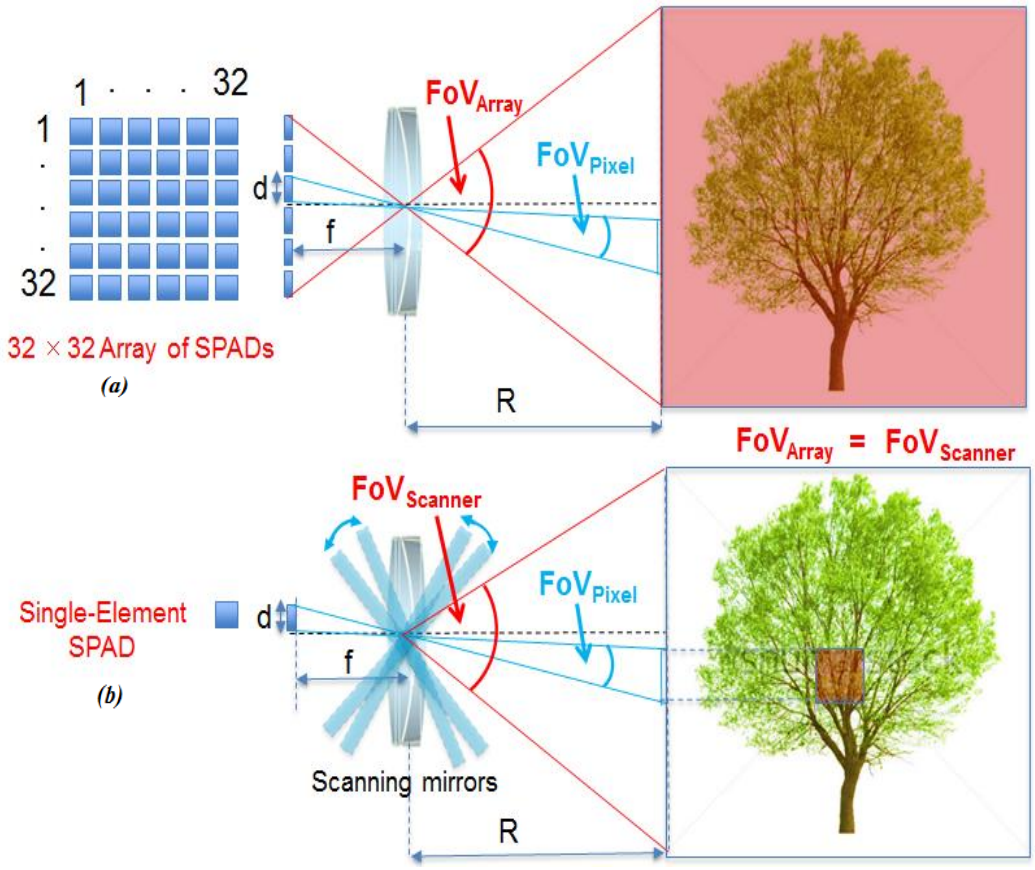

Figure 3.5. Illustration of a pixel FoV for the non-scanned array configuration and for the scanned single-element configuration.

At 203 mm, the aperture of the telescope yields a diffraction-limited resolution of just below 30 cm at 10 km and at a wavelength of 1550 nm, which meets the requirements. The dimensions of the telescope fit well within the breadboard and the annular mirror allows the system to operate in the mono-static configuration. However, to minimise signal loss the ratio of the beam diameter inside the optical system to the diameter of the annular aperture is required to be ≤ 25 %. In order to achieve this, the design must be optimised for an 18 mm beam diameter. This in turn imposes a constraint on the clear aperture of the scanning mirrors which need to fully accommodate the beam to within a leeway. A suitable set of programmable galvanometer *x, y* scanning mirrors of 20 mm clear aperture at 45 ° beam incidence was acquired from Cambridge Technology [8]. The mirrors are capable of providing an angular excursion of ± 20 º, a minimum scan step of 200 µrad (0.0115 º) and a maximum frequency of operation of ~ 2.8 kHz.

In addition, the dimensions of the breadboard impose constraints on the optical layout. The entire optical system assembly, with its multiple possible configurations, must fit within its dimensions.

The aim of an optical system operating in a single-photon counting mode is to efficiently couple light reflected from a target onto the active area of a detector. In previous sections it was explained that diffraction on the circular aperture of the optical system defines the limit on the smallest achievable spot diameter.

In this work the design Airy disk diameter, *q*, was made to fill 66 % of the active area of the detector pixel. The remaining 34 % leaves a substantial margin for an increase in the Airy disk diameter due to inaccuracies in the manufacturing and alignment. Increasing this fraction puts efficient light coupling into the active area at risk due to reduced margin for errors. On the other hand, whilst reducing the fraction would create more room for inaccuracies, it would impose tighter requirements on aberrations and would impose the requirement of a shorter focal length lens.

3.4.1 Specifications for the Non-Scanned Array and for the Single-Element Scanned Configuration

Optical performance specifications defined for the non-scanned Gm-array optical receiver are shown in Table 3.2 while Figure 3.6 illustrates some of its main parameters such as the array diagonal length, array side length, array diagonal FoV, array side FoV, object diagonal length and object side length. The array has a side FoV of 0.052 º and a diagonal FoV of 0.073 º which corresponds to an object side length of 9.03 m and object diagonal length of 12.77 m at 10 km.

Optical performance specifications defined for the single-element scanned receiver are shown in Table 3.2. Figure 3.7 illustrates the main parameters such as scanned (32 × 32) detector diagonal length, scanned (32 × 32) detector diagonal FoV, scanned (32 × 32) object diagonal length, single-element detector diagonal FoV, (32 × 32) detector side length, scanned (32 × 32) detector side FoV, scanned (32 × 32) object side length and single-element detector side FoV.

For the Gm-array configuration, the system aperture, focal length and the wavelength of operation define the Airy disk diameter (Eq. 3.1) as being equal to 66 µm. In turn, the diameter of the Airy disk defines the system spatial resolution; although by design it is equivalent to 66 % of the 100 µm pixel pitch, after the manufacturing and assembly process, the measured spot size is expected to be ≤ 100 µm. According to Eq. 3.3, this yields a spatial resolution of 28.2 cm at 10 km.

	Array	Single-Element
Object distance (m)	10000	
Aperture diameter (m)	0.203	
Wavelength (nm)	1550	
Number of detector pixels (square array)	32	1
Pixel pitch (μm)	100	25
Array side length (mm)	3.200	-
Array diagonal length (mm)	4.525	-
Airy disk diameter (μm)	66	16.500
Airy disk diameter (μrad)	18.640	
Airy diameter fraction of pixel pitch	0.66	
Focal length (mm)	3542.570	885.739
Array side FoV (º)	0.052	-
Array diagonal FoV (º)	0.073	-
Array object side length (m)	9.07	-
Detector side length (μm)	-	25
Detector diagonal length (μm)	-	35
Single-element detector diagonal FoV (º)	-	0.0023
Single-element detector side FoV (º)	-	0.0016
Scanned (32 × 32) detector side FoV (º)	-	0.052
Scanned (32 × 32) detector diagonal FoV (º)	-	0.073
Scanned (32 × 32) object side length (m)	-	9.03
Scanned (32 × 32) object diagonal length (m)	-	12.77

Table 3.2. Optical performance specifications for the non-scanned 32 × 32 Gm-array and the scanned single-element optical receiver.

The single-element detector collects a signal from a side FoV of 0.0016 º and a diagonal FoV of 0.0023 º. The role of the scanning mirrors is to rotate the FoV of the single-element detector in 32 horizontal and 32 vertical steps; covering side FoV of 0.052 º and diagonal FoV of 0.073 º. This provides 9.03 m and 12.77 m side and diagonal object side length respectively at 10 km which matches that of the non-scanned Gm-array system. For this configuration, the detector pitch is equal to 25 μm and hence the required Airy disk diameter is 16.5 μm.

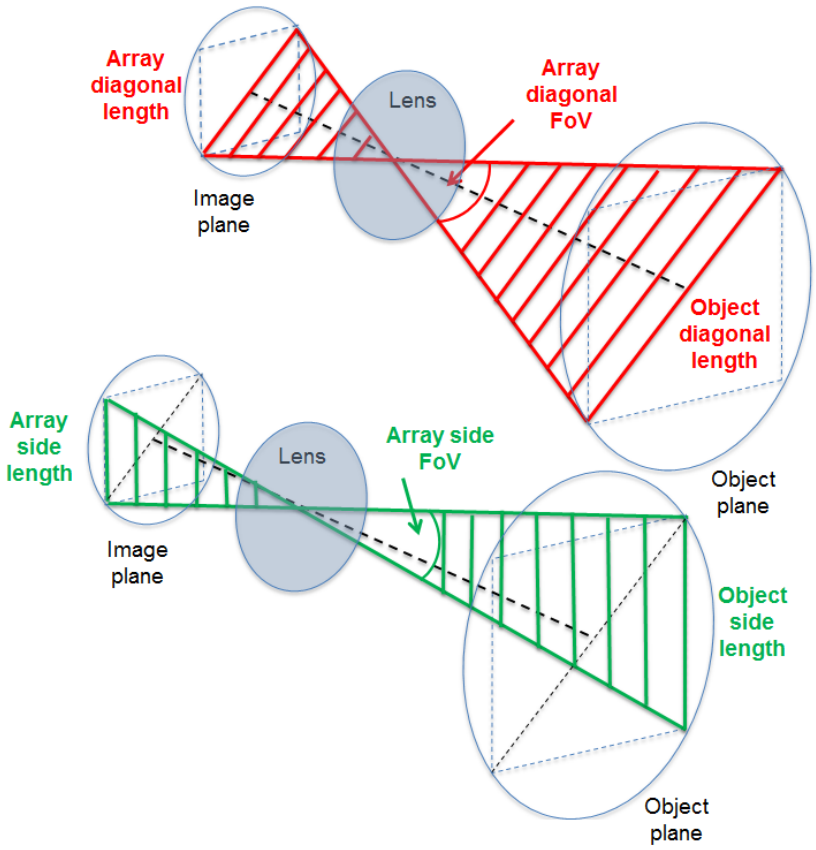

Figure 3.6. Diagram illustrating parameters of the non-scanned array configuration.

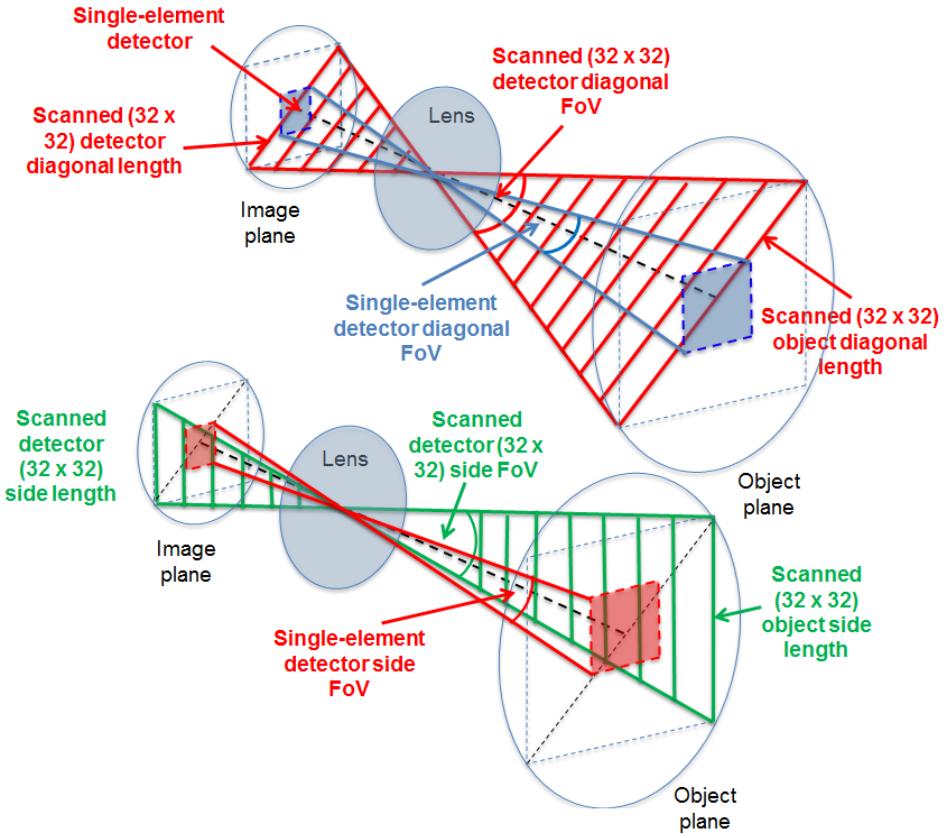

Figure 3.7. Diagram illustrating parameters of the scanned optical system incorporating the single-element detector.

3.5 General System Layout

The general system layout is shown in Figure 3.8. It consists of three modules: a transmitter, a receiver and timing electronics. Within the receiver there is a telescope and an eyepiece which collects the return signal from infinity and images it onto the exit pupil of the telescope where the *y* scanning mirror is located. The mirror 1 (FM1) is used to fold the optical path in order to contain the beam within the dimensions of the breadboard and to allow space for the mechanical assembly. A set of relay lenses in between the *x* and *y* scanning mirrors is used to form a 4f system which images the exit pupil of the telescope, initially formed on the *y* scanning mirror, onto the *x* scanning mirror which eliminates the possibility of distortion in a scan pattern as the mirrors rotate. The beam is then directed onto the annular mirror which reflects the beam towards the lens, focusing it onto the detector.

The lens placed in front of the detector is inter-changeable depending on whether the single-element or the Gm-array is used. Additionally, a removable folding mirror (FM2) can be placed on the path between the scanning mirror *x* and the annular mirror, providing the option of two-dimensional monitoring of the FoV in the visible-band during the set-up phase. This mirror must be removed during data collection.

The transmitter comprises a fibre laser and a collimating lens chosen to provide the required beam divergence. The divergence of the beam is adjusted for ether bi-static or mono-static operation. In the mono-static configuration, the folding mirror (FM3) is inserted to divert the laser beam onto the optical axis of the receiver through the aperture in the annular mirror. In the bi-static configuration, the mirror is removed and the beam is directed onto the target along a path parallel to that of the returned beam.

The transmission path of the laser beam for the system operating in a mono-static mode has been modelled and it has been confirmed that it is possible to transmit the beam through the reflective telescope with a central obstruction while avoiding clipping from optical components.

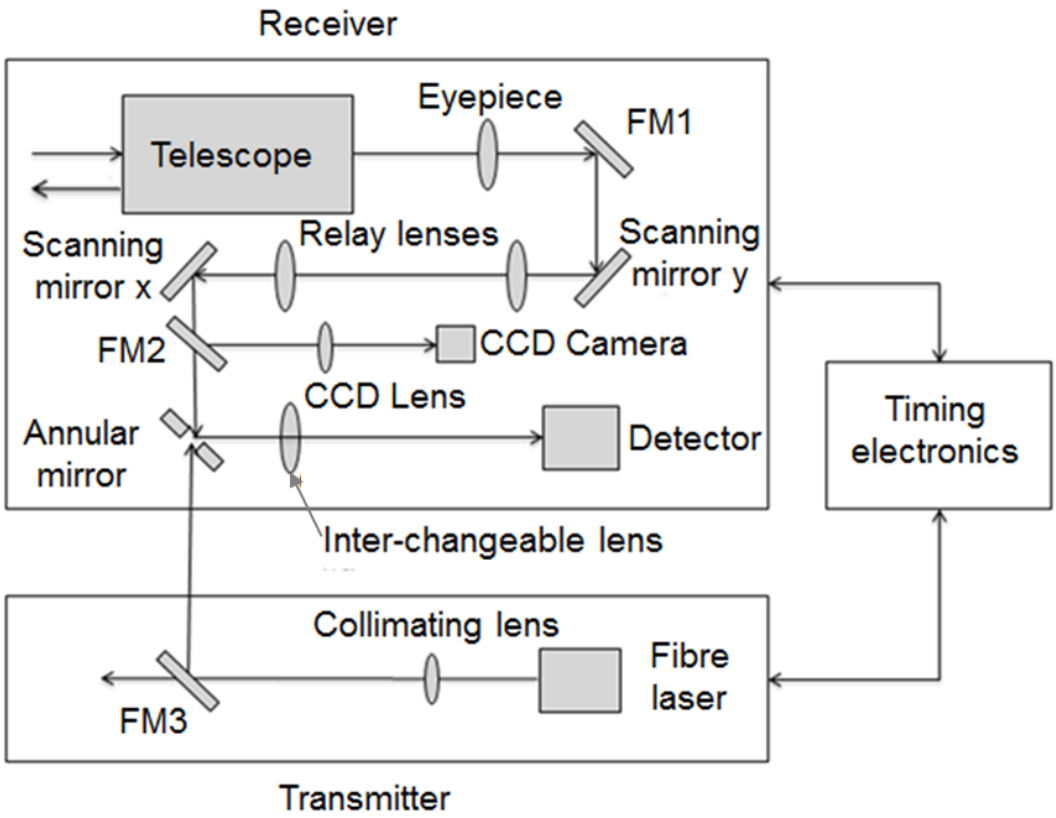

Figure 3.8. Schematic diagram of the system architecture. Folding mirror, FM1, and the annular mirror direct the light onto a detector. FM3 is used in a mono-static configuration.

In addition to the transmitter and receiver the system also consists of the timing electronics module which accurately time-stamps each transmitted laser pulse and each photon received at the detector according to a common time reference. When the system operates in the scanning mode, the timing electronics is required to trigger movement of the scanning mirrors at appropriate intervals.

The proposed architecture allows the system to operate in the following modes:

- Mode A – Scanned / Single-element detector (25 μm pixel diameter) / Bi-static configuration;

-Mode B – Non -scanned / 32 × 32-element detector (100 μm pixel pitch) / Bi-static configuration;

- Mode C – Scanned / Single-element detector (25 μm pixel diameter) / Mono-static configuration;

- Mode D – Non-scanned / 32 × 32-element detector (100 μm pixel pitch) / Mono-static configuration;

Modes A and C use the same receiver setup (single element, scanned) where the transmitter is set up in a bi-static configuration for the mode A and in a mono-static configuration for the mode C. Modes B and D incorporate a Gm-array operating in a non-scanning mode, where the transmitter is set up in a bi-static configuration for the mode B and in a mono-static configuration for the mode D.

3.6 The Importance of Pupil Imaging on Scanning Mirrors

The image of an aperture stop as seen from object space is the entrance pupil [9]. Likewise, the image of the stop as seen from image space is known as the exit pupil of the system [9]. In most cases the entrance pupil of a telescope is located at the aperture stop and therefore rays arriving at the system at different angles meet in this area [10][11]. In scanning optical systems the exit pupil must be positioned at the location of both scanning mirrors, otherwise, the position of rays arriving at different angles will vary during the scanning process, causing image distortions. To avoid this, one scanning mirror is placed at the location of the exit pupil of the system which is then relayed onto the other scanning mirror using a 4f system (see Figure 3.9).

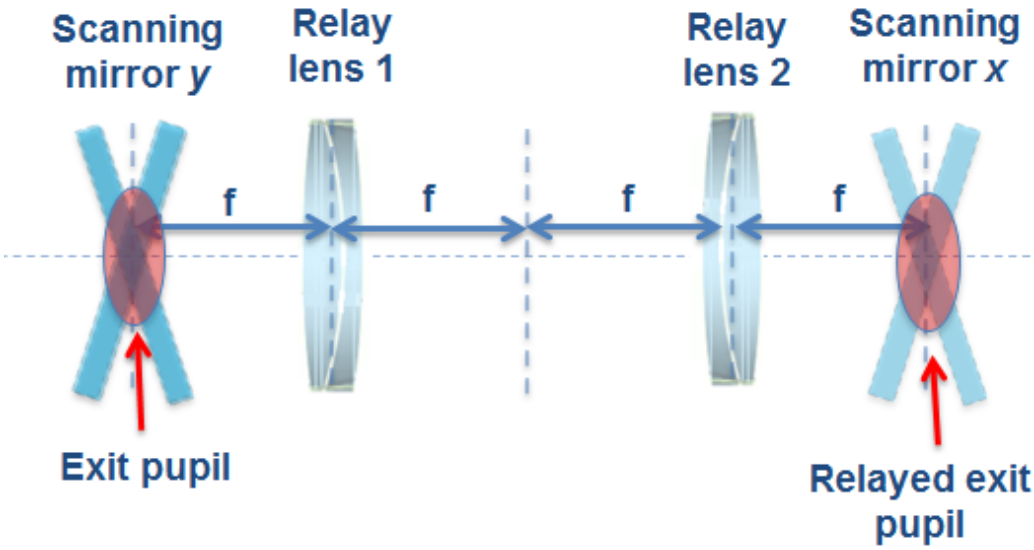

Figure 3.9. Illustration of a 4f system used to relay the exit pupil of an optical system from scanning mirror y to mirror x.

As illustrated in Figure 3.10, a 4f system enables the beam that is incident onto the aperture stop of the telescope to remain stationary on both scanning mirrors as the FoV is scanned.

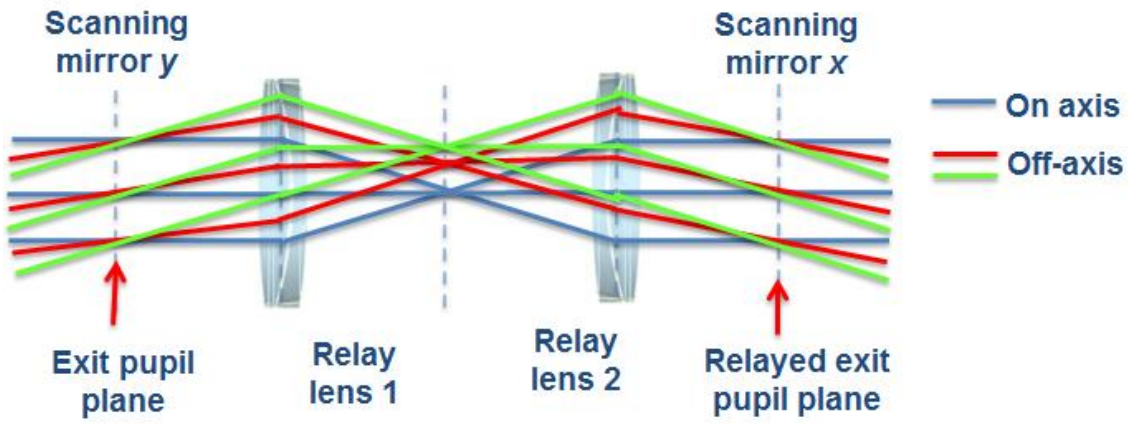

Figure 3.10. Diagram illustrating the principle of pupil imaging which allows the incident beam to remain stationary on both scanning mirrors as the FoV is scanned. The exit pupil plane is an image of the aperture stop of the telescope as seen from the object space.

3.7 Telescope Magnification

The primary function of a telescope is to enlarge the apparent size of an object located at infinity [11]. As illustrated in Figure 3.11, this is achieved by increasing the angle that rays coming from the object subtend with the optical axis. Rays from an object located at infinity (assuming range >> focal length) arrive at an aperture stop of a telescope at a very small angle, α_{IN}, which is then enlarged to α_{OUT} by using an eyepiece lens of much shorter focal length than the telescope focal length.

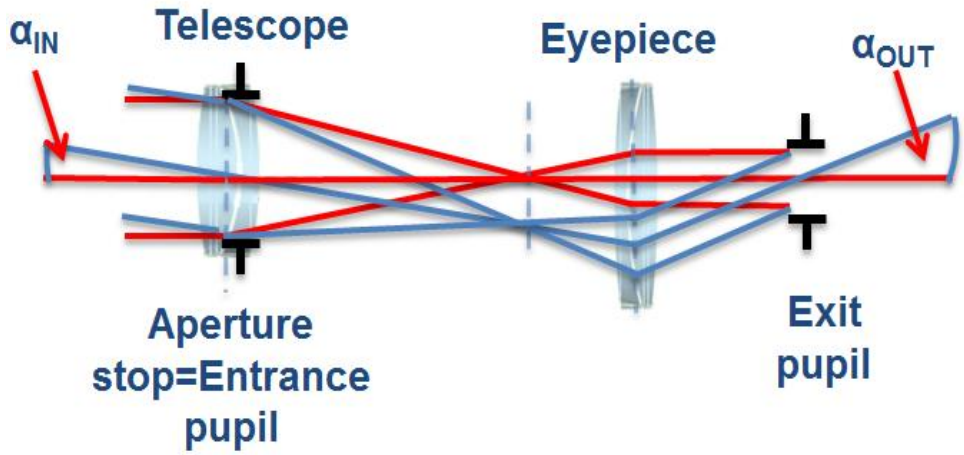

Figure 3.11. Diagram illustrating how the angle at which the beam from infinity arrives at a telescope is enlarged by an eyepiece.

The magnification, κ, of a telescope system can be expressed as the ratio between:

(a) The focal length of the telescope, $f_{telescope}$, and the focal length of the eyepiece, $f_{eyepiece}$ or;

(b) The angle at which the beam from infinity arrives at the telescope, α_{IN}, and the angle at which the beam exits the eyepiece lens, α_{OUT}.

This can be expressed by the following equation

$$\kappa = \frac{f_{Telescope}}{f_{Eyepiece}} = \frac{\alpha_{IN}}{\alpha_{OUT}} \qquad \textit{Eq. 3.4}$$

The magnification, κ, required by the lidar system is determined by the aperture diameter of the annular mirror, φ = 9 mm and by the required signal loss on the annular mirror. The required signal loss is equal to 25 %, hence, the beam diameter of the collimated beam inside of the telescope system needs to be equal to 18 mm. Since the diameter of the collecting aperture is 203 mm, it is possible to calculate the magnification required by the optical system, κ, to be the ratio of 203 mm/18 mm. Therefore, the magnification, κ, which can meet this requirement is equal to 11.28. This suggests that the minimum scanner step size increases from 0.00162 º (side FoV of the single-element scanned system) to 0.0183 º, which is still within the capability of the scanner [8].

3.8 Alignment Considerations

The 4f system and the telescope-eyepiece pair both require a high degree of collimation for the alignment of the pupil imaging to be maintained on both scanning mirrors. One of the most common and accurate ways of achieving this is by using an interferometer. A commercially available industrial Twyman-Green interferometer operating at a wavelength 633 nm was used to achieve sub-wavelength accuracy in collimation between the lenses comprising the 4f system and the telescope-eyepiece pair.

A schematic diagram of the Twyman-Green interferometer used to adjust distances between optical components is shown in Figure 3.12. It consists of a collimated laser source, a beam splitter, two mirrors and a camera system. A light source emits a beam that enters the beam splitter. The beam splitter directs the beam onto two arms of the device so part of the light is reflected onto a mirror M1 from which it is reflected back onto the beam splitter. The transmitted beam travels through components under test

and is then reflected from a mirror M2 onto the beam splitter. The two beams recombine and an interference pattern of the two wave-fronts is imaged into a camera. If a pair of relay lenses of equal focal lengths is inserted in between the beam splitter and the mirror M2 then the interference pattern observed on the camera will reflect the alignment between the two lenses. By adjusting the distance between the relay lenses such that they are two focal lengths apart from each other, the resulting wave-front will be flat producing no fringes on the camera. This type of alignment will ensure sub-wavelength accuracy.

Although there is a mismatch between the wavelength of operation of the interferometer and the design wavelength of the lidar, the aim is to implement the optical design in multiple configurations where:

- The telescope-eyepiece pair and the 4f system are optimised at 633 nm;
- The performance of the scanned single-element system is optimised at 1550 nm;
- The performance of the non-scanned 32 × 32 system is optimised at 1550 nm.

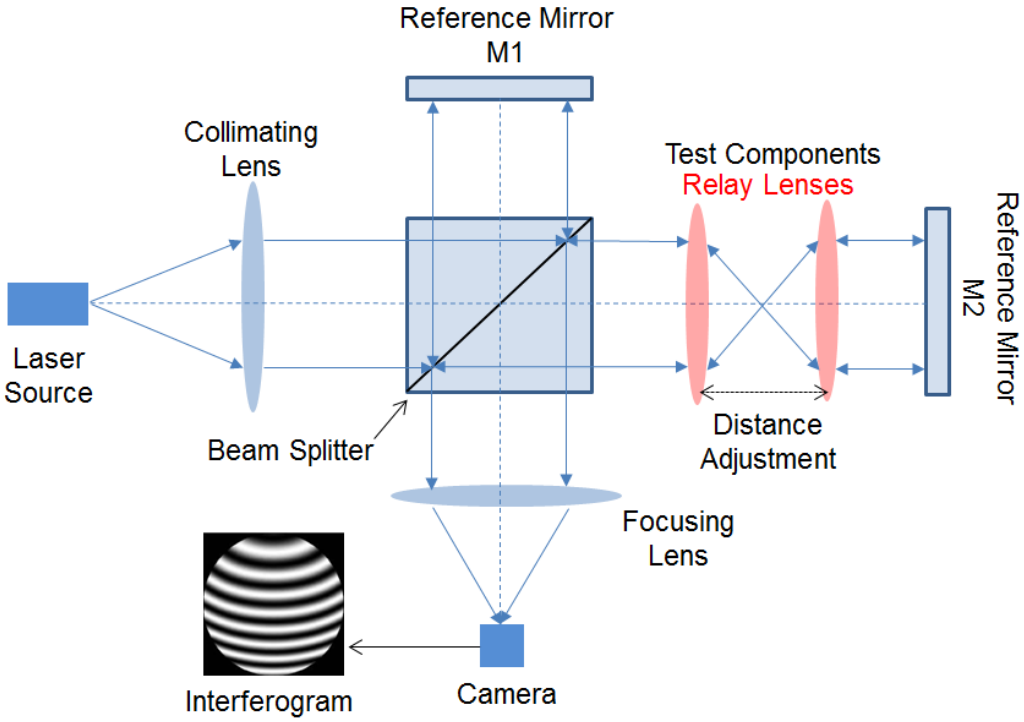

Figure 3.12. Schematic of Twyman-Green interferometer used to align optical components.

3.9 Optical Design of Receiver

In order to meet all the major specifications defined for the single-element scanned system and the 32 × 32 Gm-array system at 1550 nm and to simultaneously ensure an

afocal performance for the telescope-eyepiece pair and the 4f system at a wavelength of 633 nm, it is necessary to employ a *multiple-configuration* mode of operation which is supported by ZEMAX design package [12]. The multi-configuration tool provides a means of optimising all parameters, or variables, listed in the multi-configuration editor [12]. The process of design *optimisation* involves a successive adjustment of variables, through which a starting design is improved [13]. The improvement in the initial design is measured through a reduction in *merit function* which can be expressed as [13] [14].

$$MF = X_1^{\,2} + X_2^{\,2} + ... + X_n^{\,2} \qquad \textit{Eq. 3.5}$$

where X_i refers to a deviation from a specific design target represented by the current value, V_i, and the target value, T_i:

$$X_i = V_i - T_i \qquad \textit{Eq. 3.6}$$

X_i can depend on several independent parameters such as radius of curvature, lens thickness, lens separation, refractive index, etc. The larger the number of independent parameters the easier it is that the MF can be minimised.

The initial values of these parameters are derived from the established system architecture. The merit function is developed to meet the requirements specified in Table 3.2 for the single-element scanned configuration and for the 32 × 32 non-scanned array configuration. The merit function accounts for the beam diameter to be equal to the 18 mm on scanning mirrors and the annular mirror as well as the location of the exit pupil to be positioned at the scanning mirrors. In addition, the correction of the following aberrations is required: spherical, coma, astigmatism, field curvature, chromatic longitudinal, chromatic lateral and distortion across the FoV_{Array} and $FoV_{Scanner}$. The pupil imaging MF constrains the position of rays coming from 0.7 and 1.0 of the full diagonal 32 × 32 FoV such that the exit pupil is imaged on both scanning mirrors.

The design details of the Celestron telescope were not made available by the vendor. However, because the telescope has a diffraction limited performance, a decision to incorporate the telescope into the design as a paraxial (perfect) lens with the focal length and aperture stop diameter of that specified in the product's datasheet was made.

3.9.1 Multi-Configuration Components

The multi-configuration editor is defined for the following six configurations:

(1) 32 × 32 element detector operating in a non-scanning mode. The aim of this configuration is to optimise variables in such a way that the Airy disk diameter is 66% of the 100 µm pixel diameter at a wavelength of 1550 nm at each pixel of the array for rays arriving from angles within the FoV_{Array};
(2) Telescope-eyepiece pair. This configuration is required to achieve an afocal performance between the telescope-eyepiece pair at 633 nm;
(3) The 4f system. The system is required to have an afocal performance for the 4f system at 633 nm;

An additional three configurations are required for the single-element scanned system. The purpose of this is to optimise variables such that the Airy disk diameter is 66% of the 25 µm pixel diameter at 1550 nm for rays arriving from all angles within the FoV_{Pixel} for scanning mirrors extending the FoV_{Pixel} to $FoV_{Scanner}$ (which is equal to the FoV_{Array}). To achieve this, the following configurations are introduced to ensure the diffraction limited performance for the scanning mirrors pointing at the following regions of the FoV:

(4) 0º (nominal);

(5) 0.026° (detector side length);

(6) 0.036° (detector diagonal length).

3.9.1 Receiver System Layout

The optimisation process with the multi-configuration components generated the optical layout shown in Figure 3.13. L(a) represents a lens allowing the system to operate with the array in a non-scanning mode while lens L(b) enables the scanned operation with a single-element (SE) SPAD detector. In this way, the mode of operation can easily be switched by replacing only one lens.

Controlling and minimising aberrations was achieved by placing sufficient weight on MF aberration operands while allowing for a high degree of freedom (i.e. a sufficient number of independent variables) during the optimisation process. However, this was

only possible when an aspheric surface was used for each lens with an exception of the lens L(a). To ensure diffraction-limited performance across the fields of view of the array and the scanner the lens L(b) required an aspherical component with a conic parameter, *Cp* = -1.09 while the eyepiece and relay lenses required a conic parameter of *Cp* = -0.63 and *Cp* = -2.05 respectively.

The conic parameter, *Cp*, is used in the following formula:

$$y - 2Rx + (C_p + 1)x^2 = 0 \qquad \textit{Eq. 3.7}$$

where R is the radius of curvature of a surface [11]. This formula is used in geometric optics to specify oblate elliptical (*Cp* > 0), spherical (*Cp* = 0), prolate elliptical (0 > *Cp* > 1), parabolic (*Cp* = -1) and hyperbolic (*Cp* < 0) surfaces [11].

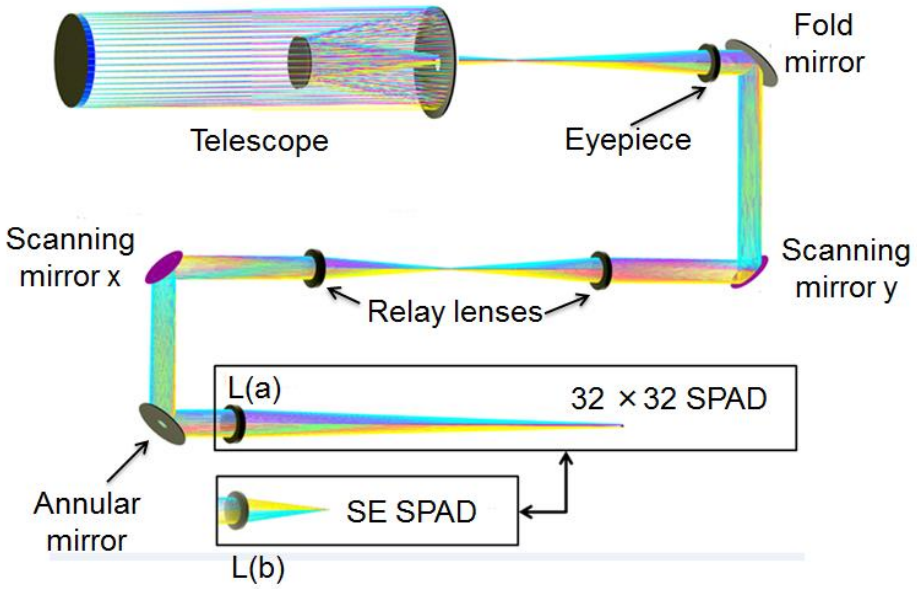

Figure 3.13. Layout of the optical system of the receiver: L(a) represents a lens required for the non-scanned mode with the array detector and L(b) represents a lens required for the scanned mode with a single-element (SE) SPAD detector.

Manufacturing of aspherical lenses adds complexity and increases the cost and lead time, therefore, the optimisation was carried out extensively before an attempt to introduce an aspheric coefficient to any of the system's surfaces.

3.9.2 Spot Diagram

The result of the geometric ray-tracing performed by ZEMAX can be used to predict the appearance of a point image on any plane within the optical system with a reasonable degree of accuracy [11]. This was to be achieved by dividing the entrance

pupil of the system into a large number of equal areas and tracing multiple rays from the object point through the centre of each of the small areas [11]. The more rays that are traced, the more accurate the representation of the geometrical image is.

A geometric spot diagram was produced to estimate the shape of the spot at the detector plane with reference to the Airy disk for different fields of view of the optical system (see Figure 3.18) [12]. The incorporation of different fields of view during the analysis is important because aberrations increase at higher angles [6]. This type of diagram shows the effect of aberrations on the focal spot; it does not however take into the account diffraction on the aperture.

Characteristics of a focal spot on the detector plane for the non-scanned system operating with the Gm-array are presented on the ZEMAX-generated spot diagram shown in Figure 3.14. The Airy disk diameter is in good agreement with the specification; it is equal to 66 µm; in addition the focal spot fits well within the Airy disk for FoV = 0 ° (nominal), the FoV = 0.026 ° (detector semi-side) and FoV = 0.036° (detector semi-diagonal).

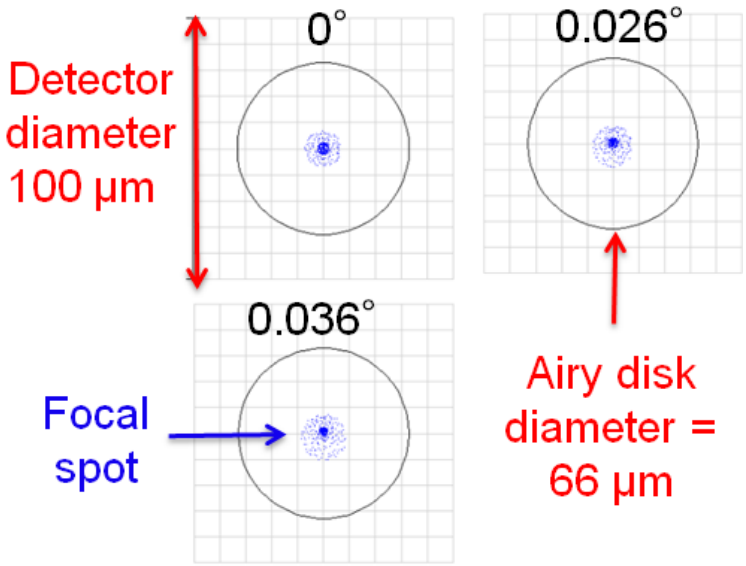

Figure 3.14. ZEMAX-generated focal spot diagram for the single-element scanned system where (a) represents the spot produced FoV_{Array} = 0 ° (nominal), FoV = 0.026 ° (array semi-side) and FoV_{Array} = 0.036 ° (array semi-diagonal).

Figure 3.15 shows the ZEMAX-generated focal spot diagram for the single-element scanned system where:

- Figure 3.15(a) represents the spot produced for 0 (0 °), 0.7 (0.0008 °) and 1 (0.0011 °) × semi-FoV_{Pixel} for scanning mirrors *x*, *y* at 0 ° tilt;

- Figure 3.15(b) represents the spot produced for 0 (0 °), 0.7 (0.0008 °) and 1 (0.0011 °) × semi-FoV_{Pixel} for scanning mirrors *x*, *y* at 0.026 ° tilt;
- Figure 3.15(c) represents the spot produced for 0 (0°), 0.7 (0.0008 °) and 1 (0.0011 °) × semi-FoV_{Pixel} for scanning mirrors *x*, *y* at 0.036 ° tilt.

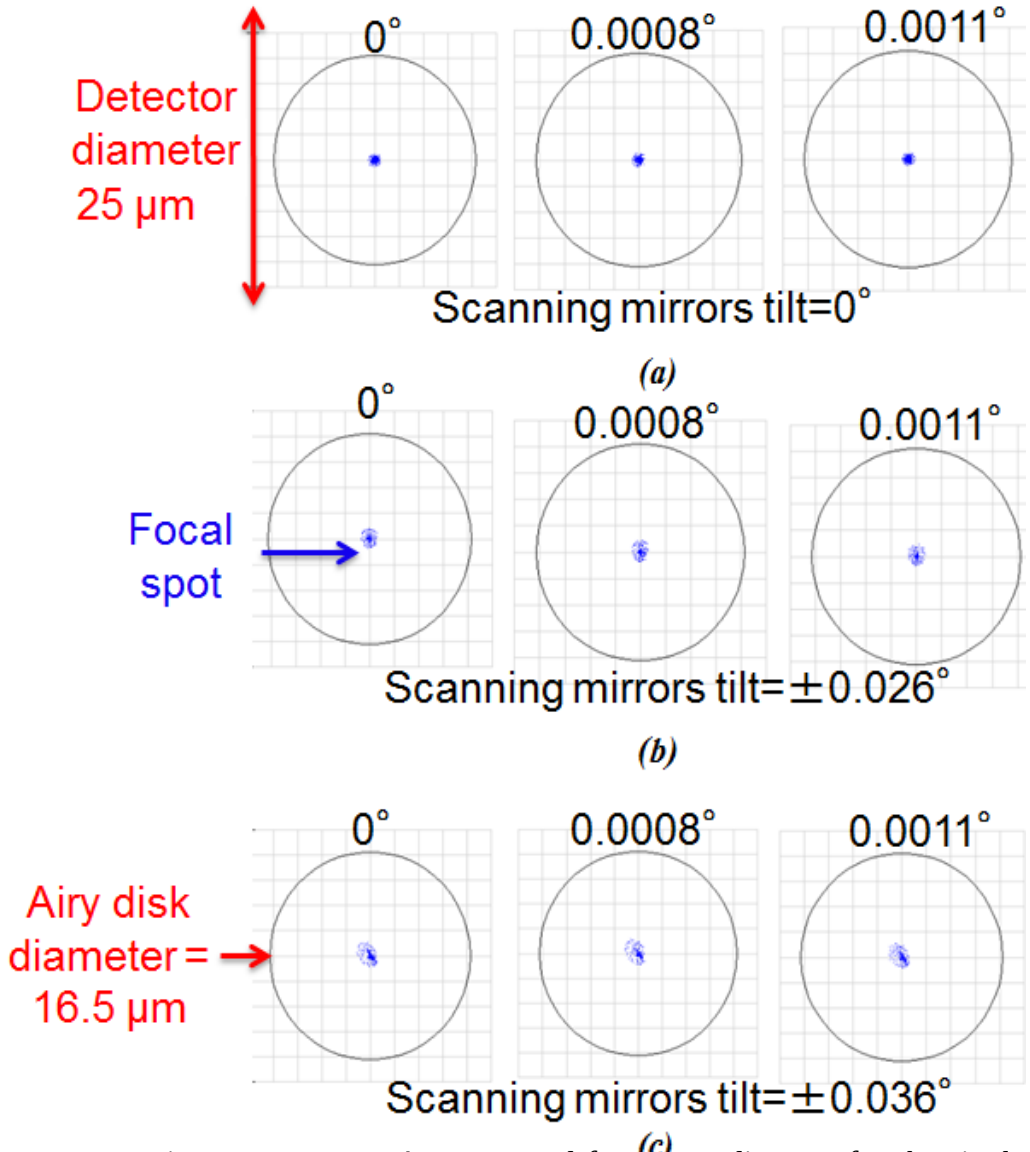

Figure 3.15. ZEMAX-generated focal spot diagram for the single-element scanned system where (a) represents the spot produced for 0 (0 °), 0.7 (0.0008 °) and 1 (0.0011 °) × semi-FoV_{Pixel} for scanning mirrors x, y at 0 ° tilt, (b) represents the spot produced for 0 (0 °), 0.7 (0.0008 °) and 1 (0.0011 °) × semi-FoV_{Pixel} for scanning mirrors x, y at 0.026 ° tilt and (c) represents the spot produced for 0 (0 °), 0.7 (0.0008 °) and 1 (0. 0011°) × semi-FoV_{Pixel} for scanning mirrors x, y at 0.036 ° tilt.

In all cases, the Airy disk diameter is equal to 16.5 µm, which is 66 % of the 25 µm detector diameter and demonstrates that the focal spot fits well within the diameter of the Airy disk. This shows a good match with the specifications.

3.9.2.1 Point Spread Function

The irradiance distribution generated by an optical system that results from a single point source in object space is called a *point spread function* (PSF) [11]. Although the source is a point, the image is not; it is blurred by the effects of diffraction and aberrations. A method applied by ZEMAX to calculate the PSF is the Fast Fourier Transform (FFT) algorithm which decomposes a spatial distribution into a frequency domain distribution in an efficient manner. Figure 3.16(a) shows a ZEMAX-generated PSF for the 32 × 32 non-scanned system for the nominal (0°) FoV and a graph of relative irradiance while Figure 3.16(b) shows a PSF cross-section in µm. As expected, the FWHM of the FFT PSF is < 66 µm.

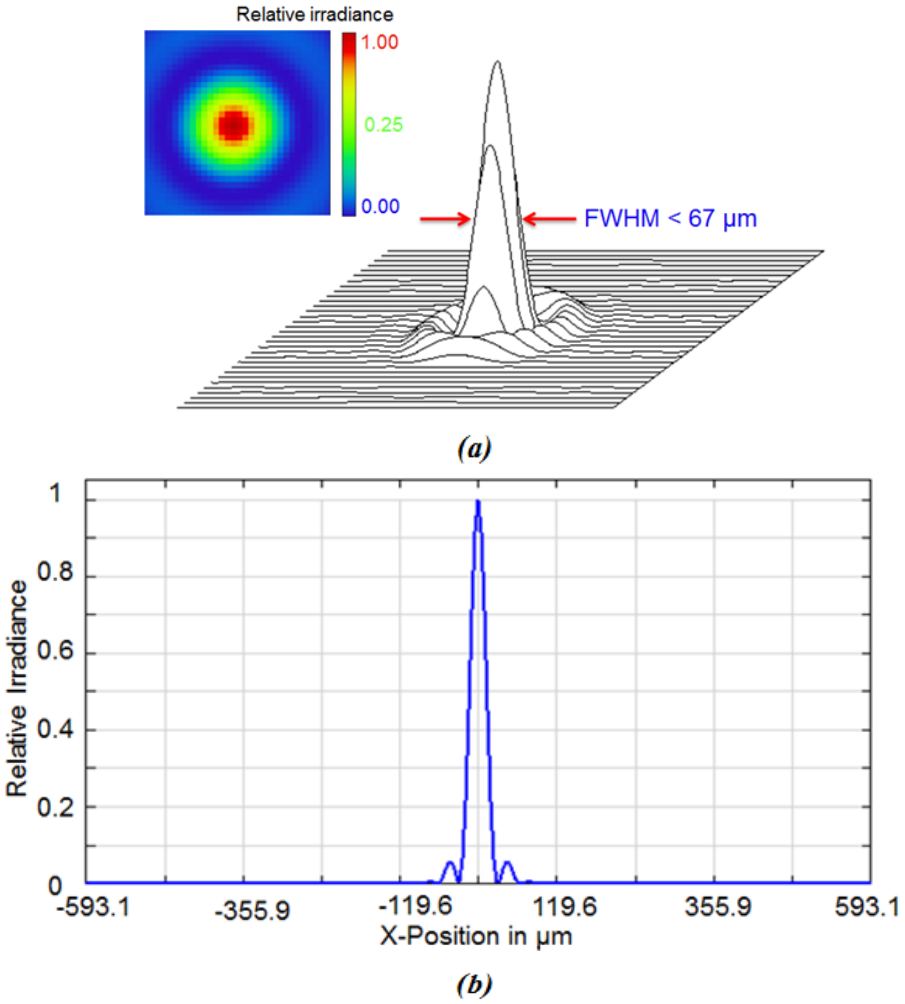

Figure 3.16. ZEMAX-generated Fast Fourier Transform point spread function for a 32 × 32 non-scanned configuration at nominal (0°) FoV: (a) surface plot and a cross-section of normalised intensity, (b) PSF cross-section in µm.

Figure 3.17 shows a ZEMAX-generated PSF for the single-element scanned system for the nominal (0 °) FoV. As expected, the FWHM of the FFT PSF is < 17 µm.

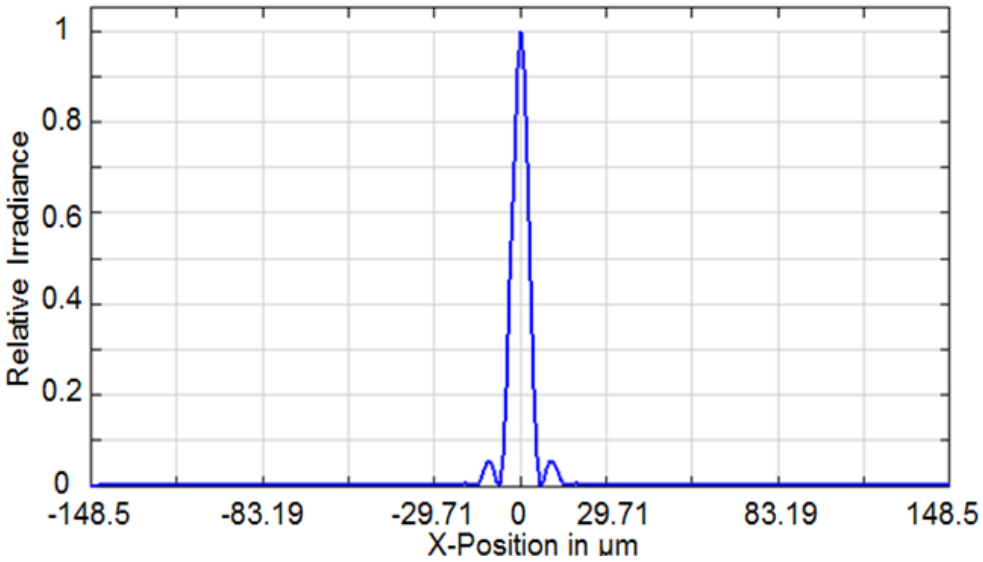

Figure 3.17. ZEMAX-generated Fast Fourier Transform point spread function for a single-element scanned sub-system at nominal (0 °) FoV: a cross-section of normalised intensity.

3.9.2.2 Through Focus Depth Diagram

The concept of *depth-of-focus* is based on the assumption that for a given optical system, there exists a blur due to defocusing of a small enough size that it will not adversely affect the performance of the system [11]. Depth-of-focus is defined by the amount by which the image plane can be shifted along the optical axis and which will introduce no more than an acceptable amount of blur [11].

Modelling depth-of-focus is useful in predicting the degree of allowed defocus on the detector plane before the image starts to degrade beyond the diffraction limit and exceeds the diameter of an Airy disk, thus, imposing tolerances on the mechanical design. Through-focus diagrams of the detector plane generated in ZEMAX are useful in analysing depth-of-focus [12]. The through-focus analysis was performed for the 32 × 32 non-scanned system (shown in Figure 3.19) and for the single-element scanned system (shown in Figure 3.20) for the rays arriving at the optical system at three angles:

- 0°(nominal) to the optical axis (see Figure 3.18(a)),
- For the beam travelling from the side FoV_{Array}, at 0.026 ° to the optical axis (see Figure 3.18(b));
- For the beam travelling from the diagonal FoV_{Array}, at 0.036 ° to the optical axis (see Figure 3.18(c)).

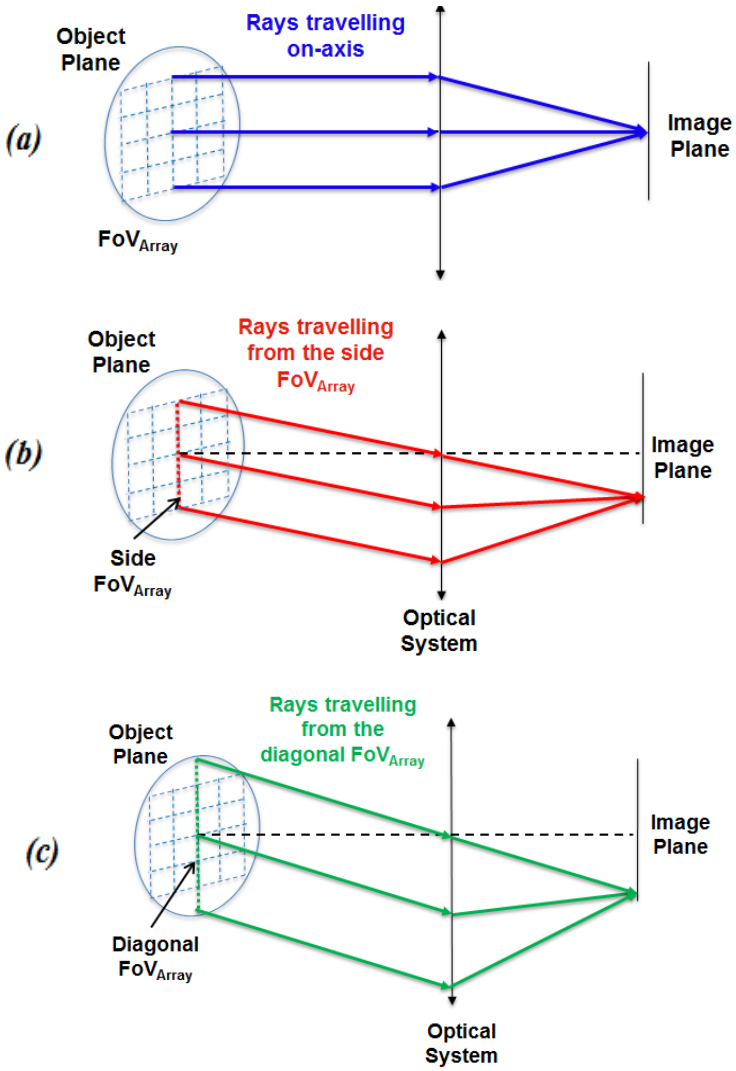

Figure 3.18. Diagrams showing rays arriving at the optical system (a) on axis, (b) from the side FoV_{Array} and (c) from the diagonal FoV_{Array}.

The array configuration has a long focal length of ~ 3.5 m, which provides a large depth-of-focus of approximately ± 800 µm from the best focus plane. Beyond this region the blur due to the defocus exceeds the size of the Airy disk diameter and thus the system is no longer diffraction-limited. This result suggests that the design provides a reasonable alignment tolerance of the focal spot on the detector plane.

The single-element scanned system has a shorter focal length of ~ 0.87 m; this is about four times less than in case of the non-scanned system and therefore the depth-of-focus is shorter. The depth-of-focus is approximately ± 60 µm. Beyond this region the blur due to the defocus exceeds the Airy disk diameter and thus the system is no longer diffraction-limited. This suggests that the alignment tolerance for this system is low and requires the mechanical stage supporting the detector to provide a sufficient degree of adjustment on a micrometre scale.

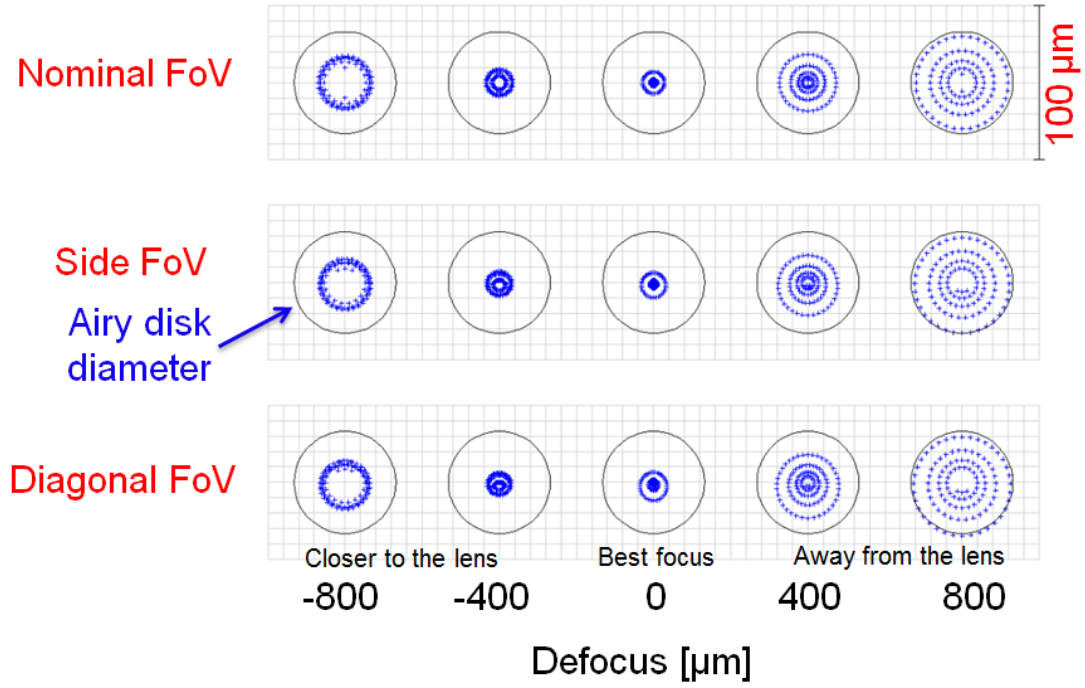

Figure 3.19. Through-focus spot diagram for the 32 × 32 non-scanned sub-system at nominal (0 °) FOV, side (0.026 °) FOV and diagonal (0.036 °) FOV.

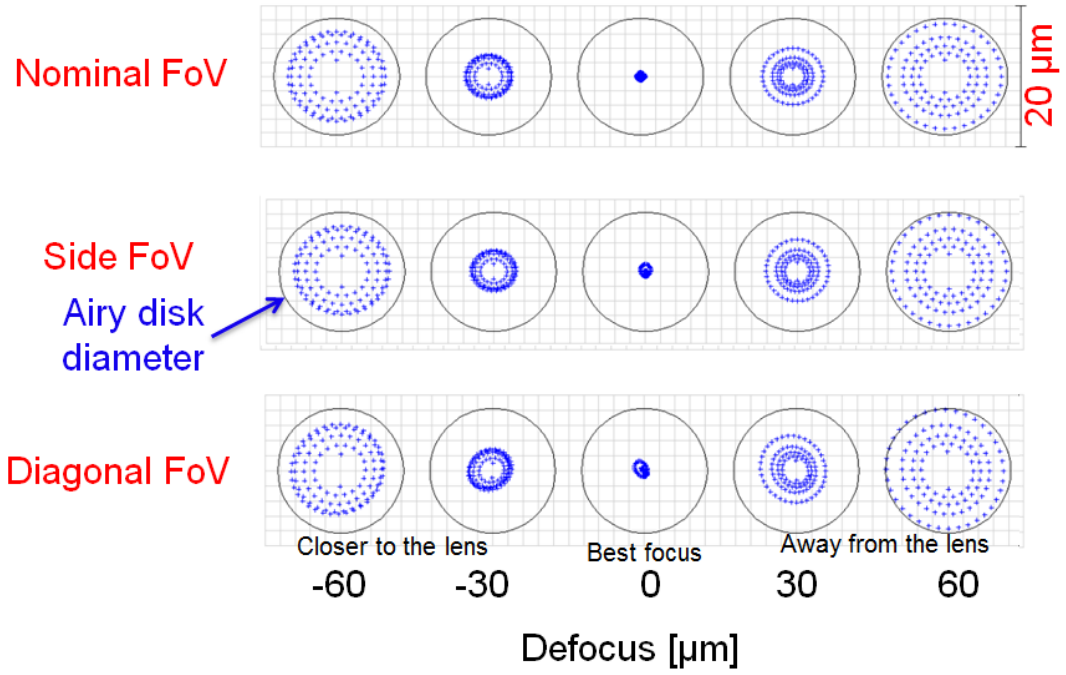

Figure 3.20. Through-focus spot diagram for the single-element scanned sub-system for scanning mirrors pointing at nominal (0 °) FOV, side (0.026 °) FOV and diagonal (0.036 °) FOV.

3.10 Depth of Field

The *depth-of-field* is the amount by which the object may be shifted before the blur of the image becomes unacceptable [11]. The size of the acceptable spot in this lidar system depends on the pixel size. Depth-of-field is of interest because, although the design range for the system is 10 km, it is useful to conduct performance tests over a variety of different ranges. For this purpose it is necessary to know the nominal range at which to focus the system in order to achieve diffraction limited performance throughout the required span of ranges.

The far and near depth-of-field was investigated in ZEMAX. The simulation was executed for a range of system focus distances (ranging from tens of metres to infinity). Table 3.3(a) shows results of the simulation for the 32 × 32 non-scanned system. The data was calculated for the worst-case scenario where the system collects the signal arriving from the edge of the FoV_{Array}. The result shows that when the system is focused at ≤ 26 m, the focal spot significantly exceeds the diameter of the Airy disk, suggesting that beyond this range the system is not diffraction limited. Below 26 m, the depth-of-field is equal to zero until 100 m and then gradually increases.

Hyperfocal distance (HD) is a useful measure to calculate because it describes the closest distance at which the image is in focus when the lens is focused at infinity [11]. In the case of the array configuration, the HD is equal to 10.5 km. Table 3.3(b) shows results of the simulation for the single-element scanned system. The data was calculated for the worst-case scenario where scanning mirrors point at the edge of the FoV_{Array}. The result shows that when the system is focused at ≤ 80 m, the focal spot significantly exceeds the diameter of Airy disk, suggesting that at locations less than this range the system is not diffraction limited. Between 80 m and 1900 m, the depth-of-field it is close to zero and then it gradually increases. The HD is equal to 11.3 km.

The quality of the image created by an optical system is not only degraded by diffraction on the system aperture but also by lens aberrations. Geometrical aberrations result from the failure of a lens system to form a diffraction-limited focal spot [15]. Only when aberrations are minimised or eliminated, the image is focused to an Airy disk which represents the best possible outcome for most optical systems.

Focus distance [m]	Diffraction-limited depth-of-field			
	(a) Array		(b) Single-Element	
	Near [m]	Far [m]	Near [m]	Far [m]
≤ 26	Beyond diffraction limit		-	
≤ 80	80	80	Beyond diffraction limit	
100	100	100	100	100
500	480	520	500	500
1000	910	1000	1000	1000
2000	1650	2400	2000	2300
3000	2300	3700	3000	4000
4000	2800	5400	2900	6000
5000	3300	7500	3400	8000
6000	3700	10,000	3800	10,000
7000	4100	13,000	4500	14,000
8000	4400	16,000	4700	20,000
9000	4800	20,000	5000	27,000
10,000	5000	26,000	5400	39,000
11,000	5200	34,000	5600	59,000
12,000	5400	43,000	5900	90,000
13,000	5600	90,000	6100	300,000
Infinity	10,500	Infinity	11,300	Infinity

Table 3.3. Table showing depth-of-field values for the array and for the single-element configurations depending on the distance at which the system is focused. The data is generated for the worst-case scenario where scanning mirrors are pointing at the edge of the FoV_{Array}.

3.10.1 Seidel Aberrations

Seidel codified the primary aberrations and derived analytical expressions for their determinations. For this reason, the main image defects are typically referred to as the Seidel aberrations and are classified as spherical aberration, coma, astigmatism, field curvature, distortion as well as longitudinal and lateral chromatic shift [11].

Assuming that an optical system is symmetrical about its optical axis, then the object point as lying on the *y* axis at a distance from the optical axis equal to *h* can be defined. In order to do that, a ray starting from the object point (see Figure 3.21) and passing through the system aperture at a point described by its polar coordinates (s, θ) is considered. The ray intersects the image plane at the point *x'*, *y'*.

The equation which describes the image plane intersection coordinates *x'* and *y'* as a function of *s*, *h* and θ is a power series expansion and is given by [11]

$$\begin{aligned} y' = {} & A_1 s\cos\theta + A_2 h + B_1 s^3\cos\theta + B_2 s^2 h(2+\cos 2\theta) \\ & + (3B_3 + B_4) s h^2\cos\theta + B_5 h^3 + C_1 s^5\cos\theta \\ & + (C_2 + C_3\cos 2\theta) s^4 h + (C_4 + C_6\cos^2\theta) s^3 h^2\cos\theta \\ & + (C_7 + C_8\cos 2\theta) s^2 h^3 + C_{10} s h^4\cos\theta + D_1 s^7\cos\theta + \ldots \end{aligned} \qquad \textit{Eq. 3.8}$$

and

$$\begin{aligned} x' = {} & A_1 s\sin\theta + A_2 h + B_1 s^3\sin\theta + B_2 s^2\sin 2\theta + \\ & + (B_3 + B_4) s h^2\sin\theta + C_1 s^5\sin\theta + C_3 s^4 h\sin 2\theta \\ & + (C_5 + C_6\cos^2\theta) s^3 h^2 + (C_4 + C_6\cos^2\theta) s^3 h^2\sin\theta \\ & + C_9 s^2 h^3\sin 2\theta + C_{11} s h^4\sin\theta + D_1 s^7\sin\theta + \ldots \end{aligned} \qquad \textit{Eq. 3.9}$$

where A_n, B_n are constants, and *s*, *h* and θ have been defined in Figure 3.21. Terms *A* relate to the paraxial, or first order, imagery. All the other terms in Eq. 3.8 and Eq. 3.9 are called transverse aberrations and represent the distance by which the ray misses the ideal image point. The terms *B* are called the third-order, or Seidel, aberrations where B_1 is spherical aberration, B_2 is coma, B_3 is astigmatism, B_4 is filed curvature, and B_5 is distortion. Similarly, *C* terms are called fifth order aberrations and terms *D* are seventh order aberrations [11].

Spherical aberration can be defined as the variation of focus with aperture (Figure 3.22 (a)). The rays close to the optical axis come to a focus (intersect the optical axis)

very near the paraxial focus position. However, as the ray height increases the position of the ray intersection with the optical axis moves farther and farther from the paraxial focus creating a blur. The magnitude of this aberration depends on the height of the ray [11].

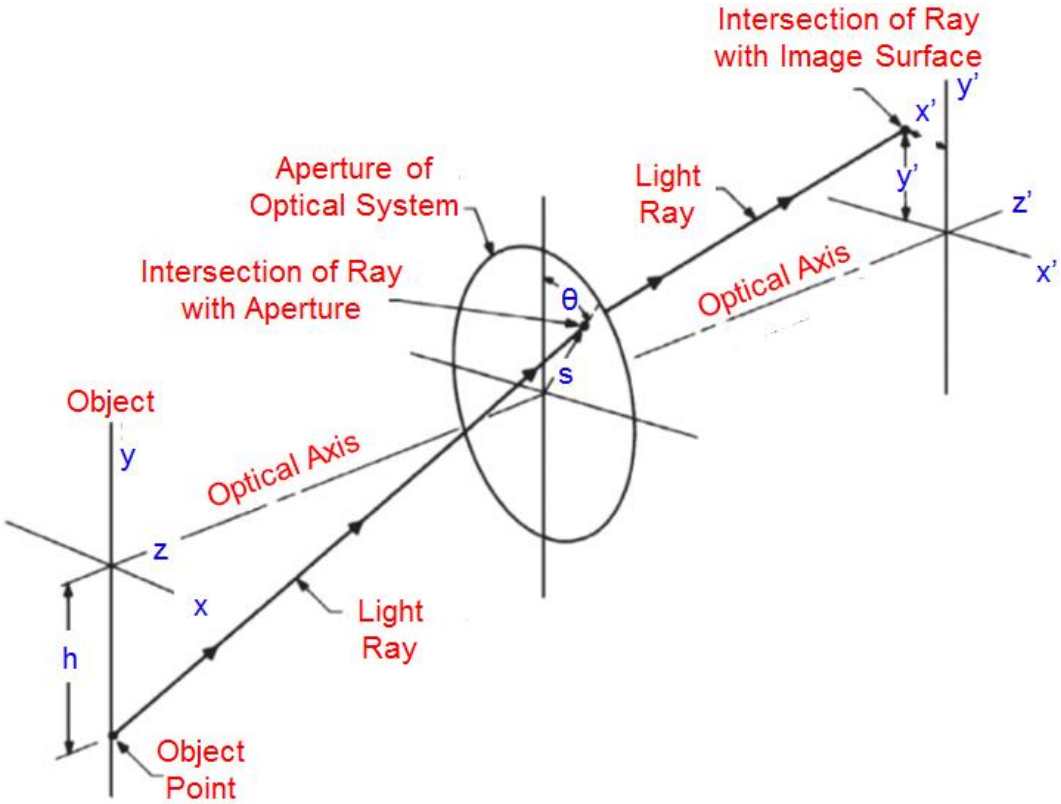

Figure 3.21. A ray from the point y = h, (x = 0) in the object plane passes through the aperture of an optical system at a point defined by its polar coordinates, (s,θ), and intersects the image plane at x', y' [11].

Coma can be defined as the variation of magnification with aperture. When a bundle of oblique rays are incident on a lens with coma, the rays passing through the edge portions of the lens may be imaged at a different height than those passing through the centre of the lens (see Figure 3.22(b)) [11].

Astigmatism occurs when the tangential and sagittal images do not coincide (see Figure 3.22(c)). In the presence of astigmatism, the image point source is not a point but takes form of two separate lines. Between the astigmatic focal points the image is an elliptical or circular blur [11].

Every lens has associated with it field curvature, also called Petzval curvature, caused by the index of refraction and surface curvatures. As a result, there is a longitudinal

departure of the focal surfaces from the ideal image surface, which is usually flat (see Figure 3.22(d)).

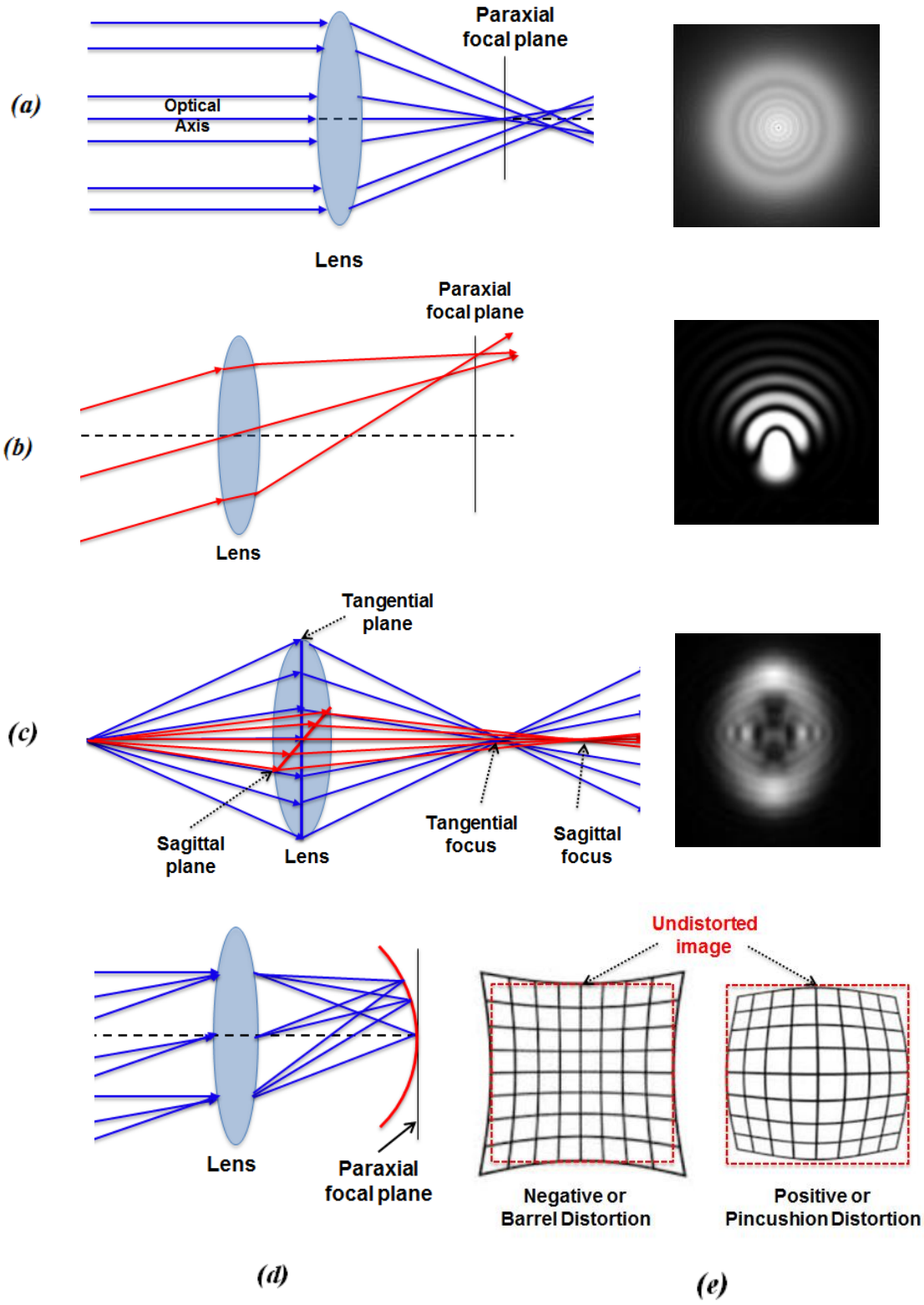

Figure 3.22. Five Seidel aberrations: (a) spherical, (b) coma, (c) astigmatism, (d) field curvature, (e) distortion [15].

When the image of an off-axis point is formed farther from the axis or closer to the axis than the ideal image height, the image of an extended object is said to be distorted

(see Figure 3.22). The amount of distortion is represented by the displacement of the image from the paraxial position and can be expressed as a percentage of the ideal image height [11] [16].

The index of refraction varies as a function of wavelength; as a result, lenses fail to focus light of different wavelengths to the same point. This causes shorter wavelengths to be more strongly refracted so that the blue light is brought to a focus closer to the lens than red rays. The distance along the axis between the two focal points is called chromatic aberration and is illustrated in Figure 3.23. This variation occurs along the optical axis (longitudinal chromatic aberration) as well as in a plane parallel to the optical axis (transverse chromatic aberration) [11].

Often it is impossible to completely eliminate aberrations, it is however possible to minimise their effect or trade-off one aberration against another. A common way of aberration minimisation involves the deliberate introduction of aberrations with opposite signs such that they cancel each other out. Lenses with aspherical surfaces can often be used to help minimise or even eliminate aberrations. However, aspheric lenses are typically made to order and are usually very specific to a particular application.

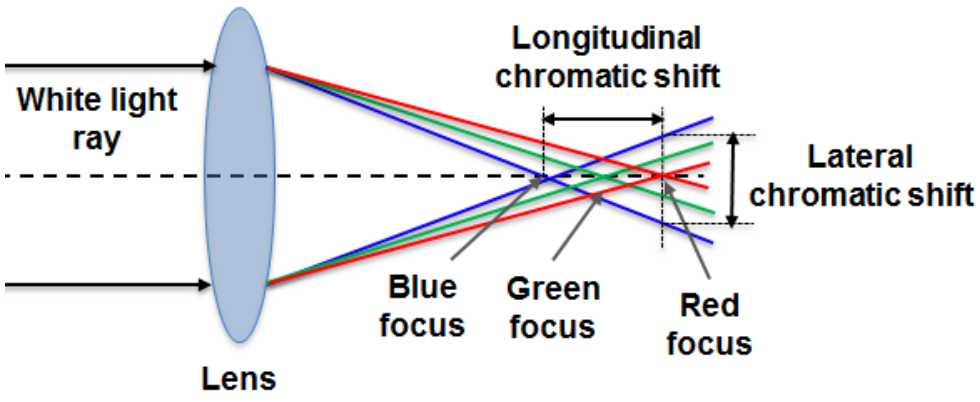

Figure 3.23. Schematic diagram illustrating longitudinal and lateral chromatic aberration.

Several runs of the ZEMAX optimisation process enabled the total sum of aberrations to be minimised to the diffraction limit level. The dominant aberrations in the design were spherical and coma and were present on the eyepiece, relay lenses and on the L4(a) lens. Other surfaces contained negligible level of aberrations. By introducing an equal but opposite amount of the dominant aberrations at the relay lenses the total

sum of aberrations in the system was minimised to a negligible total wavefront shift in respect to the pixel size of the detector at the focal plane.

Field curvature and distortion were also minimised for both configurations. For the scanned system the field curvature increased linearly across the $FoV_{Scanner}$, reaching 0.0008 % of the FoV_{Pixel}. This amount of distortion is negligible.

For the array the maximum field curvature for the rays coming from the diagonal FoV_{Array} was 45 µm with respect to the best focus position at that angle, which is less than the single pixel detector width of 100 µm. Distortion increased across the FoV_{Array}, reaching 0.01% of the entire image height at the diagonal of the FoV_{Array}. This amount of distortion is equal to an image displacement of 45 % of the pixel at the corner of the array, suggesting that it might result in signal cross-talk if alignment tolerances are not tightly controlled. A slight shift in the image position at the very corner of the array will not have a significant impact on the overall image quality.

3.11 Transmitter

Each of the four configurations of the system described in section 3.5 require a transmitter of a specific divergence. Each transmitter consisted of a commercially sourced collimating lens and a beam expander. The optical design for the transmitter is far more straightforward than that of the receiver and incorporates commercial off-the-shelf lenses. The physical optics propagation (POP) function available within ZEMAX was used to confirm that the design is able to provide the required divergence. Later chapters detail the analyses that were performed for three transmitter modes where:

- Chapter 4 explains the design of a transmitter for the single-element detector scanning system in a bi-static configuration;

- Chapter 5 describes the design of a transmitter for the single-element detector scanning system in a mono-static configuration;

- Chapter 6 outlines the design of a transmitter for the Gm-array system in a bi-static configuration.

3.12 Tolerance Analysis

The ZEMAX lens optimisation process is concerned with achieving the expected lens performance and it does not take into account errors related to manufacturing, assembly and alignment. The real-world hardware related errors can, however, significantly alter and degrade the optical performance [10]. It is therefore important to perform budgeting of manufacturing and alignment errors for each optical component in the system to ensure that system meets the specification [10]. This is called *tolerance analysis* and its purpose it to determine what are the acceptable errors which allow the required performance level to be met at a reasonable cost.

The first step in tolerance analysis is to determine possible sources of error for each surface such as: manufacturing errors (surface radius of curvature, wedge, thickness, conic constant and surface irregularity); material defects (index of refraction and dispersion); misalignment errors (element tilt and decentre). The main parameters that are used in ZEMAX tolerance analysis include: surface curvature, lens thickness, distance between optical elements, conic constant, surface tilt in x and y, surface irregularity and lens refractive index [12].

Subsequently, the deviation from the nominal value is established and inserted into the tolerance data editor. Tolerance parameters, such as tolerance of surface curvature and lens thickness, are identified for a specific surface in the system such as surface of scanning mirrors, or for a group of surfaces such as relay lenses. The nominal, or design value of the parameter is then used in the tolerance analysis together with the maximum and minimum deviation from the design.

When aligning an optical system it is possible to compensate for errors by, for instance, adjusting the position of the image plane where a photo-sensitive detector is located to find the best focus position. This type of adjustment is called a *compensator* and is also included in the tolerance data editor. When the system is perturbed from its nominal state during the tolerance analysis and the focal spot quality drops, adjusting the compensator value minimises the overall negative effect of perturbations.

Subsequently, a sensitivity analysis is performed by perturbing each of the tolerance parameters within the available degree of freedom. The consequence of these

perturbations is measured for each parameter in terms its effect on the spot radius and is displayed in the form of a difference between the required spot radius and the spot radius resulting from the maximum and minimum change in a tolerance parameter. Some parameters will affect the spot radius more than others. ZEMAX returns a list of "worst offenders" which refers to those parameters which have the most significant effect on the spot radius. This provides an insight into which tolerances can be loosened and which have to be tightened from the manufacturing and/or assembly point of view. Those tolerances that are highly sensitive and affect the spot diameter the most need to be tightened, whereas those that exhibit low sensitivity to change can be increased. After adjustments to tolerances, the sensitivity analysis is performed again. This process is repeated until the performance specification is met to within the allocated budget. If this proves impossible, certain specifications may need to be relaxed.

Sensitivity analysis computes the change in the spot radius by using the root-sum-square assumption. For each tolerance the change in performance from the nominal is squared and then averaged between the minimum ($\Delta^2_{i\_Min}$) and maximum value ($\Delta^2_{i\_Max}$). The total change, C, can be then calculated from summing the averaged squared values over all tolerances as follows [12]

$$C^2 = \sum_i \frac{\Delta^2_{i\_Min} + \Delta^2_{i\_Max}}{2} \qquad \textit{Eq. 3.10}$$

When the final set of tolerances resulting in an acceptable C^2 are established, Monte Carlo analysis simulation can be performed. Unlike the sensitivity analysis, the Monte Carlo method simulates the effects of all perturbations simultaneously [12]. For each Monte Carlo simulation cycle, tolerances for each parameter are randomly set between the minimum and maximum range using a statistical distribution model [12]. By default, all parameters follow a normal distribution with a total of four standard deviations between the minimum and maximum value [12]. For example, a lens thickness of 6 mm with a tolerance of ± 0.5 mm will be assigned a random thickness between 5.5 mm and 6.5 mm with a normal distribution centred on 6 mm and a standard deviation of 0.5.

The Monte Carlo cycle is typically repeated 15 - 20 times and compensators are adjusted for each cycle. The cumulative effect of each cycle can be represented graphically. For example, the variation in the size and position of the focal spot on the

detector plane in respect to a reference point and the Airy disk diameter can be plotted. This is very useful in visualising the effect of variations in tolerances on the focal spot shape and position.

3.12.1 Tolerance Analysis of the Receiver System

The tolerance analysis was performed in five stages. Figure 3.24 illustrates which components were included in each stage. This form of analysis is suitable for systems that consist of multiple components and which are required to work in multiple configurations. The five stages of the analysis involve the following components: (1) telescope and eyepiece; (2) relay lenses; (3a) 32 × 32 non-scanned system (lens L(a)); (3b) single-element scanned system (lens L(b)); (4) overall system.

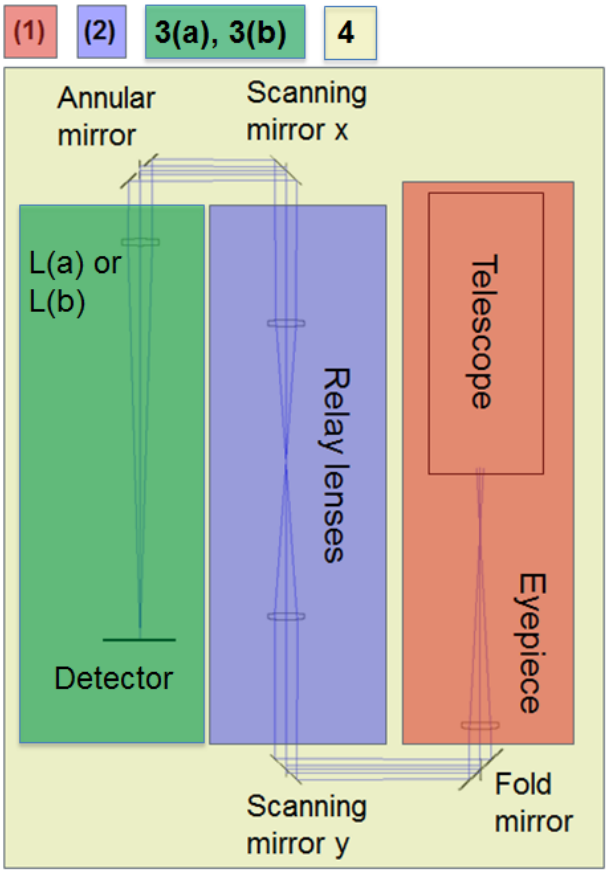

Figure 3.24. Diagram illustrating which components were included in each of the four stages of the tolerance analysis. Stage (1) includes the telescope and the eyepiece; stage (2) includes relay lenses; stage (3a) includes the 32 × 32 Gm-array and (3b) single-element scanned detector; stage (4) includes the overall system.

3.12.1.1 Tolerance Analysis Stage 1 (Telescope and Eyepiece)

As illustrated in Figure 3.25, stage 1 of the tolerance analysis involves the telescope and the eyepiece lens. The telescope is represented as a thin lens surface (s1) and the eyepiece is a singlet lens consisting of two surfaces: s2 (spherical) and s3 (aspherical).

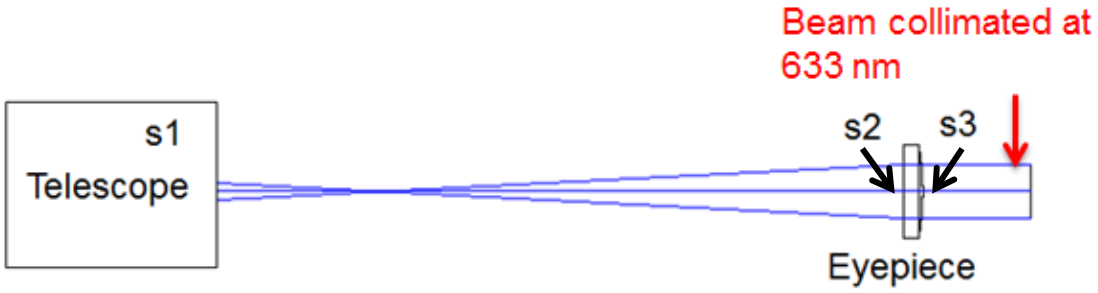

Figure 3.25. Optical components involved in the stage (1) of the tolerance analysis: a telescope represented by a thin lens of surface s1 and an eyepiece which is a singlet lens consisting of two surfaces: s2 (spherical) and s3 (aspherical).

The purpose of these elements is to collect a beam coming from infinity and to produce a collimated output at 633 nm. The focal length of this sub-system is infinite and therefore the system is referred to as *afocal*. In afocal systems, the Airy disk diameter is expressed in terms of the angular divergence limited due to diffraction on the aperture. The tolerance analysis is performed with the aim of producing a diffraction-limited wave-front divergence as the beam escapes the eyepiece.

At the initial stage of the tolerance analysis, the values of tolerances are based on an approximate judgement and are then iteratively adjusted according to the results of the sensitivity analysis. The process of tightening or relaxing of the initial values is based on the ZEMAX estimated changes to the spot divergence using the root-sum-square method (see section 3.12).

The sensitivity analysis was run and indicated that the parameters contributing to the majority of performance change in beam divergence were *x*, *y* tilt of the eyepiece and the conic constant of surface 3. After multiple iterations of sensitivity analysis the final values of the tolerance parameters were derived and are shown in Table 3.4. Tolerance parameters are specified for surfaces and elements, where elements consist of a group of surfaces.

Surface tilt is specified separately for each surface of the eyepiece as well as for the entire element. This is due to the two-fold nature of lens elements error. Lenses are manufactured with an error called a wedge effect, meaning that surfaces can be tilted with respect to each other due to a tooling inaccuracy. In addition, when the lens element is mounted, it can again be tilted with respect to the optical axis as a whole. The combination of these errors can have a significant impact on system's performance. It may be important to mitigate this effect by taking appropriate measures when designing a mechanical assembly.

During the alignment process of the telescope and eyepiece it is possible to adjust the distance between these two elements. This parameter is therefore used as a compensator in the tolerance analysis. The role of a compensator is to provide an additional degree of freedom required in the system optimisation process.

Tolerance parameter	**Surfaces or elements**	**Tolerance**
Surface radius of curvature	Surface 1, 2, 3	± 10 fringes
Thickness between surfaces	Between surfaces 1-2 and 2–3	± 0.1 mm
Surface tilt *x, y* (wedge)	Surface 2, 3	± 0.017º
Surface irregularity	Surface 1, 2, 3	± 0.5 fringe
Surface conic constant	Surface 3	± 1
Element decentre *x, y*	Telescope, eyepiece	± 0.35 mm
Element tilt *x, y*	Eyepiece	± 0.3º
Element refractive index	Eyepiece	± 0.001
Element Abbe number	Eyepiece	± 1% (0.678)
Compensator	Air gap surface 1 - eyepiece	± 0.03 mm
Test wavelength	633 nm	

Table 3.4. Parameters used in tolerance analysis of the telescope and eyepiece.

In ZEMAX, the analysis of afocal systems is performed with an Airy disk diameter expressed in angular units. This refers to the divergence of the nearly-collimated beam resulting from diffraction from the system's aperture. In order to simulate the impact of tolerances on the system shown in Table 3.4, a Monte Carlo analysis was conducted. The analysis involved 20 runs based on normal statistics. For each run the impact of tolerances on the beam divergence in the image plane in respect to the Airy disk diameter was recorded. Figure 3.26 shows a spot diagram of the system without the impact of tolerances and Figure 3.27 shows the blur resulting from random

variations in tolerances after 20 runs of the Monte Carlo simulation. The result of the simulation shows that the tolerances allow the spot to remain within the Airy disk diameter and therefore the system maintains diffraction limited performance.

The Monte Carlo statistics of the compensator indicates that the thickness between the telescope and the eyepiece varies between 222.176 mm and 223.21 mm with a mean of 222.7 mm. Provided that the telescope-eyepiece distance can be adjusted using a mechanical zoom (on which the eyepiece is mounted with respect to the static telescope) within a range of movement over 1 mm and a step size on the scale of a fraction of the wavelength (~ 10 µm), interferometer alignment will be able to provide a tolerance of several fringes, ensuring diffraction limited performance of these components after the alignment.

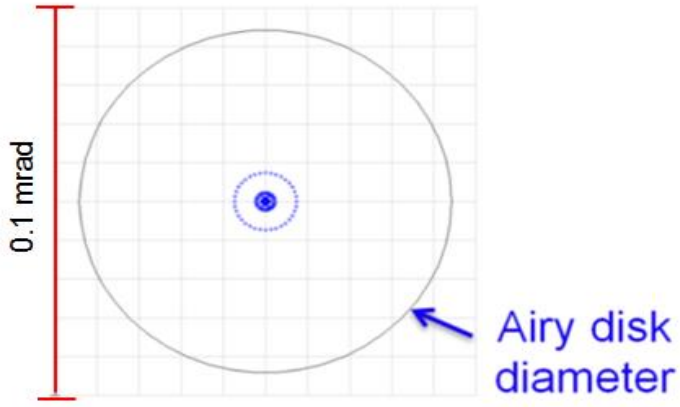

Figure 3.26. ZEMAX generated spot diagram in the image plane of the afocal system consisting of the telescope and eyepiece. This diagram does not consider the impact of tolerances.

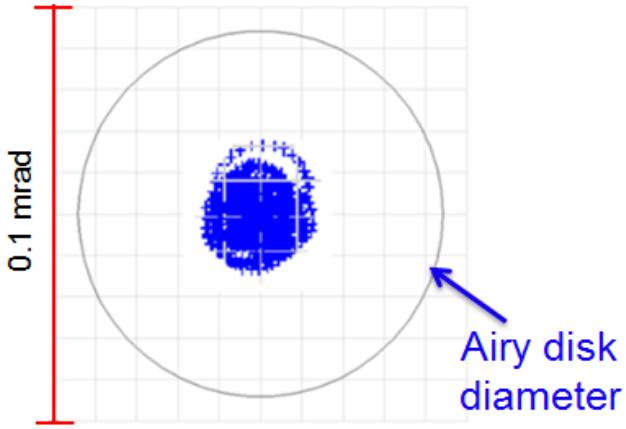

Figure 3.27. ZEMAX generated spot diagram in the image plane of the afocal system consisting of the telescope and eyepiece. This diagram consists of the overlaid result of 20 Monte Carlo runs using tolerance analysis.

3.12.1.2 Tolerance Analysis Stage 2 (Relay Lenses)

Stage 2 of tolerance analysis is concerned with the relay lenses. Relay lens 1 collects the beam collimated by the telescope while the role of relay lens 2 is to maintain the collimation of the beam at 633 nm. As illustrated in Figure 3.28 both relay lenses are identical singlets with one spherical (s7 and s8) and one aspherical surface (s6 and s9). The aim of the tolerance analysis is to maintain diffraction-limited divergence of the beam at 633 nm as it escapes the pair of relay lenses.

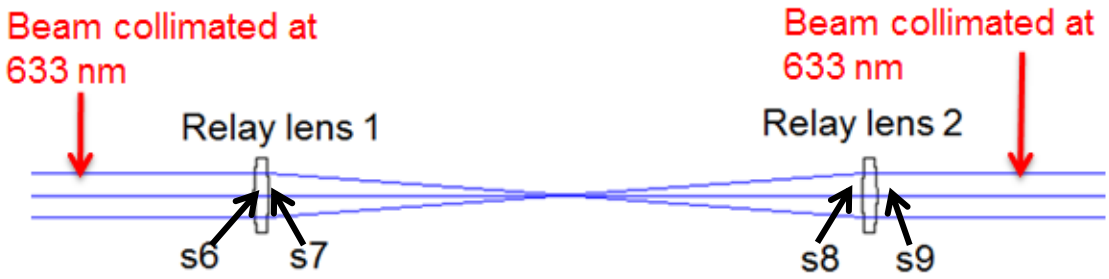

Figure 3.28. Optical components involved in the stage 2 of the tolerance analysis: relay lens 1 with surfaces s6 (aspherical) and s7 (spherical) and a relay lens 2 with surfaces s8 (spherical) and s9 (aspherical).

Similarly to the tolerancing process described in the earlier section, the tightening or relaxing of the initially set tolerance values was based on the changes to the spot divergence estimated by ZEMAX. According to the sensitivity analysis, the parameters contributing to the majority of performance change are the *x* and the *y* tilt of both of the relay lenses and the conic constant of the two aspherical surfaces. After multiple iterations of sensitivity analysis the final values of the tolerance parameters were derived and are shown in Table 3.5.

Due to the magnification occurring at the telescope-eyepiece pair as well as the movement of scanning mirrors the beam enters the relay lenses at relatively high angles. This contributes to higher order aberrations and therefore requires slightly tighter tolerances, especially on the most sensitive parameters such as the element tilt and conic constant, than the telescope-eyepiece pair tolerances shown in Table 3.4.

Monte Carlo analysis was performed to investigate the effect of perturbations for all tolerance parameters on the focal spot size. The analysis involves executing multiple independent simulations where all tolerance parameters are simultaneously perturbed at a random amount between the minimum and maximum value.

Tolerance parameter	Surfaces or elements	Tolerance value
Surface radius of curvature	Surface 6, 7, 8, 9	± 10 fringes
Thickness between surfaces	Between surfaces 6-7, 7-8 and 8-9	± 0.1 mm
Surface tilt *x*, *y* (wedge)	Surface 6, 7, 8, 9	± 0.017º
Surface irregularity	Surface 6, 7, 8, 9	± 0.5 fringe
Surface conic constant	Surface 6, 9	± 0.03
Element decentre *x*, *y*	Relay lens 1, relay lens 2	± 0.1 mm
Element tilt *x*, *y*	Relay lens 1, relay lens 2	± 0.1º
Element refractive index	Relay lens 1, relay lens 2	± 0.001
Element Abbe number	Relay lens 1, relay lens 2	± 1% (± 0.678)
Compensator	Air gap between surfaces 7-8	± 1 mm
Test wavelength	633 nm	

Table 3.5. Parameters used in tolerance analysis of the relay lenses.

Figure 3.29 shows a spot diagram of the system without the effect of tolerances and Figure 3.30 shows the blur resulting from random variations in tolerances after 20 runs of the Monte Carlo simulation. The result of the simulation shows that the tolerances confine the spot to a region within the Airy disk diameter and therefore the system maintains the diffraction limited divergence within the specified tolerances.

A compensator (defined in section 3.12) used in this sub-system is the adjustment of the air gap between the surface s7 and surface s8. The Monte Carlo statistics for this type of compensator indicates that the thickness between the two relay lenses varies from the 251.248 mm nominal thickness to the minimum of 250.971 mm and the maximum of 251.526 mm. This suggests that a mechanical zoom capable of 0.555 mm adjustment between the relay lenses is required. The lenses can be then mounted in two separate tubes and joined by a mechanical zoom. In addition, a mechanism allowing the adjustment of tilt and decentre between the two lenses is required in order to provide a diffraction limited performance.

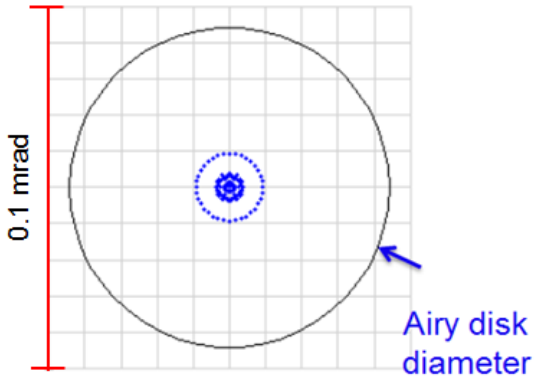

Figure 3.29. ZEMAX generated spot diagram in the image plane of the afocal system consisting of two relay lenses. This diagram does not show the effect of tolerances.

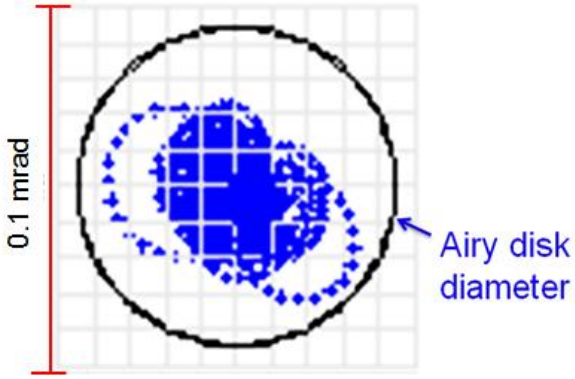

Figure 3.30. ZEMAX generated spot diagram in the image plane of the afocal system consisting of the telescope and eyepiece. This diagram consists of the overlaid result of 20 Monte Carlo runs using tolerance analysis.

3.12.1.3 Tolerance Analysis Stage 3a (32 × 32 Non-Scanned System)

The illustration shown in Figure 3.31 shows the components used in the stage 3a analysis. This stage involves lens L3(a) which collects the beam collimated at 633 nm and creates a diffraction-limited focal spot at a wavelength of 1550 nm within the plane of the array detector.

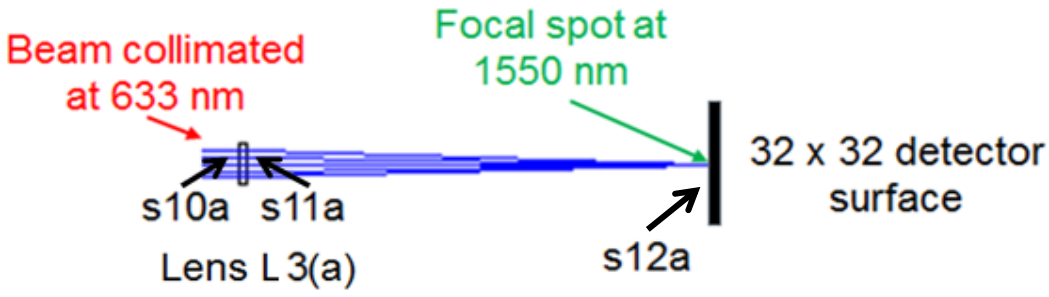

Figure 3.31. Components involved in the stage 3a of the tolerance analysis: a spherical lens, L3(a) with two surfaces s10a and s11a and a surface of the detector.

Lens L3(a) is a spherical lens with surfaces s10a and s11a. According to the sensitivity analysis, the main parameters which contribute to a change in the optical performance are the *x*, *y* tilt of the spherical lens as well as the irregularity of surfaces s10a and s11a. The final values of tolerance parameters were derived and are shown in Table 3.6.

Monte Carlo analysis was performed to investigate the effect of perturbations for all tolerance parameters on the focal spot size. Figure 3.32 shows a spot diagram of the system without the effect of tolerances and Figure 3.33 shows the focal spot after 20 runs of the Monte Carlo simulation. The result of the simulation shows that the tolerances allow the spot to remain within the Airy disk diameter and therefore the system maintains diffraction limited performance within the specified tolerances. However, the position of the spot varies across the *x* and *y* axes in the detector plane (250 µm × 250 µm).

Tolerance parameter	**Surfaces or elements**	**Tolerance**
Surface radius of curvature	Surface s10a and s11a	± 10 fringes
Thickness between surfaces	Between surfaces s10a and s11a	± 0.1 mm
Surface tilt *x*, *y* (wedge)	s10a and s11a	± 0.017°
Surface irregularity	s10a and s11a	± 0.5 fringe
Element decentre *x*, *y*	Lens L3(a)	± 0.1 mm
Element tilt *x*, *y*	Lens L3(a)	± 0.1°
Element refractive index	Lens L3(a)	± 0.001
Element Abbe number	Spherical lens	± 1% (± 0.678)
Compensator	Air gap between surface s11a and s12a	± 2 mm
Test wavelength	1550 nm	

Table 3.6. Parameters used in tolerance analysis of lens L3(a).

The compensator used in this sub-system is the adjustment of the air gap between lens L3(a) and the detector plane. The Monte Carlo compensator statistics indicate that ± 1.85 mm of adjustment in the focal plane from the nominal focus position and ± 125 µm along the *x* and *y* directions are required. This can be achieved by mounting the array on a micrometre translation stage with an *x*, *y* and *z* adjustment which would maximise the signal on a detector pixel.

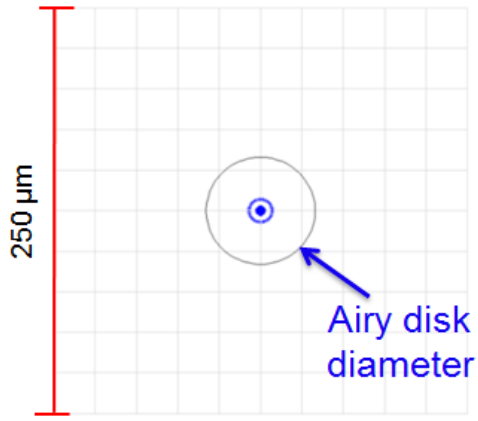

Figure 3.32. ZEMAX generated spot diagram produced by the lens L3(a) on the detector surface at 1550 nm. This diagram does not consider the effect of tolerances.

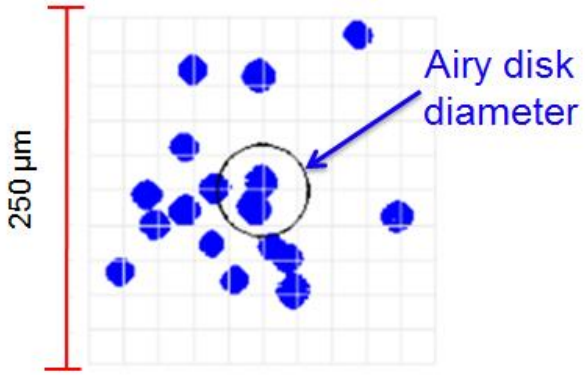

Figure 3.33. ZEMAX generated spot diagram produced by the lens L3(a) on the detector surface at 1550 nm. Each spot is a result produced after one Monte Carlo analysis. A total number of 20 Monte Carlo analyses was performed and shows the extent of variation in the spot location across the detector plane.

3.12.1.4 Tolerance Analysis Stage 3b (Single-Element Scanned System)

The illustration shown in Figure 3.34 illustrates components which are involved in stage 3b of the tolerance analysis. Lens L3(b) contains two surfaces s10a (aspherical) and s11b (spherical). This lens collects the beam collimated at 633 nm and focuses it onto the surface of the single-element detector (surface s10b) at a wavelength of 1550 nm. According to the sensitivity analysis, the main parameters that contribute to the change in performance are radius of curvature and the thickness between surfaces s10b and s11b, as well as the tolerance on the conic constant of surface s10b. Tilt and decentre of surfaces and elements have a minor impact on the performance.

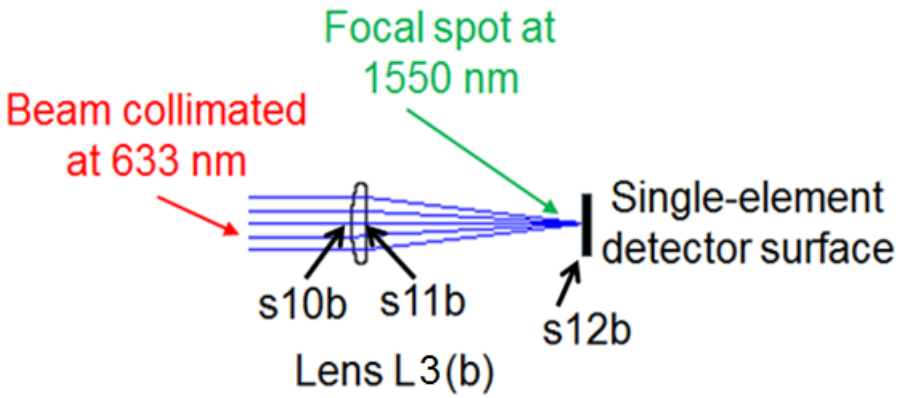

Figure 3.34. Components involved in the stage 3b of the tolerance analysis: a spherical lens L3(b) with two surfaces s10b and s11b and a surface of the detector, s12b.

The final values of the tolerance parameters were derived and are shown in Table 3.7.

Tolerance parameter	**Surfaces or elements**	**Tolerance value**
Surface radius of curvature	Surface s10b and s11b	± 10 fringes
Thickness between surfaces	Between surfaces s10b and s11b	± 0.1 mm
Surface tilt *x*, *y* (wedge)	s10b and s11b	± 0.017º
Surface irregularity	s10b and s11b	± 0.5 fringe
Element decentre *x*, *y*	Lens L3(b)	± 0.1 mm
Element tilt *x*, *y*	Lens L3(b)	± 0.1º
Element refractive index	Lens L3(b)	± 0.001
Element Abbe number	Lens L3(b)	± 1% (± 0.678)
Compensator	Air gap between surface s11b and s12b	± 1 mm
Test wavelength	1550 nm	

Table 3.7. Parameters used in tolerance analysis of lens L3(b).

Monte Carlo analysis was performed based on normal statistics. Figure 3.35 shows a spot diagram of the system without the impact of tolerances and Figure 3.36 shows the result of random variations in tolerances after 20 runs of the Monte Carlo simulation. The result shows that the tolerances allow the spot to remain within the diameter of Airy disk and therefore the system maintains diffraction limited performance within the set tolerances. However, the position of the spot varies across the *x* and *y* axes on the detector plane (170 µm × 170 µm).

The compensator used in this sub-system is the adjustment of the air gap between lens L3(b) and the detector plane. The Monte Carlo compensator statistics indicate that

± 0.23 mm of adjustment along the focal plane from the nominal focus position and ± 125 µm along the *x* and *y* directions are required. This can be achieved by mounting the single-element detector on a micrometre translation stage with an *x*, *y* and *z* adjustment to maximise the signal on the detector pixel.

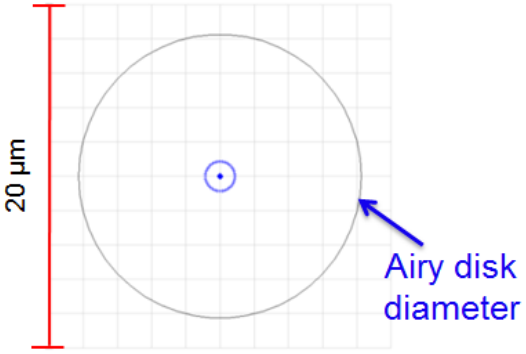

Figure 3.35. ZEMAX generated spot diagram produced by the lens L3(b) on the detector surface at 1550 nm. This diagram does not consider the impact of tolerances.

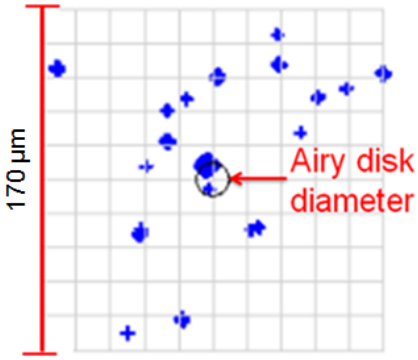

Figure 3.36. ZEMAX generated spot diagram produced by the lens L3(b) on the detector surface at 1550 nm. This diagra consists of the overlaid result of 20 Monte Carlo runs.

3.12.1.5 Tolerance Analysis Stage 4a and stage 4b (Overall System Performance)

In stages 1, 2, 3a and 3b of the tolerance analysis it was shown that the chosen tolerances ensure that each of the four sub-components in Figure 3.24 can perform to the expected level. The aim of the final stage of the tolerancing process is to ensure that all the sub-components assembled together on a breadboard can maintain the required level of performance for both the 32 × 32 non-scanned detector (stage 4a) and for the single-element scanned detector (stage 4b). This phase of the analysis investigates the impact on overall performance of the tilt and position errors of the optical elements involved in the design. Table 3.8 shows tolerance parameters set up

for these components, in addition to those already shown in Table 3.4, Table 3.5, Table 3.6 and Table 3.7.

Surfaces or elements	**Tolerance parameter**	**Tolerance value**
Telescope and eyepiece	Position along the optical axis	± 1 mm
	Tilt *x, y*	± 0.5º
	Decentre	± 0.5 mm
Fold mirror position	Position along the optical axis	± 1mm
	Tilt *x, y*	± 0.1º
	Decentre	± 0.5 mm
	Surface irregularity	± 1 fringe
Relay tube	Position along the optical axis	± 1 mm
	Decentre	± 0.2 mm
	Tilt *x, y*	± 0.2º
Scanning mirror *x* and *y*	Position along the optical axis	± 0.5 mm
	Tilt *x, y*	± 0.1º
	Decentre	± 0.5 mm
	Surface irregularity	± 1 fringe
Annular mirror	Position along the optical axis	± 1mm
	Tilt *x, y*	± 0.1º
	Decentre	± 0.5 mm
	Surface irregularity	± 1 fringe
Compensator 1	Fold mirror tilt *x, y*	± 0.5º, ± 0.5 mm
Compensator 2	Annular mirror tilt *x, y*	± 0.5º, ± 0.5 mm
Compensator 3	Longitudinal position of detector in the focal	± 2 mm
Compensator 4	Lateral position of detector in the focal plane	± 2 mm
Test wavelength	1550 nm	

Table 3.8. Parameters used in the stage 4 of the tolerance analysis.

The sensitivity analysis indicated that the parameters which have the most serious effect on the size of the focal spot are the surface irregularity of all the mirrors. It is therefore important to use mirrors with surface irregularities of the required standard of ± 1 fringe. After 20 runs of Monte Carlo analysis, the result indicated that chosen tolerances and compensators allow the system to provide the diffraction limited

performance for the 32 × 32 non-scanned detector and for the single-element scanned detector.

The result of ray tracing for the rays coming from the edge of the FoV after 20 runs of the Monte Carlo analysis performed in ZEMAX for the Gm-array showed that the variation in movement of elements after each run did not result in clipping on the optical components. Although the position of the focal spot on the detector plane varies, compensating the *x*, *y* location of the detector allows the optical signal to be centred on the active area of the detector. A similar effect was achieved for the single-element detector.

The required tolerances can be achieved by the following steps: purchasing optical elements that meet the specifications; using the interferometer in the optical alignment of some of the components; using a helium-neon (He-Ne) laser and pinholes to align the optical components on the breadboard in accordance to the optical design.

3.13 Mechanical Design

The assistance of a mechanical engineer proficient in using Computer Aided Design (CAD) software was recruited in order to support the mechanical design. The aim of this was to help minimise the project lead-time and ensure that tasks were completed in agreement to the project management plan. The role of the engineer was to confirm that all the mechanical components involved in the opto-mechanical design meet the criteria specified during the tolerance analysis.

A CAD model of the transceiver is shown Figure 3.37. The majority of components involved in the mechanical assembly were commercially sourced and their dimensions were imported into the CAD design. Some of the components such as the telescope base-plate, scanning mirror assembly, annular mirror holder and laser assembly were designed by the mechanical engineer according to the specifications and were manufactured in the Selex ES workshop. The laser transmitter assembly was designed to provide sufficient degree of freedom for the beam alignment in *x*, *y* and *z* directions.

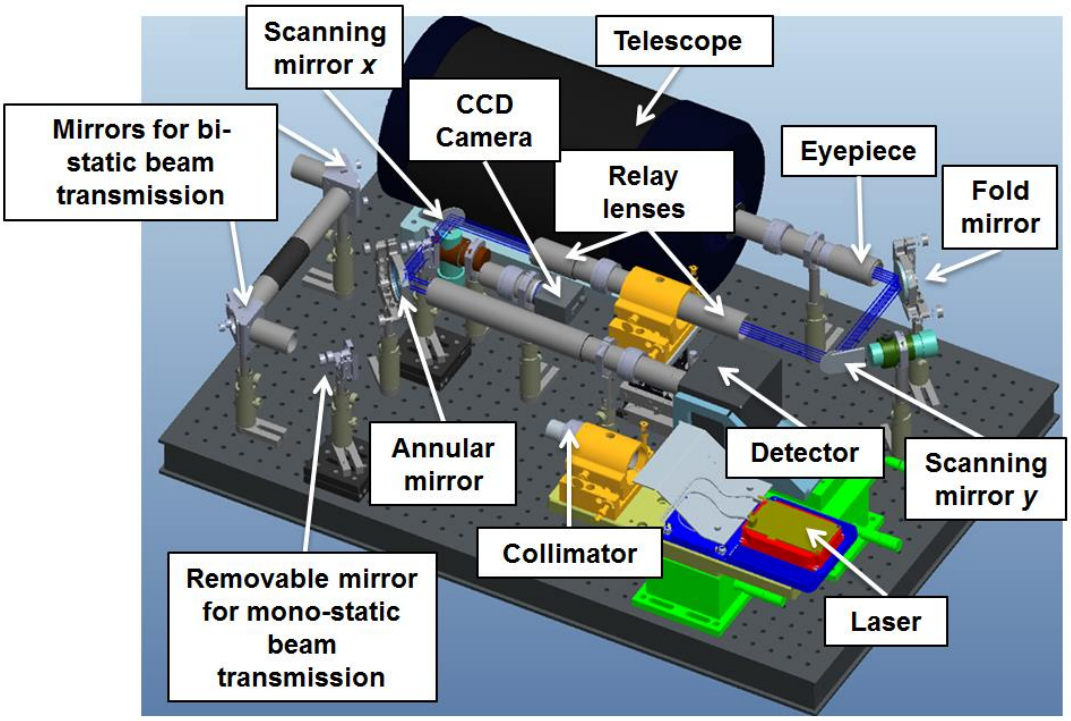

Figure 3.37. CAD model of the transceiver assembly.

3.13.1 Enclosure

For laser safety reasons, the transceiver was enclosed. A custom-made enclosure system which forms a light-tight box fitting over all the optical elements in the system was used (see Figure 3.38). The enclosure was also designed by the mechanical engineer and manufactured in-house in accordance to requirements set by a qualified laser safety officer. The part was manufactured out of lightweight folded aluminium alloy sheet with braised corners. There were three exits from the cover: the aperture of the telescope (also used as a mono-static transmitter beam exit), the bi-static transmitter beam exit and a downward facing exit port for equipment power and communications cables. The box was located within a gutter which was mounted around the optical breadboard. The exit port was located at the bottom of the gutter. The inside of the aluminium box was covered in a black flocked self-adhesive paper in order to aid light-proofing. The lid was opened and closed via hinges located at both sides of the breadboard. When the lid was opened it locked in place vertically using locking clips so that it was unable to fall back into place unexpectedly.

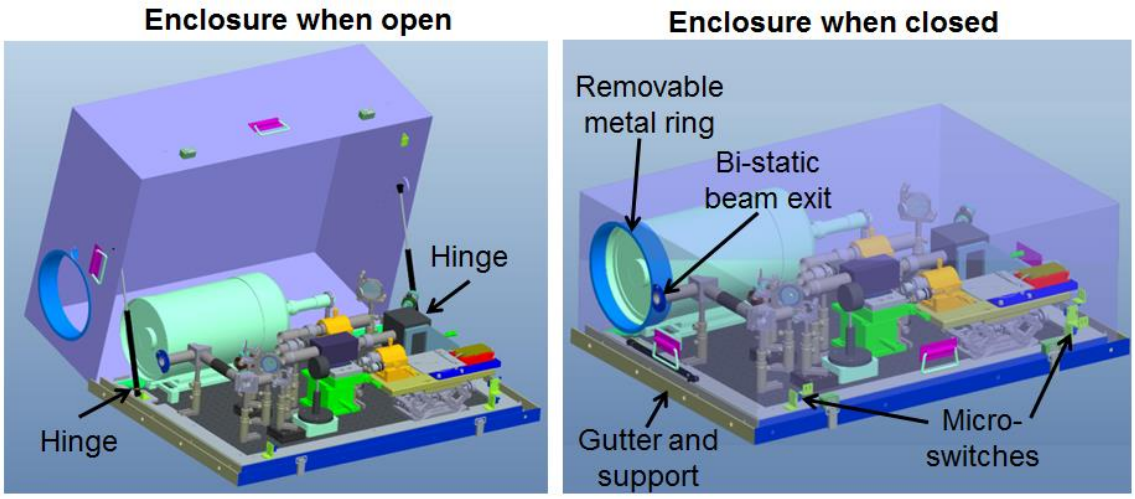

Figure 3.38. CAD model of the enclosure.

3.13.2 Optical Alignment

The receiver was aligned in five phases:

(1) Alignment of the telescope and the eyepiece on the interferometer at a wavelength of 633 nm;

(2) Alignment of the relay lenses on the interferometer at 633 nm;

(3) Alignment of the optical components of the transmitter and receiver on the breadboard using pinholes and a He-Ne laser;

(4) Alignment of transmitter divergence using a parabolic mirror;

(5) Bore-sighting of the transmitter and detector using the parabolic mirror.

The interferometer used during the alignment process was a commercially available Twyman-Green interferometer operating at a wavelength of 633 nm. Both the telescope and the eyepiece were assembled on a base plate while the relay lenses were assembled in a tube and underwent the alignment by being placed in the path of one of the arms of the interferometer.

A reference wave-front reflected from a flat mirror and a wave-front that has been altered after travelling through the elements under test created an interference pattern which could be viewed on a monitor. A non-rotating zoom-housing was used to adjust the distance between the tested elements at approximately 0.1 mm per revolution

without rotating the assembled elements (4.1 mm maximum travel distance). Adjustments were made until the resulting wavefront was flat, i.e. there were no interference fringes present on the monitor.

Phase four and five of the alignment are specific to the configuration of the optical system that is used in experiments (bi-static/mono-static, single-element scanned, 32 × 32 non-scanned) and are described in more detail in the following three chapters.

3.14 Scanning Mirrors

Galvanometric *x*, *y* scanning mirrors with a clear aperture of 20 mm at 45 ° were integrated into the system.

The advantage of this type of mirrors from the optical point of view is that they can rotate about a central axis in the plane of the mirror and can be located at the pupil of an optical system allowing it to remain unchanged as the mirrors rotate [17].

The galvanometer scanners provide a convenient and reliable way to perform *x*, *y* scanning of the laser beam and the FoV. However, the two mirrors have to be separated from each other [17]. This means that the optical system has to incorporate a pair of additional lenses which relay the image of the entrance pupil from one mirror to the other. This requires more complex optical design and imposes an additional cost. Galvanometric scanning mirrors can produce a steady-state deflection and follow a scan trajectory with considerable fidelity using random computer-controlled waveforms [17].

The scanner used in the design contains a moving magnet actuator which produces a rotary deflection in response to an electric current [8]. The mirrors offer an angular excursion of ± 20 ° and provide a step response of 350 µs, limiting the rate to 2.86 kHz [8]. The minimum scan step was 200 ± 8 µrad inside of the optical system which was equivalent to ~ 17 ± 0.7 µrad in the object plane. This exceeds the requirement of a step size of 28 µrad, providing an error in positioning accuracy of approximately 4 %.

The scanner is controlled by a field-programmable gate array (FPGA) which sends command transistor-transistor logic (TTL) inputs to the servo drivers of the scanning

mirrors controlled by LabVIEW control software developed by a systems engineer from Selex ES.

The procedure for calibrating scanning mirrors is described in Chapter 4.

3.15 Acknowledgements

The optical design and tolerance analysis of the receiver were performed in ZEMAX under supervision of Chris Davies of Selex ES. The mechanical design was performed in CAD by Michael Dugan of Selex ES according to the requirements specified by the author and to the tolerances based on the outcome of the tolerance analysis. The safety enclosure was designed by Michael Dugan according to the safety requirements specified by Dr. Stephen Harding of Selex ES. The laser interlock for the safety enclosure was designed and assembled by Naomi Mitchison of Selex ES.

3.16 Conclusions

A re-configurable lidar system was designed which provided a matching FoV per detector pixel for either the single-element detector operating in a scanning mode or the Gm-array operating in a non-scanning mode. The design process included the development of specifications for a long-range lidar and optimisation of the optical design such that the Airy disk diameter is 66 % of a detector pixel for rays arriving at the system from the entire FoV. It also included detailed tolerance analysis and development of the mechanical assembly required to maintain diffraction limited performance after assembly and alignment. Custom aspherical lenses were manufactured according to the outcome of the optimisation and the tolerance analysis.

In addition, the system layout and the integration between different components such as the scanning mirrors, the detector, the laser and timing electronics were briefly discussed.

The transmission path of the laser beam for the system operating in a mono-static configuration has been modelled and confirmed that it is possible to transfer the beam through the reflective telescope with a central obstruction while avoiding clipping from the optical components.

The transceiver design and assembly had to satisfy on-site health and safety regulations for handling, electrical hazard and eye-safety before being certified for use on Selex ES' premises.

References

[1] http:// www.selex-es.com documents/737448/17645869/body_mm07928_Titan _385ES_HD_LQ_.pdf

[2] A. McCarthy, X. Ren, A.D. Frera, N. R. Gemmel, N.J. Kirchel, C. Scarcella, A. Ruggeri, A. Tosi, G.S. Buller, "*Kilometer-Range Depth Imaging at 1550 nm Wavelength Using an InGaAs/InP Single-Photon Avalanche Diode Detector"*, Opt. Express, 21, 19, pp. 22098-22113 (2013)

[3] R.G. Driggers, P. Cox, T. Edwards, *"Introduction to Infrared and Electro-Optical Systems*", Artech House Inc. (1999)

[4] D. Malacara, Z. Malacara, *"Handbook of Optical Design",* Marcel Dekker, Inc. (2003)

[5] M.A. Itzler, *"Geiger-mode APD Cameras for LADAR Imaging",* Oral Presentation, Heriot-Watt University, October (2013)

[6] R.E. Fisher, B. Tadic-Galeb, P.R. Yoder, "*Optical System Design"*, SPIE Press (2008)

[7] Celestron C-GEM Series, Instruction Manual

[8] Cambridge Technology, Galvanometer Optical Scanner Instruction Manual

[9] D.C. O'Shea, "*Elements of Modern Optical Design"*, John Wiley & Sons (1985)

[10] R. Kingslake, "*Optical System Design"*, Academic Press (1983)

[11] W.J. Smith, "*Modern Optical Engineering"*, McGraw-Hill (2000)

[12] ZEMAX, User's Manual (2011)

[13] G. Hallock-Smith, "*Practical Computer-Aided Lens Design"*, Willmann-Bell Inc. (2010)

[14] J.M. Geary, "*Introduction to Optical Design with Practical ZEMAX Examples"*, Willmann-Bell Inc. (2009)

[15] E. Hecht, "*Optics"*, Adison Wesley (2005)

[16] M. Born, E. Wolf, *"Principles of Optics"*, 7th Edition, Cambridge University Press (1999)

[17] G.E. Marshall, *"Optical Scanning"*, Marcel Dekker (1991)

Chapter 4

Evaluation of the Transceiver in Bi-Static Configuration with a Scanned Single-Element SPAD Detector

4.1 Introduction

This chapter describes experimental results acquired with the lidar system operating in a bi-static configuration with a single-element InGaAs/InP SPAD (i.e. described as mode A in previous chapters). Details on the transmitter design, scanning mirrors calibration, the laser source, the InGaAs/InP single-element detector, timing electronics scheme, the alignment and setup of the system used in experiments are described.

Theoretical modelling of the system losses was performed and evaluated against the real-life measurement. Instrumental response function of the system was measured and three-dimensional ToF data was acquired. The chapter presents results which demonstrate the ability of the system to produce three-dimensional images of targets at ranges from 2.8 km to 4.2 km at spatial and depth resolution of < 30 cm. In addition, imaging through a semi-transparent sheet of netting was presented.

4.2 Bi-Static System Experimental Setup

The experimental setup was arranged in a bi-static configuration and incorporated a 25 μm pixel diameter, single-element Micro Photon Devices (MPD) InGaAs/InP SPAD detector. The system used an erbium doped fibre laser operating at a wavelength of 1550 nm, which generated 800 ps pulses at a repetition rate of 125 kHz (pulse energy of 4 μJ, 0.5 W total power).

A schematic of the system layout is shown in Figure 4.1. Photon returns from a target were collected by the receiver and recorded by a free-space SPAD detector operating in a gated mode. The signal was acquired from the $FoV_{Scanner}$ by using a pair of galvanometer scanning mirrors. Photon returns were collected at each of the 32 × 32 scan steps which corresponded to a relevant FoV_{Pixel}.

The laser beam was emitted from the optical fibre output which was coupled into a collimator and travelled through a beam expander used in reverse (which de-magnified

the beam size and increased its divergence); the optics were set up to provide the required laser beam divergence. The telescope collected a return signal from a target which was then subsequently collimated by the eyepiece. The set of relay lenses projected the image of the exit pupil from the mirror *y* to the mirror *x* while the annular mirror reflected it onto the lens L(b) which created a focal spot on the active area of the SPAD detector.

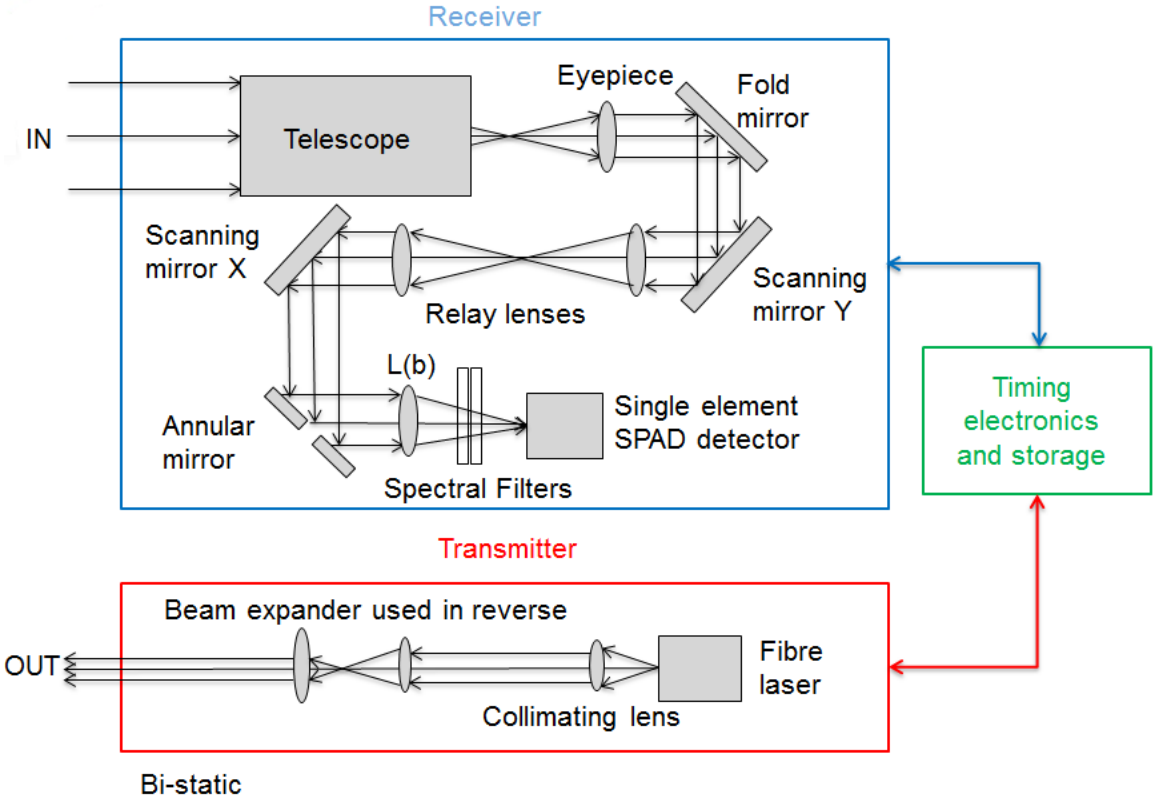

Figure 4.1. Schematic diagram of the experimental setup of the system operating in a bi-static configuration that incorporates a single-element SPAD detector operating in a scanning mode.

In order to suppress out-of-band solar background photons the following four filters were placed between the lens L3(a) and the SPAD detector:

- Two narrow bandpass filters, Semrock *NIR01-1550/3-25*, with transmission ≥ 90 % at a centre wavelength of 1550 nm ± 1.5 nm and the FWHM of 8.8 nm; and

- Two high-pass filters, Thorlabs *FEHL1000*, which have > 90% transmission for $\lambda \geq 1000$ nm and extinction of ≥ 60 dB for $\lambda < 1000$ nm.

Figure 4.2 shows a close-up photograph of the assembled bi-static scanned system mounted on a tripod in a roof laboratory where the experimental work was conducted.

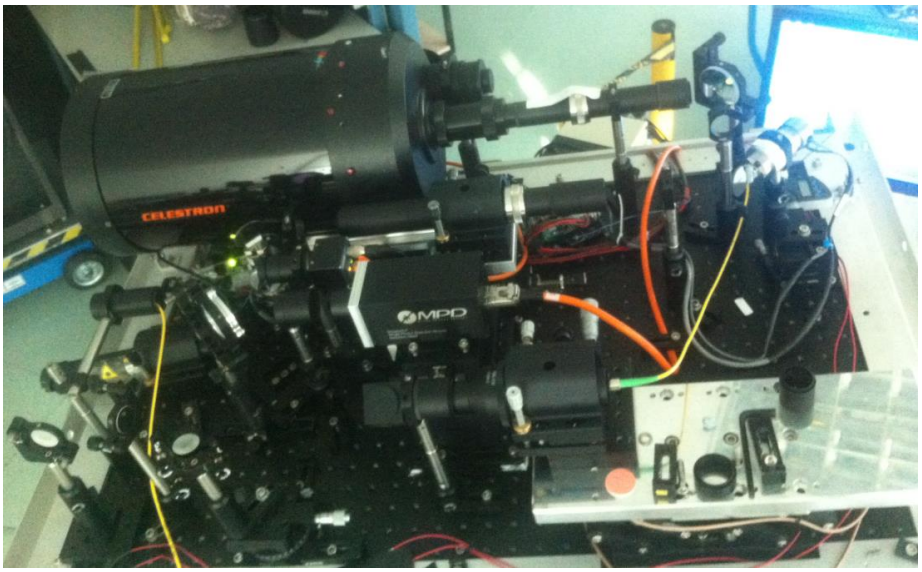

Figure 4.2. Close-up photograph of the system.

4.3 Control Electronics and Data Acquisition

A schematic diagram showing the timing electronics used to acquire experimental data is shown in Figure 4.3. A commercially sourced pulse pattern generator (PPG) was used to synchronise and gate the SPAD detector and clock the laser pulse at a frequency of 125 kHz. The rubidium clock was phase-locked with the PPG and acted as a reference source for timing synchronisation. The output power of the laser was adjusted via a current driver controlled by a PC.

The laser trigger signal was split into two by a power splitter and used to initiate a FPGA sending command TTL inputs to the servo drivers of the scanning mirrors set by control software. The time event analyser (see section 4.9) was used to time-stamp three events: a laser trigger pulse, a photon event recorded by the detector and an FPGA trigger pulse signifying movement of scanning mirrors. An acquisition time per scan point was adjustable through the scanner control software via a PC and the timing was collected from 32 × 32 scan points with 1 ps temporal resolution.

The FPGA was set up to trigger after clocking a certain amount of laser trigger pulses; e.g. for the laser operating at a pulse repetition rate of 125 kHz - if the required acquisition time was 1 s - then the FPGA recorded 125,000 pulses before releasing a pulse which triggered the movement of a scanning mirror.

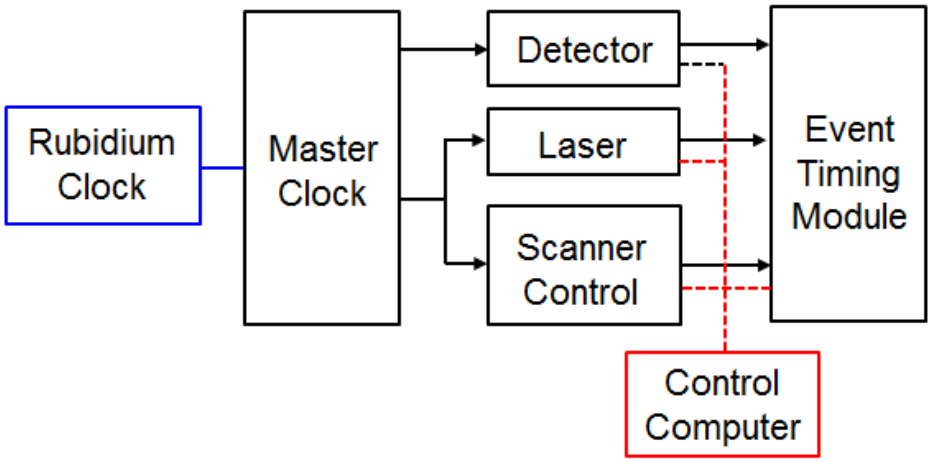

Figure 4.3. Schematic diagram showing the timing scheme used to acquire data with a single-element SPAD operating in a scanning mode.

The PPG was used to adjust the delay between the SPAD gate trigger pulse in respect to the laser/scanner trigger pulse such that, depending on the range at which the target was located in respect to the optical system, photon returns from the target were collected approximately in the centre of the SPAD gate.

A three-dimensional map of a target was generated using custom processing LabVIEW software which compiled histograms of photon arrival times for each scan point. A peak finding algorithm based on a least-squares fit (see section 4.13.1.1) was used to identify timing, hence target range information.

The data presented in this chapter was acquired with a Peltier-cooled InGaAs/InP SPAD detector from MPD. The module used a gated approach to switch the detector above avalanche breakdown (Geiger-mode) at around the expected photon arrival times. Detailed information about the detector is given in section 4.8.

4.4 Bi-Static Transmitter

The transmitter was set up to operate in a bi-static mode where the axis of the transmitted laser beam was parallel to and displaced from the optical axis of the receiver channel. As illustrated in Figure 4.4, when a single-element detector was used in the bi-static configuration, the $FoV_{Scanner}$ was simultaneously illuminated by the transmitter with a matching divergence laser beam while the detector collected a signal from one FoV_{Pixel} at a time. In the bi-static configuration, the area of FoV_{Pixel} was approximately three orders of magnitude smaller than the area of the transmitted beam. Although the bi-static configuration introduces additional energy losses when compared to the mono-

static configuration, it ultimately reduces the level of backscatter from internal components of the receiver. The backscatter is a serious problem in mono-static systems [1]. If multiple pulses are in transit, the signal reflected from the target can arrive at the detector at the same time as the back-reflections from the transmitted pulse, thus saturating the detector [2]. The approach to eliminating the backscatter in mono-static systems is described in Chapter 5.

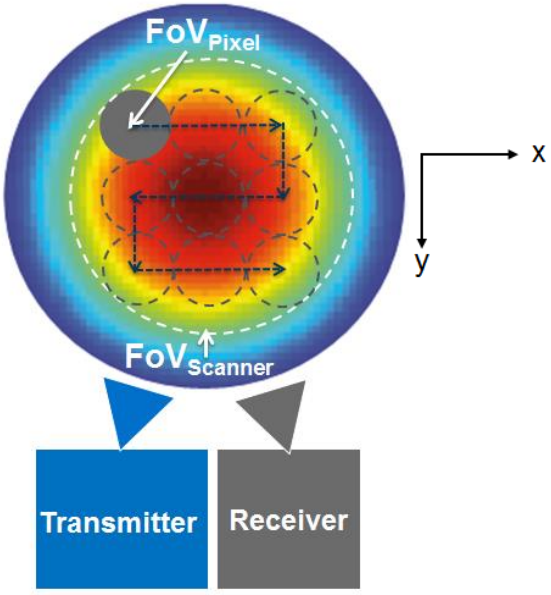

Figure 4.4. Illustration of transmitter and receiver FoV when the system operates in a scanned bi-static configuration. Scanning mirrors were programmed to scan the $FoV_{Scanner}$ in a stop-and-stare mode using a raster pattern.

As illustrated in Figure 4.4, the stop-and-stare approach was based on stepping one scanning mirror along 32 steps of the FoV, each equivalent to the FoV_{Pixel}, in the horizontal direction (along *x* axis), starting from the upper left corner of the $FoV_{Scanner}$ and then stepping one width of the FoV_{Pixel} down along the vertical direction (*y* axis) and continuing another 32 steps along the *x* axis in the opposite direction. This process was repeated 16 times until the entire $FoV_{Scanner}$ was covered. The mirrors were controlled by the FPGA which sends voltage commands to the scanning mirrors.

4.4.1 Transmitter Design

The transmitter was designed for a Gaussian beam of 1/e diameter to flood-fill the $FoV_{Scanner}$ (see Figure 4.5). At 1/e the irradiance falls down to $0.368 \times I_{Max}$ and this ensures that the beam irradiance across the $FoV_{Scanner}$ does not rapidly drop between the

centre and the edge of the field. The 1/e beam divergence required to fill the $FoV_{Scanner}$ was 1.3 mrad.

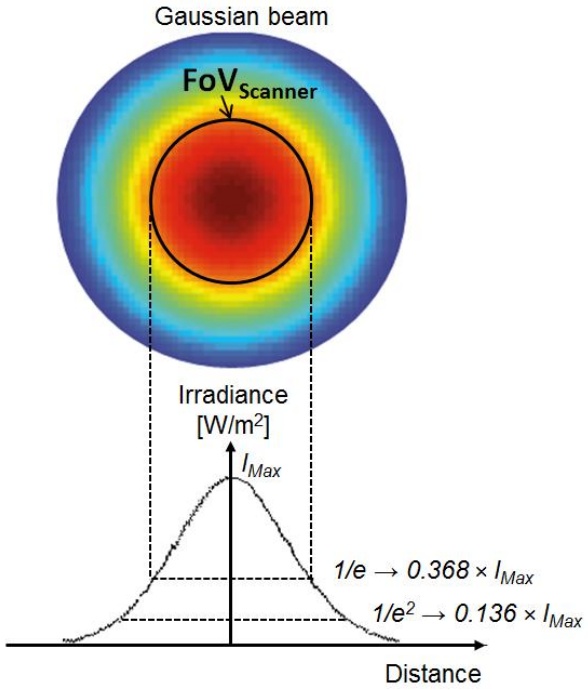

Figure 4.5. The $FoV_{Scanner}$ was flood-illuminated by a Gaussian beam of 1/e divergence where the irradiance falls down to 0.368 × I_{Max}.

A schematic diagram of the bi-static transmitter setup is shown in Figure 4.6. A laser fibre output was mechanically combined with a collimating lens via a SMA connector. A commercially available 3× beam expander used in reverse was then added along the path of the beam and the distance between the two lenses of the expander were adjusted to provide the required beam divergence.

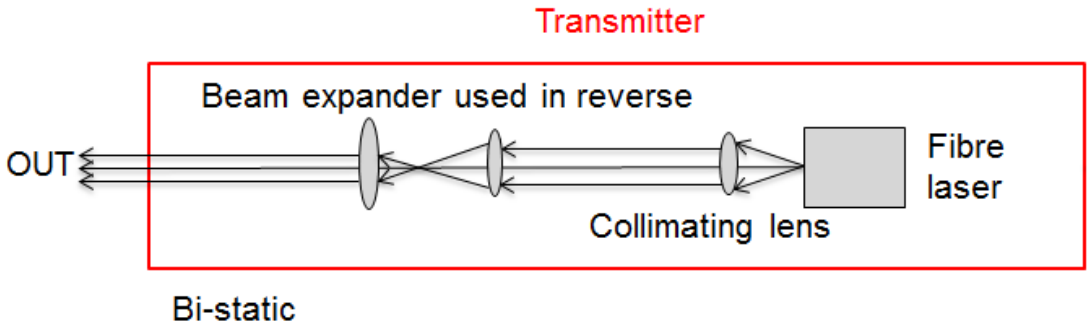

Figure 4.6. Schematic diagram of the bi-static transmitter designed to operate in a scanning system with a single-element SPAD detector and a beam expander used in reverse.

In the experiment, an off-the-shelf collimation package with a lens of focal length f = 37 mm was combined with an SMA-28 Corning fibre of mode field diameter D = 10.5 µm at 1550 nm [3] providing the 1/e divergence angle, $\theta° \approx 0.021$ ° (362 µrad) with the output beam diameter of 9 mm.

The 3× beam expander used in reverse de-magnified the beam and increased the beam divergence to $\theta° \approx 0.063$ ° (1.1 mrad). In order to illuminate the $FoV_{Scanner}$, the transmitter divergence $\theta° \approx 0.074$ ° (1.3 mrad 1/e) is required. The distance between the two lenses comprising of the beam expander was adjusted to increase the divergence from 1.1 mrad to the required 1.3 mrad.

4.5 Bi-Static Transmitter Divergence Measurement

The divergence of the transmitted beam was measured using an off-axis parabolic mirror. A parabolic mirror collimates light coming from a point source located at its focus. In turn, a collimated beam incident on a parabolic mirror is focused at its focal point. If an off-axis portion of the parabolic mirror is cut out of a parent parabola, then the beam will focus off-axis to the optical centreline of the off-axis portion and the mirror is referred to as an *off-axis parabolic mirror* [4]. This is illustrated in Figure 4.7. Such a mirror is characterised by a parameter called *zonal radius* which defines the distance between the optical centreline of the off-axis parabola and the optical axis of the parent parabola [4]. Off-axis parabolic mirrors are useful in optical alignment.

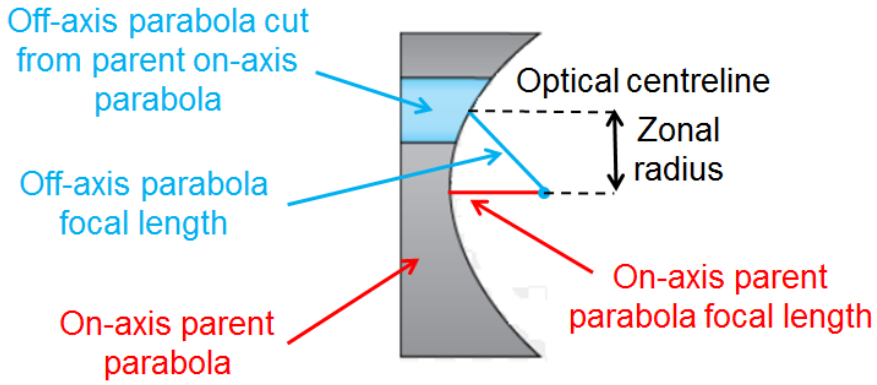

Figure 4.7. Illustration of an off-axis parabolic mirror.

The off-axis parabolic mirror was used in the optical alignment and had a focal length of f = 5 m and a zonal radius of 21.3 cm. The divergence of the transmitter was measured using the setup shown in Figure 4.8. A CW laser beam operating a wavelength of 1550 nm was propagated through the transmitter. The angle of the laser beam in respect to the optical centreline of the parabolic mirror was set up such that the focal spot created at the focal point of the mirror was positioned at the zonal radius (23.1 cm). This confirmed that the laser beam propagated approximately parallel to the optical axis of the mirror. An infrared Xenics camera was positioned in the focal plane

of the mirror, 5 m away from the centre of the mirror, on which the laser spot diameter was monitored.

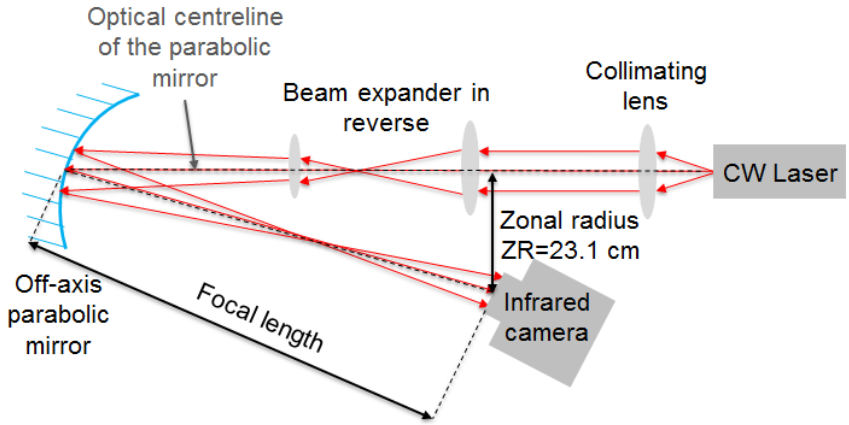

Figure 4.8. Setup used to measure the transmitter beam divergence.

From geometrical optics it is known that the beam divergence is given by

$$\theta^\circ \approx \left(\frac{D}{f}\right)\left(\frac{180^\circ}{\pi}\right) \qquad \textit{Eq. 4.1}$$

where D is the diameter of the focal spot measured on the infrared camera and f is the focal length of the parabolic mirror (f = 5 m).

An image of the focal spot recorded by the camera is shown in Figure 4.9. An intensity profile of the spot was plotted along the horizontal and vertical directions in respect to the number of camera pixels and is shown in Figure 4.10. The width of the camera pixel is 30 µm.

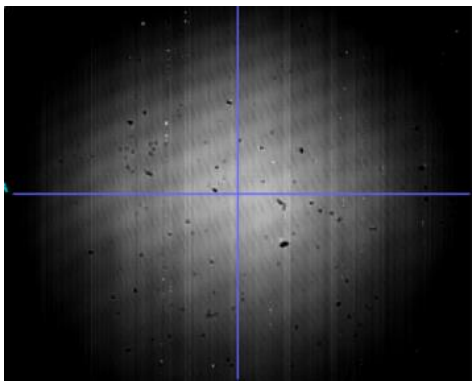

Figure 4.9. Image of a focal spot recorded by the infrared camera. The fringing is resulted from interference from neutral density (ND) filters mounted in front of the infrared camera used to avoid detector saturation.

From Figure 4.10, the 1/e diameter of the laser spot is equivalent to ~ 773 arbitrary units and the beam diameter is approximately 214 pixels. This corresponds to a ~ 6 mm

beam diameter. After substituting this result to Eq. 4.1 the divergence of the laser transmitter was calculated to be ~ 1.3 mrad (1/e) which matched the required value.

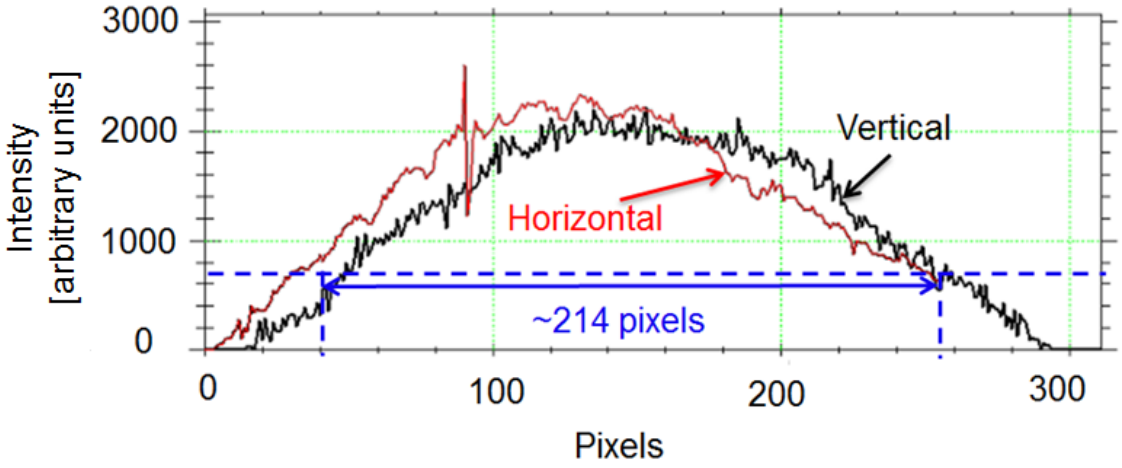

Figure 4.10. Intensity profile across the horizontal and vertical directions of the focal spot recorded by the infrared camera.

4.6 Site Laser Safety

The experimental investigation required a strict compliance with Selex ES' certified safety procedures for experiments conducted on the company premises.

Tasks involved in the alignment and experiments required the potential hazards (their severity and likelihood of occurrence) to be identified for risk assessment and mitigation. Control measures required to reduce all risks were proposed and were included in a safe system of work (SSoW) document.

One of the most important hazards is laser safety for the pulsed laser used in the lidar system (see section 4.7). Two auxiliary lasers were used for alignment: a continuous-wave (CW) fibre laser of a 1550 nm wavelength and He-Ne free-space laser of a 633 nm wavelength. The CW fibre laser did not require any specific safety measures to be accounted for because it was classified as class I. The He-Ne laser, classified as class III R, required a filter which reduced its power to ≤ 10 mW. The Manlight laser was class IV and required a switch on/off procedure, which included confirming the laser power before propagating the laser beam outside of the laboratory window.

It is important to consider laser safety measures for outside use. The extended nominal-ocular hazard distance (*ENOHD*) refers to a distance from a laser source at which the energy per unit area becomes lower than the maximum permissible exposure (*MPE*) for

the skin and cornea when viewed through magnifying optics, such as binoculars. The *ENOHD* is given by [5] [6]

$$ENOHD = \frac{1}{\varphi}\sqrt{\frac{4PG}{\pi MPE}} \qquad \textit{Eq. 4.2}$$

where φ is 1/e beam divergence in radians, P is the power of the source, MPE is a maximum permissible exposure for a 1550 nm wavelength laser and G is the optical gain factor of the magnifying optics that is given by

$$G = T \times M^2 \qquad \textit{Eq. 4.3}$$

where T is transmission and M is magnification of the magnifying optics [5].

When binoculars of magnification, M = 10 and transmission, T = 80 %, are used then G = 80. At a wavelength of 1550 nm the MPE = 1000 W/m^2. For a laser power of P = 2 W (which is the maximum power at which the laser used in experiments can operate) and the lowest beam divergence achievable with the transmitter of φ = 197 µrad (1/e), the *ENOHD* is 2291 m.

For outside use the laser safety documentation stipulated that there would be no buildings within the *ENOHD* and the line-of-sight assessed from the laboratory window. The hazard assessment and laser safety calculations were approved by the site safety officer. These approvals provided the necessary authorisation to conduct the field trials.

4.7 Laser Source

The laser source used in the experiments was a semiconductor pulsed diode-pumped fibre laser manufactured by Manlight. A diode laser pumps the active gain medium which is a double-clad erbium/ytterbium (Er/Yb) doped optical fiber [7]. It provides a diffraction limited randomly polarized beam of a 1550 nm wavelength and 800 ps pulse duration at a pulse repetition rate of 125 kHz and pulse energy of 4 µJ (optical power of 0.5 W). The laser is controlled by a PC using software via an RS232 interface where the laser driving current and the driving frequency can be controlled via the RS232 port.

4.8 Single-Element InGaAs/InP SPAD Detector

The single-element detector used in experiments described in this chapter is an InGaAs/InP SPAD with 25 µm active area diameter and timing jitter of 100 ps manufactured by Micron Photon Devices [8]. The detector is sensitive to single photons in the wavelength range 900 nm - 1.7 µm and is based on a separate absorption and multiplication structure described in section 2.9.2.2.

The InGaAs/InP SPAD uses gated quenching where the device is disabled for a programmable period of time, T_{OFF}, which resets the voltage and enables the majority of trap centres filled during the avalanche to empty [8]. As illustrated in Figure 4.11, the Geiger mode is allowed during the gate on period, T_{ON}, where the SPAD is biased above the breakdown voltage, V_B, with an excess bias of V_{EX}. During the gate-off period, T_{OFF}, the SPAD is biased below the breakdown voltage, V_{BL} [9].

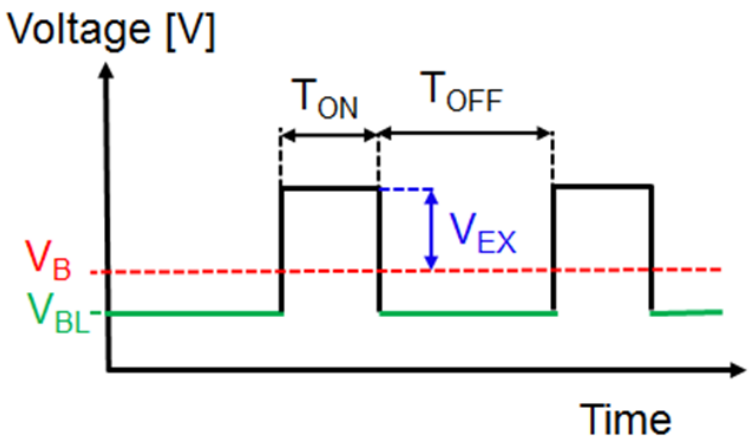

Figure 4.11. Graph illustrating gated quenching in a SPAD module.

The particular detector module design confined the hold-off time, $T_{OFF,}$ to be equal or greater than gate period, T (see Figure 4.12) [9]. As a result, after the photon is detected, at least one subsequent gate is disabled [9].

In a free running mode the SPAD count rate, CR_{FR}, is defined by

$$CR_{FR} = \frac{N_P}{t} \qquad \textit{Eq. 4.4}$$

where N_P is the number of photon counts recorded by a SPAD and t is the integration time [9]. However, when the detector operates in a gated mode, the count rate is affected by the gate period, T, and the gate width, T_{ON}, hence the gated count rate per second, CR_G, can be calculated from the following

$$CR_G = CR_{FR}\frac{T_{ON}}{T} \qquad \textit{Eq. 4.5}$$

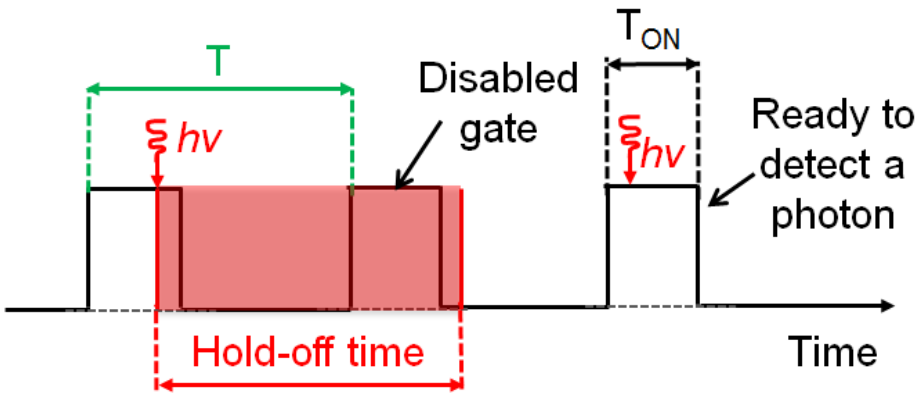

Figure 4.12. Diagram illustrating how the hold-off time affects the ability of a SPAD to detect a photon.

Each time a photon is detected a number of subsequent gates are inactive because of the hold-off time, T_{HO}. The number of inactive gates, N_{IG}, depends on the hold-off time, gate period and the number of photon counts and is given by

$$N_{IG} = \frac{T_{HO}}{T} CR_G \qquad \textit{Eq. 4.6}$$

Therefore, the number of gates that remain active to detect a photon, N_{AG}, decreased from *1/T* to

$$N_{AG} = \frac{1}{T} - (\frac{T_{HO}}{T} CR_G) \qquad \textit{Eq. 4.7}$$

Assuming that the counts are distributed uniformly over time, the number of counts per period, CR_P, is given by

$$CR_P = CR_G T \qquad \textit{Eq. 4.8}$$

Thus, the count rate after the count loss due to hold-off time, CR_{HO}, is

$$CR_{HO} = CR_P N_{AG} \qquad \textit{Eq. 4.9}$$

which can be written as

$$CR_{HO} = CR_G (1 - T_{HO} CR_G) \qquad \textit{Eq. 4.10}$$

The equation is only valid for CR_G limited to $(2T_{HO})^{-1}$. For count rates higher than that the hold-off correction factor becomes very high which results in high errors in CR_{HO}. The gate period, T, and hold-off time, T_{HO}, are both programmable. The gate can be triggered internally and externally with a TTL pulse [8]. According to the manufacturer's specifications, the SPAD detector provides photon detection efficiency of ~ 30 % at 1550 nm (V_{EX} = 5 V) and timing jitter of approximately 100 ps. The dark

count rate (DCR) at an operating temperature of T = 230 K and excess bias V_{EX} = 2.5 V is < 30 kc/s (for 20 μs hold-off time) [8].

The gate width ultimately limits the depth in the image plane across which the signal from a target can be recorded. A wide gate allows the signal to be collected from an extended target which stretches across tens of meters. A 500 ns gate allows a 75 m depth penetration capability while a 10 ns gate allows a 1.5 m depth to be penetrated.

4.9 Time Interval Analyser

The time interval analyser used in the setup was a HydraHarp400. The unit had up to 8 independent input channels, a count rate of up to 12 Mcps per channel, a minimum time bin width of 1 ps and maximum number of time bins of 65536 with acquisition times of 1 ms - 100 hours [10].

The device collects time-tags in blocks of memory, where one memory cell holds photon events in one corresponding *time bin*. A time-bin represents a time interval within which the corresponding timing events are recorded and thus represents the timing accuracy with which an optical waveform can be reproduced. A short time-bin width in conjunction with the large number of time-bin samples signal shape adequately [11].

4.10 Calibration of Scanning Mirrors

Scanning mirrors were calibrated using the parabolic mirror and the Xenics camera. The setup is shown in Figure 4.13.

The scanning mirrors were powered up and the voltage was set to 0 V (on-axis position). As shown in Figure 4.13, a CW 1550 nm wavelength laser beam was inserted into the receiver through the annular mirror and aligned such that it was decentred and parallel to the optical axis of the receiver. The beam was emitted from the receiver through the side of the telescope and was reflected from the off-axis parabolic mirror which was aligned such that the optical axis of the receiver coincided with the optical axis of the mirror. The Xenics camera was positioned at the mirror's zonal radius ZR = 23.1 cm away from the optical axis at the focal length f = 5 m.

As explained in Chapter 3, one angular step of the scanning mirrors is required to match the system's spatial resolution of 28 µrad. Figure 4.14 shows the laser beam intersecting the parabolic mirror (represented by a thin lens) at an angle of 28 µrad and 896 µrad (32 steps) with respect to the optical axis. The beam focuses at a camera plane at a distance of 140 µm and 4478 µm from the optical axis respectively.

Applying voltage to the scanning mirrors changes their angle in respect to the optical axis of the optical system. This results in a deflection of the laser beam from its original (0 V) position corresponding to the on-axis propagation. By measuring the displacement of the deflected beam on the Xenics camera from the on-axis position it is possible to assign appropriate levels of voltage corresponding to the required scanner step value in the detector plane.

The displacement was measured using the Xenics camera software which returns the distance between the chosen positions on an image in pixels. Since the pixel size of the camera is known, the displacement and thus the angle at which the laser beam travels onto the parabolic mirror can be measured.

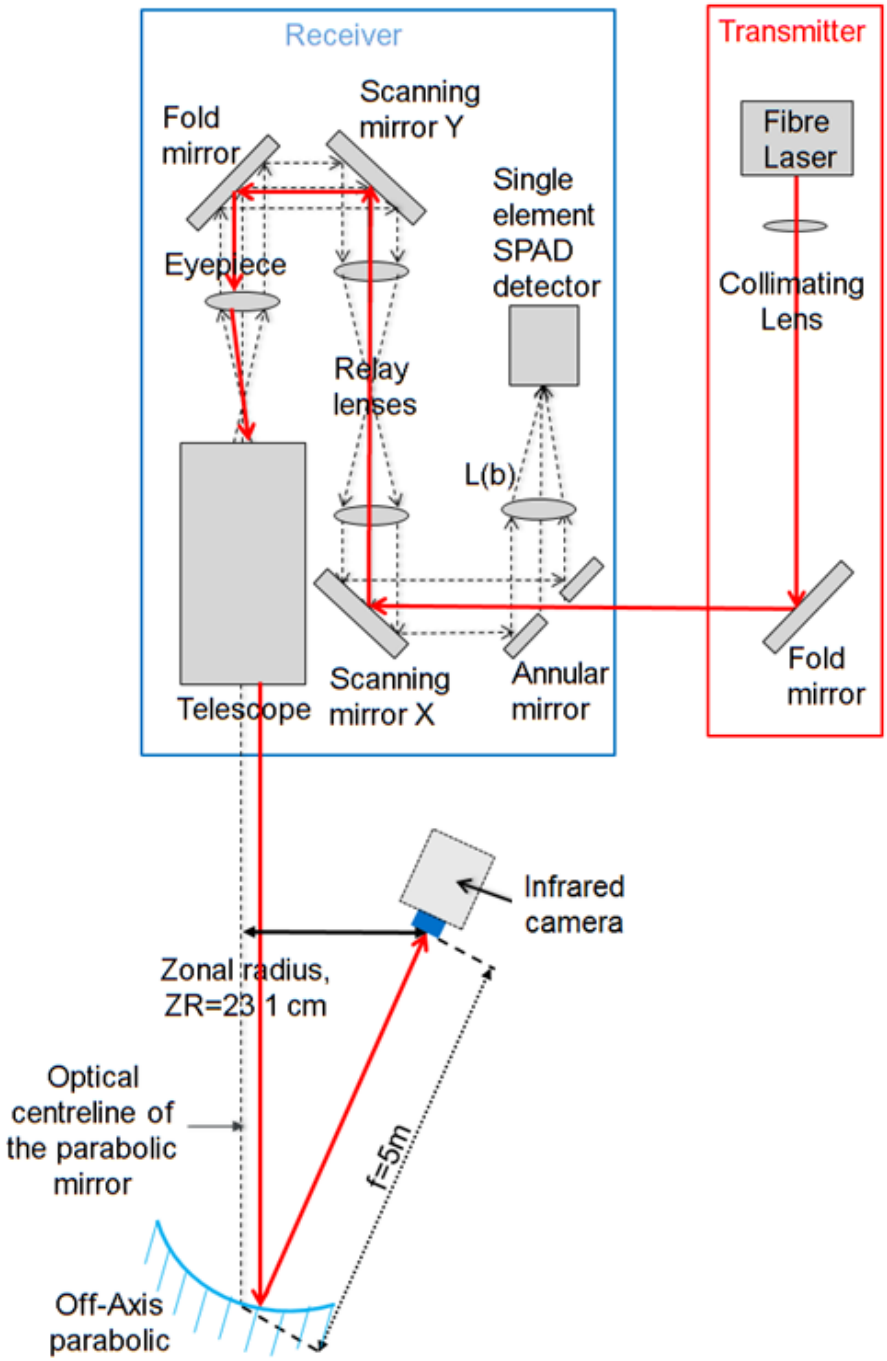

Figure 4.13. Setup used for calibration of scanning mirrors. The laser beam was inserted into the receiver through the annular mirror and travelled through the system onto the parabolic mirror which focused it onto the infrared camera.

Figure 4.15 shows an image registered by the Xenics camera where arrow "*A*" indicates the on-axis beam position with 0 V applied to the mirrors.

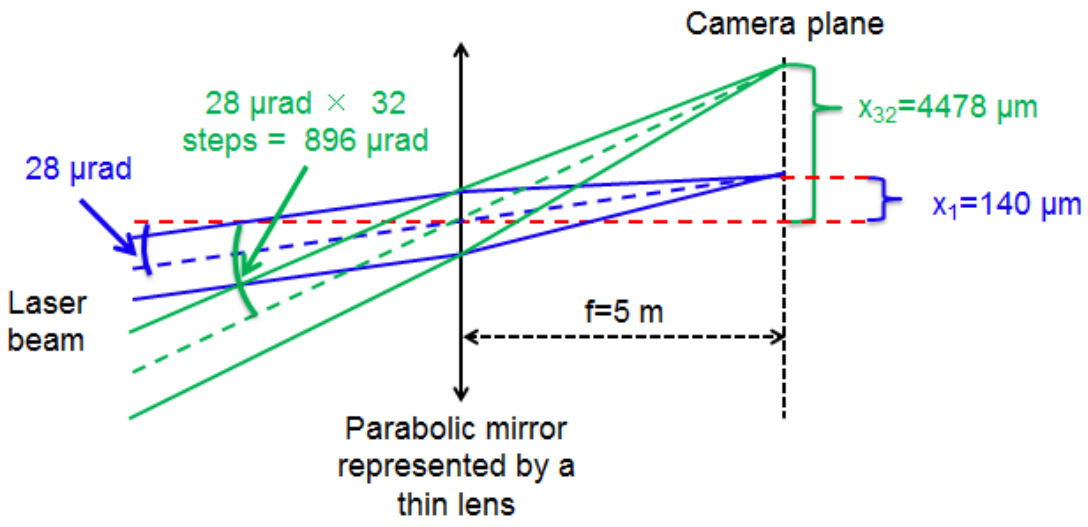

Figure 4.14. Illustration of the setup used for the calibration of the scanning mirrors where, for simplicity, the parabolic mirror is represented by a thin lens.

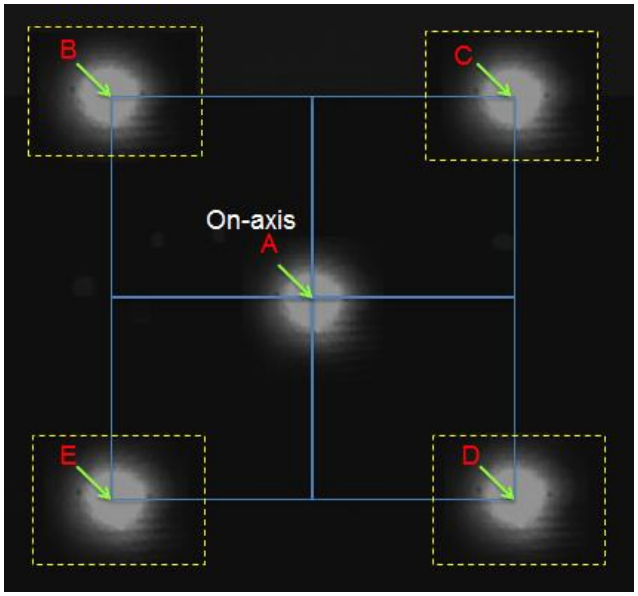

Figure 4.15. Image of the focal plane of the parabolic mirror where the arrow "A" indicated the on-axis beam position with 0 V applied to the scanning mirrors.

The distance between points *BC*, *ED*, *BE* and *CD* was measured and was equal to approximately 140 pixels. This indicated the distance of 4480 µm, which was equivalent to the required 896 µrad, corresponding to 32 steps in *x* and *y* direction, 28 µrad each. In addition, distances between the points *AB*, *AC*, *AD* and *AE* were measured and corresponded to approximately 99 pixels each. This suggests that points *B*, *C*, *D* and *E* were positioned symmetrically from the point *A* located on-axis.

In order to achieve the above displacements of the laser beam in the focal plane of the parabolic mirror, the voltage applied to the *x* scanning mirror was V_x = 13.4 mV and to the *y* scanning mirror was V_y = 19.7 mV per step equivalent to 28 μrad.

4.11 Target Locations

The system was sited in a laboratory which provided access to an urban landscape with a range of up to 10.5 km and varying altitude along the line of sight. Figure 4.16 shows locations of targets used in the alignment and experiments as well as the location of Selex ES where the transceiver was located. The map was taken from Google Maps [12] from which approximate distances to the target locations were estimated. Those distances are as follows: Haymarket chimney: ~ 2.8 km, Napier University: ~ 4.2 km and Braids Hill: ~ 6.6 km.

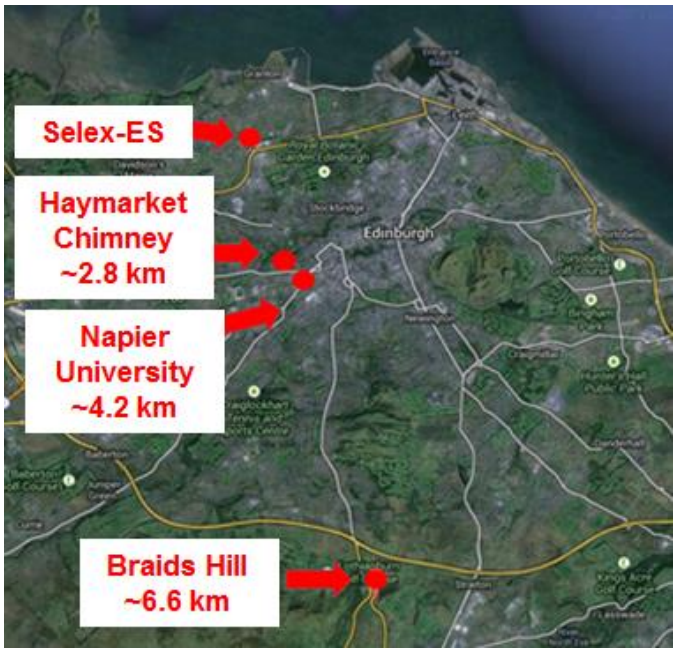

Figure 4.16. Map of Edinburgh showing locations of targets in comparison to Selex ES where the transceiver was located.

4.12 Transceiver Bore-Sighting Procedure

The initial stage of the optical alignment procedure was performed using multiple pinholes and a He-Ne laser. Phase five of the alignment (see section 3.13.2) required the receiver to be bore-sighted with the transmitter over the system's range of operation. The purpose of the bore-sight is to ensure that the FoV of the detector is located approximately at the centre of the transmitted laser beam (with a tolerance of few detector pixels projected at the FoV) over a maximum range of 10 km.

Figure 4.17 shows an optical setup used for bore-sighting of the transmitter and the receiver. The parabolic mirror was positioned such that a collimated and expanded He-Ne laser beam travelling from the back of the optical system through the centre the pinholes placed in the system during the initial alignment phase was pointing at the centre of the mirror and was located approximately 5 m away from the aperture of the telescope. The scanning mirrors were powered up during the alignment and were kept at a constant voltage of 0 V. The tip and tilt of the parabolic mirror was adjusted to position the focused He-Ne beam at the focal point of the mirror and at the zonal radius, 23.1 cm away from the centre of the telescope. At the location of the focal spot, a laser fibre holder was mounted to which a CW fibre laser operating at a wavelength of 1550 nm was connected. The 1550 nm beam from the fibre holder was highly divergent and fully illuminated the parabolic mirror. After being reflected from the parabolic mirror, the beam propagated along the same axis (equivalent to the optical axis of the system) as the He-Ne laser, throughout the optical system.

The tip and tilt of the annular mirror were adjusted such that the CW 1550 nm laser beam propagated along the breadboard mounting holes and was levelled with the breadboard. The position of the beam was marked with two pinholes. The lens L3(b) was then placed and aligned such that the beam still travelled along the two pinholes. The single-element detector was then placed at the approximate design distance from the back of the lens L3(b) and its active region was positioned close to the location of the CW beam.

The focal plane of the parabolic mirror, where the fibre source was placed, corresponded to an object located on-axis at infinity. Aligning the detector's active area in a focal plane that corresponds to the position of an infinite range on-axis image allowed an approximate infinity alignment of the optical system in laboratory conditions.

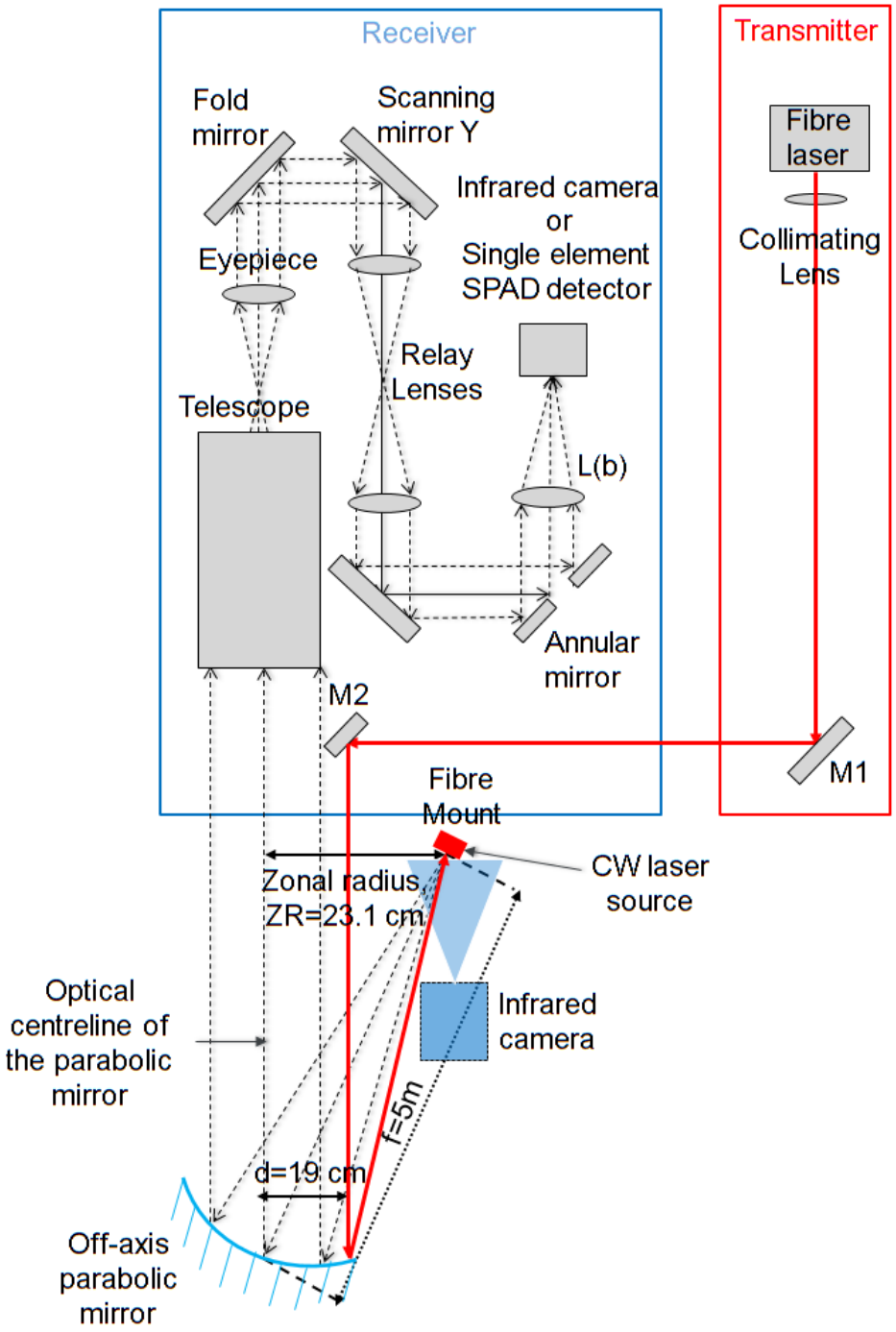

Figure 4.17. Optical setup used for the bore-sighting of the transmitter and the receiver.

Scanning mirrors were used to scan the FoV of the detector across 17 × 17 pixels to define where the fibre source point was located in respect to the optical axis of the receiver. Figure 4.18 shows a series of intensity images of the fibre source. Figure 4.18(a) shows a "donut" shape beam located off-centre of the image. This suggested that the detector was defocused and located off-axis. Figure 4.18(b)-(l) shows images of the point source after the position of the SPAD was adjusted along *x, y* axis and defocused until the beam was centred and focused to one pixel.

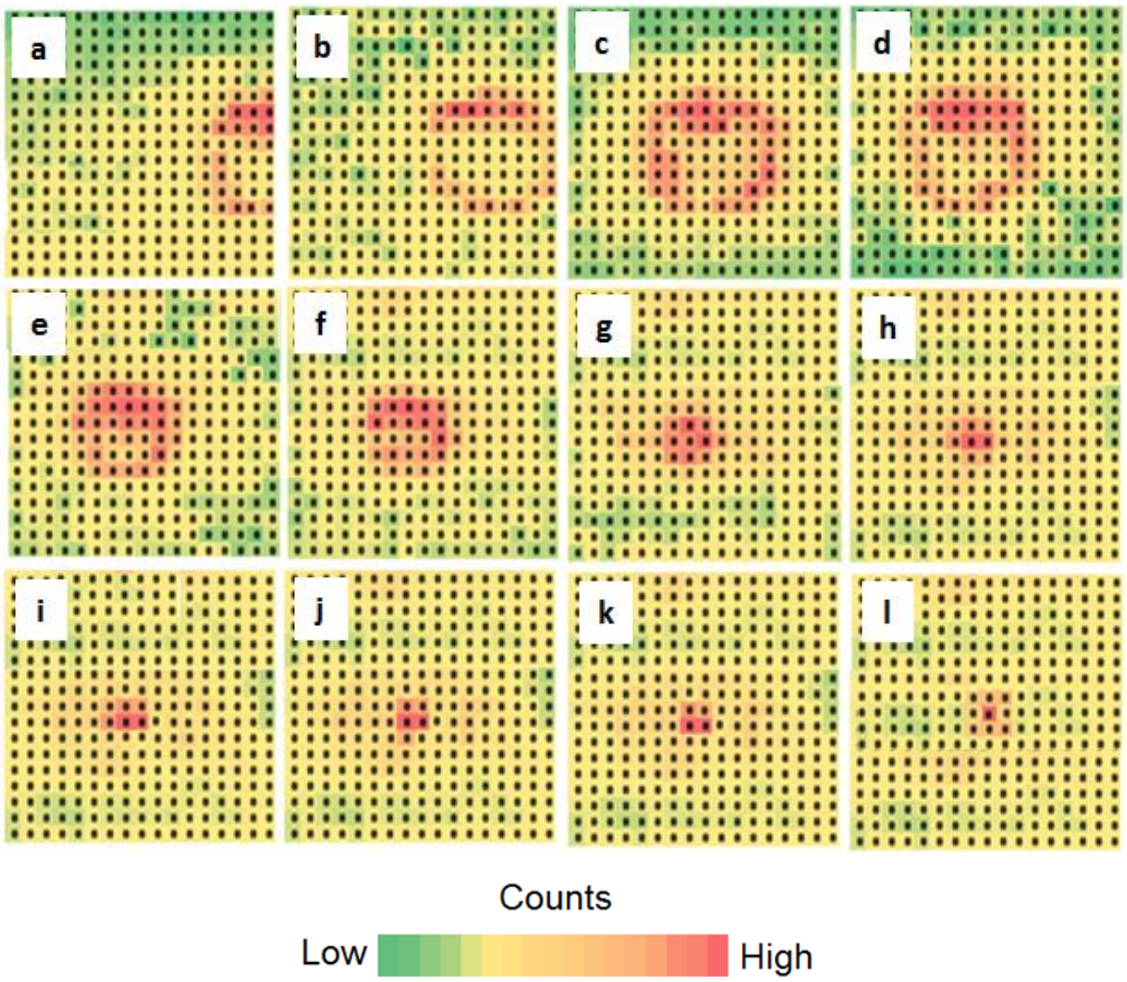

Figure 4.18. Intensity images of 17 × 17 pixels of the fibre source located in the focal point of the parabolic mirror acquired with a single-element scanning SPAD. The colour scale is linear.

Having established the position of the SPAD which is conjugate to an on-axis infinite point source, the laser transmitter was bore-sighted with the SPAD. This process involved the adjustment of two mirrors, M1 and M2 (Figure 4.17) such that the transmitted laser beam overlapped with the fibre source (FS) so that both, the transmitter and receiver were aligned to an on-axis infinite object. In order to confirm this, a Xenics camera was used. First, the fibre source was switched on and a pixel indicating the position of the fibre core was marked on an image produced by the Xenics camera placed in front of it. Then, the fibre source was switched off and the laser transmitter was switched on, the mirrors M1 and M2 were tweaked, producing an overlap of the transmitter focal spot on the pixel indicating the approximate position of the fibre core. The centre of the FoV of the CCD camera was then bore-sighted to the same point source.

After the laboratory-based alignment the setup was experimentally confirmed by using the corner cube retro-reflector over a range of 6.6 km. In this case, as shown in Figure 4.19, the position of the detector focus required a minor adjustment in order to focus the laser beam to approximately one pixel, where the pixel size represented the image of the detector projected onto the object plane, which is smaller than the corner cube diameter at 6.6 km. A riflescope was then bore-sighted to the position of the corner cube.

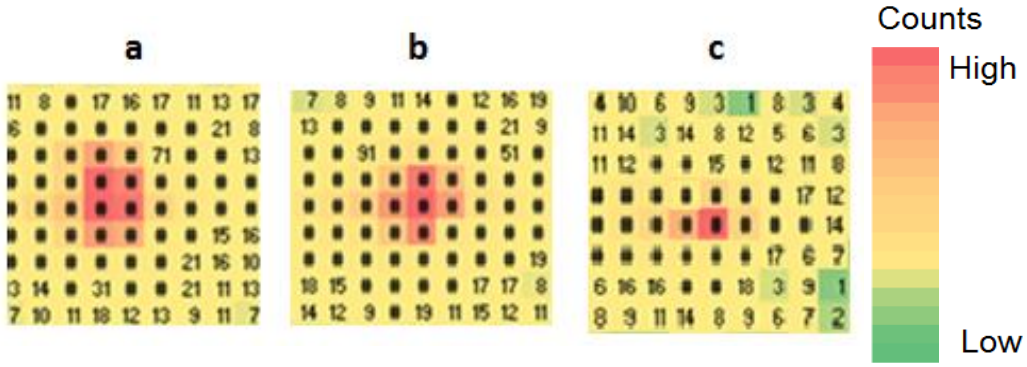

Figure 4.19. Intensity images of 9 × 9 pixels of the corner cube retro-reflector located over 6.6 km produced by the single-element SPAD configuration. Image (c) confirms that an image from infinity is focused to approximately one pixel. The colour scale is linear.

4.13 Experimental Results

Measurements were taken in bright daylight over distances of ~ 2.8 km (Haymarket chimney) and ~ 4.2 km (Napier University). The solar background counts fluctuated between 500 cps – 3000 cps, depending on the weather conditions. During the experiments the SPAD detector operated in a "low noise" mode, enabling lower achievable DCR of 30 kcps at an expense of detection efficiency (~ 30 %) operating with 3 V excess bias, 20 µs hold-off time, 125 kHz external trigger and temperature of 265 K. The gate width applied to the detector varied between 100 ns and 500 ns which corresponded to an image depth of 15 m and 75 m respectively.

4.13.1 Haymarket Chimney

Over a range of ~ 2.8 km an industrial chimney of unknown dimensions was scanned; a visible-band photograph of the target is shown in Figure 4.20. A delay between the external SPAD gate on trigger and the laser pulse trigger was generated by the PPG and was equal to 3275 ns. This ensured that photon returns were located in the centre of a 500 ns gate.

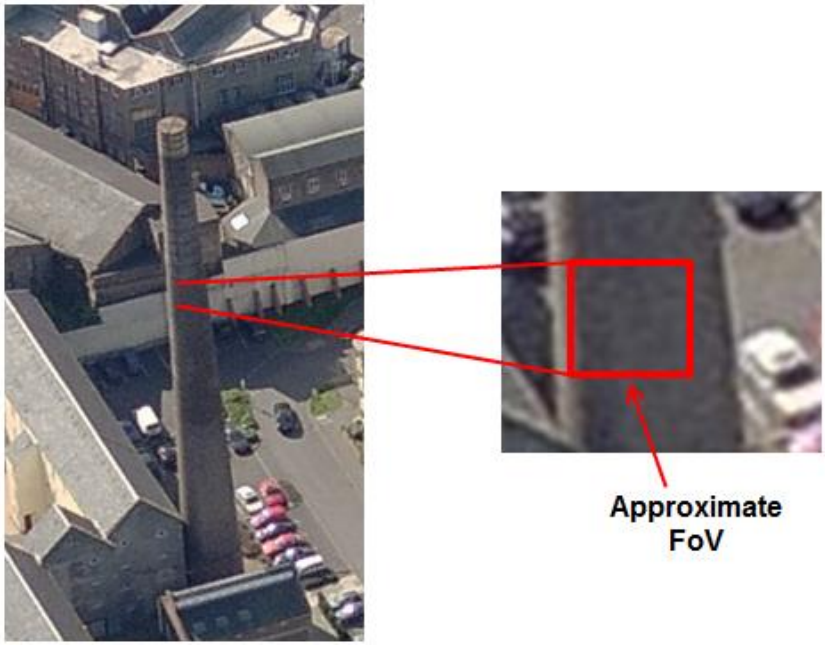

Figure 4.20. A visible-band, wide FoV photograph of the Haymarket Chimney located ~ 2.8 km from the laboratory.

The data was acquired over 32 × 32 pixels with a scan step representing 7.8 cm and 1 s acquisition time per pixel giving the total acquisition time of 17.1 min. Raw plotted depth data of different viewpoints of the target is shown in Figure 4.21(a), (b) and (c). Figure 4.21(a) is an intensity scatterplot where a pixel colour represents at a peak of a histogram at each scan point. Figure 4.21(c) shows the target from a top view on which its curvature can be observed.

Both the radius of curvature of the chimney and the taper angle visible in Figure 4.21(b) were calculated. To calculate the radius of curvature, *r*, an arc of known width, *W*, and height, *x*, were considered as shown in Figure 4.22.

From Pythagoras theorem

$$\left(\frac{W}{2}\right)^2 + m^2 = r^2 \qquad \textit{Eq. 4.11}$$

where

$$m = r - x \qquad \textit{Eq. 4.12}$$

Thus the radius of curvature, *r*, is given by

$$r = \frac{x}{2} + \frac{W^2}{8x} \qquad \textit{Eq. 4.13}$$

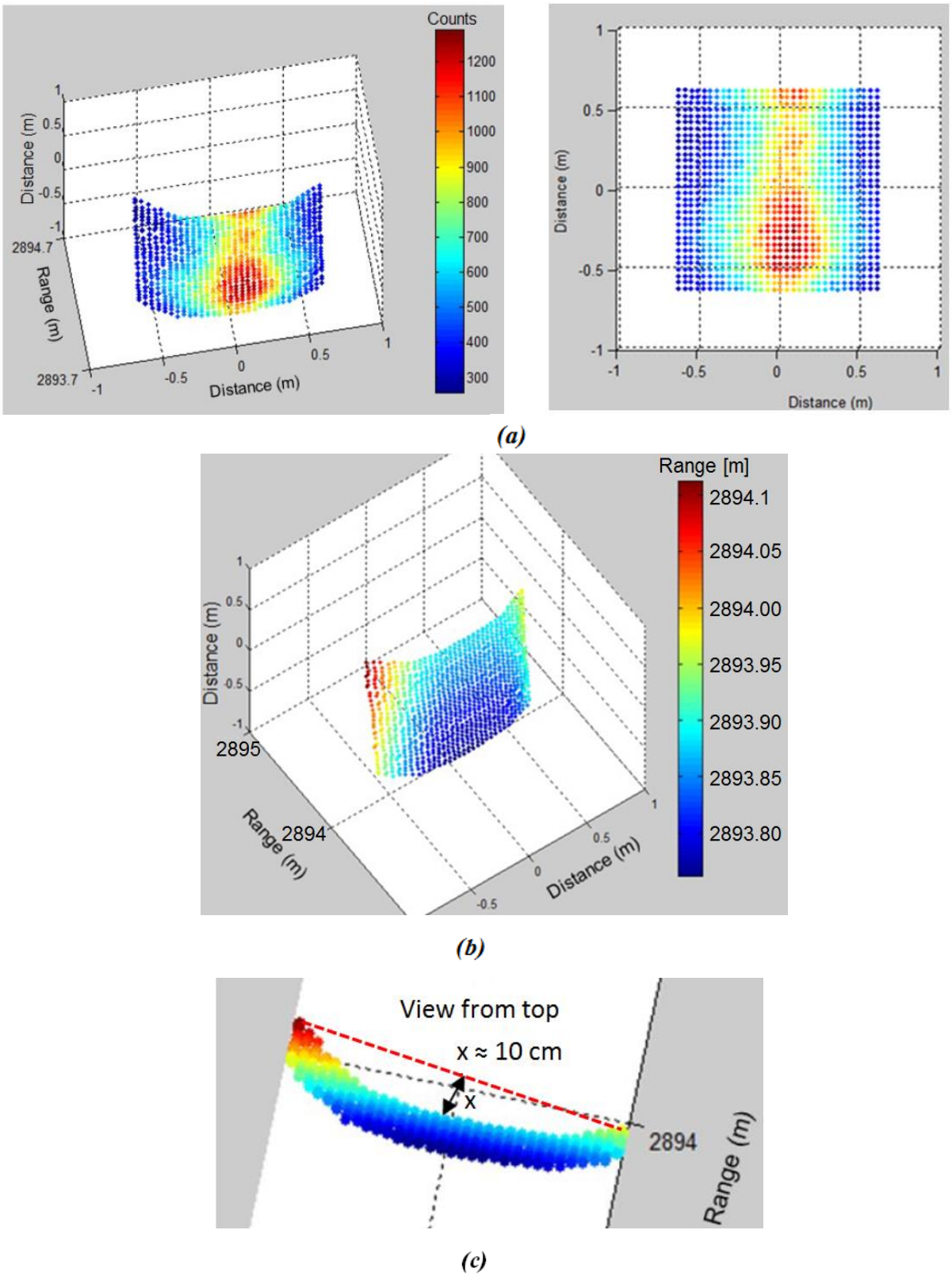

Figure 4.21. Depth profile measurements of an industrial chimney acquired over a distance of ~ 2.8 km with 32 × 32 scan steps with a scan step resolution of 7.84 cm and 1 s acquisition time per pixel. Images (a), (b) and (c) are scatterplots of raw data where in (a) pixel colour represents the number of counts registered at a peak of a histogram at each scan point, and in (b) and (c) pixel colour represents range

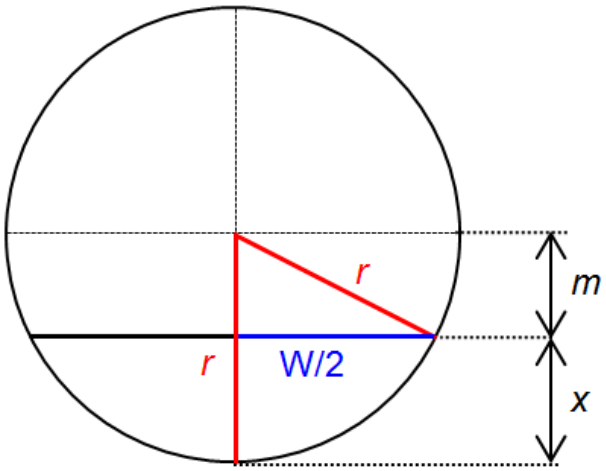

Figure 4.22. A circle of a radius of curvature, r, with an arc of width W/2 and height, x.

From the analysis of data x = 0.1 m and W varies from $W_{min} \approx 0.87$ m (top of the image) and $W_{max} \approx 1$ m (bottom of the image). From Eq. 4.13, the radius of curvature of the chimney at the top of the image, $r_{min} \approx 0.9$ m and the radius of curvature of the chimney at the bottom of the image $r_{max} \approx 1.0$ m. The difference between the radii of curvature at the top and the bottom of the image r_{max} - $r_{min} \approx 0.2$ m and the chimney height and the chimney height within the image was measured to be $k \approx 1.285$ m (see Figure 4.23).

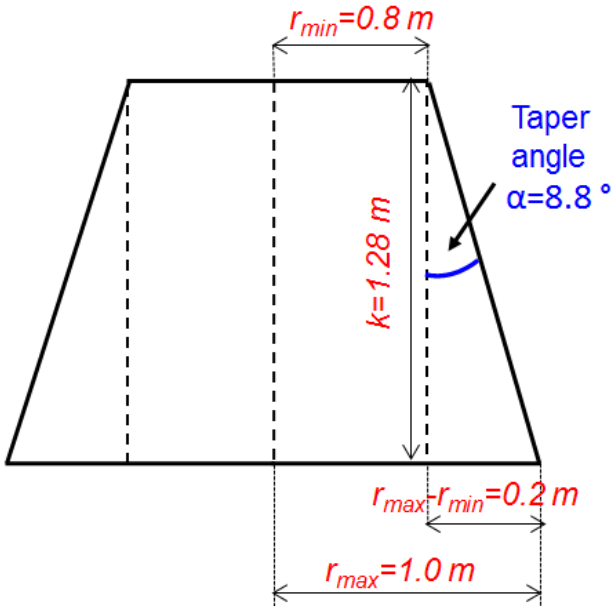

Figure 4.23. Side view layout of the chimney.

Thus, the taper angle, α is given by

$$\alpha = \arctan\left(\frac{r_{\max} - r_{\min}}{k}\right) \qquad \textit{Eq. 4.14}$$

From Eq. 4.14 the taper angle of the chimney α = 8.8 °.

As shown in Figure 4.21(a), the distribution in the number of photon counts across the *x* axis of the image resembles a Gaussian intensity distribution.

4.13.1.1 Depth Profile Retrieval

During a depth measurement, the detected photon returns were time-tagged by the TCSPC module and transferred to the control computer where software generated a histogram of photon returns for each scanned pixel. The histograms, produced with 50 ps wide bins, were analysed using a peak finder method. The peak finder finds a peak in the histogram based on least-squares curve fitting. The method yields good results in analysing data which can be judged by a number of well-defined criteria and is relatively simple and easy to implement. [13].

Least-squares curve fitting minimises the square of the error between the experimental data points and the values of the fitting function. In this case the quantity res^2 expressed by [13]

$$res^2 = \sum_{i=1}^{n} W_i [f(x_i) - y_i)]^2 \qquad \textit{Eq. 4.15}$$

is minimised, where $f(x_i)$ is the i-th element of the array of y values of the fitted model and y_i is the i-th element of the data set (x_i, y_i). In this equation W_i is the weighting factor for the i-th data point and n is the total number of data points [13]. Typically, a quadratic polynomial is fitted into a set of data by the means allowing locations of peaks to be identified with a precision determined by a user-defined number of consecutive data points used in the fitting process [13].

The analysis of the experimental data was conducted in LabVIEW using an in-bulit Peak Detector function [14] which is based on an algorithm that performs least-squares fit described by Eq. 4.15 to a sequential group of data points. Number of data points used in the fit was specified by the user. The weight, W_i, was set to 1 for all data points.

For each peak, the least-squares fit was tested against a user defined threshold (typically above the background level), thus, peaks lower than the threshold were ignored [14] [15].

The algorithm calculated the time-of-flight, *t*, corresponding to the identified peak. This value was then used to calculate the range, *R*, to the target. Since there are multiple pulses in transit, establishing the absolute range was not possible without the prior

information about the approximate location of a target. In this case this information was extracted from Google Maps. The absolute range was calculated from

$$R = \frac{(mp + t)c}{2} \qquad \textit{Eq. 4.16}$$

where m is the number of a gates prior to the gate in which the signal is expected to be detected (e.g. if the target is located at an approximate range of 2.8 km and an 8 µs gate period - corresponding to 1.2 km distance is applied - then m = 2) and p is the gate period which is equal to 8 µs. The estimated absolute range to the chimney was 2893.9 m.

4.14 Distance Ranging Lidar - Power Budget

A simplified diagram of a distance ranging lidar system is shown in Figure 4.24. The FoV of the receiver is determined by the size of active area of the detector and the focal length of the receiver. A laser beam of a half-divergence angle, θ_{Div}, is emitted onto a target plane located at normal incidence to the optical axis of the laser transmitter over a range, R, along the axis which coincides with the optical axis of the receiver. It is assumed that the laser source illuminates the area, A_B, with a radius, r_b, with a beam of a uniform intensity distribution.

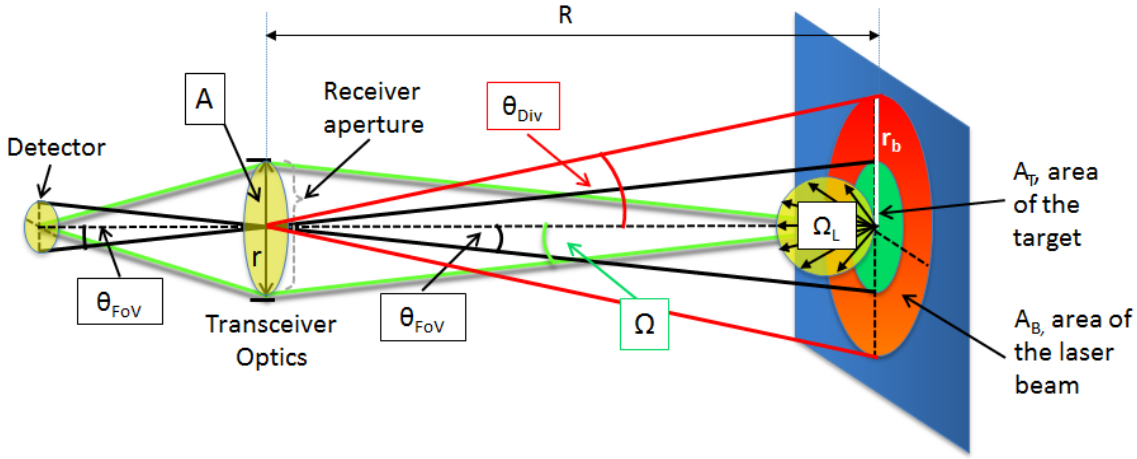

Figure 4.24. Schematic diagram illustrating geometry of a simple distance-ranging lidar system.

The irradiance (power per unit area incident on a surface), E, of the laser beam projected on the target plane at a range, R, is [16]:

$$E = \frac{P_0}{A_B} \qquad \textit{Eq. 4.17}$$

where P_0 is the laser power and A_B is the area of the laser beam and given by

$$A_B = \pi(\theta_{DiV} R)^2 \qquad \textit{Eq. 4.18}$$

Therefore, the power, P_{Det}, collected at the area of telescope aperture, A_T, and focused onto the detector by the transceiver optics is

$$P_{Det} = \frac{P_0 A_T \rho}{A_B} = \frac{P_0 A_T \rho}{\pi(\theta_{DiV} R)^2} \qquad \textit{Eq. 4.19}$$

where ρ is reflectivity of the target surface.

In the following two sub-sections two scenarios where the beam reflection from a target the surface of which is (a) Lambertian (b) a retro-reflective corner cube are considered.

4.14.1 Lambertian Target

A Lambertian target illuminated with a uniform beam behaves as an extended source and will radiate a certain amount of power per unit solid angle called radiant intensity, *I*, according to Lambert's law [16]:

$$I = I_0 \cos\theta \qquad \textit{Eq. 4.20}$$

where I is the intensity of a small incremental area of the target in a direction at an angle θ, and I_0 is the intensity of the incremental area in the direction of the normal to the target surface [16].

The irradiance, E_L (Wcm^{-2}), radiated from a flat Lambertian surface illuminated with a source of radiance N ($Wsr^{-1}cm^{-2}$) into a hemisphere is [16]:

$$E_L = \pi N \qquad \textit{Eq. 4.21}$$

Therefore, the solid angle which a Lambertian surface radiates, into, Ω_L, is

$$\Omega_L = \frac{E_L}{N} = \pi \qquad \textit{Eq. 4.22}$$

If the area of a Lambertian target is within the FoV of the detector element (as shown in Figure 4.24), then, the irradiance collected by the aperture and subsequently by the detector, E_{Det}, is limited by the ratio of the solid angle subtended by the circular receiver aperture of area A and radius r, at the centre of the detector FoV, Ω, and the solid angle into which the illuminated Lambertian target radiates the scattered energy from the source, Ω_L [17].

Where Ω is

$$\Omega = \frac{A}{R^2} \qquad \textit{Eq. 4.23}$$

Thus, the total power collected at the detector from a Lambertian target, P_{DetL}, is

$$P_{DetL} = P_{Det}\frac{\Omega}{\Omega_L} \qquad \textit{Eq. 4.24}$$

After substituting Eq. 4.19 and Eq. 4.23 into Eq. 4.24, P_{DetL}, is given by

$$P_{DetL} = \frac{P_0 A_T A\rho}{\pi^2 \theta_{DiV}{}^2 R^4} \qquad \textit{Eq. 4.25}$$

Assuming that the area of the target fills the entire FoV of the optical system then

$$A_T = \pi r_{FoV}^2 = \pi \theta_{FoV}{}^2 R^2 \qquad \textit{Eq. 4.26}$$

and

$$A = \pi r^2 \qquad \textit{Eq. 4.27}$$

where θ_{FoV} is the semi-angle of a diagonal FoV for a single detector pixel equal to 0.0011 ° (1.996×10^{-5} rad). P_{AL}, for a Lambertian target is given by

$$P_{DetL} = P_0\left(\frac{r^2\rho}{R^2}\right)\left(\frac{\theta_{FoV}}{\theta_{Div}}\right)^2 \qquad \textit{Eq. 4.28}$$

4.14.2 Corner Cube Retro-Reflector

A corner cube retro-reflector (see Figure 4.25(a)) consists of three, mutually perpendicular, intersecting flat surfaces (Figure 4.25(b)) which reflect light back towards the source and are characterised by high reflectivity [18].

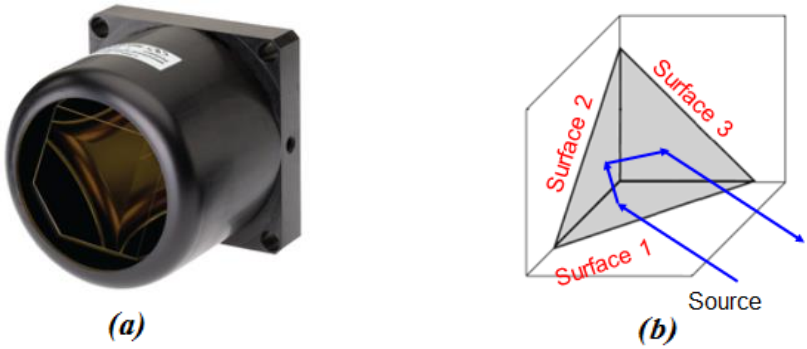

Figure 4.25. (a) Assembly of a retro-reflective corner cube; (b) geometry of a corner-cube which consists of three mutually perpendicular, intersecting flat surfaces [18] [19].

If the target is a retro-reflective corner-cube then

$$P_{DetCC} = P_{Det}\frac{\Omega}{\Omega_{CC}} \qquad \textit{Eq. 4.29}$$

Where Ω is the solid angle subtended by the circular receiver aperture of area A and radius r, at the centre of the detector FoV and Ω_{CC} is a solid angle into which an illuminated corner cube radiates the energy from the source.

The divergence of light reflected from a corner cube is limited by the diffraction on its circular aperture and on the accuracy to which reflective surfaces of the cube were manufactured and assembled to (beam parallelism).

The divergence due to the diffraction limit, θ_{Diff}, is

$$\theta_{Diff} = \frac{2.44\lambda}{D_{CC}} \qquad \textit{Eq. 4.30}$$

where D_{CC} is diameter of the corner cube and λ is the wavelength of illuminating light [20]. For a corner cube of 10 cm clear diameter illuminated by a 1550 nm wavelength beam, θ_{Diff} = 37.82 µrad. The parallelism of the beam produced by the corner cube used in experiments quoted by the manufacturer is ± 1.5 arcsec [19], this is equivalent to 14.54 µrad and shows that the diffraction on the aperture is the limiting factor on the beam divergence.

In this case

$$\Omega_{CC} = \frac{A_{Diff}}{R^2} = \frac{\pi\theta_{Diff}{}^2 R^2}{R^2} = \pi\theta_{Diff}{}^2 \qquad \textit{Eq. 4.31}$$

Hence the power collected by the detector, P_A, for a corner cube is given by:

$$P_{DetCC} = \frac{P_0 A_{CC} A \rho_{CC}}{R^4 \pi^2 \theta_{DiV}{}^2 \theta_{Diff}{}^2} \qquad \textit{Eq. 4.32}$$

where A_{CC} is the area of the corner cube and ρ_{CC} is reflectivity of the corner cube.

4.14.3 Other Losses

Additional losses are associated with:

- Atmospheric attenuation, τ_A, for a round trip between the transmitter, target and receiver;
- System throughput, γ_T, reduced by :
  - Reflection and transmission at the telescope, mirrors and lenses;
  - Telescope obstruction;
  - Annular mirror;

- Single-photon detection efficiency of the SPAD detector, $SPDE_{Det}$.

Therefore, the total power collected by a detector, P_{TDetL}, for a Lambertian target is

$$P_{TDetL} = P_{DetL}(2\tau_A R)\gamma_T SPDE_{Det} \qquad \textit{Eq. 4.33}$$

Assuming that the effects of turbulence are negligible, the total power collected by a detector, P_{TDetCC}, for the corner cube is

$$P_{TDetCC} = P_{DetCC}(2\tau_A R)\gamma_T SPDE_{Det} \qquad \textit{Eq. 4.34}$$

Atmospheric loss, τ_A, at 1550 nm is approximately: (a) 0.2 dB/km in clear weather and visibility of 23 km, (b) 2 dB/km in haze and visibility of 4 km and (c) 34 dB/km in fog and visibility of 0.5 km [21].

System throughput loss varies depending on configuration. In bi-static configuration the transmitter and receiver paths are separate and hence the system throughput loss is only encountered on the receiver path. However, in mono-static configuration the laser beam is transmitted through the receiver and therefore encounters losses associated with reflectivity and transmission of optical components.

The telescope was coated with StarBright XLT visible coating. The transmission at 1550 nm was measured at Selex ES and was reported to be equal to approximately 85 % [22] [23].

The system consisted of two path folding mirrors of 98.5 % reflection, two scanning mirrors of 98 % reflection and five singlet lenses coated for a 1550 nm wavelength, each of transmission equal to 99 %. In addition, there is a 33 % loss on the telescope obstruction [23]. The total throughput loss is 49 % (- 2.9 dB)

$SPDE_{Det}$ at a wavelength of 1550 nm reported by the manufacturer as is ~ 30 %.

4.15 Total Estimated System Losses

After substituting Eq. 4.28 to Eq. 4.33 P_{Det}/P_0 for a Lambertian target is

$$\frac{P_{TDetL}}{P_0} = \left(\frac{r^2\rho}{R^2}\right)\left(\frac{\theta_{FoV}}{\theta_{Div}}\right)^2 (2\tau_A R)\gamma_T SPDE_{Det} \qquad \textit{Eq. 4.35}$$

After substituting Eq. 4.32 to Eq. 4.34 P_{Det}/P_0 for a corner cube reflector is

$$\frac{P_{TDetCC}}{P_0} = \left(\frac{P_0 A_{CC} A \rho_{CC}}{R^4 \pi^2 \theta_{DiV}{}^2 \theta_{Diff}{}^2} \right) (2\tau_A R) \gamma_T SPDE_{Det} \qquad \textit{Eq. 4.36}$$

The attenuation of laser power, ε, in decibels [dB] is given by

$$\varepsilon = 10 Log_{10} \frac{P_{TDet}}{P_0} \qquad \textit{Eq. 4.37}$$

The attenuation of laser power for a Lambertian target, ε_L, in decibels [dB] is

$$\varepsilon_L = 10 Log_{10} \left(\frac{r^2 \rho}{R^2} \right) \left(\frac{\theta_{FoV}}{\theta_{Div}} \right)^2 (2\tau_A R) \gamma_T SPDE_{Det} \qquad \textit{Eq. 4.38}$$

And the attenuation of laser power for a corner cube, ε_{CC}, in decibels [dB] is

$$\varepsilon_{CC} = 10 Log_{10} \left(\frac{P_0 A_{CC} A \rho_{CC}}{R^4 \pi^2 \theta_{DiV}{}^2 \theta_{Diff}{}^2} \right) (2\tau_A R) \gamma_T SPDE_{Det} \qquad \textit{Eq. 4.39}$$

Total system losses for a Lambertian target were calculated from Eq. 4.38. Table 4.1 shows the result of the calculation, which includes the break-down list of each factor from Eq. 4.38.

Loss factor	Attenuation, ε [dB]	
	R = 2893 m	R = 4180 m
$\left(\frac{r^2 \rho}{R^2} \right) \left(\frac{\theta_{FoV}}{\theta_{Div}} \right)^2$	- 125.2	- 128.
$2\tau_A R$	- 1.2	- 1.7
γ_T	- 2.9	- 2.9
$SPDE_{Det}$	- 5.2	- 5.2
Total	**- 134.5**	**- 138.3**

Table 4.1 Total system losses calculated for the bi-static scanned configuration and a Lambertian target located over ranges: R = 2839 m and R = 4180 m. Assumed parameters: clear weather, visibility of 23 km at 1550 nm (τ_A = 0.2 dB/km) and ρ = 25%.

Total system losses for a corner cube were calculated from Eq. 4.39. Table 4.2 shows the result of the calculation, which includes the break-down list of each factor from Eq. 4.39.

Based on the estimated attenuation values the expected photon count rate is calculated in the following section.

Loss factor	Attenuation, ε [dB]	
	R = 2893 m	R = 4180 m
$\frac{A_{CC} A \rho_{CC}}{R^4 \pi^2 \theta_{DiV}{}^2 \theta_{Diff}{}^2} *$	- 102	- 109
$2\tau_A R$	- 1.2	- 1.7
γ_T	- 2.9	- 2.9
$SPDE_{Det}$	- 5.2	- 5.2
Total	**- 112**	**- 119**

Table 4.2. Total system losses calculated for the bi-static scanned configuration and the corner cube located over ranges: R = 2839 m and R = 4180 m. Assumed parameters: clear weather, visibility of 23 km at 1550 nm (τ_A = 0.2 dB/km) $A_{CC} = 7.85 \times 10^{-3} m^2$ (corner cube diameter=10 cm), A = 0.0324 m^2, ρ_{CC} = 98 %.

4.16 Expected Photon-Count Rate

For laser output power, P_0 = 0.5 W and ε = -134.5 dB (Lambertian target at a range R = 2839 m, see Table 4.1), power on detector is: $P_{DetL} = 1.75 \times 10^{-14}$ J/s (from Eq. 4.28). Since photon energy at a wavelength of 1550 nm is 1.28×10^{-19} J, the count rate per second on detector is CR_{FR} = 137 kcps. If the detector, operates in a gated mode with gate period, T = 8 μs, and gate width, T_{ON} = 500 ns, then from Eq. 4.5 the count rate is limited to CR_{Gated} = 8.5 kcps. Due to the hold-off time, T_{HO} = 20 μs, the count rate is limited further to CR_{HO} = 7.1 kcps (see Eq. 4.10). The expected count rate per pixel was calculated for a Lambertian target located at 4180 m using the same principle; results are shown in Table 4.3.

	Expected approximate count rate, CR_{HO} [kcps]	
Range, R [m]	2839	4180
Lambertian target	7.1	3.4

Table 4.3. Expected approximate count rate, CR_{HO}, for a Lambertian target located over a range, R, of 2839 m and 4180 m. Data calculated for the hold-off time T_{HO} = 20 μs, acquisition time of 1 s and gate width, T_{ON} = 500 ns.

This suggests that the probability of photon count per laser pulse (at 125 kHz) is 5.7 % at a range of 2839 m and 2.7 % at 4180 m which is approximately within the required 5 % to prevent pile-up.

4.16.1.1 Instrumental Response Function

Time-tags representing transmitted laser pulses, photon events recorded by the SPAD and movement of the scanning mirrors were recorded with 1 ps bin resolution. The time difference between each recorded photon return and a foregoing transmitted laser pulse was calculated and represented on a histogram for each scan point. An instrumental response function (IRF) for a 15 × 4 scan point of the chimney measured over acquisition time of 1 s with a 500 ps gate width was generated with a bin width of 50 ps and is shown in Figure 4.26.

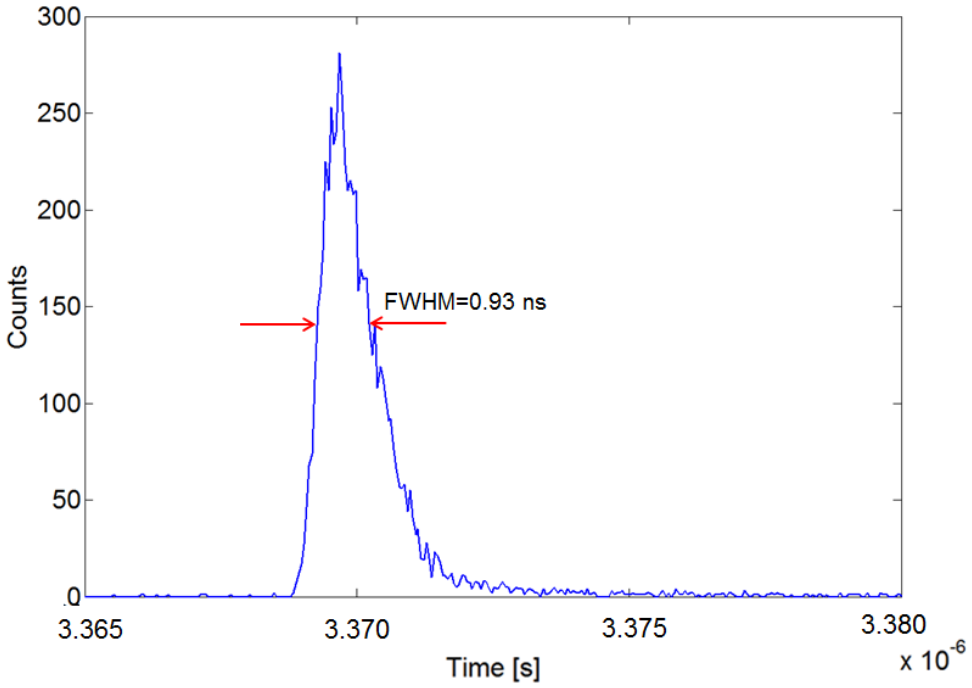

Figure 4.26. A plot of an instrumental response function. FWHM of the function was measured to be 0.93 ns which represents depth resolution of 14 cm.

The shape of the IRF resembles a typical behaviour of a detector impulse response function which represents the shape of the laser pulse, jitter of timing electronics and the slow diffusion tail of the detector. The effect of the electronics timing jitter is evident as a broadening of the histogram peak [24]. The full width at half maximum (FWHM) of the IRF represents the system timing jitter Δt = 0.93 ns. The depth resolution Rs_{Depth} of the system was calculated from Eq. 4.40 and is equal to 14 cm.

$$Rs_{Depth} = c\Delta t / 2 \qquad \textit{Eq. 4.40}$$

The IRF was calculated for the scan position pointing approximately at the centre of the image where the surface of the chimney is perpendicular to the optical axis of the transceiver. The curvature of the chimney over the extent of the imaged FoV, shown in Figure 4.21(c), introduced a variation in range of $x \approx 10$ cm, however, this is smaller compared to the Rs_{Depth} of the system.

The histogram produced for the pixel in row 1, column 1 of the image (1 s acquisition, T_{ON} = 500 ns) is shown in Figure 4.27. Integration under the histogram was performed to estimate the count rate and signal-to-background ratio during the acquisition time.

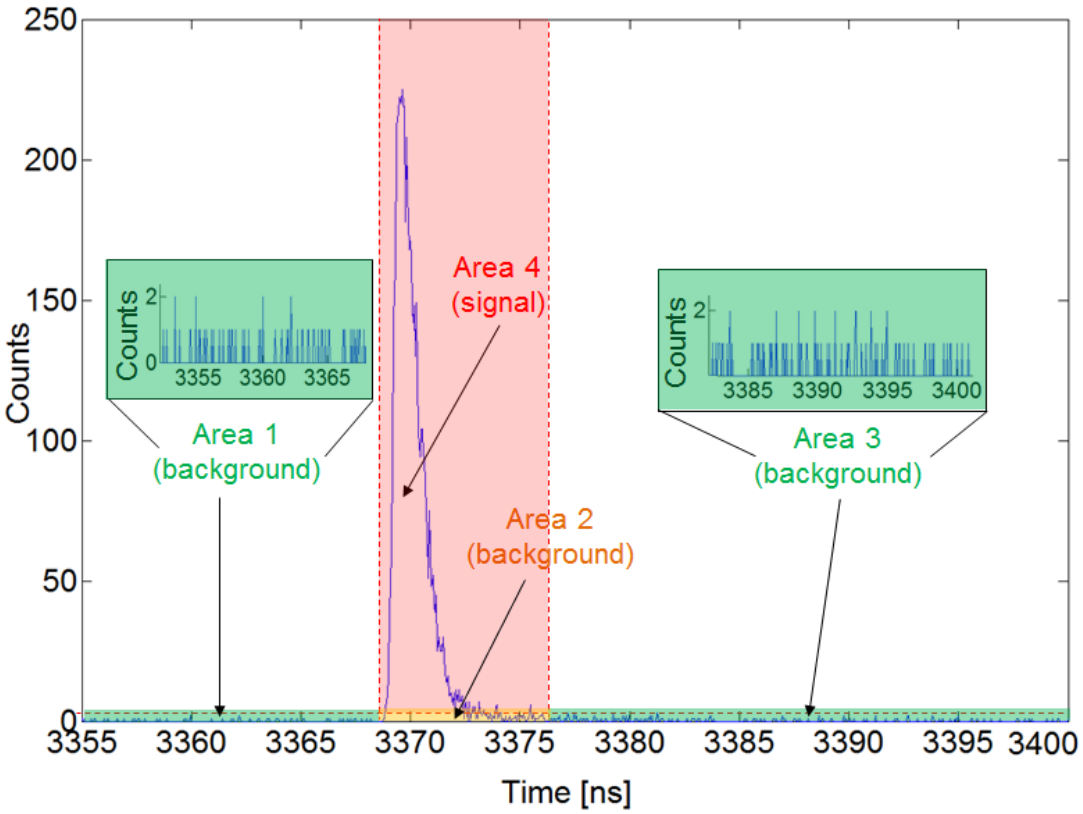

Figure 4.27. Histogram for pixel in row1 and column 1 showing area 1, 2 and 3 with background counts and area 4 with signal counts.

The histogram, generated with a bin width of 50 ps (10,000 bins in total for the 500 ns gate), was divided into several areas:

- Area 1 - 3120 ns to 3368.75 ns, 4975 bins (background counts);
- Area 2 - 3368.80 ns to 3373 ns, 84 bins (background counts);
- Area 3 - 3373.05 ns to 3620 ns, 4939 bins (background counts);
- Area 4 - 3368.80 ns to 3373 ns, 84 bins (signal counts).

Areas 1, 2 and 3 contain background counts (solar and dark counts) whereas area 2 contains signal counts. In order to establish signal to background ratio and the count rate from the target the number of the background counts that arrived during the same time as the signal needs to be calculated. By estimating the average number of counts per bin within the area 1 and 3 it is possible to estimate the number of background counts present during the time when the signal arrived (area 2).

The integration under the histogram within the area 1 showed that the total number of counts within that area (4975 bins) is 1827 and within the area 3 (4939 bins) it is 1840. The total number of bins under the area 1 and 2 is 9734, thus the average number of background counts is 0.37 counts per bin. There are 84 bins under area 2, therefore the average number of background counts recorded within the time during which the signal arrived is 31.1 cps. The total number of counts under the entire histogram is 10 kcps. Subtracting the total counts due to background (3.7 kcps), the count rate due to signal is 6.3 kcps. This is less than the predicted value of 7.1 kcps (see Table 4.3).

There is a difference of 0.8 kcps between the experimental and theoretical data. The difference is likely to originate from underestimated losses on the optical components. The position of the focal spot may oscillate along *x* and *y* direction on the focal plane due to turbulence causing the energy to partially miss the detector. In addition, the theoretical model assumes that the target is Lambertian with reflectivity equal of 25 % however, it is possible that the reflectivity of the chimney is different to the assumed value.

Subsequently, a signal-to-background ratio (SBR) and signal-to-noise ratio (SNR) were estimated. From Eq. 2.18, SBR = 6.3 kcps / 31.1 cps = 202.6, suggesting that the background level was very low when compared to the level of signal. From Eq. 2.19, SNR = 79. The SNR is high, suggesting that the useful signal dominates over the noise.

The uncertainty in the distance measurement, σ_{Dist}, was also calculated (Eq. 2.20). For σ_{Jitter} = 0.93 ns (FWHM of the IRF) and N_T = 6.3 kcps, $\sigma_{Dist} = 1.17 \times 10^{-11}$ s, which is equivalent to 3.5 mm.

4.16.2 Napier University Wall

Over a range of ~ 4.4 km a flat wall of a Napier University building was imaged. Figure 4.28 shows a photograph of a visible-band wide FoV image of the scene.

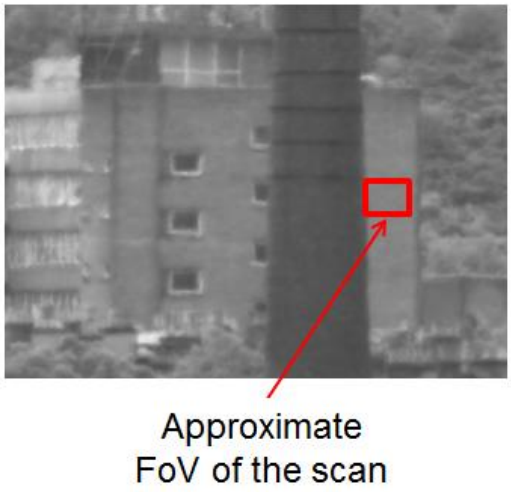

Figure 4.28. A visible-band, wide FoV photograph of the Napier University wall located ~ 4.4 km from the laboratory.

A delay between the laser trigger pulse and the SPAD gate on external trigger was generated by the PPG and was equal to 3890 ns. The data was acquired with a 100 ns gate width over 32 × 32 pixels with a scan step representing 12 cm and 0.5 s acquisition time per pixel giving the total acquisition time of 8.5 min. Raw plotted depth data of the target is shown in Figure 4.29.

A common form of a linear equation in the two variables x and y is

$$y = mx + b \qquad \textit{Eq. 4.41}$$

where m determines the gradient of the line and b determines the point at which the line crosses the y axis [25]. A top view of the wall is shown in Figure 4.30. A linear fit to the raw data points of the top view acquired over 0.5 s per scan point is given by $y = 0.4286\,x + 4489.3$. Since

$$m = \tan\beta \qquad \textit{Eq. 4.42}$$

where β is the angle of the line in respect to the sight, then for $m = 0.4286$ the slope of the wall is $\beta = 23.2$ ° [25].

The average width measured across the data points shown in Figure 4.30 *is* $\Delta w = 30.2$ cm with a standard deviation of 1.5 cm. This suggests that the peak occurs within the FWHM of the IRF of 1 ns which equivalent t to 30 cm.

Figure 4.31 shows the distribution of peak photon counts across the image of the wall. It resembles a Gaussian distribution of the illuminating beam, with a vertical smear potentially caused by turbulence. The distribution of the laser beam is less disrupted along the horizontal direction compared to the vertical and this permitted the approximate location of the centre of the beam to be established. It can be noted from

Figure 4.31 that there is ~ 1.5 m displacement between the centre of the transmitted laser beam and the centre of the scan indicating the angular beam misalignment of 0.167 mrad. This is an error in alignment and should have been corrected during the alignment process, ideally on a flat surface perpendicular to the line of sight. Due to the time limit imposed on access to the roof laboratory window this was not possible. However, the consequence of this error is not severe because it was possible to detect a sufficient number of counts across the entire image required to build up a histogram and to detect a peak.

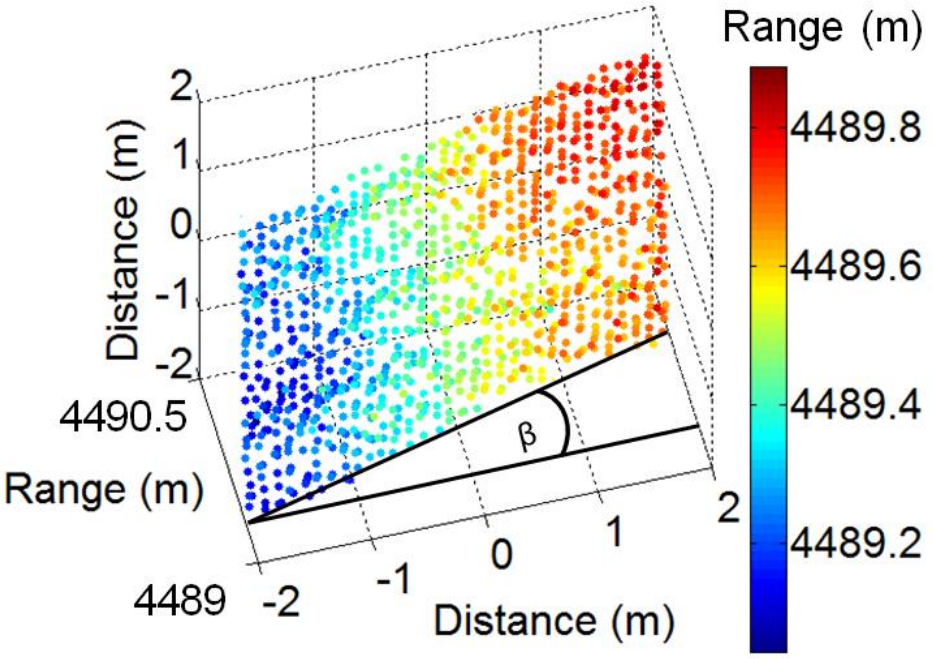

Figure 4.29. Depth profile measurements of a flat wall acquired over a distance of ~ 4.4 km with 1 s acquisition 32 × 32 scan steps, scan step resolution of 12 cm and 0.5 s acquisition time per pixel. The image is a scatterplot of raw data where pixel colour represents the range.

Measured count rate for the average signal in row A (see Figure 4.31) was ~ 3 kcps which was lower than the theoretical estimate of 3.4 cps (see Table 4.3). Apart from the underestimated losses on the optical components and turbulence, this can be also caused by the angle of incidence of the wall, which is at 23.2 ° to the line of sight. The theoretical model, however, assumes normal incidence and a Lambertian target.

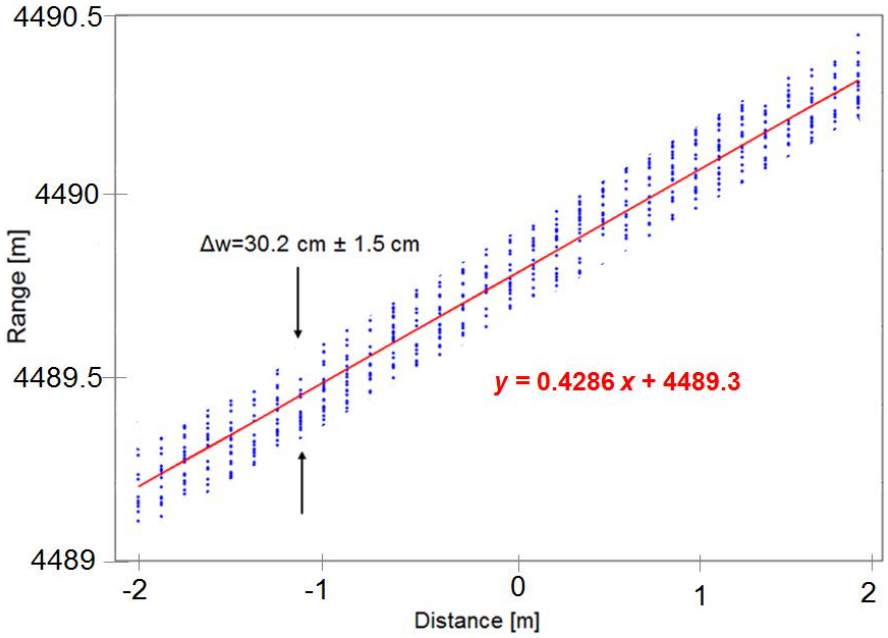

Figure 4.30. Top view of the wall with a linear fit to the data points.

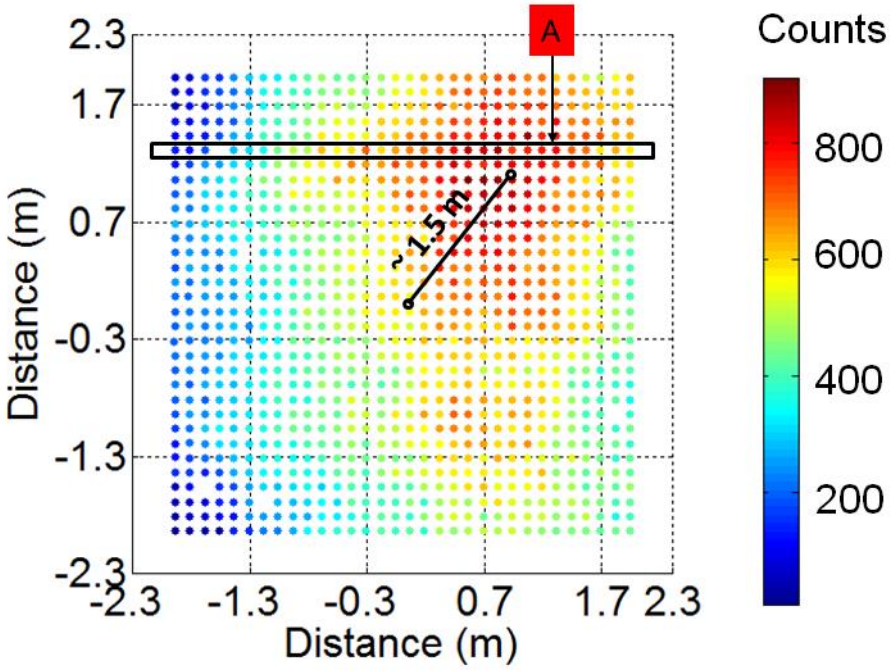

Figure 4.31. The distribution of photon counts across the wall showing a displacement between the centre of the laser beam and the scan centre for a 0.5 s acquisition time per pixel. Area "A" highlights a row from which the data is used for the count rate analysis.

4.16.3 Imaging Through a Semi-Transparent Net

More complex targets were imaged, such as the one shown in Figure 4.32(a). The scene consisted of multiple surfaces: a sheet of safety netting mounted on scaffolding approximately 2 m in front of a building wall and a rectangular object which presumably is an elevator control box (Figure 4.32(b)).

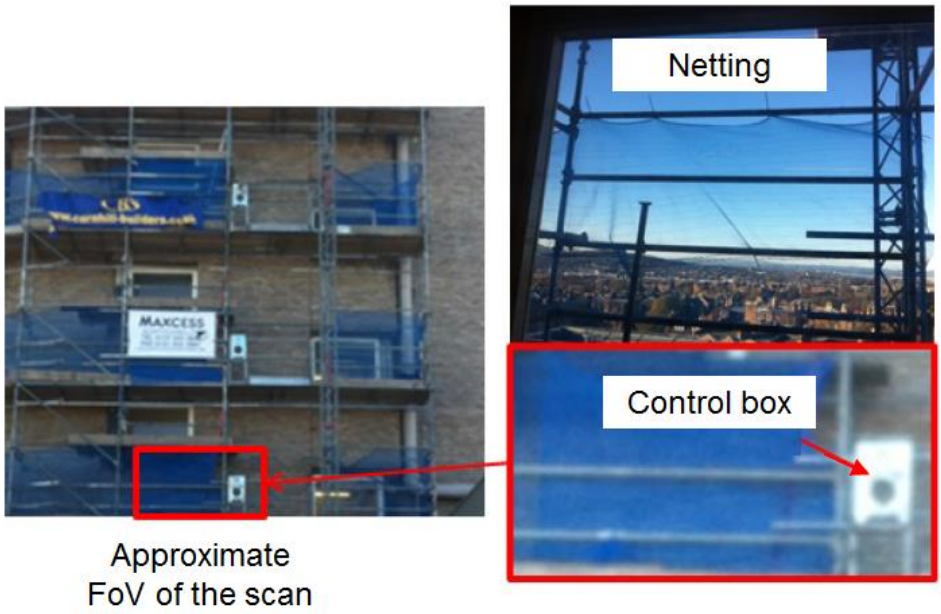

Figure 4.32. A visible-band, wide FoV photograph of the scaffolding located ~ 4.2 km from the laboratory, indicating approximate FoV of the scan.

A delay between the laser trigger pulse and the SPAD gate was generated by the PPG and was equal to 3890 ns. The target located at a range of ~ 4.2 km was scanned with 32 × 32 scan points with acquisition times varying between 200 ms and 8 ms with a gate width of 100 ns. An intensity scatterplot of data with varying acquisition times is shown in Figure 4.33(a1) - Figure 4.33(a6).

The figure demonstrates imaging through a surface of semi-transparent netting revealing the presence of the building wall which is not detectable on a close-up two-dimensional view shown in Figure 4.32. The details of the scene, including the netting and the control box, can still be identified with acquisition times per pixel as short as 15 ms allowing the entire scan to be acquired in 15.36 s.

Figure 4.34 shows a histogram generated with bins of 50 ps for row 30 and column 25 of the image. The three peaks on the histogram represent returns from the control box, the net and the wall. Based on the peak displacement, the distance between the box and the net is 5 cm whereas the distance from the net to the wall is 1.85 m. The absolute range to the target (wall) is 4186 m. To represent range information for each scan point in a three-dimensional plane, a two dimensional grid of 32 × 32 coordinates was generated, each coordinate could have multiple range inputs assigned which represent peaks from different surfaces. This data is then plotted in MatLab using a scatterplot function which creates a graph with dots at the locations specified by coordinates of scan points [26].

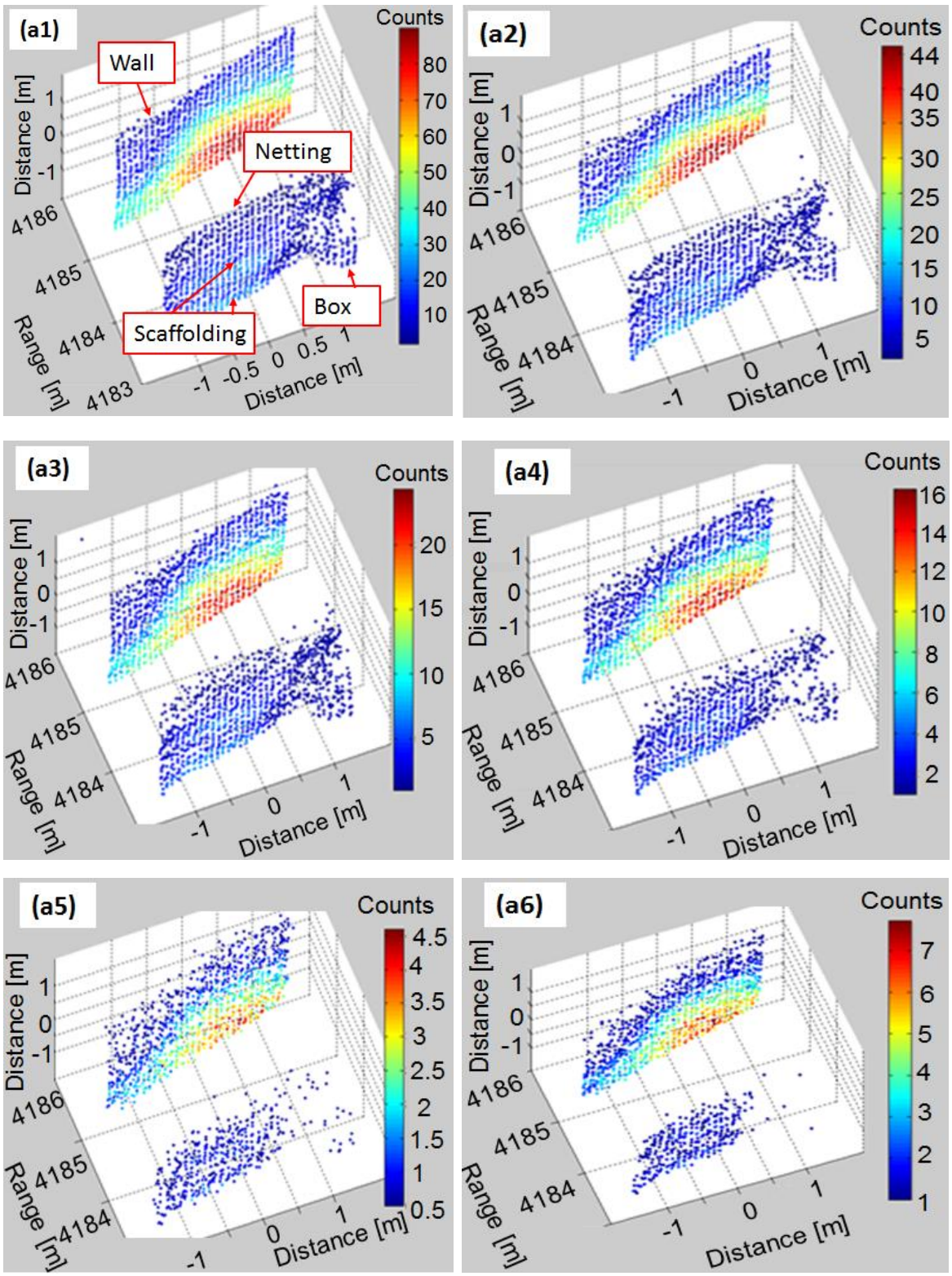

Figure 4.33. Depth profile measurements of a complex object acquired with 32 × 32 scan steps over a distance of ~ 4.2 km; (a1) to (a6) is a scatterplot of raw depth data for acquisition times varying between 200 ms to 8 ms, where acquisition time per scan point for (a1) = 200 ms, (a2) = 100 ms, (a3) = 50 ms, (a4) = 32 ms, (a5) = 15 ms and (a6) = 8 ms.

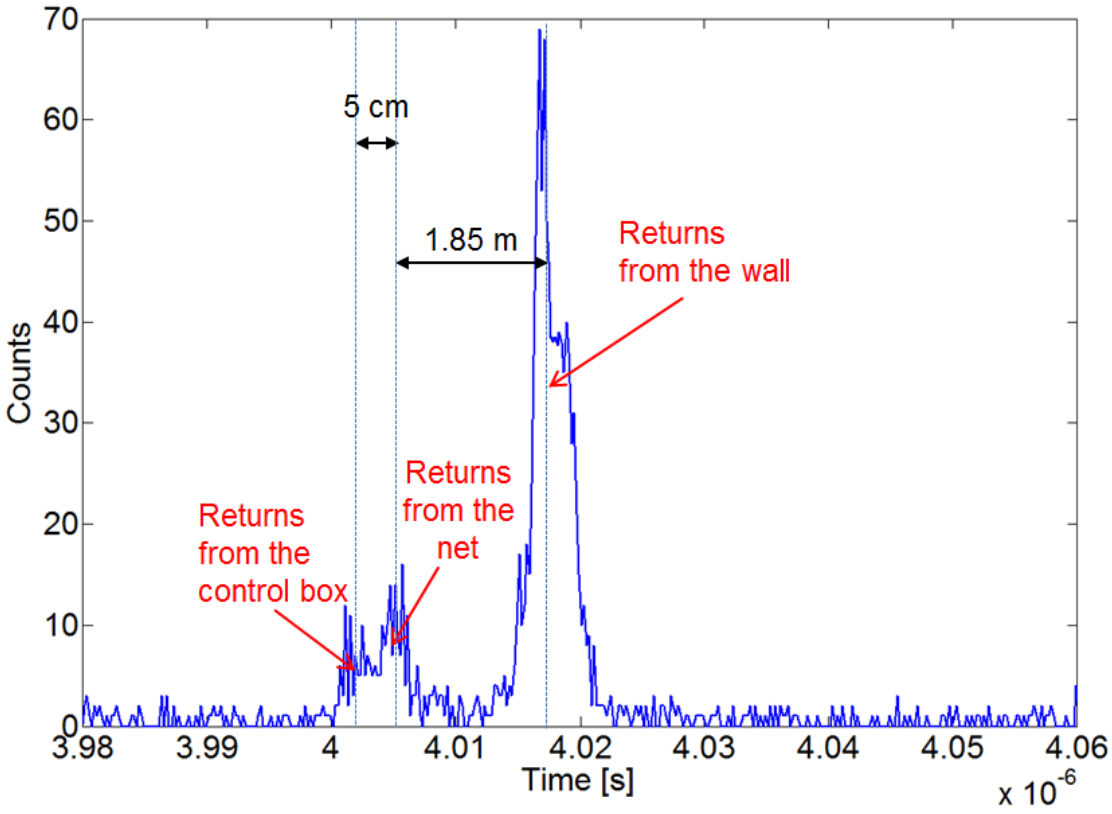

Figure 4.34. Histogram generated for row 30 and column 25 of the image with 50 ps wide bins. Returns from the control box, the net and the wall are represented by the three peaks.

4.17 Acknowledgements

The alignment of the telescope-eyepiece pair and relay lenses using the Twyman-Green interferometer was conducted with the assistance of Dr. Karen J. Gordon in the Selex ES Laser Centre of Excellence. The field trials and the transceiver bore-sighting were performed with the assistance of Dr. Karen J. Gordon, Roger Pilkington and Dr. Philip Hiskett of Selex ES. The control software for the scanning mirrors was developed solely by Dr. Karen J. Gordon. Dr. Stephen Harding of Selex ES provided advice on laser safety and all safety documentation was written with help from Dr. Karen J. Gordon.

4.18 Conclusions

This chapter presented the initial stage of the experimental work performed with the scanned single-element system in bi-static configuration where the alignment of the system, timing electronics scheme and calibration of scanning mirrors were described.

Kilometre-range depth imaging in broad daylight using a single-element SPAD in a scanned bi-static configuration was demonstrated. An IRF was measured and confirmed depth resolution of < 30 cm where the limiting factor on the depth resolution was the laser pulse of 800 ps duration.

The acquired data allowed the energy budget model to be evaluated with the experimental data and confirmed that the experimental photon count rate is close to the theoretical prediction.

The analysed raw data was represented as a three-dimensional point cloud for different types of objects scanned over ~ 2.8 km and ~ 4.2 km and allowed three-dimensional features of the objects, such as the taper angle and radius of curvature of the chimney as well as the slope of the wall in respect to the line of sight, to be identified. In addition, imaging through a semi-transparent sheet of netting was demonstrated.

It has been shown that identification of a complex scene located kilometres away is possible with a total acquisition time of ~ 15 s for a 32 × 32 image. An investigation into the possibility of decreasing the total acquisition time using different data processing techniques in presented in Chapter 5.

Due to the limited access time in the roof laboratory a more in-depth evaluation of the system was not possible. It will, however, be presented in Chapter 5.

References

[1] J.J. Degnan, D. Caplan, *"Performance of Liquid Crystal Optical Gate for Suppressing Laser Backscatter in Mono-Static Kilohertz SLR systems",* Proc. Of 15th Intern. Workshop on Laser Ranging, Australia (2007)

[2] A. McCarthy, X. Ren, A. D. Frera, N. R. Gemmel, N. J. Krichel, C. Scarcella, A. Ruggeri, A. Tosi, G. S. Buller, *"Kilometer-Range Depth Imaging at 1550 nm Wavelength Using an InGaAs/InP Single-Photon Avalanche Diode Detector",* Opt. Express, 21, 19, pp. 22098-22113 (2013)

[3] http://www.princetel.com/datasheets/SMF28e.pdf

[4] http://www.tydexoptics.com/products/spectroscopy/oap_mirrors/

[5] Safety of Laser Products, British Standards, PD IEC TR 60825-14 (2004)

[6] Safety of Laser Products, BSI Standards Publication, BS/EN/60825-1 (2014)

[7] Manlight Laser, Instruction Manual

[8] A. Tosi, A. Della Frera, A. Bahgat Shehata and C. Scarcella, "*Fully programmable single-photon detection module for InGaAs/InP single photon avalanche diodes with clean and sub-nanosecond gating transitions"*, Rev. Sci. Instrum. 83, 013104 (2012)

[9] A. Tosi, A. Dalla Mora, F. Zappa, S. Cova, M. A. Itzler, X. Jiang, *"InGaAs/InP Single-Photon Avalanche Diodes Show Low Dark Counts and Require Moderate Cooling",* Proc. SPIE, 7222, 72221G-1 (2009)

[10] HydraHarp400, Time-Correlated Single-Photon Counting system with USB Interface, Instruction Manual

[11] W. Becker, A. Bergman, G. Biscotti, A. Ruck, *"Advanced Time-Correlated Single-Photon Counting Technique for Spectroscopy and Imaging in Biomedical systems*", Proc. SPIE 5340 (2004)

[12] https://www.google.co.uk/maps

[13] D.V. O'Connor, D. Phillips, "*Time-Correlated Single-Photon Counting"*, Academic Press (1984)

[14] http://zone.ni.com/reference/en-XX/help/371361J-01/lvanls/peak_detector/

[15] L.M. Chugani R.A. Samant, M. Cerna, *"LabVIEW Signal Processing",* Prentice and Hall (1998)

[16] W.J. Smith, *"Modern Optical Engineering"*, SPIE Press (2008)

[17] P.A. Hiskett, R.A. Lamb, *"Design Considerations for High-Altitude Altimetry and Lidar Systems incorporating Single-Photon Avalanche Diode Detectors"*, Proc. SPIE, 8033, 80330F-1 (2011)

[18] W.I. Newman, *"Continuum Mechanics in the Earth Sciences",* Cambridge University Press (2012)

[19] http://search.newport.com/?q=retroreflector%2063.5%20mm

[20] E. Hecht, "*Optics"*, Adison Wesley (2005)

[21] I.I. Kim, B. McArthur, E. Korevaar, *"Comparison of Laser Beam Propagation at 785 nm and 1550 nm in Fog and Haze for Wireless Optical Communications",* Proc. SPIE, 4214, 0277-786X/01 (2001)

[22] Jeremy Copley, Selex-ES Internal Report (2009)

[23] Celestron C-GEM Series, Instruction Manual

[24] A. McCarthy, R.J. Collins, N.J. Krichel, V. Fernandez, A.M. Wallace. G.S. Buller, *"Long-Range Time-of-Flight Scanning Sensor Based on High-Speed Time-Correlated Single-Photon Counting*", Appl. Opt., 48, 32 (2009)

[25] K.A. Stroud, D.J. Booth, *"Engineering Mathematics",* 7th Edition, Palgrave McMillan (2013)

[26] http://uk.mathworks.com/help/matlab/ref/scatter.html

Chapter 5

Evaluation of the Transceiver in Mono-Static Configuration with a Scanned Single-Element SPAD Detector

5.1 Introduction

This chapter describes experimental results acquired with the lidar system operating in a mono-static configuration with the single-element SPAD (i.e. described as mode C in previous chapters). Details of the transmitter design, timing electronics, the alignment, bore-sighting and backscatter mitigation based on an electrical gating approach are described.

In order to assess the depth resolution of the system measurements of the instrumental response function and resolution tests were performed. A surface-to-surface resolution test is described where the peak finder technique applied to raw data and to a cross-correlation between a histogram and a normalised instrumental response function are compared. It was demonstrated that when the data is cross-correlated with the instrumental response function, surface-to-surface resolution increases, the quality of an analysed three-dimensional image increased and the total acquisition time decreases.

Finally, depth images of different types of objects such as an electricity pylon, foliage, terrain and buildings acquired over distances between 800 m and 10.5 km are presented. In addition, image mosaicing of an object with up to 100 × 235 scan points is shown.

5.2 Mono-Static System Experimental Setup

The experimental setup was arranged in a mono-static configuration and incorporated a 25 μm diameter pixel, single-element InGaAs/InP SPAD detector described in section 4.8. The system used an erbium-doped fibre laser operating at a wavelength of 1550 nm, which generated 800 ps duration pulses at a repetition rate of 125 kHz (see section 4.7). The maximum average laser power used in experiments was 10 mW to comply with laser eye-safety precautions and was within the class 1 range. This was equivalent to 0.8 nJ per pulse.

The system architecture is shown in Figure 5.1. Photon returns from a target were collected by the receiver and recorded by the SPAD detector operating in a gated mode. The signal was acquired from the $FoV_{Scanner}$ by employing a pair of galvanometer scanning mirrors.

The laser beam was transmitted from a fibre which was coupled into a collimator and a beam expander and then injected into the main system through the annular mirror. The optical components of the collimator were set up to provide the required laser beam divergence for the beam channelled along the direction parallel and displaced from the optical axis of the telescope. The telescope collected a return signal from a target which was then subsequently collimated by an eyepiece. The set of relay lenses projected the image of the exit pupil from the mirror *y* to the mirror *x* while the annular mirror reflected it onto the lens L(b) which created a focal spot on the active area of the SPAD detector.

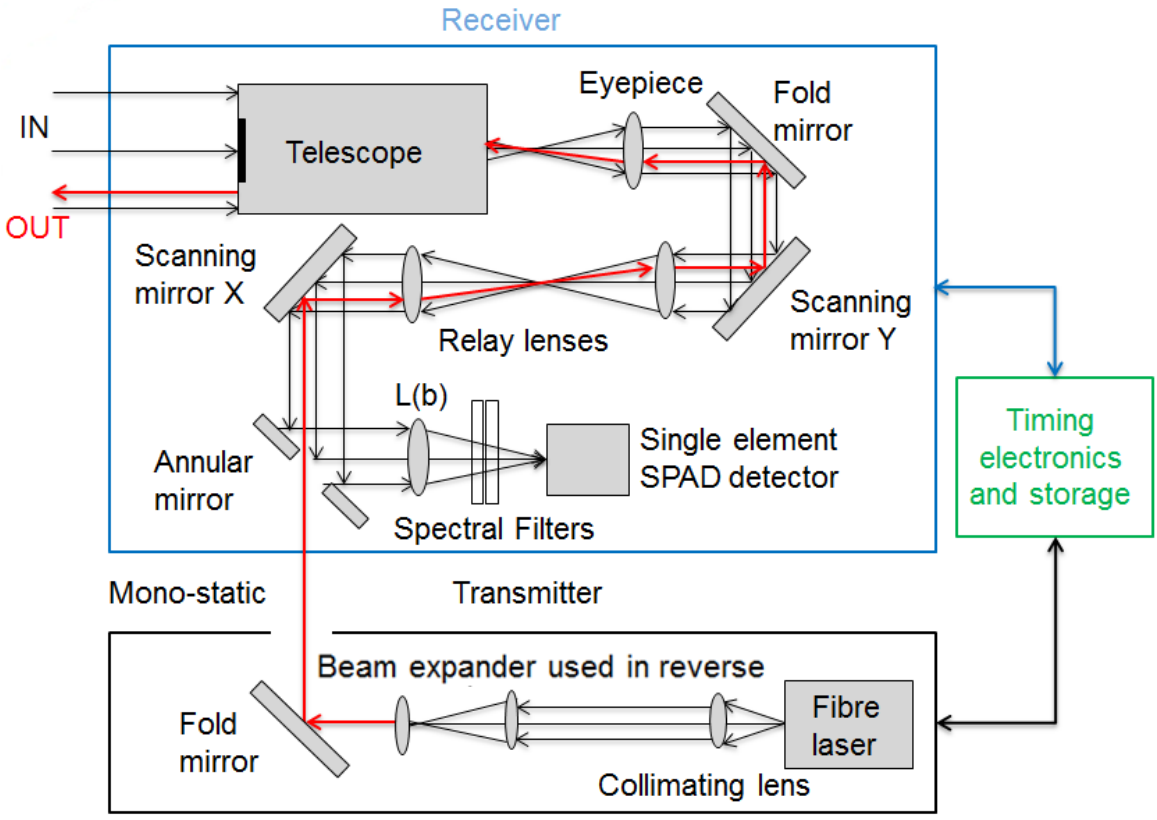

Figure 5.1. Schematic diagram of the experimental setup of the system operating in a mono-static configuration with a scanned single-element SPAD detector.

In order to suppress out-of-band solar background photons filters listed in section 4.2, were placed between the lens L3(b) and the SPAD detector:

5.3 Time Interval Analyser

The time interval analyser used in the setup was a GuideTech GT658PCI device. The unit had two independent input channels and an external arm input. The arm input enabled the time interval analyser to start a block of measurements after an external TTL signal was supplied.

The device provided a count rate of up to 12 Mcps per channel and a minimum time-bin width of 80 ps with the maximum number of 1 million time tags for both channels.

5.3.1 Control Electronics, Data Acquisition and Analysis

A schematic diagram showing the timing electronics used to acquire experimental data is shown in Figure 5.2. A commercially sourced digital delay and pulse generator was used to synchronise and gate the SPAD detector and clock the laser pulse at a frequency of 125 kHz. The output power of the laser was adjusted via a current driver controlled by a PC.

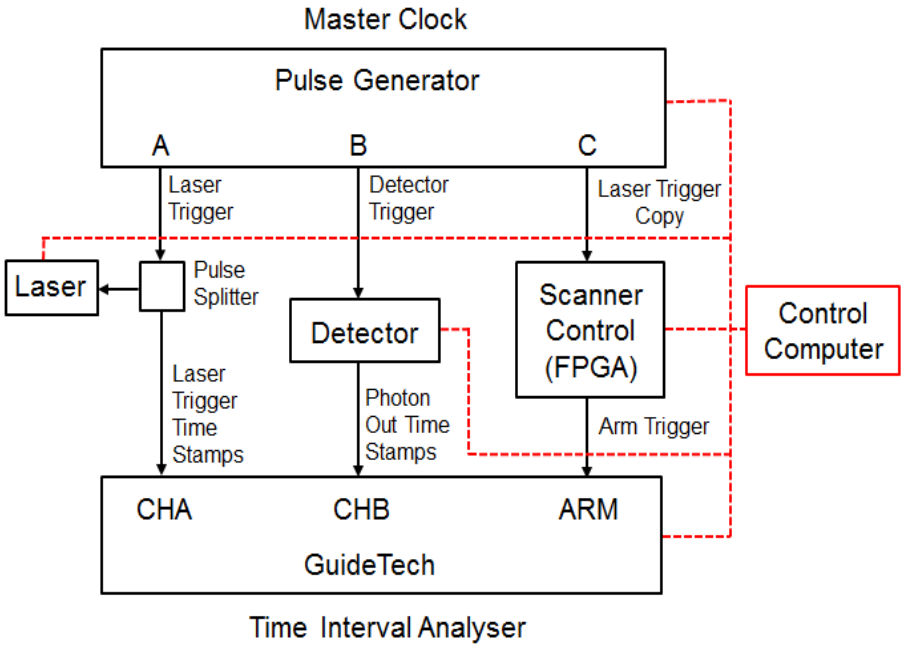

Figure 5.2. Schematic diagram showing a timing scheme used to acquire data with a single-element SPAD operating in a scanning mono-static configuration.

The laser trigger signal was split into two by a power splitter and used to initiate the scanner FPGA, sending TTL pulses to the servo drivers of the scanning mirrors set by a control software. The event timing analyser – GuideTech – was used to continuously

time-stamp two events: laser trigger pulses and photon events recorded by the detector. Similarly to the bi-static arrangement described in Chapter 4, the FPGA was set up to trigger scanning mirrors after clocking a certain number of laser trigger pulses and released a TTL pulse after a scanning mirror moved. This pulse initiated an arm input of the GuideTech which started acquiring time tags from channel A and channel B. During the time-tag acquisition the GuideTech was synchronised to an internal 50 MHz time base. After each scan point, the time counting process was re-set to a common starting reference at the time-interval analyser.

The delay generator was used to adjust the delay between the SPAD gate trigger pulse with respect to the laser/scanner trigger pulse such that, depending on the range at which the target was located in respect to the optical system, photon returns from the target were collected approximately in the centre of the SPAD gate.

The acquisition time at the GuideTech was adjusted by setting a number of laser trigger time tags acquired by channel A. The maximum number of tags that could be collected by the GuideTech was one million, which, at a laser operation of 125 kHz limited the acquisition time to approximately 8 s per pixel. The time tags were collected with 80 ps temporal resolution which was set by the intrinsic limitations of the time interval analyser.

The data acquisition process was controlled by software in the following sequence:

- Laser trigger is enabled, pulses are emitted and travel towards a target, the return photons are collected by the telescope and recorded by the SPAD detector;
- The FPGA clocks in “copy of laser trigger” pulses (see Figure 5.2) and uses them as a base for setting the acquisition time;
- GuideTech software starts, this includes configuring and initialising the electronics board;
- Scanner control software starts which moves scanning mirrors according to a user-defined and specified in a script voltage;
- After clocking a certain number of laser trigger pulses, approximately equal to the acquisition time, the FPGA releases a TTL pulse which initialises the GuideTech arm input;

- GuideTech initialises channel read-out operations, arrays for storing time-tags and starts time-tag acquisition for channel A (laser trigger pulses) and channel B (photon events recorded by the SPAD) and stops when the initialised array is full;
- The acquisition time set on the scanner control software is required to be about 25 % longer than the time-tag acquisition time to allow enough time for the data to be stored and saved;
- After the data from the first pixel is stored the GuideTech resets and "waits" for the next pulse from the FPGA to arrive (which signifies that the scanning mirrors have moved to the next position) and the process repeats until the scanning mirrors cover the $FoV_{Scanner}$.

The scanner control applies voltage to the mirror *x* and *y* in a sequence which follows a user defined script. After a mirror moves, a pulse is released which activates the arm input of the GuideTech collecting time-tags from channel A and channel B. Time tags from channel A are marked with a marker "0" (laser trigger time stamps) while tags from channel B are marked with a marker "1" (photon event time stamps). The time tags from both channels are then sorted with respect to the time and combined into one row with the corresponding markers in another row; data representative of each scan point is separated by a marker "2" and appended to the previous data in a text file. Table 5.1 shows an example of a text file for two scan points (the data has been altered for the purpose of illustrating the principle); the first column shows a series of time stamps and the second column shows a marker for each of the time stamp. The first marker "2" indicates that a mirror moved into the correct location and that the data acquisition has started. Each subsequent "2" marker separates a set of data collected for different scan points.

A three-dimensional map of a target is generated in the following steps:

- LabVIEW software extracts a set of data corresponding to each scan point and calculates the ToF for each detected photon by subtracting the photon arrival time from the time of previous laser pulse trigger;
- A histogram of ToF for each detected photon is generated for every scan point;
- Each histogram is analysed using the peak finding method. The peak finder finds a peak in a histogram based on the least-squares fitting which minimises the square of the error between the experimental data points and the values calculated from the

fitting function (see section 4.13.1.1). Typically, a quadratic polynomial is fitted into a set of data allowing locations of peaks to be identified [5].

- The software calculates a timing location for each peak from which the range information is calculated;
- The data is collected in a text file where the *x* and *y* coordinate of the scan point for each identified peak is listed with the maximum number of photon counts present in a peak and a range to the target corresponding to each peak;
- This data is then used as an input file for a MatLab code which produces a three-dimensional scatterplot [1].

Time [s]	Marker	
0.00000412171754785	2.00000000000000000	Scan point 1
0.00001212171754785	0.00000000000000000	
0.00002012180118410	0.00000000000000000	
0.00002349884804623	0.00000000000000000	
0.00002812188380046	1.00000000000000000	
0.00003612188380046	0.00000000000000000	
0.00004412188380046	0.00000000000000000	
0.00004741115479302	0.00000000000000000	
0.00005212205071600	1.00000000000000000	
0.00006012205071600	0.00000000000000000	
0.00006812205071600	0.00000000000000000	
0.00007146357821780	0.00000000000000000	
0.00007612221709644	1.00000000000000000	
0.00000787460754260	0.00000000000000000	Scan point 2
0.00001116393289812	2.00000000000000000	
0.00001587469965596	0.00000000000000000	
0.00002387469965596	1.00000000000000000	
0.00003187469965596	0.00000000000000000	
0.00003516930739789	0.00000000000000000	
0.00003987488476104	0.00000000000000000	
0.00004787488476104	1.00000000000000000	
0.00005587488476104	0.00000000000000000	
0.00005916537998264	0.00000000000000000	
0.00006387506991694	0.00000000000000000	
0.00007187506991694	1.00000000000000000	
0.00007987506991694	0.00000000000000000	
.	.	
.	.	
.	.	
0.00000785702068976	2.00000000000000000	Scan point n
0.00001114537998264	0.00000000000000000	
0.00001585702068976	1.00000000000000000	
0.00002385711290097	0.00000000000000000	
0.00003185711290097	0.00000000000000000	
0.00003515921461397	0.00000000000000000	
0.00003985711290097	1.00000000000000000	
0.00004785729910990	0.00000000000000000	
0.00005585729910990	0.00000000000000000	
0.00005915243783437	0.00000000000000000	
0.00006385729910990	1.00000000000000000	
0.00007185739078237	0.00000000000000000	
0.00007985748189625	0.00000000000000000	

Table 5.1. A set of example data acquired by the system with time stamps in the first column and markers in the second row. Marker "2" indicates the movement of a scanning mirror to the position defined by a script, marker "0" indicates laser pulse trigger and marker "1" indicates a photon event.

5.4 Transmitter

The transmitter was designed to operate in a mono-static mode where both, the transmitter and the receiver have a common optical axis. As illustrated in Figure 5.3, when a single-element detector is used in the mono-static configuration, the $FoV_{Scanner}$ is sequentially illuminated by the transmitter of divergence ~ 2.5 times larger than the FoV_{Pixel} which is 104 µrad (1/e) and 40 µrad respectively. The backscatter from internal components is mitigated using electrical gating of the SPAD detector (see section 5.5 for details).

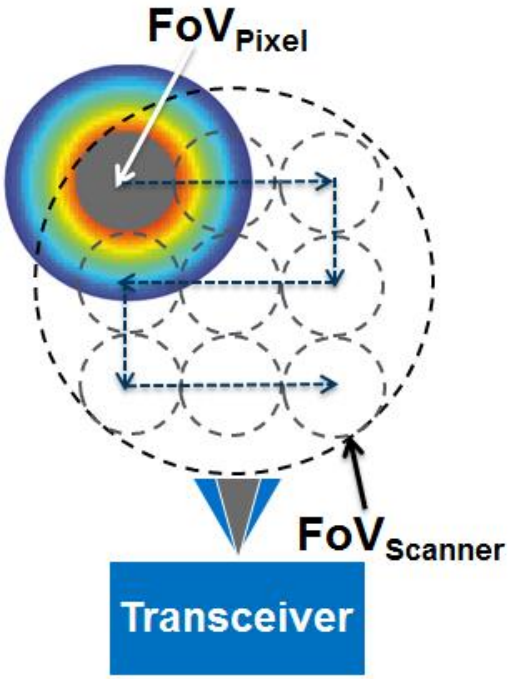

Figure 5.3. Illustration of transmitter and receiver FoV when the system operates in a scanned mono-static configuration. Scanning mirrors were programmed to scan the FoV in a stop-and stare mode using a bi-lateral pattern

As illustrated in Figure 5.3, the stop-and-stare approach, described in section 4.4 is applied.

5.4.1 Transmitter Design

A schematic diagram of the mono-static transmitter setup is shown in Figure 5.4. A laser fibre output was mechanically combined with a collimating lens via a SMA connector. A 3× beam expander used in reverse was then mounted along the path of the beam and the distance between the two lenses of the expander was adjusted to provide the beam divergence of 104 µrad.

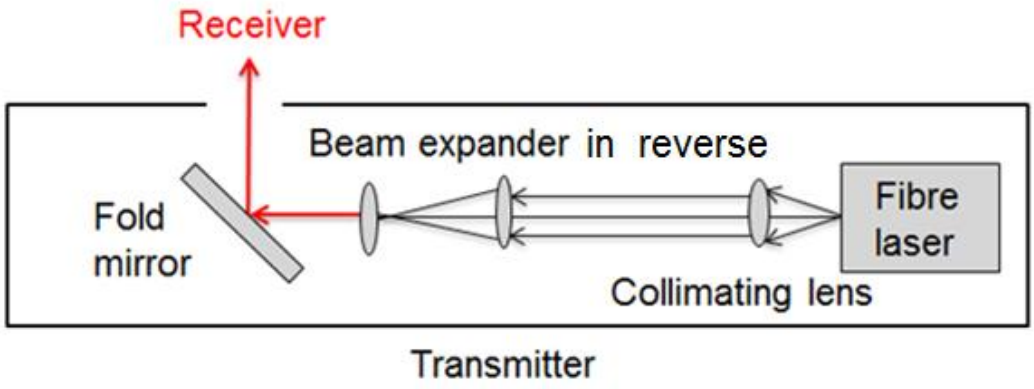

Figure 5.4. Schematic diagram of the mono-static transmitter designed to operate in a scanning system that incorporated a single-element SPAD detector.

In this experiment, an off-the-shelf collimation package with a lens of focal length f = 15.58 mm was combined with an SMA-28 fibre of mode field diameter D = 10.5 µm at 1550 nm providing the 1/e divergence angle, $\theta° \approx 0.022°$ (3.9×10^{-4} rad) with the output beam diameter of 1.8 mm [2]. The 3× beam expander used in reverse de-magnified the beam to a 0.6 mm diameter (which fitted in between the edge of the annular mirror and the telescope obstruction) and increased the beam divergence to $\theta° \approx 0.066$ ° (1.7×10^{-3} rad). After travelling through the receiver optics the beam diameter increased by the system magnification, M = 11.28. Thus, at the output of the telescope the beam divergence was $\theta°_{Output} \approx 0.006$ ° (104 µrad) 1/e.

Ideally, the beam divergence at the intensity of 1/e is required to be slightly larger than the FoV_{Pixel} (40 µrad). The divergence of a collimator is a trade-off between its divergence and the beam diameter. Achieving low divergence with a small beam diameter that could fit between the edge of the annular mirror and the telescope central obstruction with a fixed magnification of the telescope-eyepiece pair meant that the lowest possible divergence with off-the-shelf components is 104 µrad.

5.4.2 Transmitter Divergence Measurement

The mono-static transmitter divergence measurement was performed based on the same principle as described in section 4.5. The divergence of the transmitter was measured to be 110 µrad (1/e diameter) which is close to the required 104 µrad.

5.5 Backscatter Mitigation

When the transmitted beam propagates through optics along the receiver path it causes back-reflections which are then focused onto the detector. The back-reflected signal, if not properly attenuated, can damage the detector or interfere with the signal from a target.

To eliminate back-reflections from optical components the detector was set up to operate in a gated mode where an electrical signal switched the SPAD above the avalanche breakdown voltage at pre-programmed intervals for time durations between 1 - 1000 ns. In this case the signal could only be detected if it arrived within the gate window (see Figure 5.5).

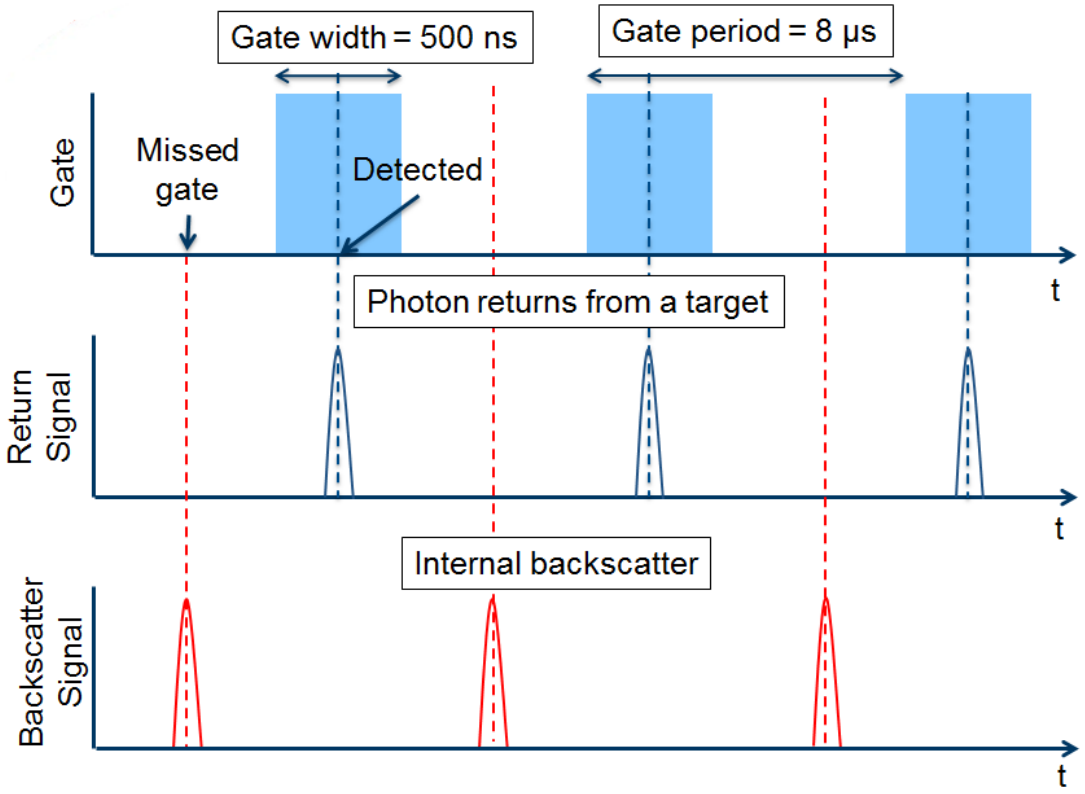

Figure 5.5. Timing diagram illustrating backscatter mitigation.

A delay between the laser trigger pulse and the SPAD gate trigger was chosen (between 1 ns – 8 µs) depending on the range to the target which ensured that the return signal arrived within the gate. The signal from internal back-reflections reaches the detector much earlier (tens of nanoseconds round-trip) compared to the return from a long-range target (thousands of nanoseconds) and therefore typically arrives at the detector during the hold-off time and is not detected.

When the delay between the laser pulse and the SPAD gate trigger is 0 s (no delay) then the attenuated backscatter signal from optical components can be detected. A histogram of backscatter acquired with scanning mirrors positioned on-axis is shown in Figure 5.6. There are eight peaks that can be resolved; each representing a reflection from a specific optical component in the transceiver. The time difference between the first and the last peak is ~ 20 ns which correspond to approximately 6 m round-trip distance between some of the components in the telescope and the annular mirror located closest to the detector. The last peak has the highest magnitude and probably results from the back-reflection from the corrective plate of the telescope.

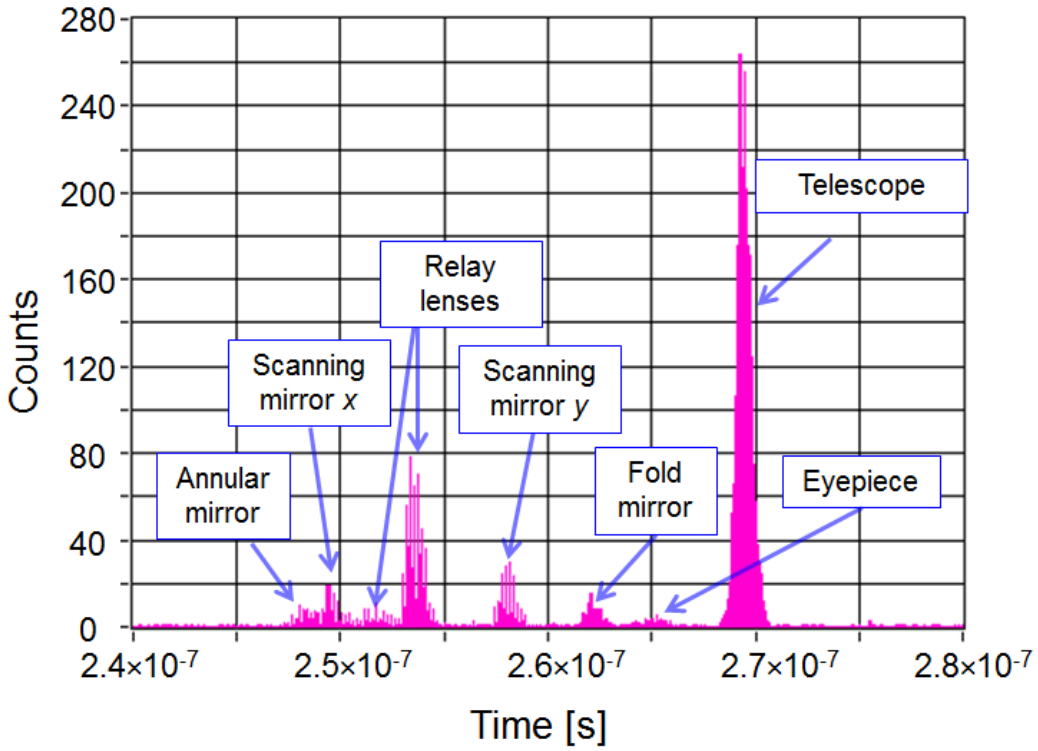

Figure 5.6. Histogram showing multiple peaks resulted from the signal back-reflections from internal components.

The backscatter will appear periodically at the frequency of 8 µs (gate and laser repetition period); if an object of interest happens to be positioned at a range equivalent to a multiplication of 8 µs (1.2 km, 2.4 km, 3.6 km, etc.) then the backscatter signal will coincide with the return from the target. Temporarily changing the laser repetition and gate trigger rate can solve this issue.

5.6 Target Locations

The system was sited in a laboratory which provided access to an urban and countryside environment with a range of up to 10.5 km and varying altitude along the line sight.

Figure 5.7 shows locations of targets used in the alignment and experiments as well as the location of Selex ES where the transceiver was located. The map was taken from Google Maps [3] from which approximate distances to the target locations were identified. Some of the main targets and experimental sites included: a clock tower (~ 800 m), Stewart Melville College (~ 3 km), Craiglockhart Hill (~ 5.6 km), a pylon (~ 6.8 km) and Ski Slope (~ 9.4 km).

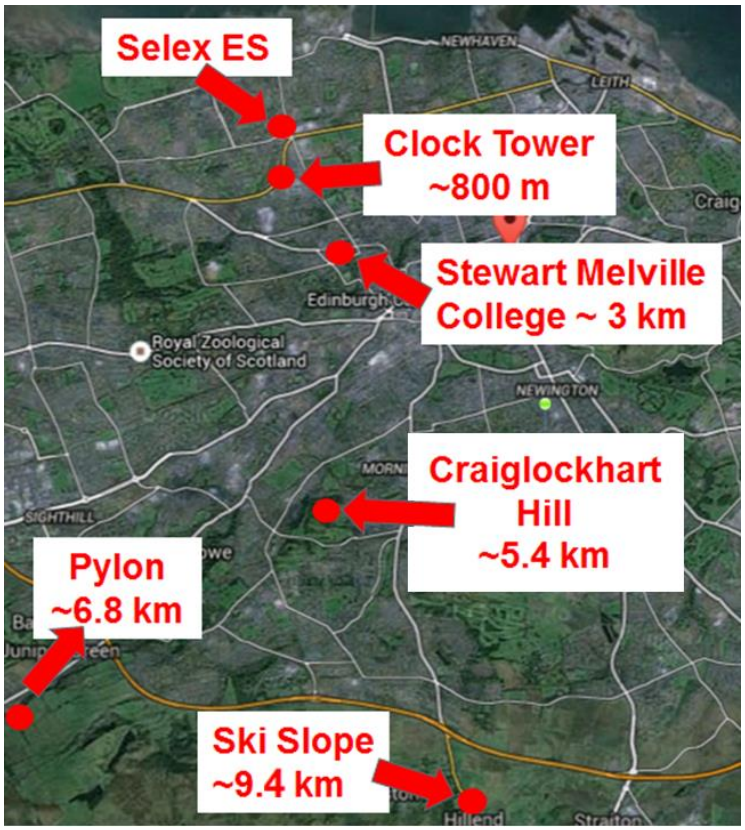

Figure 5.7. Map of Edinburgh showing locations of targets in comparison to Selex ES where the transceiver was located.

5.7 Transceiver Bore-Sighting Procedure

Initially the Xenics camera was placed in the detector plane of the lens L(b) shown in Figure 5.8 and focused on the Ski Slope at ~ 9.4 km. The system was then pointed at the parabolic mirror and the laser beam coming out of the transmitter was injected into the system through the annular mirror about 2 mm off-axis and propagated parallel to the optical axis. The beam was emitted from the telescope and was directed onto the parabolic mirror; the mechanical centre of the mirror coincided with the optical axis of the system. The tip and tilt of the mirror were adjusted such that the laser beam focused at its focal plane and the zonal radius. A fibre mount was then placed in that location, which acted as an on-axis infinite point source.

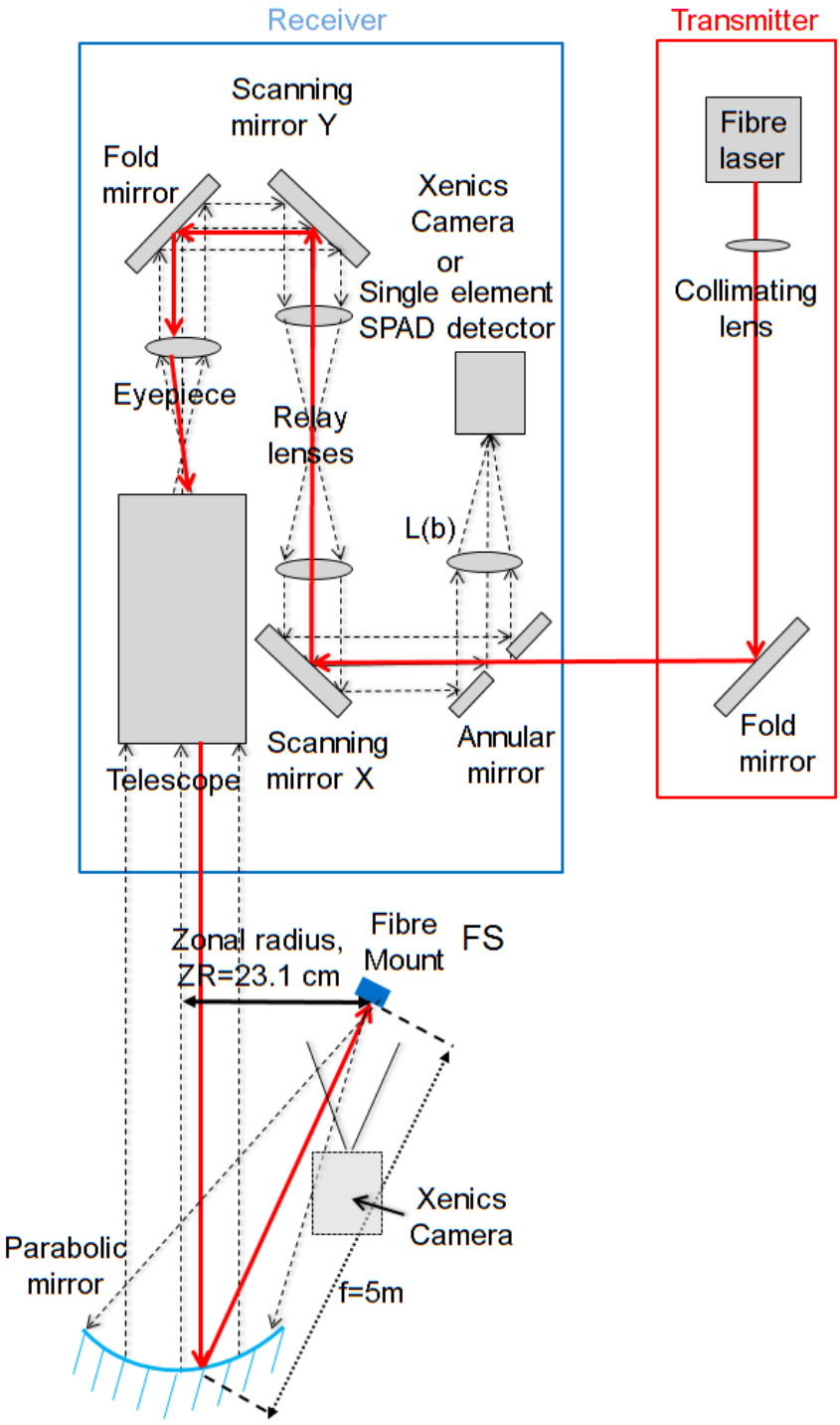

Figure 5.8. Optical setup used for the bore-sighting of the transmitter and the receiver.

The position of the Xenics camera was marked with a series of lens tubes secured to the breadboard and removed from the system. The SPAD detector was then inserted into the system and secured to the tubes of a matching tube thread size – at this point its position was approximately correct to collect the signal from the fibre source. The FoV of the system was scanned in order to determine the position of the image of the fibre on the detector plane. The detector's *x*, *y* position and defocus were adjusted until the image was focused to the size of the detector pixel and positioned at the centre of the

scan, i.e. the optical axis of the system. Figure 5.9 shows a series of intensity images generated during the SPAD alignment procedure with the final position shown in Figure 5.9(d) illustrating the spot focused to one pixel at the centre of the scan.

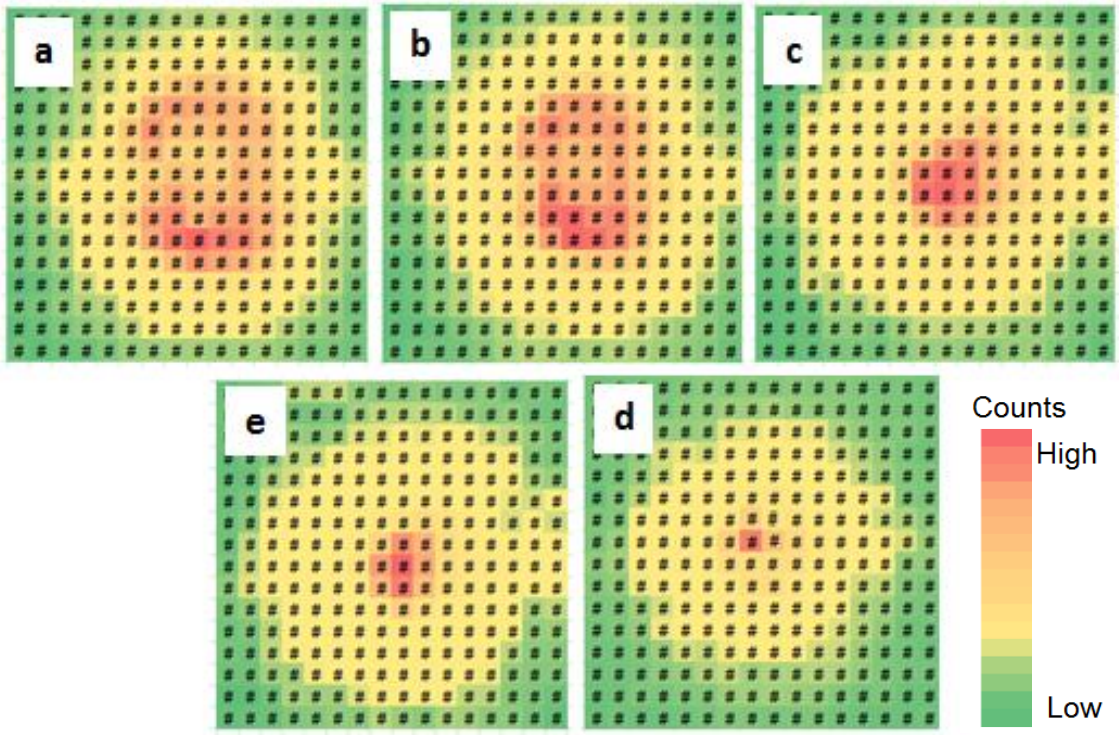

Figure 5.9. Intensity images of 16 × 16 pixels of the fibre source (FS) located in the focal point and the zonal radius of the parabolic mirror acquired with a single-element scanning SPAD. The colour scale is linear.

Once the position of the SPAD was adjusted to an on-axis infinite point source, the laser transmitter was bore-sighted with the SPAD. This involved an adjustment of the transmitter's fold mirror until the position of the transmitter's beam overlapped with the position of the fibre source imaged on the Xenics camera. To accomplish this the FS fibre source was switched on and an area of ~ 5 × 4 pixels, indicating the position of the fibre core on the FS plane, was marked on an image (region A in Figure 5.10) produced by the Xenics camera placed in front of it. Then, the fibre source was switched off and the transmitter was switched on, the fold mirror was adjusted, producing an overlap between the focal spot of the transmitted beam on the pixel indicating the approximate position of the fibre core. The centre of the FoV of the CCD camera was then bore-sighted to the same point source.

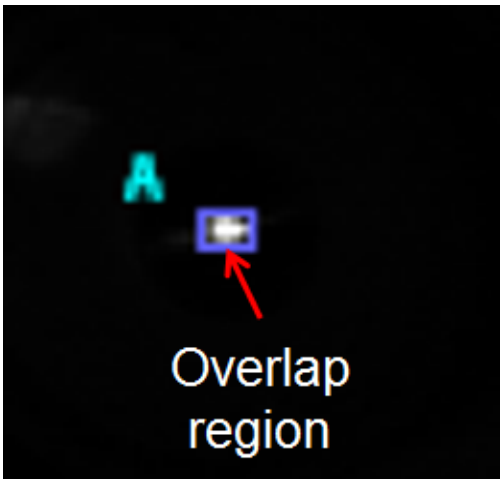

Figure 5.10. Xenics camera image illustrating an overlap between the beam from the transmitter and the beam from the fibre source within an area of ~ 5 × 4 pixels.

Following the laboratory-based alignment the alignment was experimentally confirmed by using the corner cube retro-reflector over a range of 9.4 km which, according to the optical design, provides diffraction limited depth of field of approximately 5.2 km to 33 km (see section 3.10). In this case the position of the detector focal position required a minor adjustment in order to focus the laser beam to approximately one pixel, where the pixel size represented the image of the detector projected onto the object plane, which was smaller than the corner cube diameter at 9.4 km. A riflescope was then bore-sighted to the position of the corner cube.

5.8 Experimental results

Measurements were taken in varying weather conditions and different times of the day over ranges discussed in section 5.6. The SPAD detector was operated in a "low noise" mode (described in section 4.13) with detection efficiency of ~ 30 %, 3 V excess bias, 20 μs hold-off time, 125 kHz external trigger and temperature of 265 K. The gate width applied to the detector varied between 100 ns and 500 ns which corresponds to image depth of 15 m and 75 m respectively.

5.8.1 Instrumental Response Function

The instrumental response function of the system measured with a corner cube located at Craiglockhart Hill is shown Figure 5.11. The FWHM is equal to 0.85 ns which is equivalent to the depth resolution of 12.7 cm. Similarly to the bi-static setup, the shape

of the response function is a convolution of the laser pulse width, timing response of the electronics and the SPAD detector.

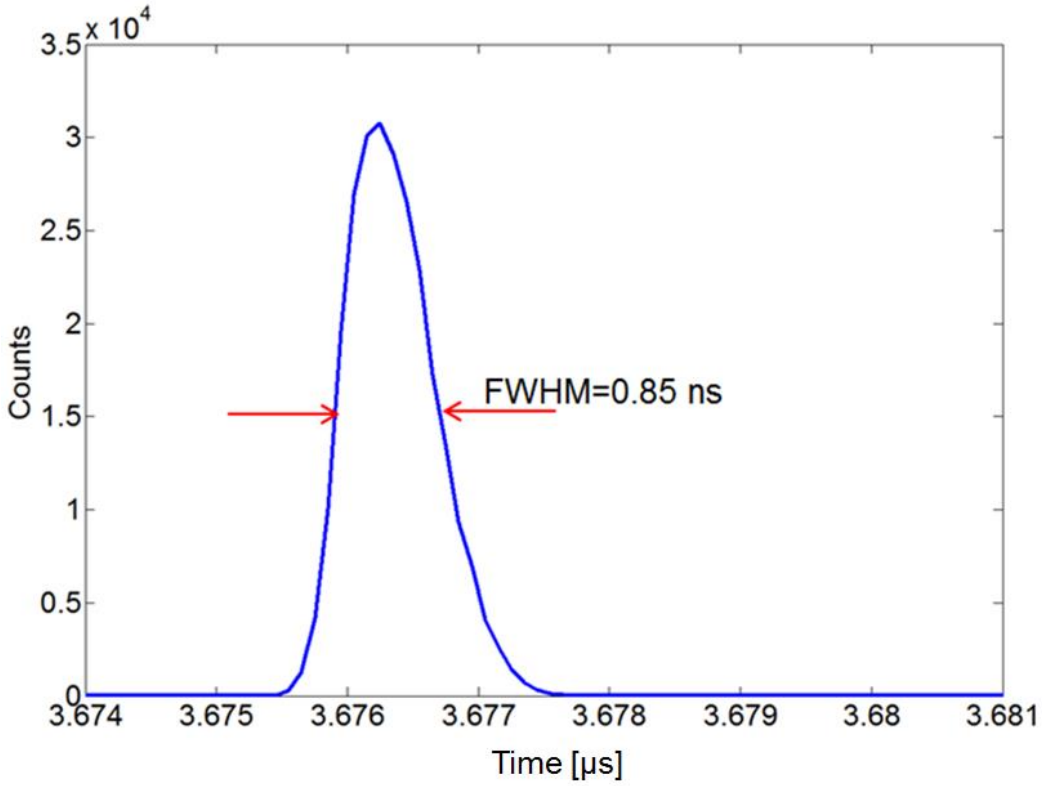

Figure 5.11. Instrumental response function of the mono-static single-element detector configuration.

5.8.2 Peak Identification Methods

In Chapter 4 the only method used to identify a peak in a histogram and the associated temporal position was the peak finder based on least-squares fit to the raw data. In this chapter, a more sophisticated method is also used which involves cross-correlation between the data and the normalised instrumental response function.

5.8.2.1 Cross-Correlation Technique

A cross-correlation with an instrumental response of a system is a technique which discriminates random noise spikes by comparing shapes of the histogram generated from raw data to an instrumental response function of the system which acts as a reference. This technique allows a system to operate at higher background noise levels (both system induced and solar) or with lower number of photon returns from a target.

Cross-correlation is a measure of correlation between two periodic signals [4]. For two discrete signals $u(t)$ and $v(t)$ the cross-correlation $w(t)$ is defined as

$$w(t) = u(t) \otimes v(t) = \sum_{i=-\infty}^{\infty} u^*[i]v[i+t] \qquad \textit{Eq. 5.1}$$

where symbol $\otimes$ denotes correlation and * denotes complex conjugate [5].

By calculating a cross-correlation between the signal and the normalised instrumental response of the system it is possible to discriminate against random noise peaks and to amplify the probability of finding a target signal return [6]. The technique is used to detect the presence of a waveform of known structure, i.e. instrumental response function that contains additive noise.

According to the cross-correlation theorem, by multiplying the Fourier transform of one function by the complex conjugate of the Fourier transform of the other function, a Fourier transform of their correlation can be calculated [7] [8].

$$u(t) \otimes v(t) = F^{-1}[F\{u(t)\} \times F^*\{v(t)\}] \qquad \textit{Eq. 5.2}$$

Calculating cross-correlation between two waveforms is typically faster when calculated in frequency domain [9]. For results discussed in this thesis cross correlation is calculated in LabVIEW using Eq. 5.2.

5.8.2.2 Depth Profile Retrieval

During a depth measurement, the detected photon returns were time-tagged by the TCSPC module and transferred to the control computer where software generated a histogram of photon returns for each scanned pixel. These histograms were produced for raw data or for data cross-correlated with an instrumental response function (see section 5.8.2.1) and the least-squares peak finding method was applied to both raw and cross-correlated data to identify the peak location using a method described in section 4.13.1.1.

The algorithm calculated the time-of-flight, *t*, corresponding to the identified peak. This value was then used to calculate the range, *R*, to the target. There are multiple pulses in transit and therefore establishing the absolute range was not possible without prior information about the target range. In this case the expected range information was extracted from Google Maps which was then used to estimate the number of gates prior to the gate in which a return from a target is expected (see section 4.13.1.1).

The absolute range for data cross-correlated with the instrumental response function was calculated from

$$R = \frac{[mp + (t - t_{IRF})c]}{2} \qquad \textit{Eq. 5.3}$$

where m is the number of gates prior to the gate in which the signal is expected to be detected, p is the gate period which is equal to 8 µs, t is the time-of-flight to the target corresponding to the peak produced by cross-correlating raw data with the instrumental response function and t_{IRF} is the peak location of the instrumental response function and c is the speed of light.

5.8.3 Surface-to-Surface Depth Resolution Test

A surface-to-surface depth resolution test was conducted over a range of 9.4 km (Ski Slope target location) to determine the closest distance between two surfaces that can be resolved by the system. Two rectangular targets of dimensions 16 cm × 16 cm, covered with an acrylic, white micro-prismatic retro-reflective material were mounted on an optical bench.

Figure 5.12 illustrates the experimental setup of the test as seen from the side. Target 1 was mounted at a height that was lower from the target 2 thus enabling a similar level of photon returns from both targets.

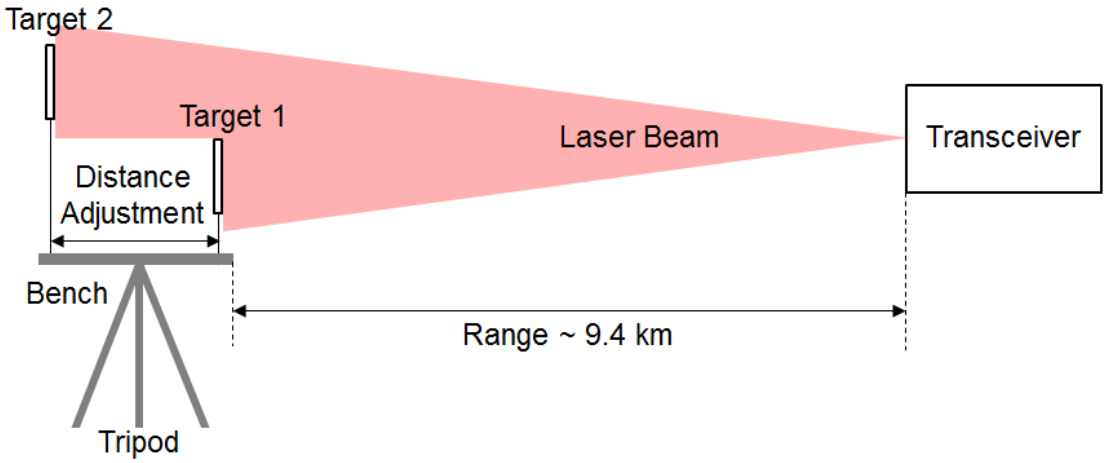

Figure 5.12. Side view of the experimental setup used in the surface-to-surface resolution test.

The distance between the surface of target 1 and target 2 was set between 30 cm and 2 cm with a ruler. The data was collected with a delay between the laser and gate trigger set to 5.41 µs and acquisition time of 0.17 s per scan point. The area of each target was relatively small compared to the range and therefore the region of interest was scanned using 8 × 8 scan steps with a step resolution smaller than the size of the targets in order to detect high level of returns. Out of the 64 recorded data points only

one, representing the highest level of returns received from both targets, was chosen for further analysis.

Two different peak identification methods; a least squares-fit of a polynomial to the raw data (see section 4.13.1.1) and a cross-correlation of the raw data with the IRF (see section 5.8.2.1), were compared.

Figure 5.13(a) and Figure 5.13(b) show histograms of returns from the two targets set 30 cm apart (± 5 mm) produced for raw data and for raw data cross-correlated with the instrumental response respectively. The distance between the two targets was calculated to be 29.7 cm and 29.9 cm using the least-squares peak finder for raw and cross-correlated data respectively. The result shows a discrepancy of 3 mm and 1 mm for the two techniques respectively, which are within the target positioning error. The cross-correlated data is much smoother when compared to the raw data. The elimination of additive noise from the signal during the cross-correlation allows the distance between the targets to be estimated with higher accuracy than in the case of the raw data. The peak level of returns from target 1 is higher than that from the target 2. This is because the target 2 was not fully covered by the transmitted beam.

Figure 5.14(a) and Figure 5.14(b) show histograms of returns from the two targets located 20 cm apart (± 5 mm) produced for raw and cross-correlated data respectively. The measured distance between the two targets is 19.5 cm with the peak finder for raw data and 20.2 cm for cross-correlated data. The result produced using the peak finder for raw data is just within the target positioning error and for cross-correlated data it is well within the target positioning error.

Figure 5.15(a) and Figure 5.15 (b) show histograms of returns from the two targets located 15 cm apart (± 5 mm) produced for raw data and for cross-correlated with the instrumental response respectively. The distance between the targets measured using the peak finder method for the raw data is 14.8 cm and for the cross-correlated data it is 14.9 cm. Again, the cross-correlation shows a higher accuracy of measurement.

Figure 5.16 (a) and Figure 5.16(b) shows histograms of returns from the two targets located 10 cm apart (± 5 mm) produced for raw and cross-correlated data respectively. The distance between the targets measured using the peak finder for raw data is 6.5 cm and for the cross-correlated data it is 8.4 cm. In this case the measurement error for the cross-correlated data is two times smaller than the error produced with the raw data.

Figure 5.17(a) and Figure 5.17(b) shows histograms of returns from the two targets located 5 cm apart (± 5 mm) produced for raw and cross-correlated data respectively. The distance between the targets measured using the peak finder for raw data is 6.7 cm and for the cross-correlated data it is 6.2 cm. Both techniques detect two targets with a significant discrepancy from the real distance. However, the result produced using the cross-correlation is closer to the real distance than the result produced using the raw data.

Figure 5.18 (a) and Figure 5.18(b) shows histograms of returns from the two targets located 2 cm apart (± 5 mm) produced for raw and cross-correlated data respectively. The distance between the targets measured using the peak finder for raw data is unresolved. The result produced using the peak finding for cross-correlation detects two targets located at a distance of 3.5 cm away. There is a significant error in the measurement. However, it is still possible to resolve the two targets.

The lower level of returns shown in Figure 5.17 and Figure 5.18 is caused by poor weather conditions (rain) occurring during data acquisition.

The combined result of the surface-to-surface resolution test for the raw data and for the cross correlation is shown in Figure 5.19.

When the two targets are $\geq$ 25 cm apart the distance between the targets using the raw data and the cross correlated data is comparable. Beyond this region the cross-correlation produces results that are closer to the real distance between the targets. It is also capable of resolving targets that are separated by a distance as short as 2 cm, which is much less than the FWHM of the instrumental response function (~ 15 cm).

Therefore, using the peak finder with raw data cross-correlated with IRF shows a superior ability of resolving targets located at short (centimetre) distance apart compared to the peak finder for raw data only.

A similar type of experiment was conducted for a peak finder technique applied to raw data and was reported in [10] [11].

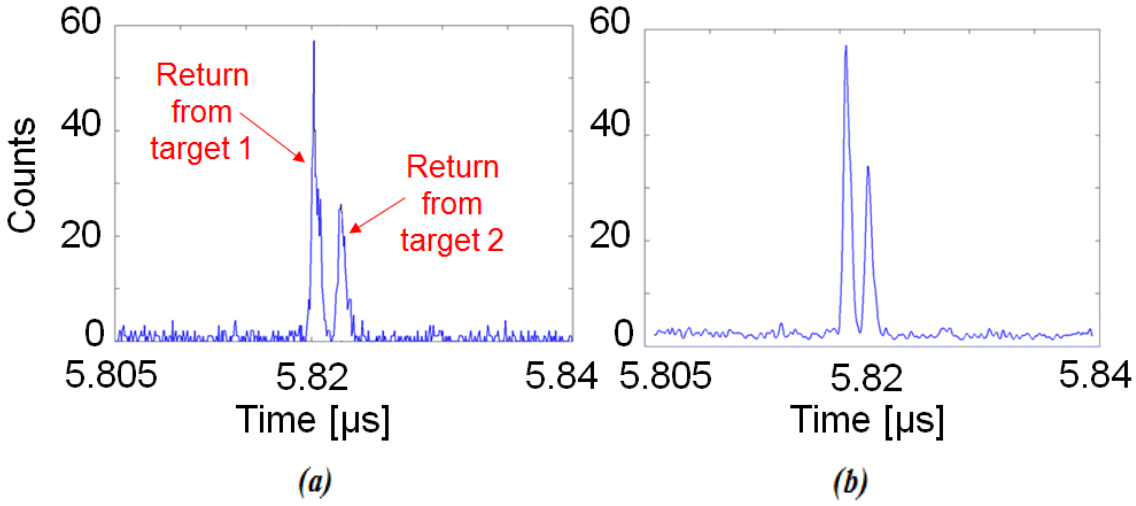

Figure 5.13. Histograms for targets located 30 cm apart generated for (a) raw data, (b) cross-correlation acquired during 0.2 s.

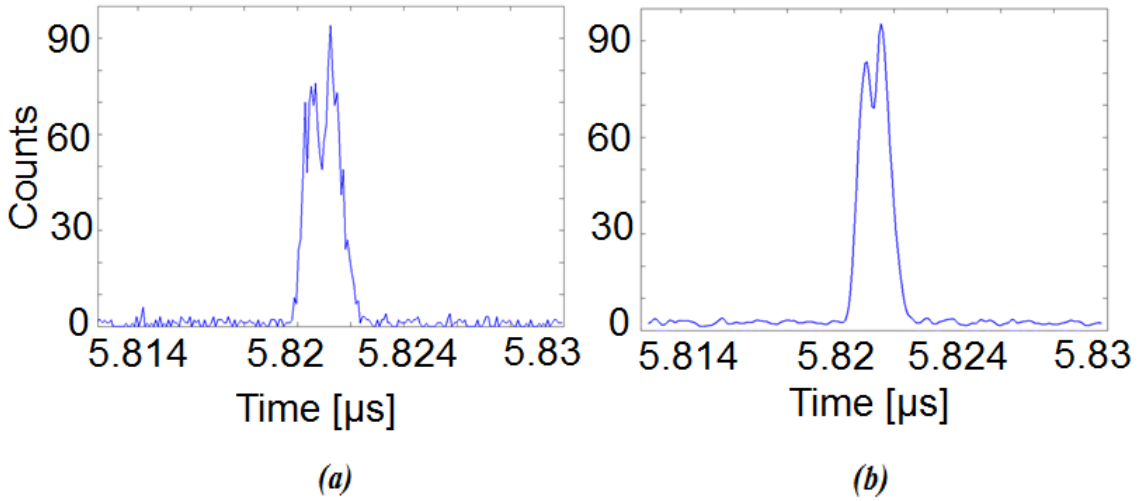

Figure 5.14. Histograms for targets located 20 cm apart generated for (a) raw data, (b) cross-correlation acquired during 0.2 s.

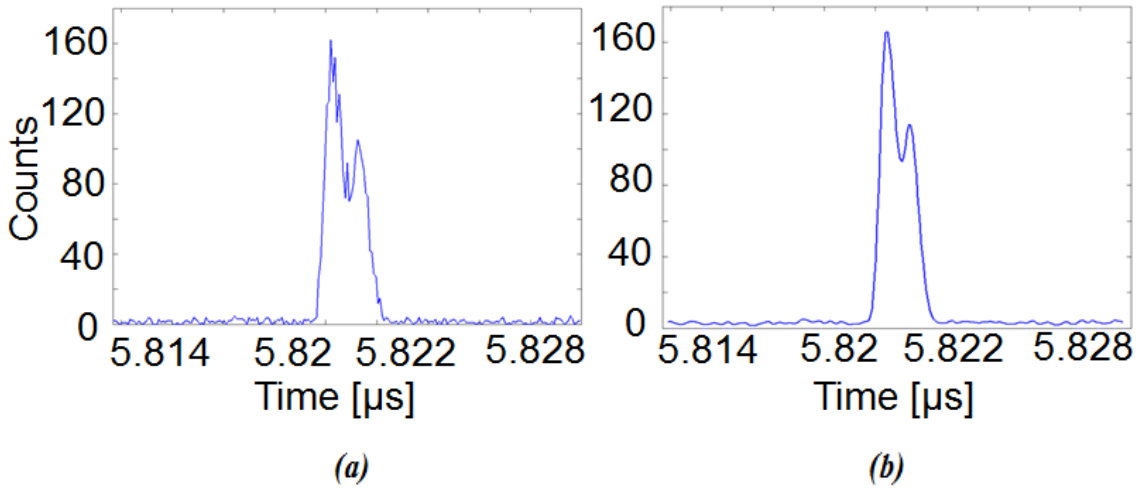

Figure 5.15. Histograms for targets located 15 cm apart generated for (a) raw data, (b) cross-correlation acquired during 0.2 s.

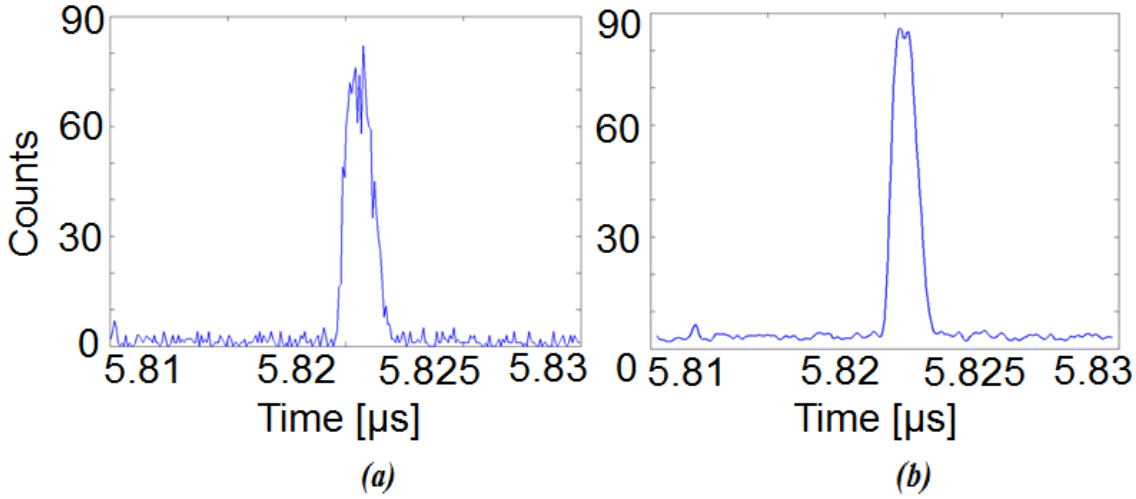

Figure 5.16. Histograms for targets located 10 cm apart generated for (a) raw data, (b) cross-correlation acquired during 0.2 s.

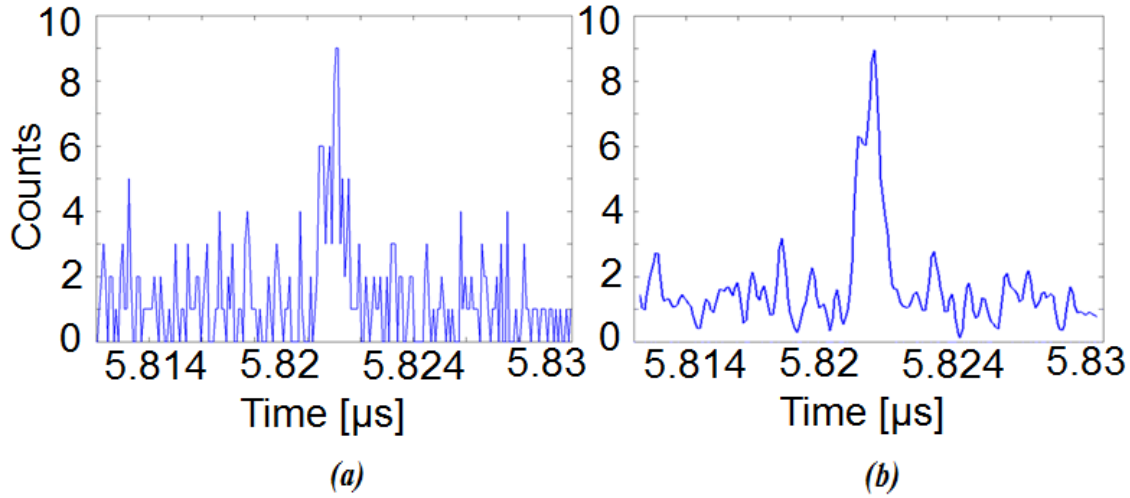

Figure 5.17. Histograms for targets located 5 cm apart generated for (a) raw data, (b) cross-correlation acquired during 0.2 s.

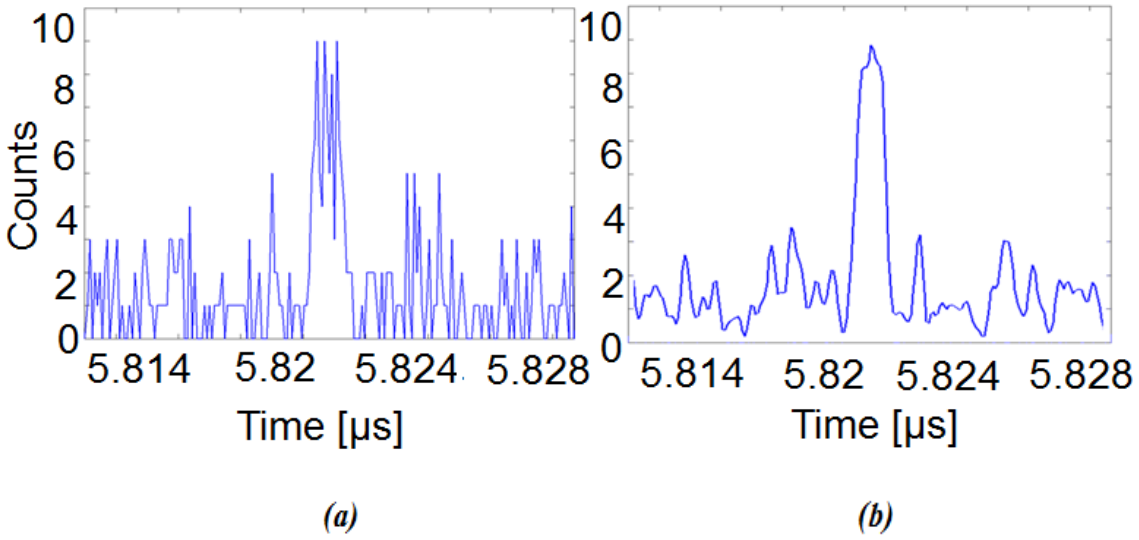

Figure 5.18. Histograms for targets located 2 cm apart generated for (a) raw data, (b) cross-correlation acquired during 0.2 s.

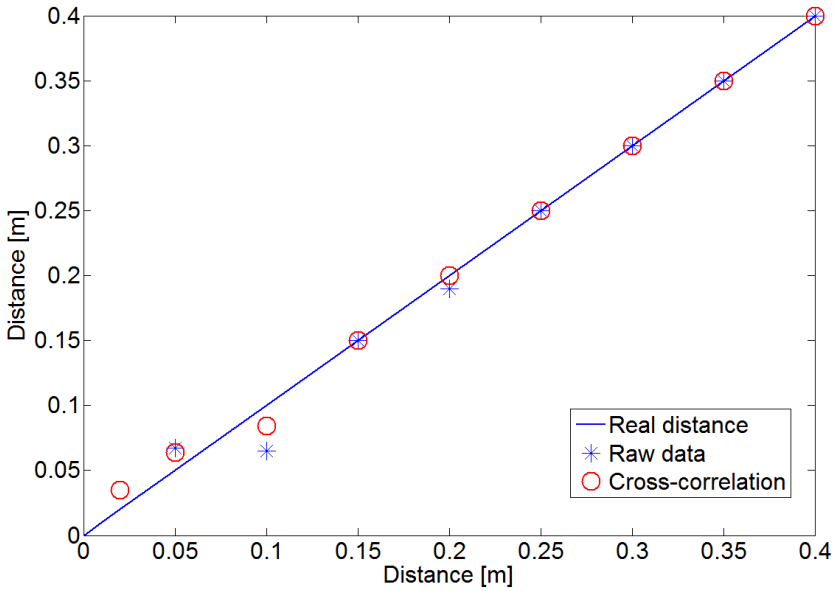

Figure 5.19. Result of the surface-to-surface resolution test conducted over a distance of 9.4 km for distance between two targets varying between 40 cm and 2 cm.

5.8.4 Spatial Resolution Test

A spatial resolution test was conducted with targets mounted on a bench secured on a tripod and located over a range of 9.4 km. The targets were arranged such that their distance was spatially adjustable as shown in Figure 5.20.

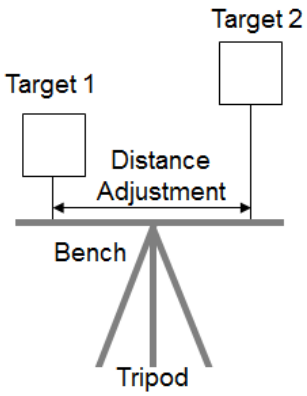

Figure 5.20. Schematic diagram of a setup used in the spatial resolution test.

The FoV was scanned using 34 × 19 scan points where each scan step corresponded to 0.25 × normal scan step, equivalent to approximately 6.5 cm over ~ 9.2 km, with the acquisition time of 0.2 s per pixel. Figure 5.21(a) shows scatterplot of the two targets spatially arranged such that the right edge of target 1 was ~ 40 cm from the left edge of the target 2. The plot resembles the targets in shape and their dimensions indicating the system is capable of spatially resolving the two targets and the distance between them

can be approximately measured. The accuracy of the measurement is determined by the calibration of scanning mirrors.

The number of counts for each target varied across the target surface indicating peak counts from 20 to 40. This variation may result from scintillation effects occurring when the beam is propagated across a long range.

Figure 5.21(b) shows a scatterplot of the targets located ~ 30 cm from each other and demonstrates that the system can spatially resolve the targets. For target distances less than 26 cm, which is approximately equivalent the FoV of the system at 9.4 km, the system is incapable of spatially resolving the targets. The same is true even if the scan step is decreased. Nevertheless, the system demonstrated spatial resolution of ~ 30 cm achieved over a range of 9.2 km as defined in the requirements.

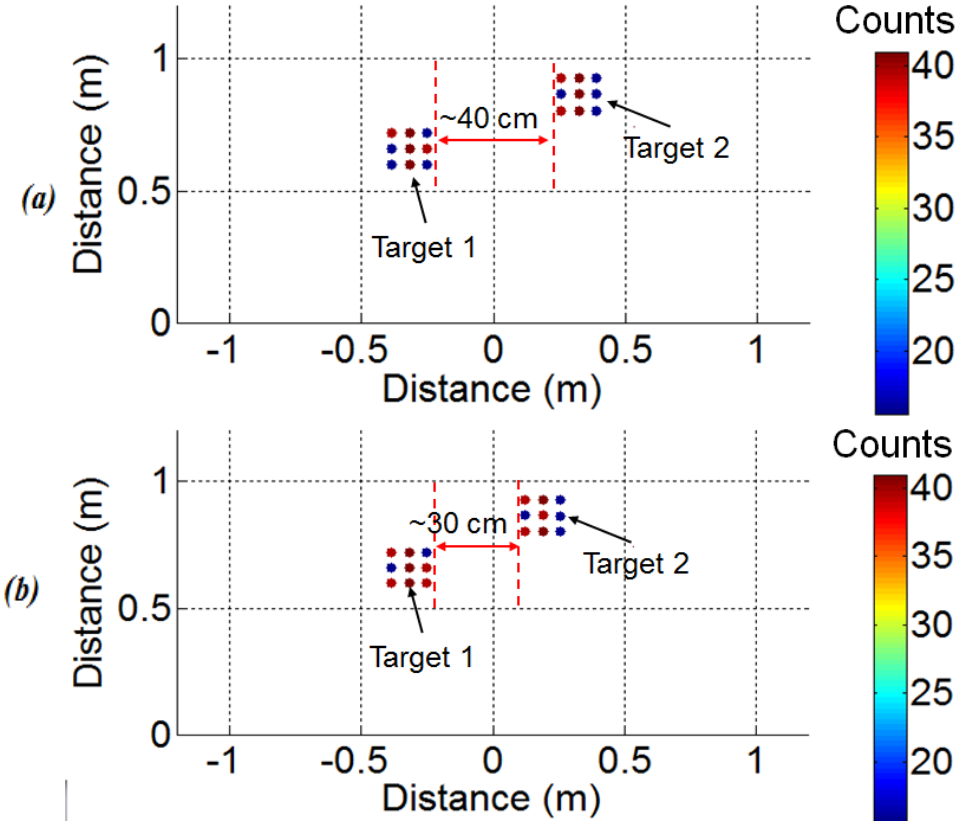

Figure 5.21. Two-dimensional scatterplot of target 1 and target 2 viewed from the front. (a) The right edge of the target 1 is ~ 40 cm away from the left edge of the target 2. (b) The right edge of the target 1 is ~ 30 cm away from the left edge of the target 2.

5.8.5 Limit on the Acquisition Time

This section compares images of an object located over a distance of 800 m using raw data and cross-correlation. The effect of decreasing the acquisition time on the quality

of images is investigated using the two methods. A visible-band image of a clock face used as a target is shown in Figure 5.22.

The object was scanned using 50 × 50 scan steps, each scan step corresponded to 2.3 cm over ~ 800 m. The data was collected with an acquisition time per scan point of 177 ms. The system was operating with a laser power of 10 mW, gate width of 500 ns, hold-off time of 20 μs and the delay between the laser trigger and the detector gate was 5200 ns.

Figure 5.22. Wide FoV, visible-band image of the target.

Scatterplots of the raw data are shown in Figure 5.23. Figure 5.23(a) shows an intensity image of the front view of the target. A high level of returns can be observed from the hands and digits of the clock. Spatial and depth details of the object can be seen in Figure 5.23(b).

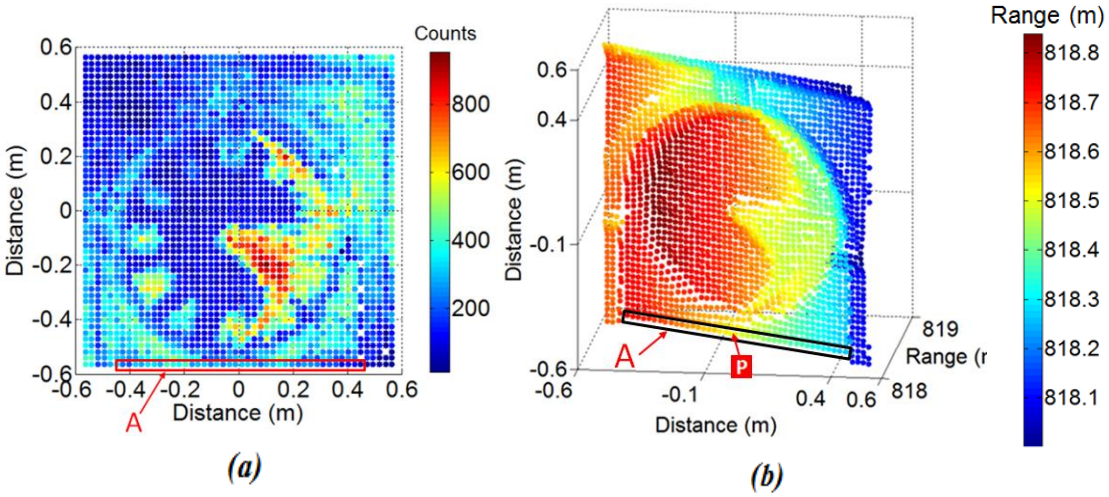

Figure 5.23. Scatterplot of raw data of a clock face acquired with 50 × 50 scan points where in (a) pixel colour represents a peak number of photon counts registered by the detector for each scan point and (b) is a front view of the image. Area A corresponds to a region of 40 pixels chosen for analysis (see section 5.9).

In order to decrease the memory requirement during the data acquisition, instead of saving time-tags for all the detected photons and released laser pulses (as described in section 5.3.1), only the time-of-flight for each photon (calculated from the difference between the detection of a photon and the trigger of a laser pulse that occurred just before the detection of a photon) was saved. Therefore, it was impossible to accurately filter out data corresponding to a fixed acquisition time. To investigate the effect of a reduction of the acquisition time on the image quality, it is assumed that the detected photons were uniformly distributed in time and the number of photon counts was gradually decreased as a proportion of the total number of detected photons, i.e. if the total number of detected photons within 177 ms was 2000, then decreasing the number of detected photons by 10 % corresponds to 17.7 ms acquisition time per pixel.

Figure 5.24 shows depth profile measurements of the target taken with 177 ms acquisition time per pixel and analysed using raw data (column "a") and the correlation with the instrumental response function (column "b"). The image produced with the data analysed using the cross-correlation technique shows smoother surfaces of the clock face and the surrounding wall, straighter lines and sharper edges of details when compared to the image analysed with the raw data. The cross-correlation technique is therefore capable of improving the visual appearance of a depth image analysed using raw data.

Figure 5.24 and Figure 5.25 show the effect of a decrease in acquisition time on depth profile measurements of the target for image processing performed on raw data and using the cross-correlation technique. The images generated using cross-correlation show a higher degree of detail in the image with significantly lower acquisition times than the raw data. For instance, a comparable degree of detail in the clock face is visible for 18 ms for raw data and 0.9 ms for cross-correlation (Figure 5.24(e) and Figure 5.24(f)). Most of the characteristic details of the target are still present in the image when the acquisition time is 10.6 ms per pixel for the raw data and 55 µs for cross-correlation (Figure 5.25(a) and Figure 5.25(b)). For this target, the cross-correlation can decrease the per-pixel acquisition time by a factor of ~ 200. For acquisition times lower than the above values the reliable target resolution decreases significantly and the identification of the target without a prior knowledge of its characteristics becomes affected. The lowest pixel acquisition time possible to provide a sufficient depth and spatial resolution is 55 µs and can be achieved with the cross-correlation technique.

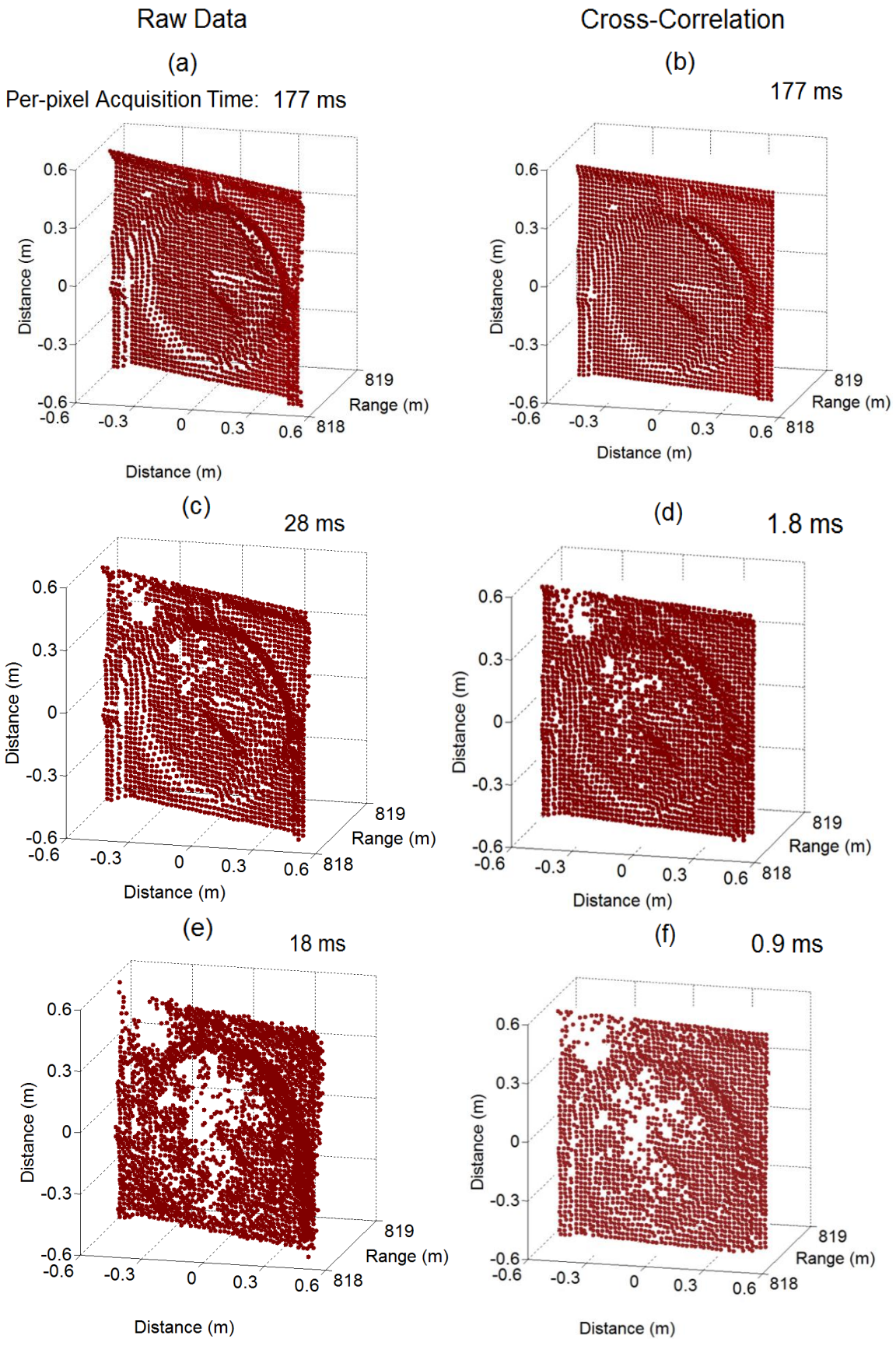

Figure 5.24. Depth profile measurements of a clock face on a tower acquired with 50 × 50 scan steps analysed using raw data (left column) and cross-correlation (right column) for different acquisition times: (a) and (b) 177 ms, (c) 28 ms, (d) 1.8 ms, (e) 18 ms and (f) 0.9 ms.

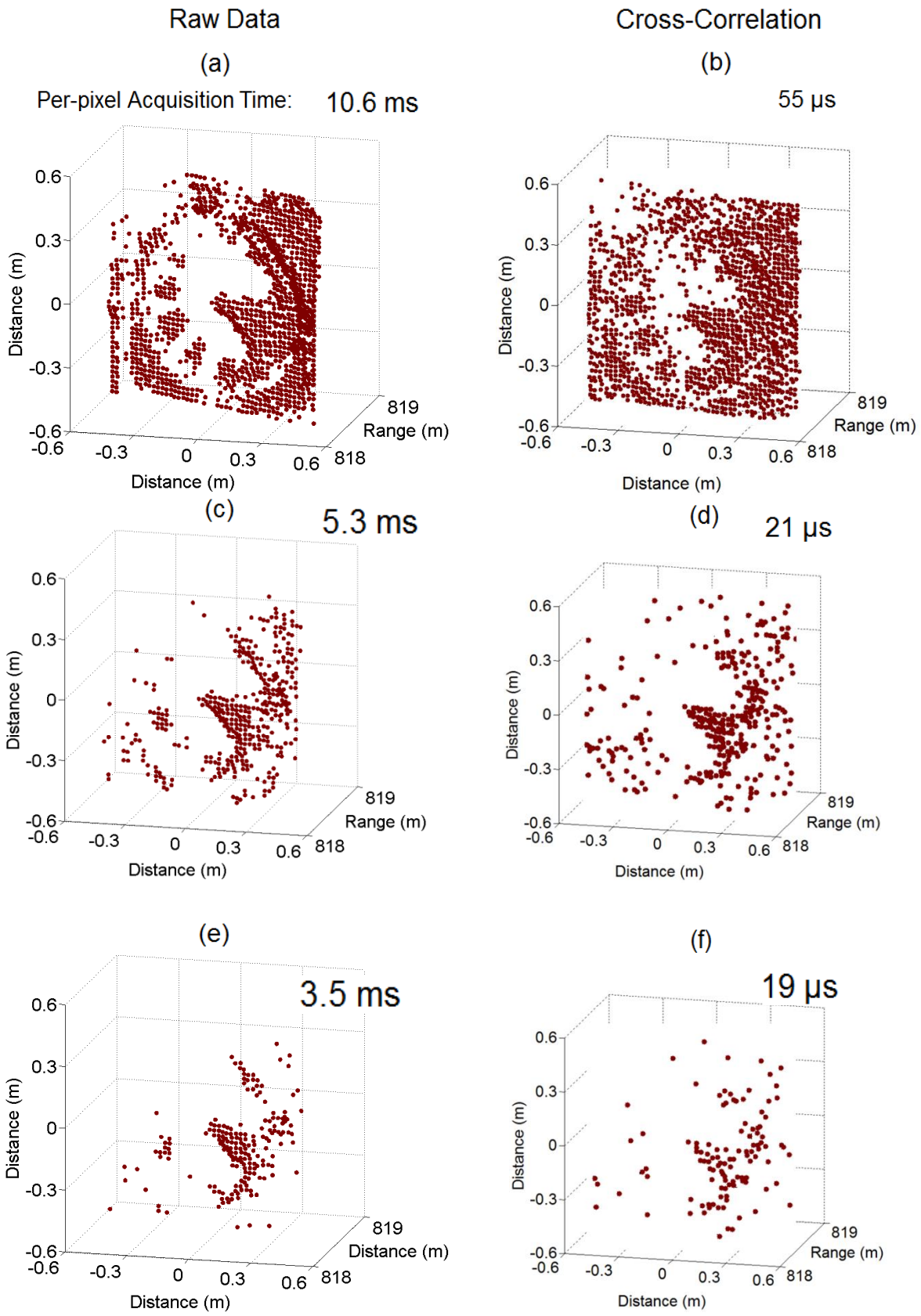

Figure 5.25. Depth profile measurements of a clock face on a tower acquired with 50 × 50 scan steps analysed using raw data (left column) and cross-correlation (right column) for different acquisition times: (a) 10.6 ms (b) 55 µs, (c) 5.3 ms, (d) 21µs, (e) 3.5 ms and (f) 19 ms.

Cross-correlation with the instrumental response function allows the total acquisition time to be decreased to approximately 52 ms per scan compared to 26 s achievable with the raw data. The cross-correlation enabled an order of magnitude decrease in total acquisition time which suggests that a single-element scanned lidar technique may be feasible when used in a deployed lidar operating at ~ 1 km range.

5.8.6 SNR vs. Acquisition Time

Figure 5.26 shows raw data histograms generated for pixel *P* (see Figure 5.23(b)) of the image clock face acquired with acquisition times varying between 177 - 3.5 ms per pixel. For that pixel, below the 3.5 ms acquisition, the signal becomes comparable with the background counts and resolving a peak among the noise becomes increasingly difficult.

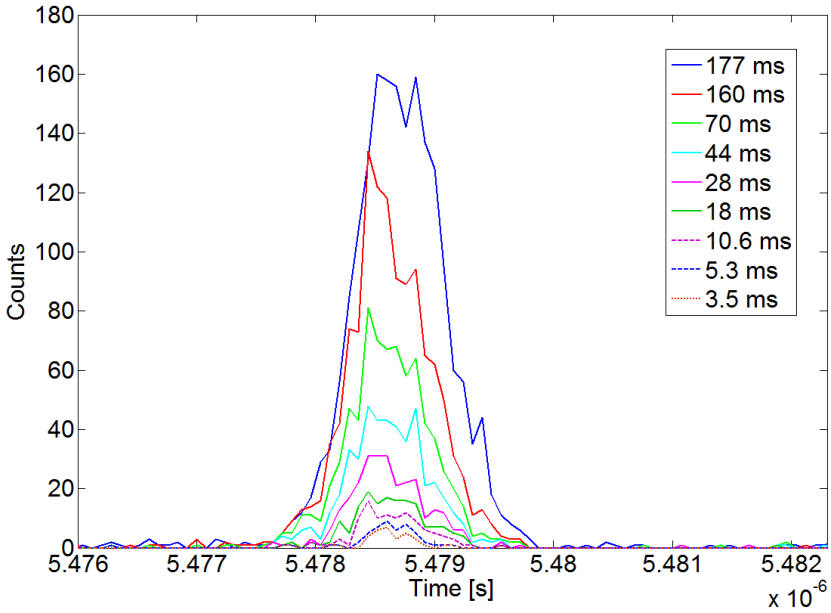

Figure 5.26. Raw data histograms for pixel P (Figure 5.23) of the clock face with per-pixel acquisition times varying between 177 ms to 3.5 ms.

Figure 5.27 shows cross-correlation data histograms generated for the pixel with acquisition times varying between 44 ms to 88 µs. At an acquisition time of 88 µs the peak corresponding to the target is still resolvable amongst the background counts on the histogram.

SNR_E was calculated from Eq. 2.19 for raw data for different acquisition times by integrating under the histogram area. For 177 ms SNR_E was 46. As the acquisition time decreases the background counts and signal counts from the target decrease, however, both background and target returns reduce in proportion to the acquisition time. For an

acquisition time of 70 ms SNR_E = 23 and for 28 ms it decreased to SNR_E = 14 reaching SNR_E = 9 for an acquisition time of 3.5 ms where resolving the peak from the background becomes impossible for raw data analysis. Cross-correlation however, enables peaks to be resolved even at such low SNR_E values.

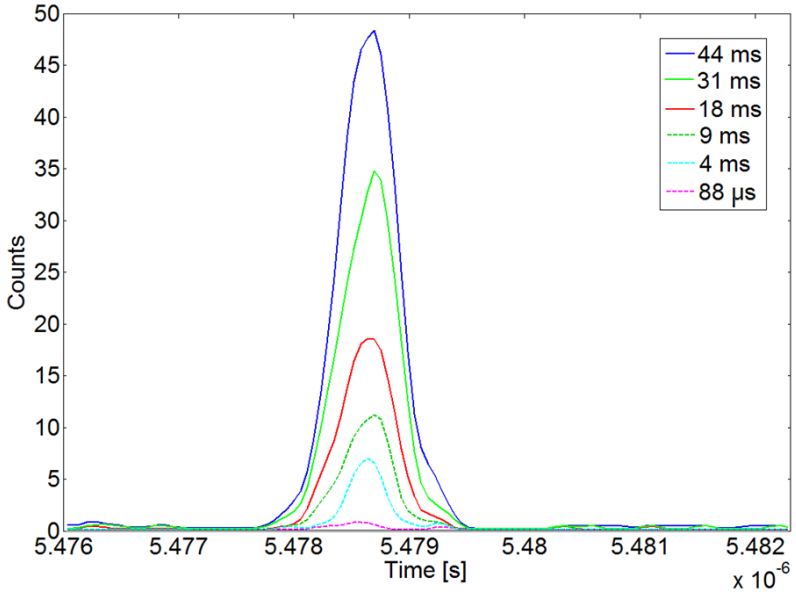

Figure 5.27. Cross-correlation data histograms for pixel P (see Figure 5.23) of the clock face with per-pixel acquisition times varying between 44 ms to 88 µs.

FWHM of return signal peaks was plotted for the same pixel against varying acquisition times for raw data and cross-correlation and is shown in Figure 5.28. It shows that in both cases, as expected, the FWHM is linear across the acquisition time until a point where there are no longer enough photons to recover the signal. The cut-off point occurs at the acquisition time of 177 ms for the raw data and at 31 ms for the cross-correlation. By minimising the noise due to the instrument response the cross-correlation method allows recovery of the peak information with less photons compared to the analysis of the raw data using the peak finder. This can be observed in the example presented in Figure 5.25.

In addition, the FWHM for data analysed using cross-correlation is on average approximately 0.3 ns shorter compared to the raw data. The cross-correlation technique filters out the noise introduced by the system response and thus allows the FWHM to be reduced which improves depth resolution as demonstrated in the surface-to-surface depth resolution test (see section 5.8.3).

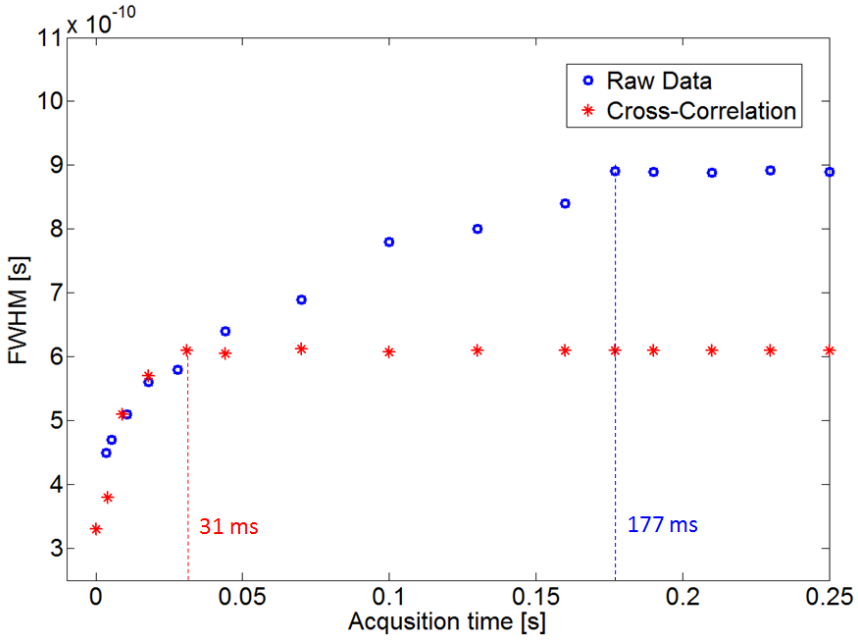

Figure 5.28. FWHM of return signal peaks plotted against varying acquisition times for raw data and cross-correlation.

5.9 Evaluation of Measured vs. Estimated Photon Count Rate

Average photon count rate due to signal under return peaks for 40 pixels located in area *A* of the image of the clock face (see Figure 5.23) was estimated to be 1.67 kc per acquisition time of 177 ms. The chosen area is located at the bottom of the clock face made out of bricks. The exact material type is not known but it is assumed to be sandstone brick based on its common use. Reflectivity of red sandstone at a wavelength of 1550 nm was measured to be approximately 25 % [12].

An estimate attenuation for a Lambertian target, ε_L, of 25 % reflectivity was calculated from Eq. 4.38 and was equal to - 111 dB. The attenuation includes the loss factor for a round trip of the laser beam through the system due to the mono-static setup. For 10 mW laser output power the power returned back onto the detector is approximately 7.9×10^{-14} W. This resulted in CR_{HO} = 8.7 kcps (Eq. 4.10) which is approximately 1.5 kcps within the acquisition window of 177 ms.

The measured number of photon counts within this acquisition time is slightly lower than estimated suggesting that the reflectivity of the material surrounding the clock face may be slightly lower. Nevertheless, the result shows a close match between the estimated and measured count rate.

5.9.1 Imaging of Different Types of Targets

In section 5.8.5 imaging of a limited range depth target (clock face as part of a wall) was presented. In this sub-section additional targets are investigated for their spatial distribution, reflectivity and structured complexity. The type of objects used to demonstrate versatility of the system included:

- Target with complex spatial and temporal features, curves as well as multiple surfaces at an angle (top of a clock tower);
- Extended depth-profile building located over long range (~ 8.8 km);
- Dense target which tests for depth and spatial resolution (a cluster of trees);
- Tower-like structure constructed from thin steel lattice (electricity pylon);
- Extended depth-profile target used to estimate terrain profile;

In addition, extending the FoV of the system by combining multiple images of a scene using image mosaicing was implemented to represent a large object.

5.9.1.1 Short-Range Imaging of Detailed Structures

A two-dimensional visible band image of the top of the clock tower is shown in Figure 5.29. The target was imaged with 85 × 85 scan points with spatial resolution of 2.8 cm per scan point. The data was acquired with 170 ms acquisition time per scan point (20 minutes total acquisition time) with 10 mW laser power and 500 ns gate.

Figure 5.29. A two-dimensional visible-band image of the top of the clock tower.

Scatterplots of the top of the clock tower are shown in Figure 5.30 and Figure 5.31. Complex features of the target shown in Figure 5.31, such as the shape of the roof, the

structure of the ribs, the shape of the gutter, a ventilation opening near the top of the roof and slats in the window shutter, could not be determined from the visible-band image. The angle of the slats estimated to be ~ 45°.

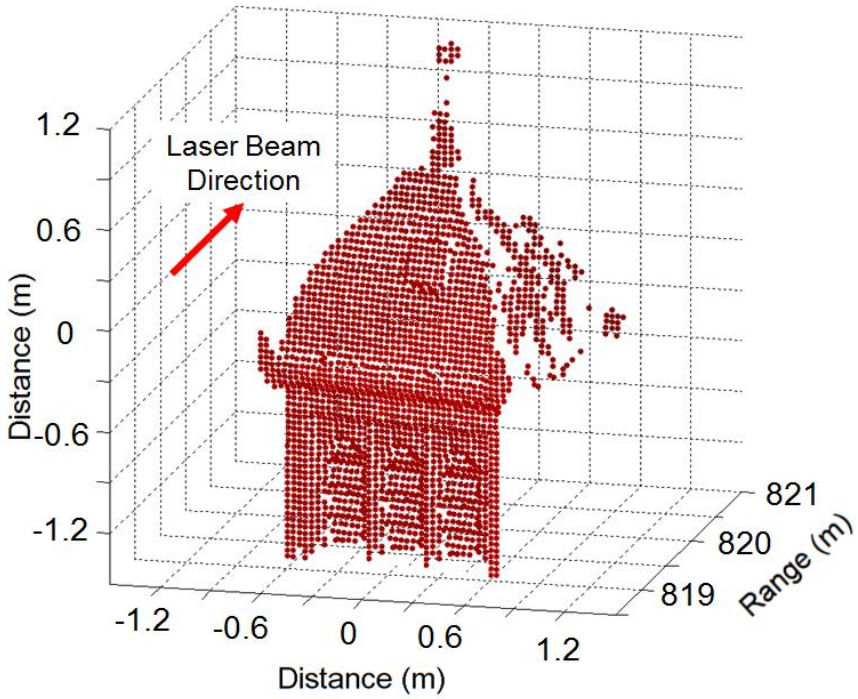

Figure 5.30. Scatterplot of the top of the clock tower at a range of ~ 800 m with an acquisition time of 170 ms per pixel.

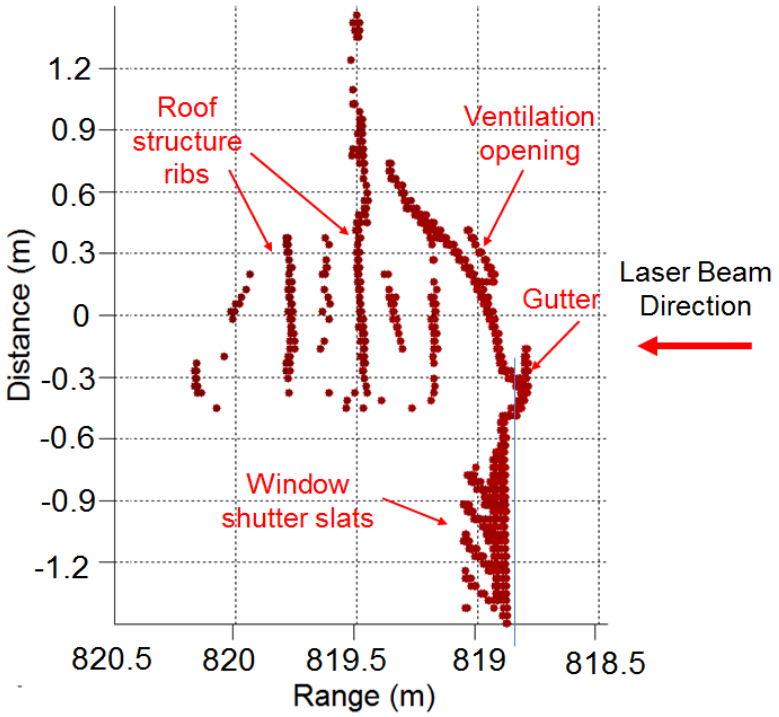

Figure 5.31. Scatterplot of the top of the clock tower at a range of ~ 800 m with an acquisition time of 170 ms per pixel showing side view of the target.

5.9.1.2 Imaging of a Building

Figure 5.32 shows a visible-band wide FoV image of a target under investigation which appears to be a small residential building. Building details are unclear; this is because the target is located too far away (at a range of ~ 8.8 km) from the transceiver for resolving detail conventionally.

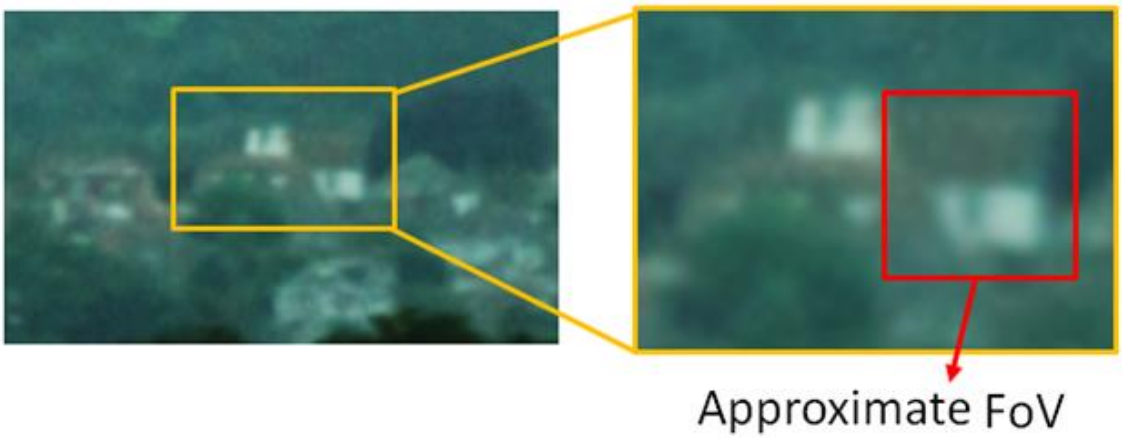

Figure 5.32. Visible-band wide FoV image of a residential building.

Figure 5.33 and Figure 5.34 shows scatterplots of the small building. The object was scanned with 32 × 32 scan points with spatial resolution of 25 cm per scan point. The delay between the laser trigger and the detector gate trigger was set to 2.7 µs. The system operated with gate width of 500 ns, 20 µs hold-off time and with the laser power output of 10 mW. Acquisition time per pixel was 0.3 s with a total scan time of approximately 5 minutes.

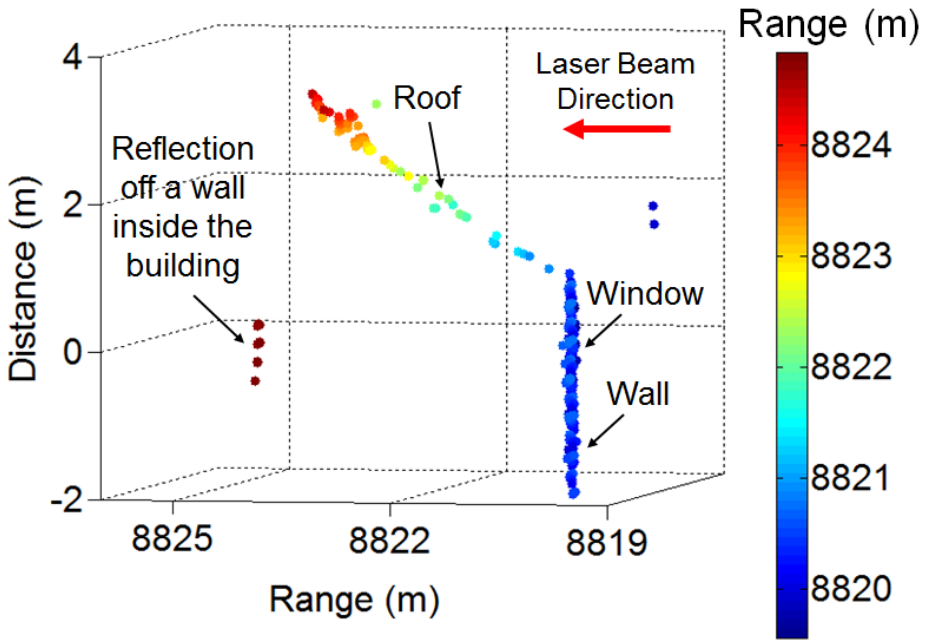

Figure 5.33. Scatterplot of a building imaged with 32 × 32 scan points over a range of ~ 8.8 km, side view of the target.

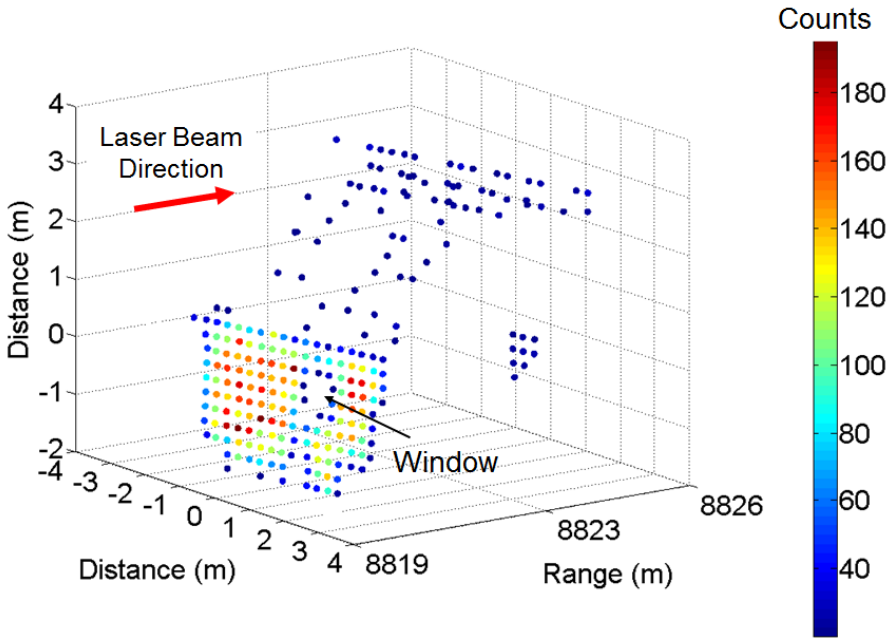

Figure 5.34. Scatterplot of a building imaged with 32 × 32 scan points over a range of ~ 8.8 km, front-side view of the target.

Using the three-dimensional scatterplots the physical structure of the object can be analysed; depth of the room was measured to be ~ 4 m (via the window).

5.9.1.3 Long-Range Imaging of an Electricity Pylon

Figure 5.35 shows a wide FoV visible-band close up image of a typical pylon. A 40 × 80 scan of a similar pylon was taken over a distance of ~ 6.8 km where each scan step corresponded to a spatial resolution of 20 cm. The data was acquired with 0.23 s acquisition time per scan point and over a 12 minutes total acquisition time. The gate width was 500 ns and laser power was set to 10 mW. The delay between the laser trigger and gate trigger was set to 6.2 µs to locate the returns at approximately the centre of each gate.

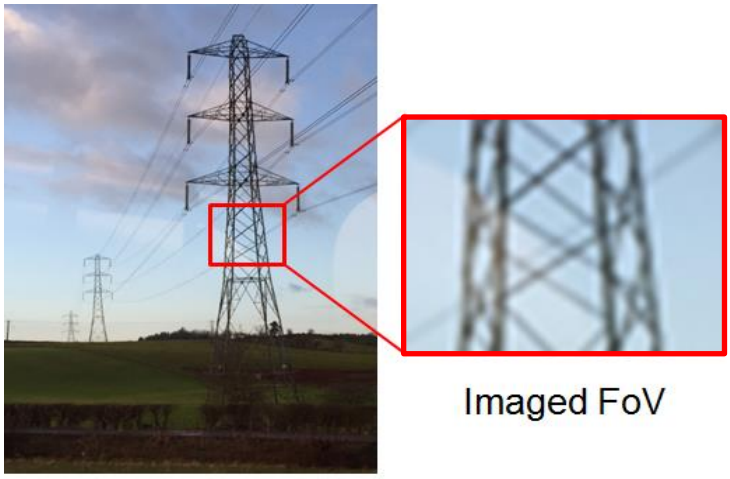

Figure 5.35. Wide FoV visible close-up image of a typical pylon.

Scatterplots of the target are shown in Figure 5.36. Data was analysed using the least-squares peak finding algorithm with two different levels of threshold. Figure 5.36(a) shows the results for a threshold of 5 counts which allows details of the structure to be identified; nevertheless, many data points caused by noise are also present. In Figure 5.36(b) the data was analysed for a threshold of 7 counts which removed the noise at the expense of detail which was not as prevalent as in the image shown in Figure 5.36(a).

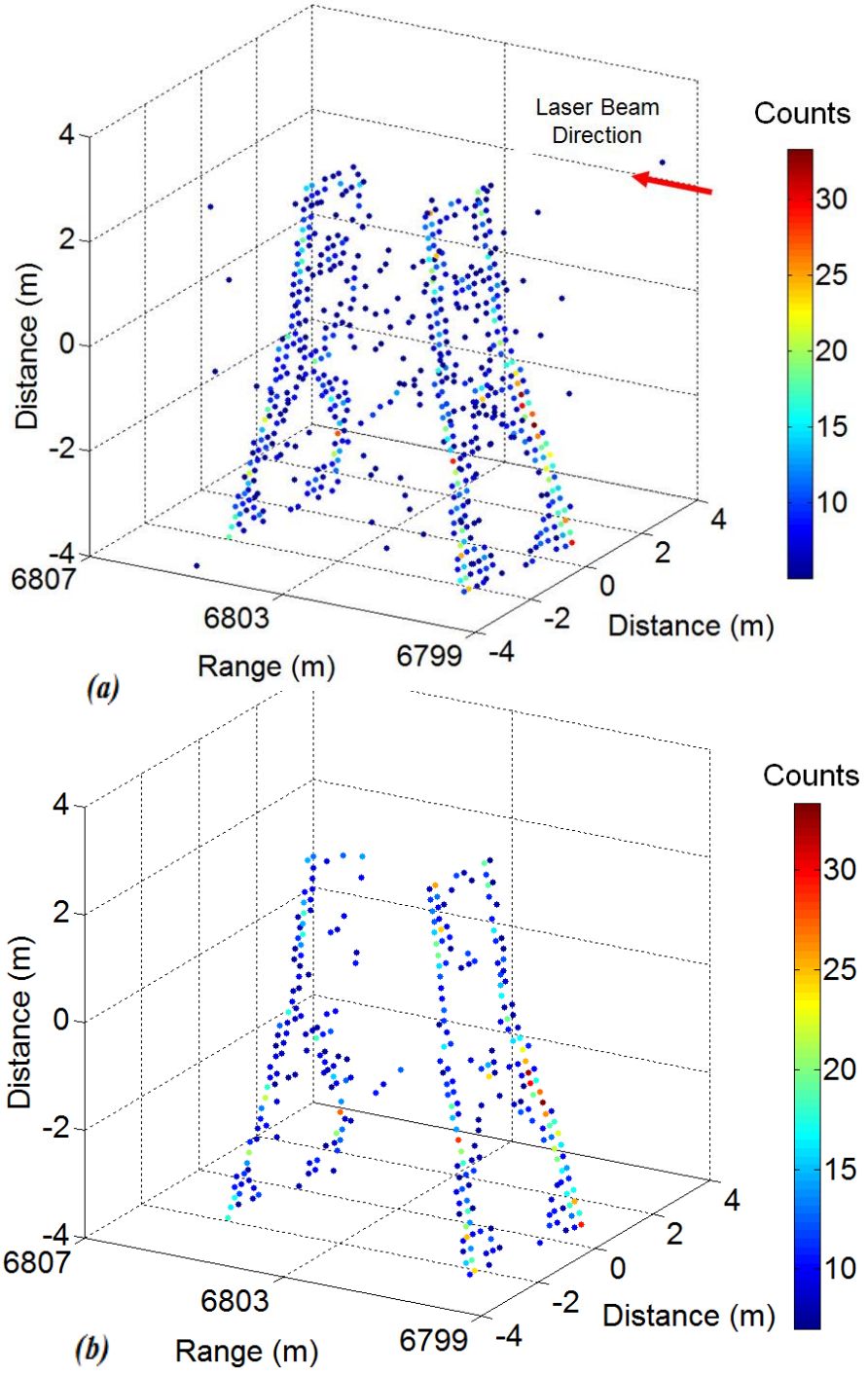

Figure 5.36. Scatterplots of a pylon acquired with 40 × 80 scan points over a distance of ~ 6.8 km where (a) is plotted for a least-squares fit based peak finder with a threshold of 5 counts, (b) is plotted for a peak finder with a threshold of 7 counts.

5.9.1.4 Imaging of Foliage

A 50 × 50 scan of foliage was taken over a range of ~ 5.4 km with spatial resolution of 15 cm per scan point and the acquisition time of 0.22 s per pixel and total scan time of ~ 9 minutes. The gate width was 500 ns and the laser power output was 10 mW. The detector operated with a hold-off time of 20 µs. Figure 5.37 shows a two-dimensional front view of the scene within which, without the three-dimensional data, it is difficult to determine the spatial relationship between the various parts of the foliage. Figure 5.38 shows a three-dimensional side-top view of the object showing multiple small and large trees dispersed across the depth of nearly 20 m.

Multiple returns for a pixel *P* marked on the scatterplot in Figure 5.38(a) have been recorded; a histogram showing peaks equivalent to three range locations: R_A = 5385.7 m, R_B = 5386.4 m and R_C = 5396.7 m is presented in Figure 5.39. Points *A*, *B* and *C* marked in Figure 5.38(b) represent the locations of those peaks.

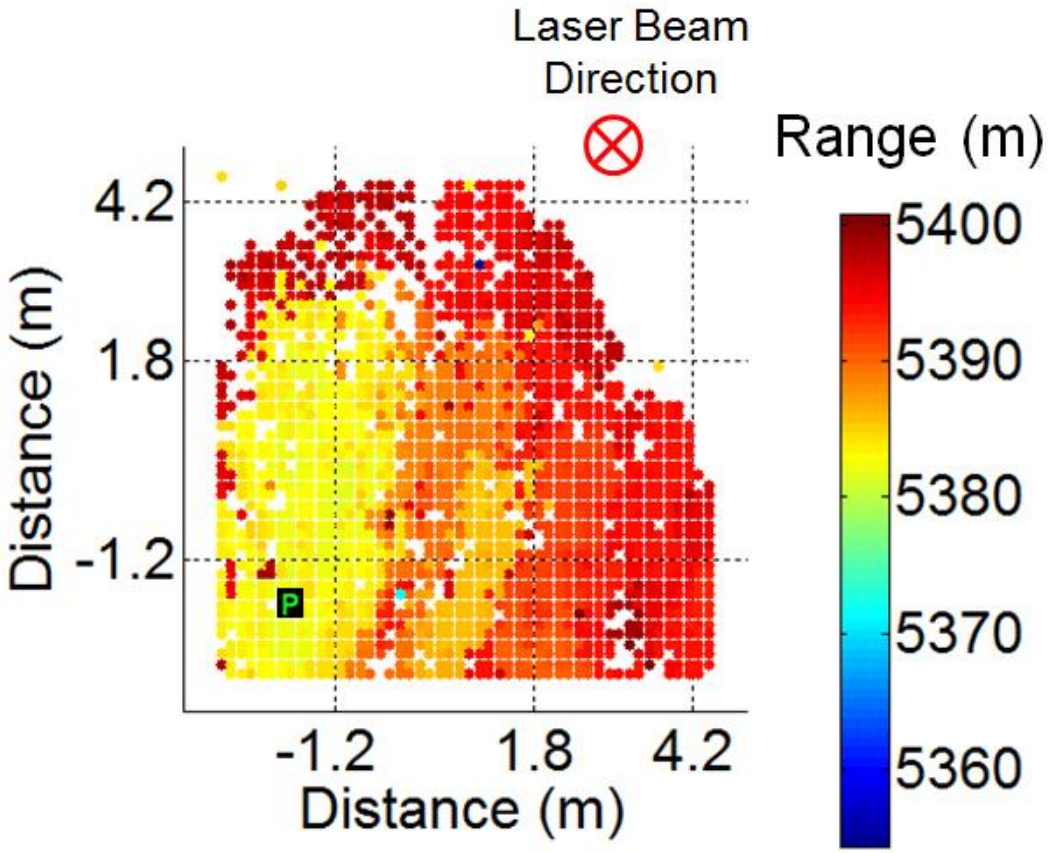

Figure 5.37. Two-dimensional, front-view, scatterplot of foliage recorded with 50 × 50 scan points over a range of 5.3 km with a per-scan point acquisition time of 0.22 s.

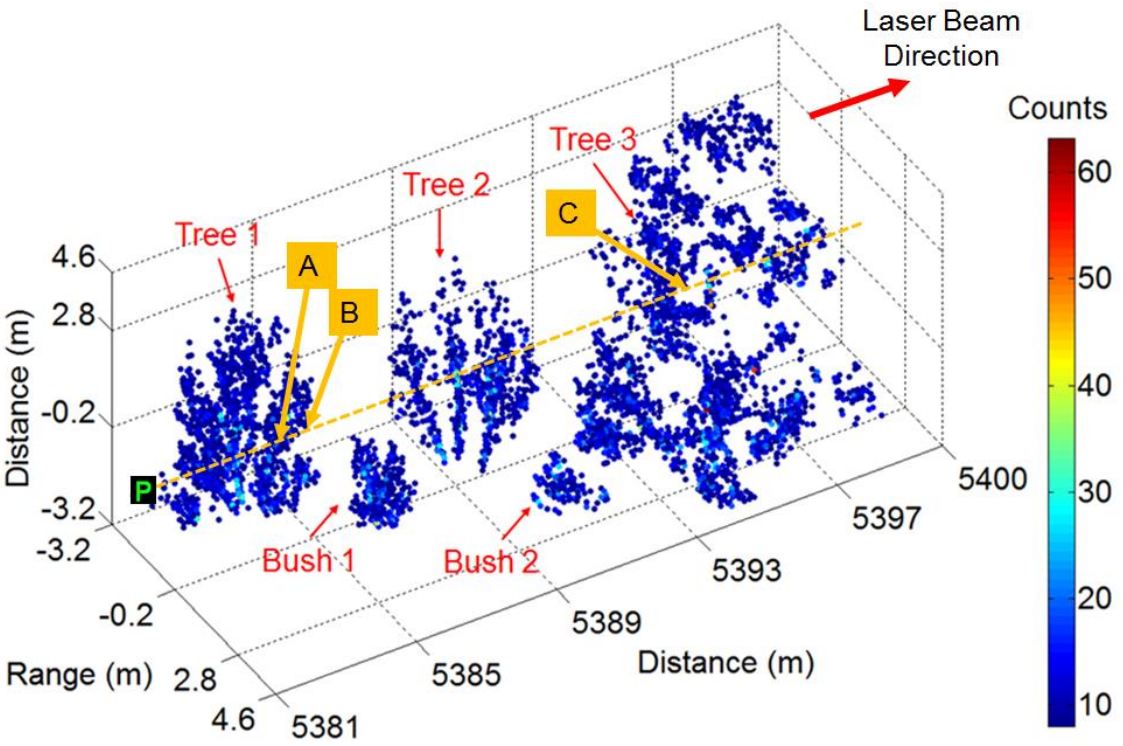

Figure 5.38. Scatterplots of foliage recorded with 50 × 50 scan points over a range of 5.3 km with a per-scan point acquisition time of 0.22 s, showing side-top view of the scene. Point P is a pixel for which a histogram shown in Figure 5.39 was plotted. Points A, B and C represent locations of peaks identified for that particular pixel.

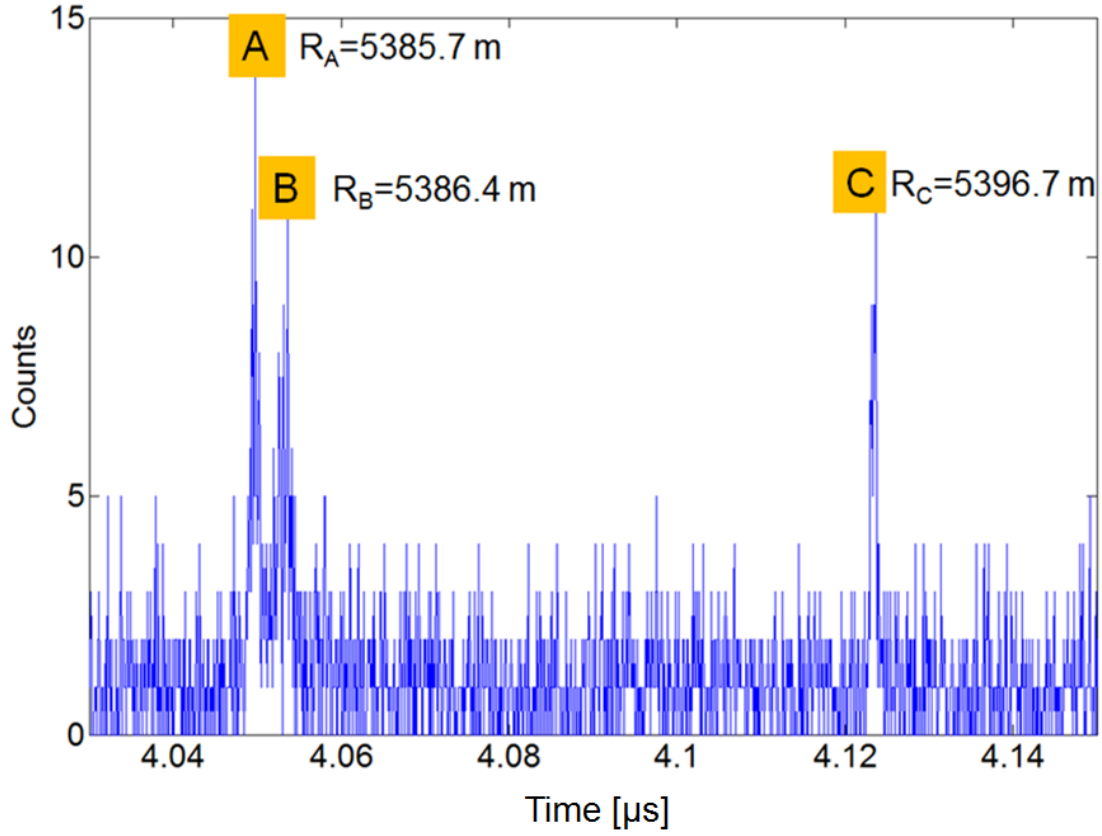

Figure 5.39. Histogram for the pixel P of the image generated for a signal recorded over 0.22 s acquisition time.

The average number of background and dark counts is 1.1 counts per 80 ps bin. Within a 500 ns gate there are 6250 bins of 80 ps width suggesting that there are approximately 7,000 c within the 0.22 s acquisition time that are due to background and dark counts. Integration under an average peak corresponding to a target return contains about 80 counts acquired over 0.22 s. This corresponds to an average count rate due to target returns of 350 cps. The expected level of counts from a Lambertian target at normal incidence located over a range of 5.3 km (attenuation of ~ 123 dB for object reflectivity of 15 %) is approximately 2.4 kcps. The normal-incidence Lambertian count rate is on average nearly seven times the actual count rate. This difference is due to the expected low return rate from foliage [13]. A detailed model of the expected level of returns from foliage was not developed as part of this thesis and thus a direct comparison was not executed.

As shown in section 5.8.5, the cross-correlation method (see section 5.8.2.1) demonstrated reduced acquisition time. The result of the acquisition time reduction for the foliage to 22 ms per scan point is shown in Figure 5.40(a) and to 11 ms and 5 ms per scan point is shown in Figure 5.40(b) and Figure 5.40(c) respectively.

At 22 ms acquisition time per scan point it is still possible to identify all the main features in the scene. At 11 ms acquisition time per scan point features can still be identified but the identification becomes more challenging to a user who has not previously seen the scatterplots produced using longer acquisition times. When the acquisition time is decreased to 5 ms per scan point the recognition of features is significantly diminished.

To further reduce the acquisition time a method called linear spatial filtering was applied. Linear filtering is an image-processing technique used to help extract missing information from images. A linear filter is implemented using a weighted sum of successive pixels. The same pattern of weights is used in each window, this means that the linear filter is spatially invariant and can be implemented using a correlation mask [14] [15] [16].

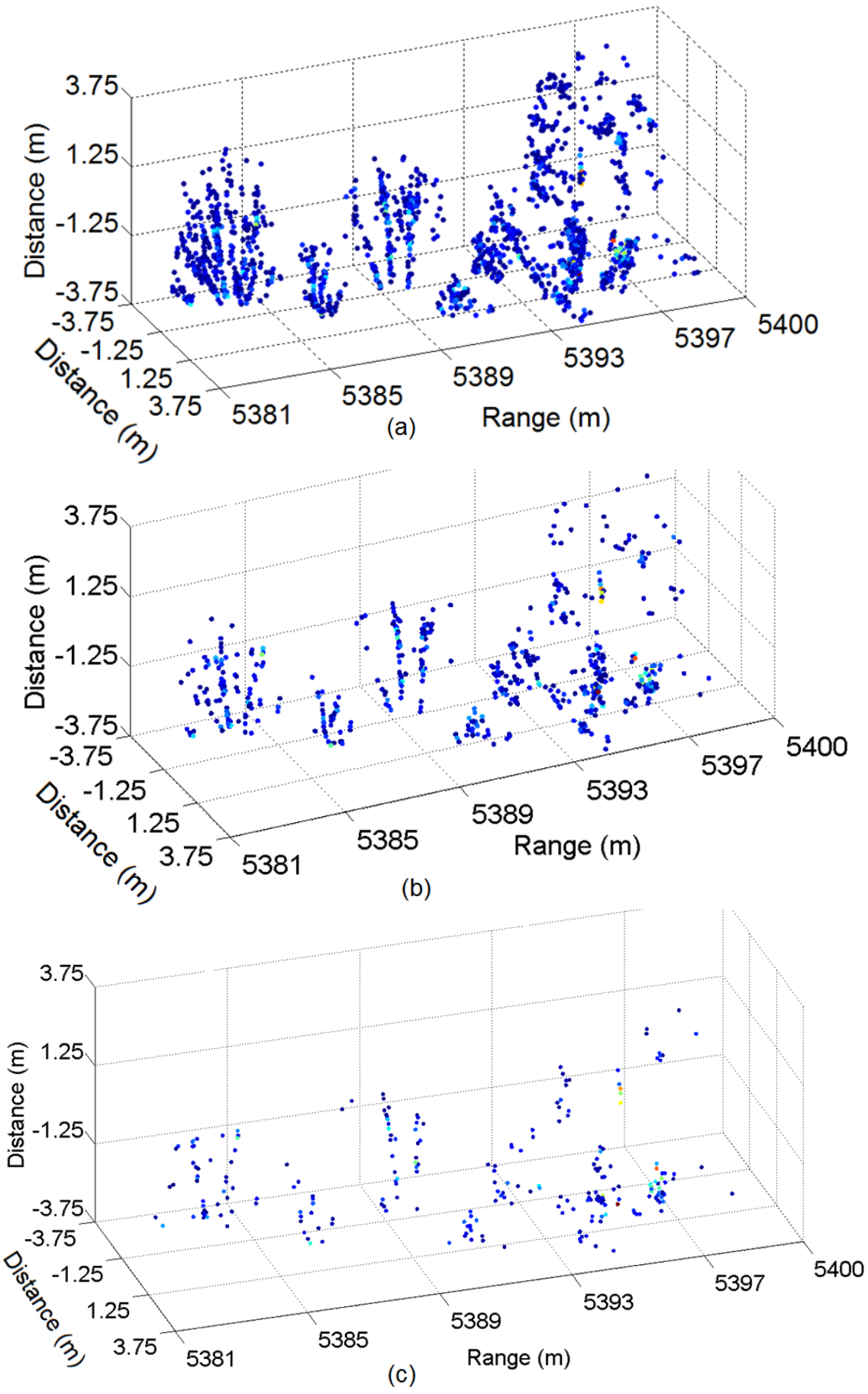

Figure 5.40. Scatterplots of foliage recorded with 50 × 50 scan points over a range of 5.3 km with a per-scan point acquisition time of (a) 22 ms, (b) 11 ms and (c) 5 ms.

A linear filter $g(i, j, z)$ is implemented to a three-dimensional image $f(i, j,z)$ creating an output image $h(i, j, z)$. The output is a correlation of $h(i, j,z)$ with the filter $f(i, j,z)$ and is represented by

$$h[i, j, z] = f[i, j, z] \otimes g[i, j, z] \qquad \textit{Eq. 5.4}$$

$$h[i, j] = \sum_{k=-N}^{N} \sum_{l=-M}^{M} \sum_{w=-G}^{G} f[k, l, z] g[i + k, j + l, z + w] \qquad \textit{Eq. 5.5}$$

where N, M and G are dimensions of the filter [14].

A three dimensional array of data was filled a number of photon counts (see Figure 5.41(a)). The array consists of 50 × 50 pixels along x, y axes; each pixel represents a distance of 15 cm. Along the z axis the range of 19 m was divided into 190 slices of 10 cm depth. When computing an output pixel at the boundary of an image, a portion of the correlation is usually off the image edge. These off-edge image pixels were filled with the first and last values. In order to compute output values for the border pixels each border of the array was padded with a one-dimensional array filled with values that were identical to those in the adjacent pixels of the main array (see Figure 5.41(b)).

A three-dimensional filter consisting of a 3 × 3 × 3 array with pixel values of 1/27 was applied to the array of data using the correlation operation with equal weights in the correlation mask. Figure 5.42(a) shows the array of data surrounded by padding and the filter. The filter was slid across the padded array; the average pixel value across 27 pixels was computed and returned into the final array as shown in Figure 5.42(b).

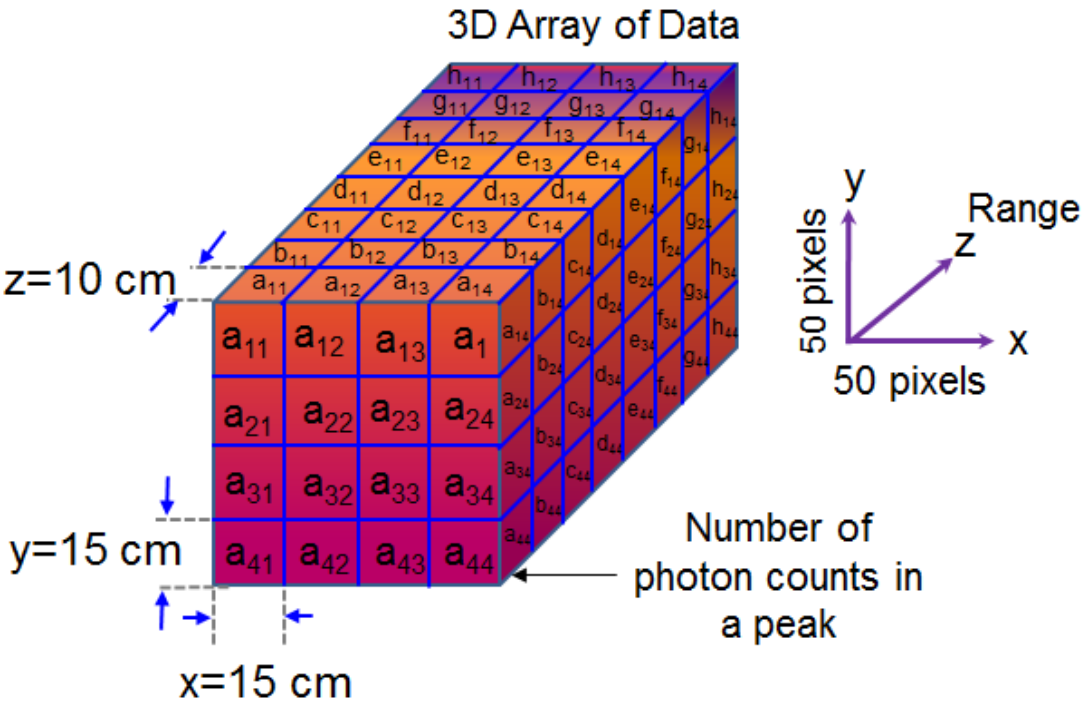

(a)

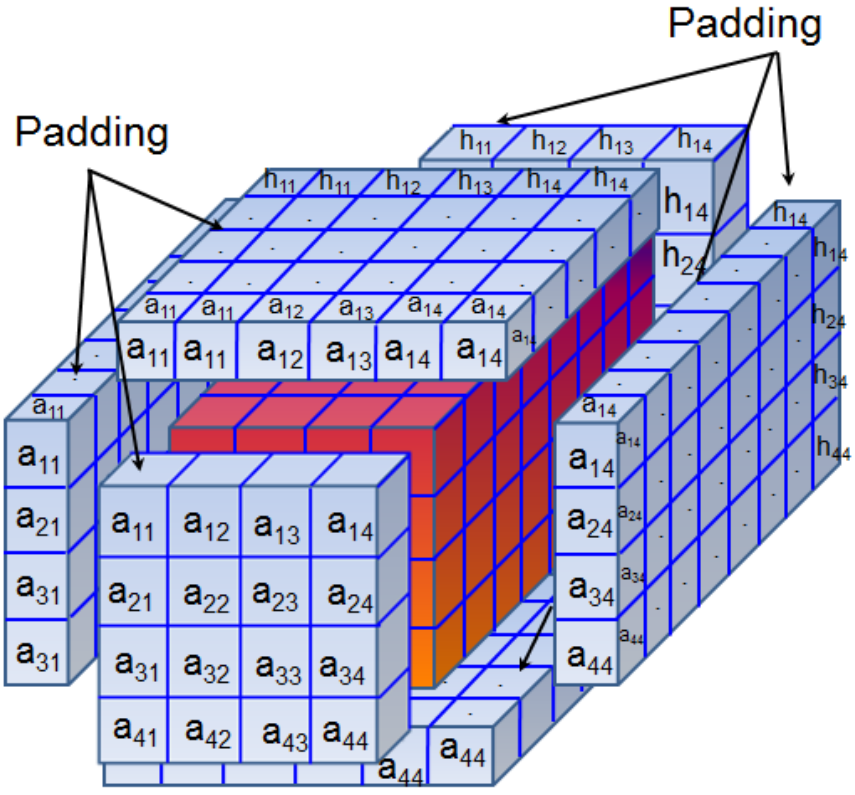

(b)

Figure 5.41. Illustration of: (a) three-dimensional array of data where each pixel represents 15 cm along x, y axes and 10 cm along z axis; (b) padding added to the six borders of the three-dimensional array. Each value in the array contains values corresponding to the number of maximum photon counts in a histogram peak generated for each pixel.

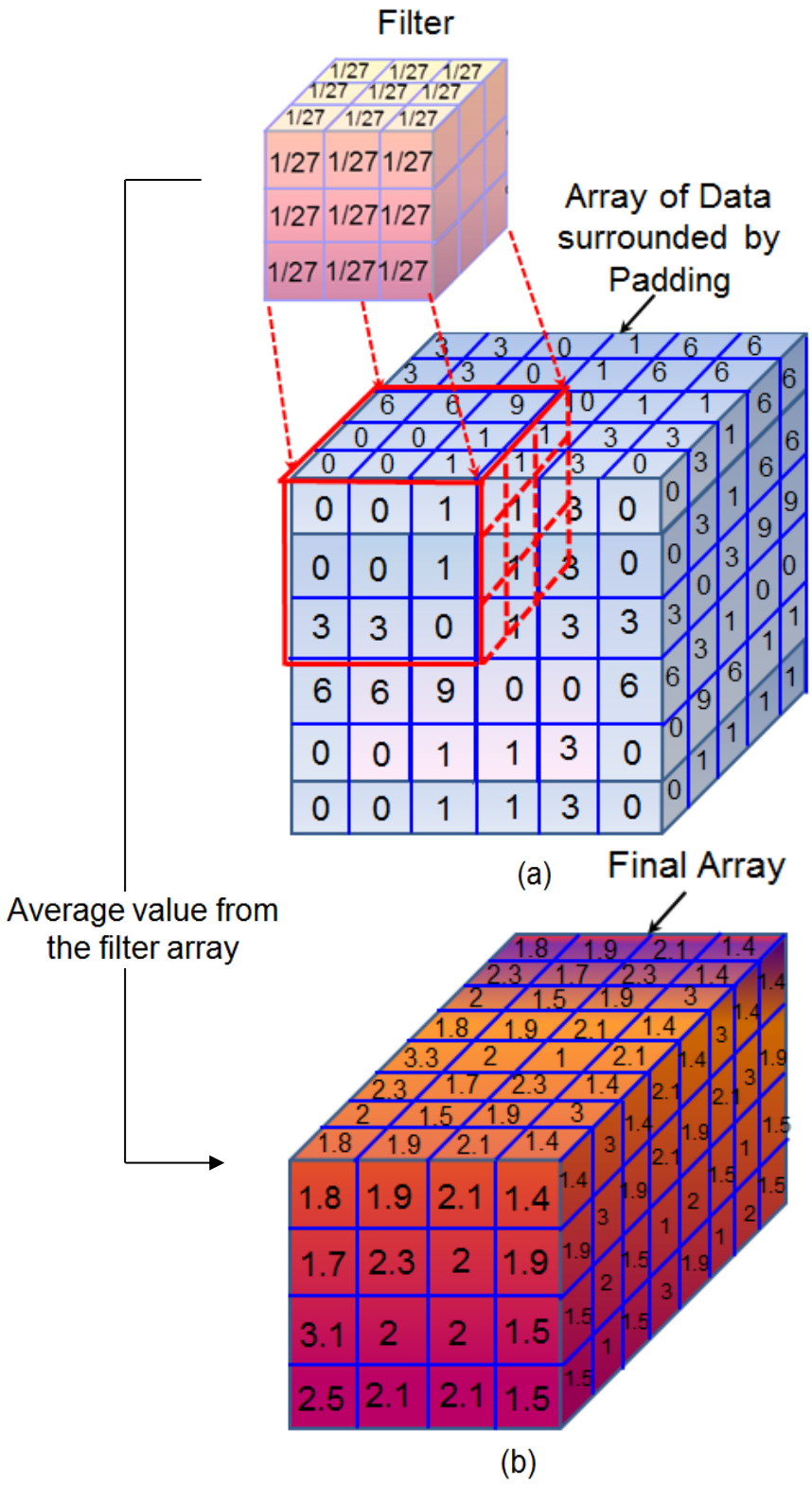

Figure 5.42. An example illustrating the mean filter using a 3 × 3 two-dimensional mask.

The spatial filtering technique was applied to scatterplots generated with 11 ms and 5 ms acquisition time (Figure 5.40(b) and Figure 5.40(c)); where the identification of features on these images was limited. The result of the spatial filtering is shown in Figure 5.43(a) and Figure 5.43(b) respectively. It shows an improvement in

highlighting some main features of the targets such as branches of tree 1 and tree 2 which can potentially facilitate target recognition. Depending on the application, using this technique may decrease the acquisition time to 11 ms or even 5 ms per scan point which would result in a total acquisition time of 27.5 s or 12.5 s.

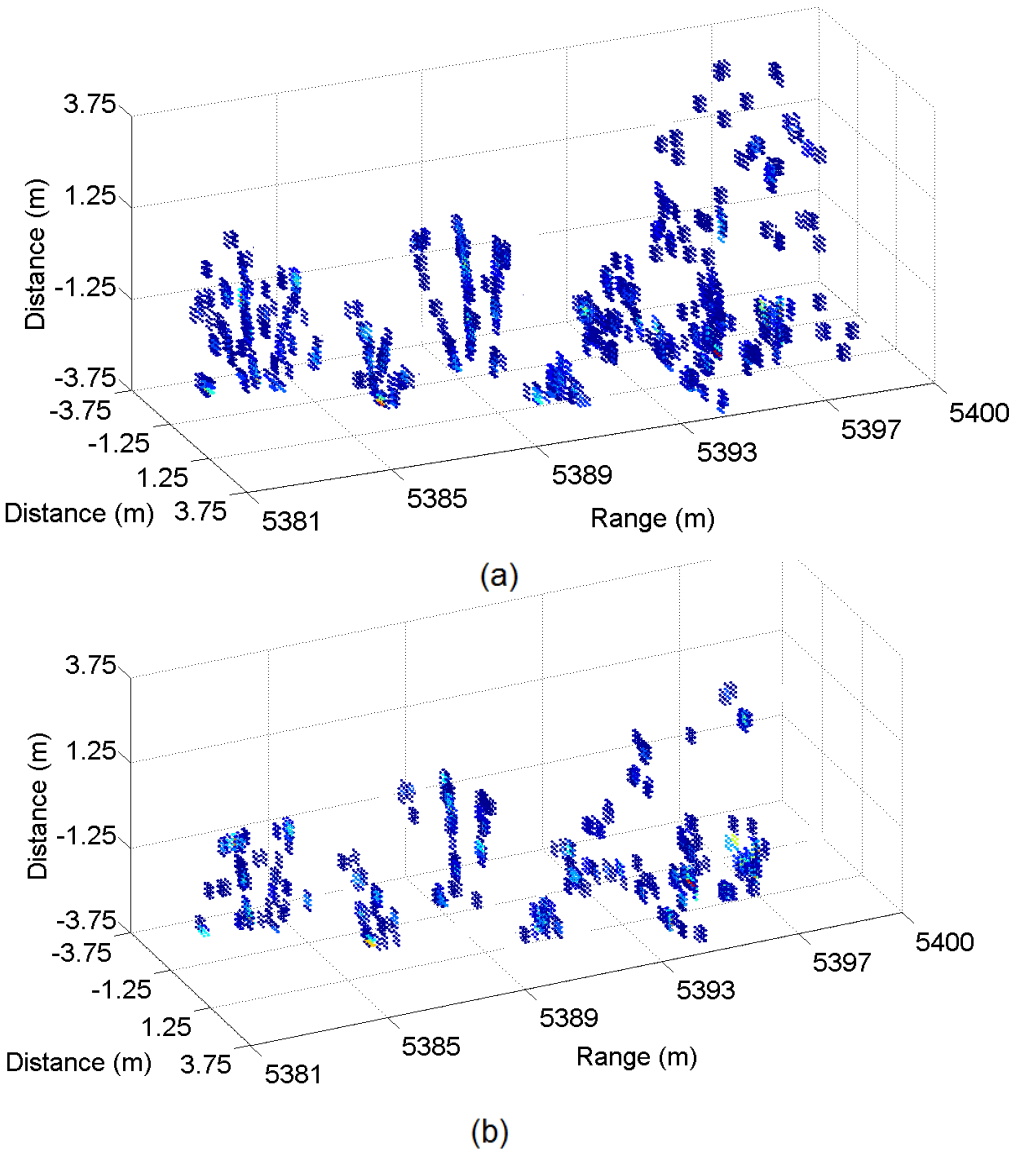

Figure 5.43. Scatterplots of foliage recorded with 50 × 50 scan points over a range of 5.3 km with a per-scan point acquisition time of (a) 22 ms, (b) 11 ms, (c) 5 ms. A three-dimensional linear spatial filter was applied to the data to recover information lost during minimising the acquisition time.

5.9.1.5 Long-Range Terrain Mapping

A 32 × 32 scan of terrain was taken over a range of ~ 10.5 km with spatial resolution of 29 cm per scan point, the acquisition time of 0.3 s per scan point and the total scan time of ~ 5 min. The gate width was 500 ns and the laser power output was 10 mW. The

detector operated with a hold-off time of 20 μs. A wide FoV visible band image of the scene is shown in Figure 5.44.

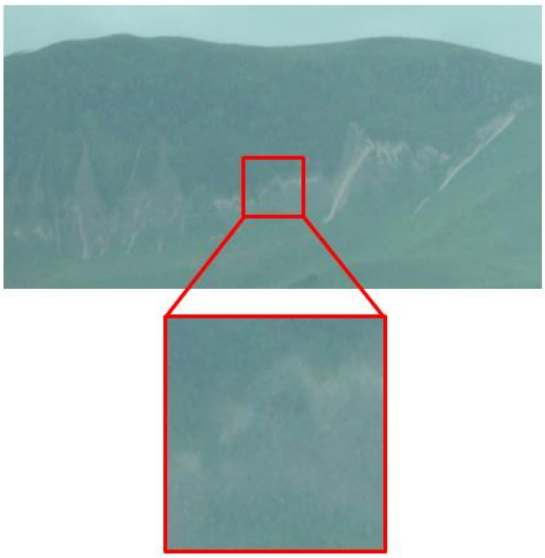

Figure 5.44. Wide FoV, visible band image of the scanned scene of the terrain located to the right of the Ski Slope on the Pentlands.

A front view and side-view scatterplots of the scene are shown in Figure 5.45 and in Figure 5.46 respectively. The terrain stretches across a range of approximately 12 m; its average slope to the line of sight was determined by calculating a linear fit to the data points. A common form of a linear equation in the two variables x and y is given by Eq. 4.41 (see section 4.16.2) where m determines the gradient of the line and b determines the intercept on the y axis [17].

Linear fit to the raw data points of the top view acquired over 0.5 s per scan point is given by $y = 0.77\ x + 10501$. From Eq. 4.42 (see section 4.16.2), the approximate angle of the slope in respect to the optical axis of the system is $\beta = \text{atan}\ (0.77) = 38\ °$.

Figure 5.47 shows a front-view scatterplot of the object which is a two-dimensional representation of the scene. The image was divided into four areas: *A1*, *A2*, *A3* and *A4*; the distance *Y* (vertical) was plotted with respect to range for each of the four areas to investigate the variation in slope angle in respect to distance *Y*.

Figure 5.48 shows how the angle slope varies across range for *A1*, *A2*, *A3* and *A4*. It can be noted that the angle of the slope is relatively uniform up to the range of 10507.5 m. Beyond that range the slope becomes steeper as the distance increases revealing a steep kink present in area *A4*.

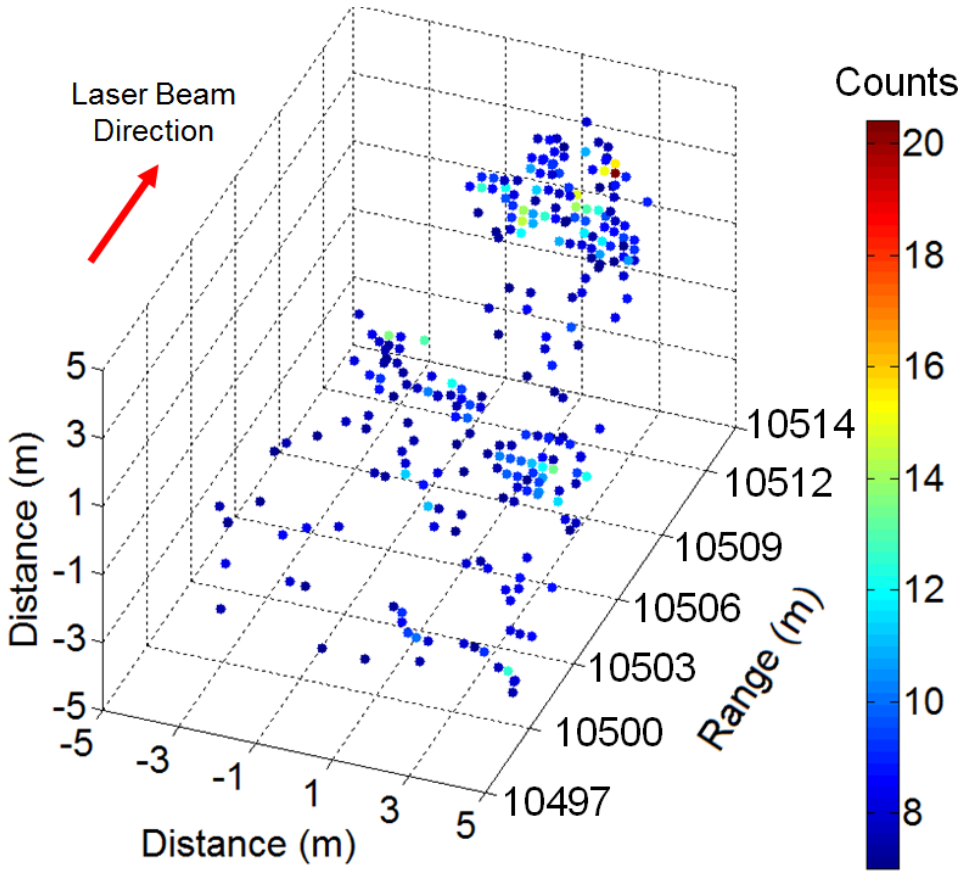

Figure 5.45. Scatterplots of terrain recorded with 32 × 32 scan points over a range of 10.5 km with a per-scan point acquisition time of 0.3 s.

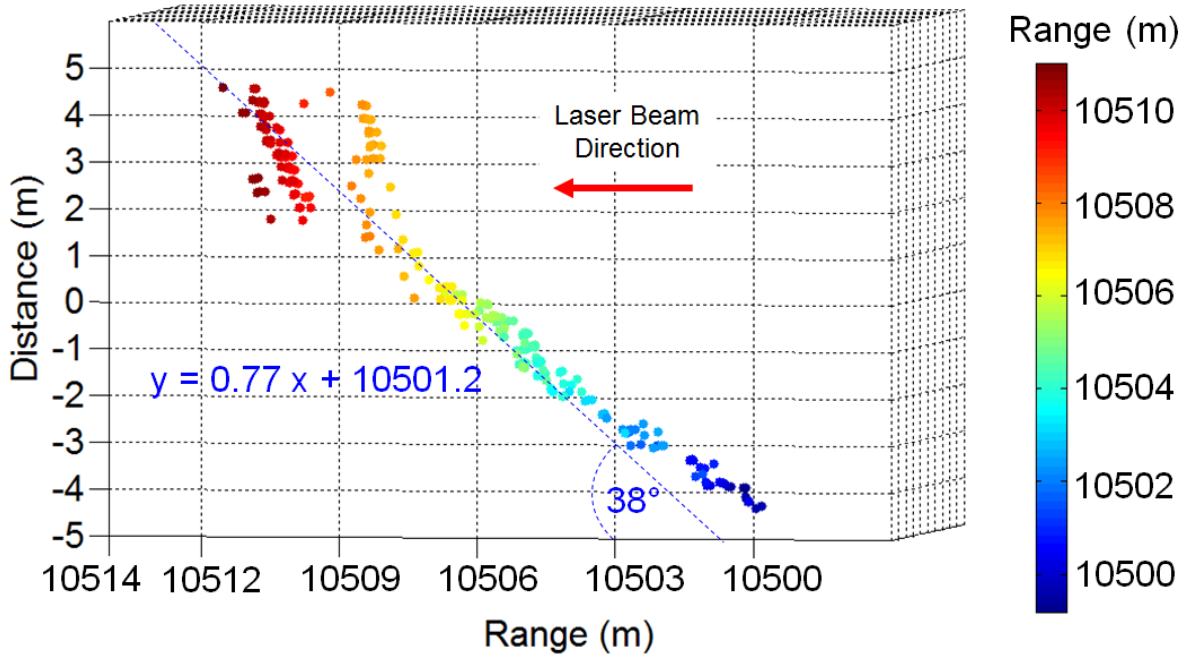

Figure 5.46. Scatterplots of a side-view of terrain recorded with 32 × 32 scan points over a range of 10.5 km with a per-scan point acquisition time of 0.3 s. Surface slope to the optical axis was estimated to be 38 °.

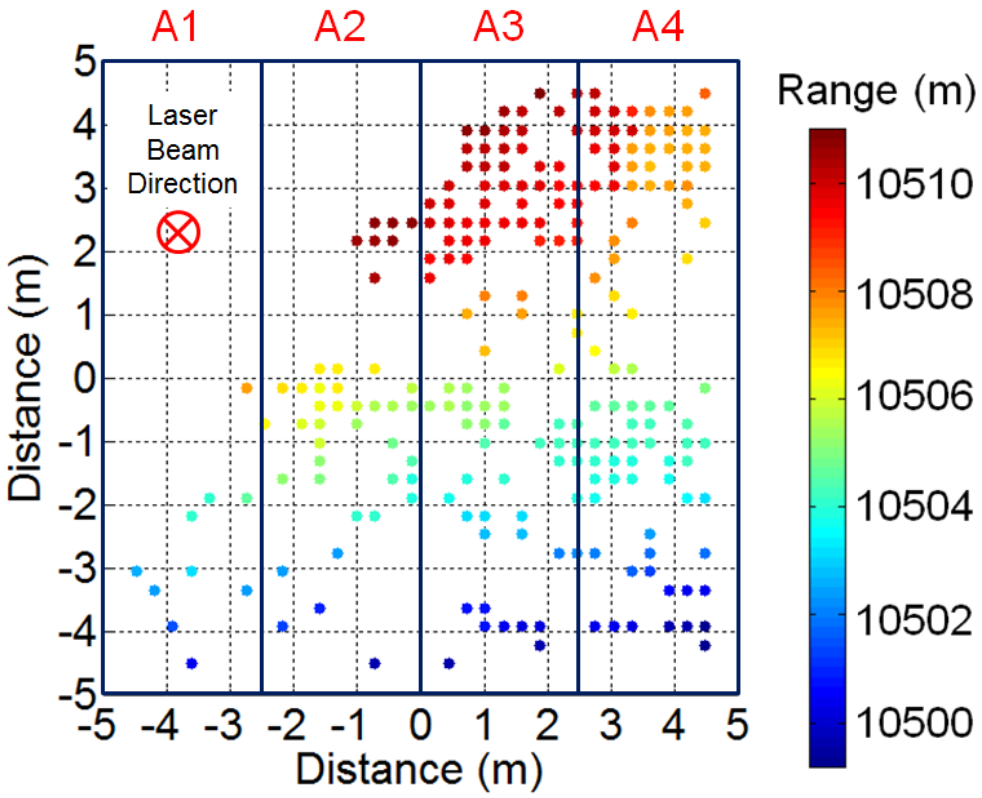

Figure 5.47. Scatterplots of a front-view of terrain recorded with 32 × 32 scan points over a range of 10.5 km with a per-scan point acquisition time of 0.3 s. The view was divided into four areas: A1, A2, A3 and A4 for analysis presented in this section.

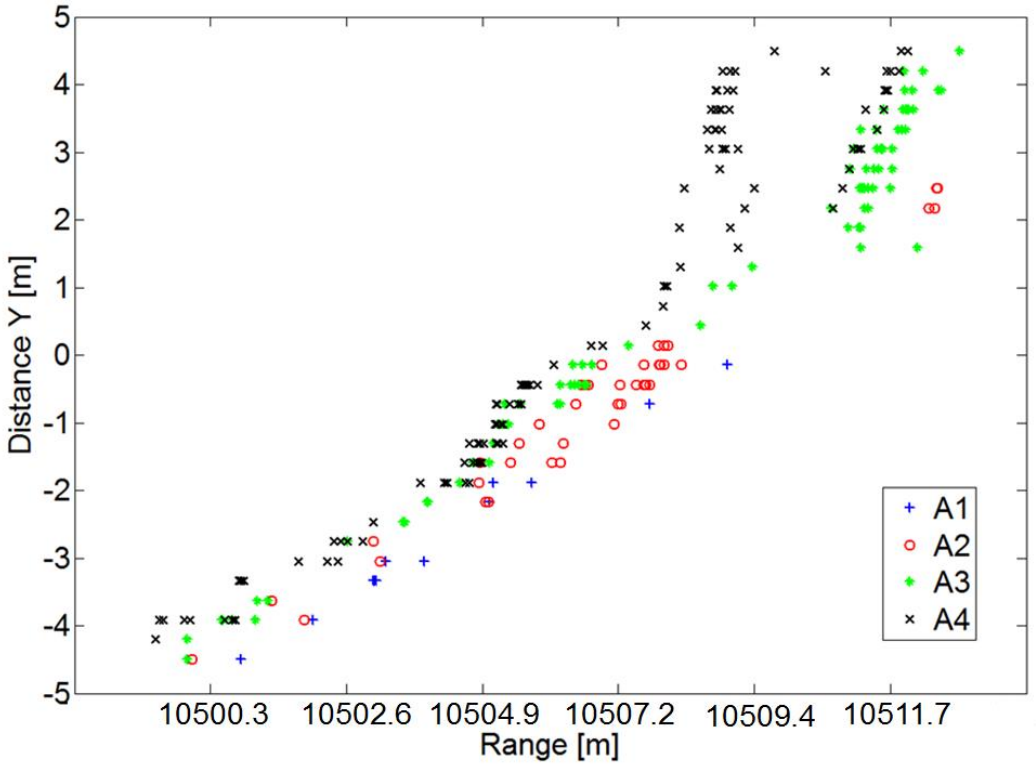

Figure 5.48. Plot showing how the slope of the terrain varies across range for four areas of the scene: A1, A2, A3 and A4 across distance Y.

5.9.1.6 Image Mosaicking

Image mosaicing refers to combining multiple images of a different FoV of a scene in a manner which increases the effective FoV of the system [18]. In this way it is possible to build large views of scenes too large to realise in the normal FoV of a system [19].

The lidar system was designed and aligned to have diffraction limited performance for 32 × 32 scan points however, the analysis shown in previous sections showed that three-dimensional images produced with up to 85 × 85 scan points can also be generated. The $FoV_{Scanner}$ was further extended and an object shown in Figure 5.49 was scanned with a scan step corresponding to a spatial resolution of 8.4 cm. To generate a three-dimensional image of a larger target, three separate, overlapping, 100 × 100 scans were taken which were combined to produce one large image representing the building.

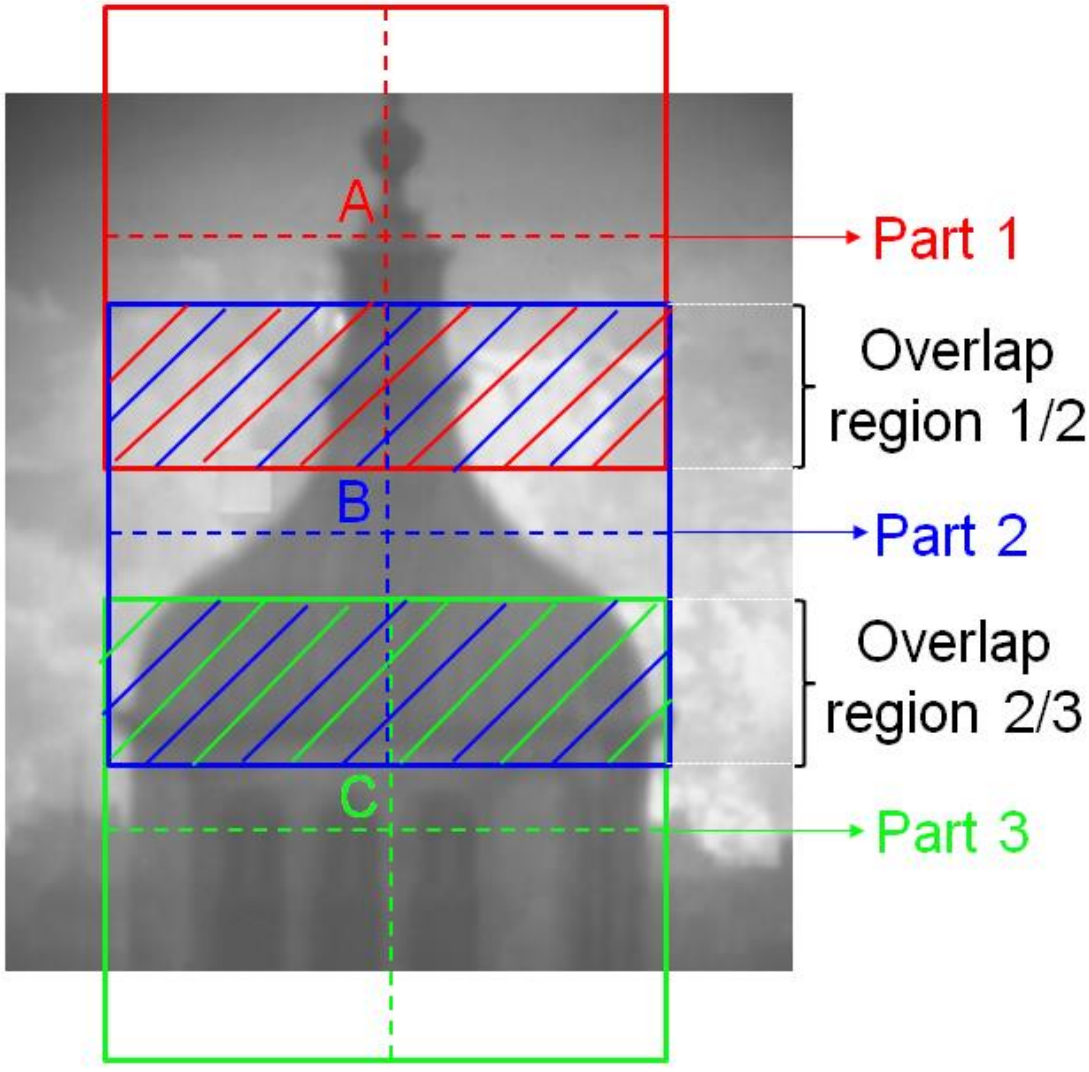

Figure 5.49. Wide FoV monochromatic image of the target taken with the CCD camera in the system. The scene was divided into three parts which were separately scanned to generate a full image of the object.

The data was acquired over a range of ~ 3 km with acquisition time of 170 ms per scan point and the gate width of 500 ns. The rifle-scope was bore-sighted with the optical axis of the system during the alignment and was used to point the system at the desired part of the target. A test run was performed to establish the relationship between dimensions of the object, the FoV of the system for a 100 × 100 scan points and the scale of the riflescope cross-hair. A 100 × 100 scan corresponded to the area of the FoV represented by a square shown in Figure 5.49. Once this was established the centre of the cross-hair of the riflescope was positioned in point *A* of the scene as illustrated in Figure 5.49 and a scan was acquired. Subsequently, the scan was taken with the system positioned with the riflescope centred at the point *B*, overlapping the previous scan area by approximately 35 % (35 pixels). And finally, the system was positioned at the point *C*, acquiring the scan with about 35 % overlap with the scan 2. The overlaps were needed for the alignment of images. A large overlap allows a higher accuracy or image alignment but requires longer acquisition time.

The acquired data was analysed for the three parts of the image, the overlapping parts of the image were merged and the remaining portion of the data was combined to produce a three-dimensional scatterplot of the building which accounted for approximately 100 × 230 scan points. The total acquisition time required to produce those images, including the overlapping parts, was 85 minutes.

Examples of different view points of the scene are shown in Figure 5.50, Figure 5.51 and Figure 5.52. The total height of the imaged building is nearly 13 m and the width is approximately 9 m. Although the scan was acquired from one vantage point the object can be viewed from many vantage points which can facilitate target identification.

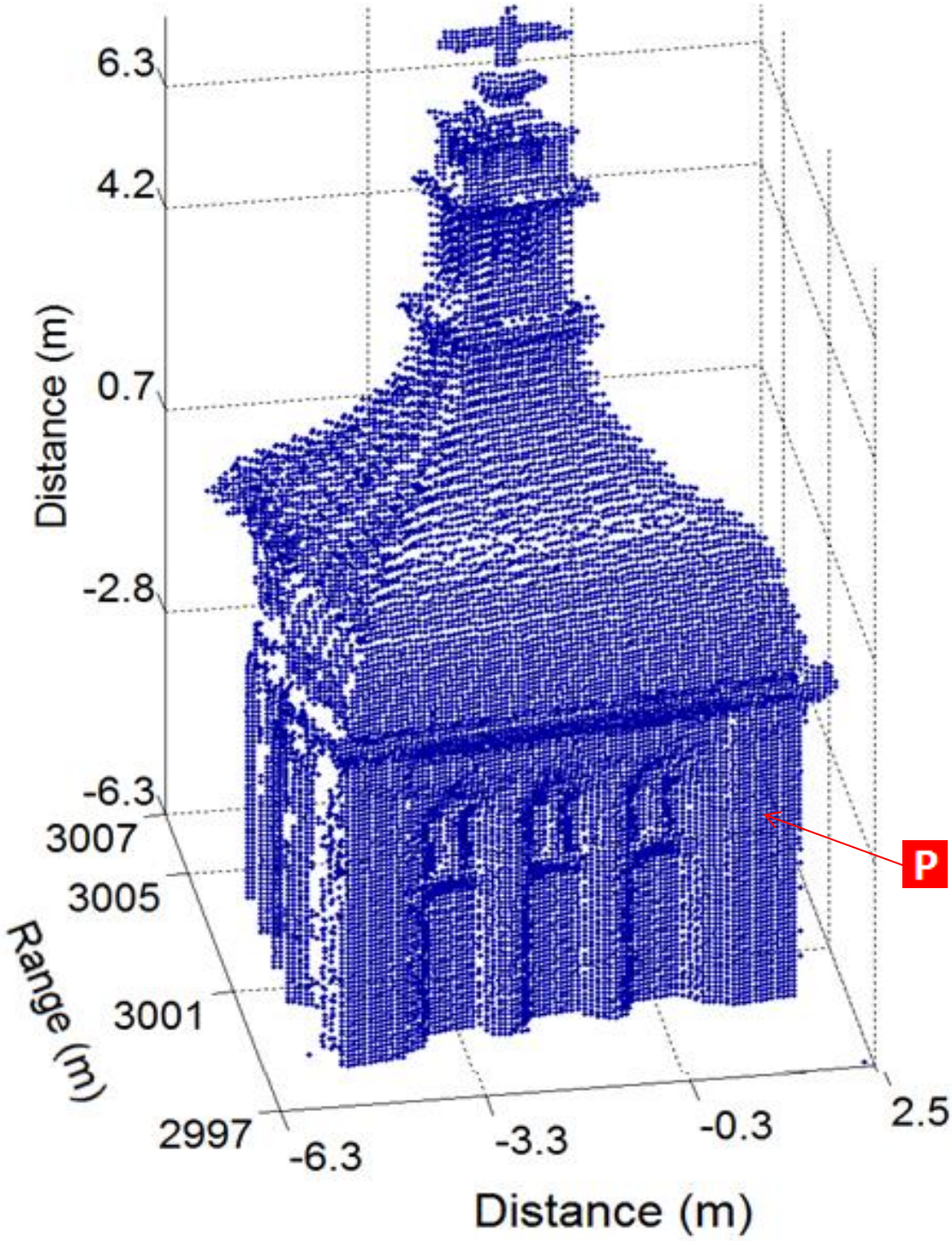

Figure 5.50. Mosaic of scatterplots of a building recorded with 100 × 230 scan points over a range of 3 km with a per-scan point acquisition time of 170 ms; top-front view. Pixel P is used for analysis presented further in this section.

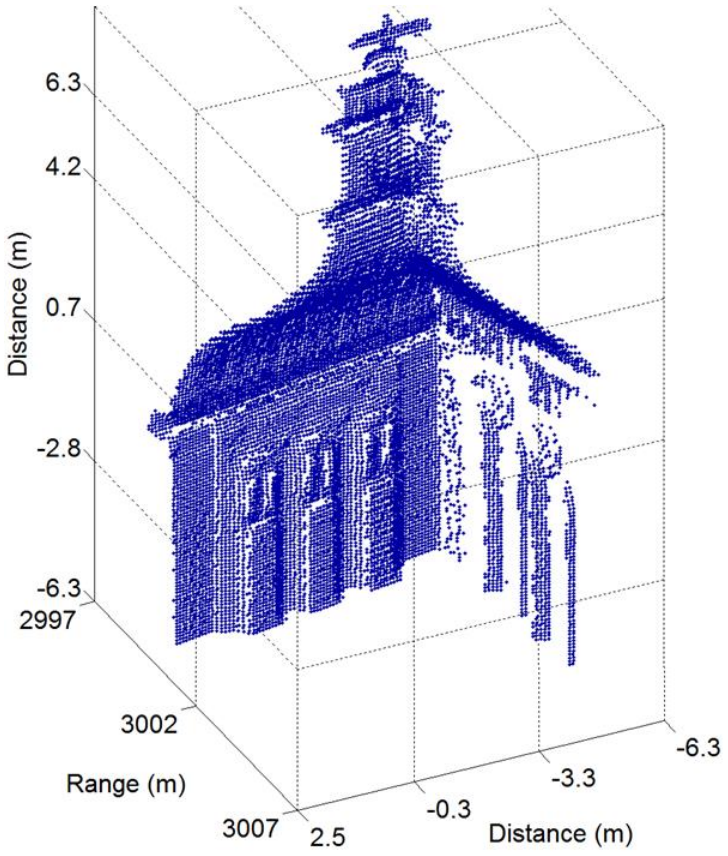

Figure 5.51. Mosaic of scatterplots of a building recorded with 100 × 230 scan points over a range of 3 km with a per-scan point acquisition time of 170 ms; bottom-right-side view.

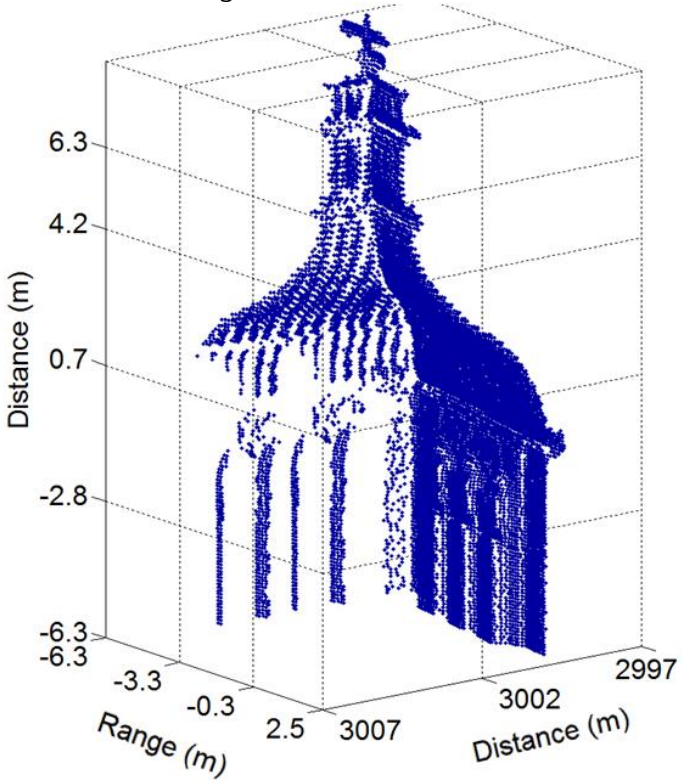

Figure 5.52. Mosaic of scatterplots of a building recorded with 100 × 230 scan points over a range of 3 km with a per-scan point acquisition time of 170 ms; bottom-left-side view.

A histogram of ToF distribution for a pixel in a region *P* of the image (see Figure 5.50) with an average response across the image of 180 counts in a peak is shown in Figure 5.53(a).

The acquisition time for that particular pixel was decreased to 8.5 ms per scan point and, as shown in Figure 5.53(b) a peak could still be distinguished amongst the background returns. It can therefore be assumed that the acquisition time per pixel can be significantly decreased allowing the total acquisition time to be decreased to 5.5 minutes. For wide FoV scene scans longer acquisition time are required. It is therefore of significant importance to apply image processing techniques which would allow acquisition times to be decreased to a sub µs regime to enable single-pixel scanned systems operating at 125 kHz rate be used in deployed lidars.

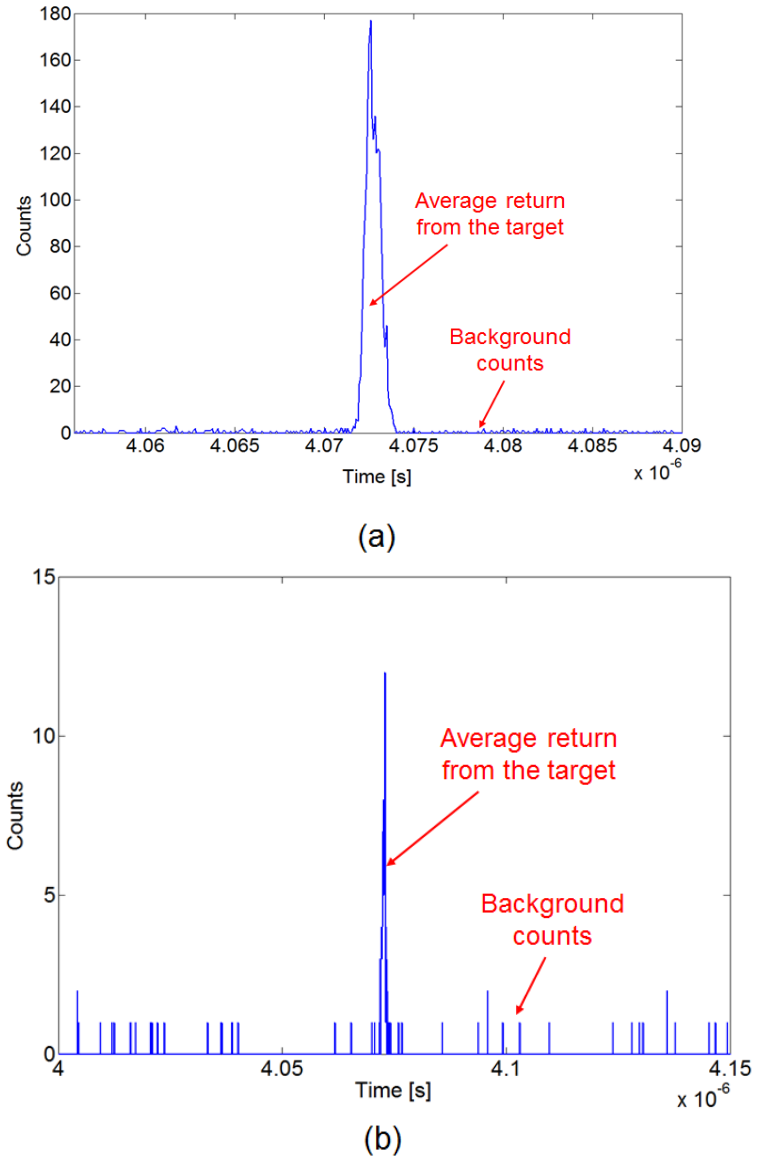

Figure 5.53. Histograms generated for a pixel in the region P of the image with (a) 170 ms acquisition time and (b) 8.5 ms.

5.10 Acknowledgements

Roger Pilkington performed site identification for potential locations of field trials. The field trials were executed with the assistance of Roger Pilkington and apprentices Jamie Natta and Dillon Finesy of Selex ES. Safety documentation for the involvement of apprentices in the field trials was completed by Dr. Peter Sinclair of Selex ES. Dr. Robert Collins of Heriot-Watt University provided advice on GuideTech programming and timing electronics and Dr. Aongus McCarthy of Heriot-Watt University provided advice for the transmitter alignment in the mono-static configuration. The GuideTech time interval analyser was provided by Prof. Gerald Buller of Heriot-Watt University.

5.11 Conclusions

In this chapter three-dimensional imaging of targets located between 800 m to 10.5 km range has been demonstrated using a single-element scanned detector in a mono-static configuration. The mono-static configuration allowed the transmitted laser beam diameter to approximately match the area of the single pixel FoV which decreased the laser power demand to 10 mW from 0.5 W required for the experiments conducted with the scanned single-element detector in bi-static configuration (see Chapter 4). The mono-static configuration shows a significant improvement in terms of system compactness, laser power requirement and laser safety precautions with comparison to the bi-static configuration.

The experimental setup, counting electronics and data acquisition have been described. The design of a mono-static transmitter was presented together with backscatter mitigation, the complex system alignment and the bore-sighting procedure.

The IRF was measured the FWHM of which was 0.85 ns. This corresponds to the depth resolution of approximately 15 cm and shows an improvement of 80 ps with comparison the IRF measured with the scanned single-element detector in a bi-static configuration. As both configurations use laser of the same pulse duration and the same single-element SPAD, it is likely that the difference in timing jitter is due to the different timing electronics used in each case.

A surface-to-surface resolution test was discussed and the data was analysed using a peak finder applied to raw data and to the data cross-correlated with the normalised

instrumental response function. The latter showed superior depth resolution ability and demonstrated the system's ability of resolving surfaces located 2 cm apart over a range of ~ 9.4 km. Spatial resolution tests were conducted and a spatial resolution of 30 cm over a range of 9.4 km was also demonstrated. This is consistent with previous reports of single-photon time-of-flight measurements where similar depth resolution characterisation was performed over a range of hundreds of metres and without the cross-correlation analysis [10].

A direct comparison between the depth and spatial resolution of the single-element scanned system in bi-static and mono-static configurations could enable a useful investigation of the impact of the difference in FWHM of the IRF on depth resolution to be performed, however the time limit on the measurements acquired with the scanned single-element detector in bi-static configuration (see Chapter 4) prevented this.

According to the optical design, the diffraction limited depth of field of the single-element scanned system focused at 9.4 km was between 5.2 km and 33 km. The size of the focal spot over those ranges was not measured however, according to the optical design simulations showed in section 3.10, a defocus exceeding the Airy disk diameter filling 66 % of the detector can be expected. The system, nevertheless, showed a capability of high resolution imaging at ranges of ~ 800 m (clock tower, section 5.8.5 and section 5.9.1.1), ~ 3 km (image mosaicing example, section 5.9.1.6). Beyond the range indicated by the design depth of field the system was still capable of acquiring high spatial resolution images of complex structures for which the recorded count rate was estimated to be close to that predicted by the power budget model (see section 5.9). This showed that the system had a large degree of tolerance for the spot diameter formed on the detector and was capable of accommodating a significant defocus. This demonstrated that the system performed near the diffraction limit implying that the alignment was performed to within the tolerance values established during the analysis.

Three-dimensional data of a target located over a distance of 800 m was analysed using the peak finder for raw data and the cross-correlation. The cross-correlation technique demonstrated improved image quality in terms of surface smoothness and sharpness of edges and, in addition, allowed the total acquisition time for a 50 × 50 scan to be reduced to 52 ms.

Long-range imaging of different types of targets such as buildings, a pylon, foliage and terrain was presented demonstrating versatility of the system in terms of identification of a wide variety of objects. The terrain was imaged at 10.5 km which is the longest range over which imaging has been demonstrated in this thesis. This is also the longest range over which imaging using an airborne single-photon scanning lidar was demonstrated in scientific literature. In the scanned single-element configuration described in Chapter 4, the maximum distance over which the imaging was demonstrated was ~ 4.2 km. Thus, the scanned single-element detector in mono-static mode showed a two-fold improvement in the target range from which returns were successfully collected. Although a high laser power of 0.5 W was used in the bi-static configuration, the large beam divergence required to cover the entire $FoV_{Scanner}$ simultaneously, resulted in the effective laser power per-pixel to be less than that applied in the case of the mono-static configuration where the transmitted laser beam extended across only several pixels. This allowed a reasonably high target return to be collected over 10 km range.

It was shown that the number of scan points for which the system was designed could be extended from 32 × 32 to 100 × 100 without any significant image distortion present. The acquisition time for returns from foliage was decreased to 22 ms per scan point. A three-dimensional spatial filtering technique was applied to the foliage data cross-correlated with the instrumental response function which allowed some of the main features of targets to be identified with an acquisition time of 11 ms per scan point, which allowed the acquisition time to be decreased to 27.5 s per frame.

Finally, image mosaicking of a large scan (approximately 5 times the value of the design $FoV_{Scanner}$) was demonstrated. The imaged target presented on the mosaic was a target located over a range of 3 km and its dimensions were 9 m × 18 m. This demonstrated that the system was capable of imaging much larger targets than assumed during the design process.

References

[1] http://uk.mathworks.com/help/matlab/ref/scatter.html

[2] http://www.princetel.com/datasheets/SMF28e.pdf

[3] https://www.google.co.uk/maps

[4] T.E. Jenkins, "*Optical Sensing Techniques and Signal Processing"*, Prentice-Hall in Optoelectronics (1987)

[5] D.V. O'Connor, D. Phillips, "*Time-Correlated Single-Photon Counting*, Academic Press (1984)

[6] A. McCarthy, N.J. Krichel, N.R. Gemmel, X. Ren, M.G. Tanner, S.N. Dorenbos, V. Zwiller, R.H. Hadfield, G.S. Buller, *Kilometre-Range, High-Resolution Depth imaging Using 1560 nm Wavelength Single-Photon Detector"*, Opt. Express, 21(7), 89-8915 (2013)

[7] R. Bracewell, R. "*The Fourier Transform and Its Applications",* McGraw-Hill (1965)

[8] A. Papoulis, "*The Fourier Integral and Its Applications",* McGraw-Hill, pp. 244-245 and 252-253, 1962.

[9] http://zone.ni.com/reference/en-XX/help/371361J-01/lvanls/crosscorrelation/

[10] G.S. Buller, R.D. Harkins, A. McCarthy, P.A. Hiskett, G.R. MacKinnon, G.R. Smith, R. Sung, A.M. Wallace, R.A. Lamb, K.D. Ridley, J.G. Rarity, *"A Multiple Wavelength Time–of–Flight Sensor Based on Time–Correlated Single–Photon Counting"*, Rev. Sci. Instrum., 76 (8), (2005)

[11] A.M. Wallace, G.S. Buller, R.C.W. Sung, R.D. Harkins, A. McCarthy, S. Hernandez–Marin, G.J. Gibson and R.A. Lamb, *"Multi–Spectral Laser Detection and Ranging for Range Profiling and Surface Characterisation"*, J. Opt. A: Pure Appl. Opt., 7, (2005)

[12] W.A. Hovis Jr., W.R. Callahan, *"Infrared Reflectance Spectra of Igneous Rocks, Tuffs and Red Sandstone From 0.5 to 22 µm",* J. OSA, 56, 5 (1966)

[13] Q. Weng, *An Introduction to Contemporary Remote Sensing*, McGraw-Hill Education (2012); pp. 10 – 30

[14] R. Jain, R. Kasturi, B.G. Schnuck, *"Machine Vision",* McGraw-Hill, Inc. (1995)

[15] R.C. Gonzalez, R.E. Woods, S.L. Eddins, *"Digital Image Processing Using MatLab*", Prentice-Hall (2004)

[16] R.A. Schowengerdt, *"Remote Sensing: Models and Methods for Image Processing",* Academic Press (1997)

[17] K.A. Stroud, D.J. Booth, *"Engineering Mathematics",* 7th Edition, Palgrave McMillan (2013)

[18] A.K. Jain, *"Fundamentals of Digital Image Processing",* Prentice-Hall (1995)

[19] R.F. Sproull, *"Principles of Interactive Computer Graphics",* McGraw-Hill (1989)

Chapter 6

Evaluation of the Transceiver in Bi-Static Configuration with a 32 × 32 Array of SPAD Detectors

6.1 Introduction

This chapter describes experimental results acquired with the lidar system operating in a bi-static configuration with a 32 × 32 array of InGaAs/InP SPADs (i.e. described as mode B in previous Chapters). The main features of the Gm-array and aspects of data acquisition, analysis and depth profile retrieval are presented. Additionally, key features of the experimental setup and optical alignment of the system are briefly discussed.

Experimental results acquired for the single-photon lidar at a wavelength of 1550 nm are described for targets located at ranges between ~ 2.8 km and ~ 6.6 km. An IRF was measured using data acquired using Haymarket chimney at a range of ~ 2.8 km as a target, the radius of curvature of which was compared with that estimated using the single-element detector in a bi-static configuration. The distance between the railings of an external staircase at Napier University building was used to test the spatial and depth resolution of the system over a distance of ~ 4.2 km. The wall at Napier University was scanned and the level of returns from this target was compared to those acquired with the scanned single-element system operating with the same laser power in a bi-static configuration. Scatterplots of a mast at Braids Hill acquired over a range of ~ 6.6 km are also shown which demonstrate the ability of the system to acquire long-range image data of complex structures.

Finally, a comparison between the single-element detector configuration and the Gm-array configuration is discussed based on system performance parameters such as detector timing jitter, laser power requirements, acquisition time and gate repetition rate as well as based on system size, weight and cost. Performance comparison between single-element and array configuration and between the mono and bi-static configurations are also discussed.

6.2 Description of the Gm-Array

6.2.1 Scope and Features

The Geiger-mode array is assembled in a complete package which contains all the necessary electronics to operate the sensor. It is a self-contained unit consisting of:

- Focal Plane Array (FPA) with an FPA sensor, power and temperature control;
- FPGA board and microcontrollers;
- Interface board comprising power control, CameraLink interface, external clock and trigger inputs [1].

Temperature and SPAD bias management are handled automatically and are regulated across a wide range of operating conditions. The unit supports both internal and external clock and trigger modes; in the internal trigger mode the image data is collected continuously at a programmable frame rate. The output data stream is transferred to a PC with bespoke control software over a standard CameraLink interface. User command and query is performed over the CameraLink serial communications channel. The system is supported by a host interface where the operating conditions can be set and monitored [1] [2].

The FPA sensor comprises the array of 32 × 32 SPAD detectors, a readout circuit, thermoelectric cooler (TEC) and a temperature sensor. The temperature is controlled by an internal control module providing the user with the ability to program and monitor temperature functions [3].

Timing data for each pixel of the FPA is buffered and formatted by the FPGA. The data is internally processed and provided to the user in the form of ToF values. The array is controlled using a PC application provided by the manufacturer [1].

Details on the camera design are provided in section 2.9.2.1.

6.2.2 Specifications

The Gm-array is sensitive to wavelengths between 920 nm and 1620 nm. It operates at a maximum frame rate of 186 kHz with an average photon detection efficiency (PDE) of 22 %, has a timing jitter of 250 ps and an average dark count rate (DCR) for the entire array of 35 kHz. The time-bin duration, T_{Bin}, is user defined with a minimum

value of 250 ps and a maximum value of 1.25 ns. The detector gate can be adjusted between 4 ns to $T_{Bin} \times 2^{13}$. The system supports three modes of CameraLink data transfer: full, medium and base with different data read-out times per frame: 3.85 µs, 7.05 µs and 13.45 µs respectively. During experiments the camera was operated in the first mode [4]. The frame rate of the detector is not limited by an additional hold-off time as it is in the case of the single-element MPD detector and thus the count rate can be estimated from Eq. 4.6 (section 4.8).

6.2.3 Data Acquisition

A graphical User Interface (GUI) provides user-friendly camera and data acquisition control. Figure 6.1 shows a screenshot of the GUI used and typical parameter settings.

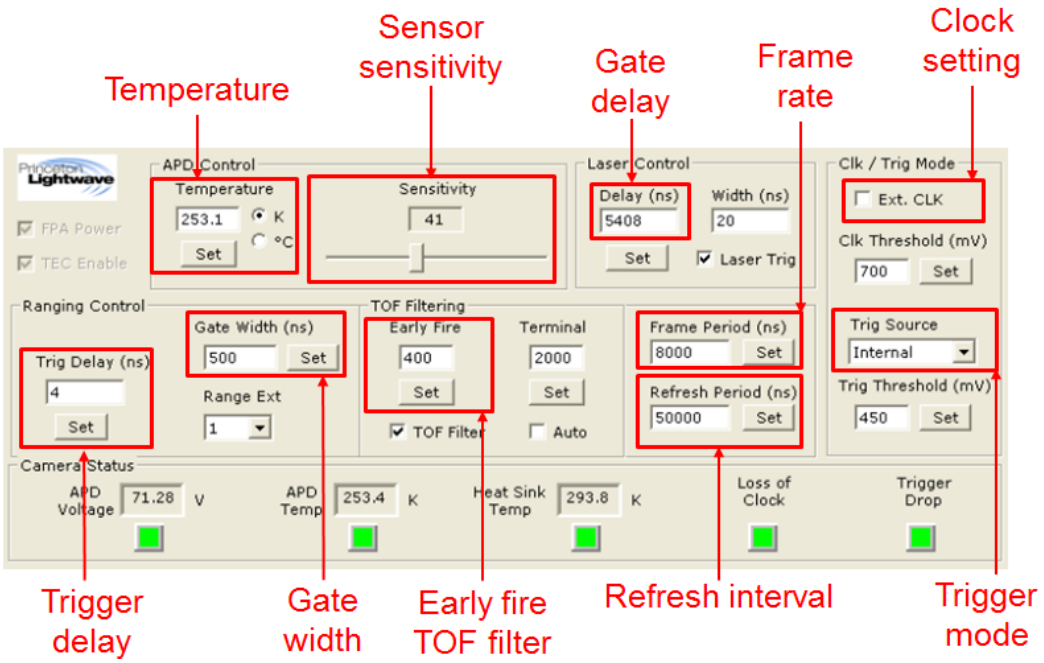

Figure 6.1. Graphical user interface supplied by the vendor for the Princeton Lightwave Gm-array.

The sensor sensitivity can be adjusted to select detection efficiencies between 0 % (setting 1) and 50 % (setting 100). The dark count rate increases with detection efficiency and varies between 0.3 kHz and 82.5 kHz. Gate delay setting allows the user to adjust the delay between the laser trigger and Gm-array gate trigger such that the target return is located within the gate. The refresh interval controls the refresh rate of the live view of a grayscale image of a target. Early fire filter can be adjusted to filter out any returns that arrive at ToF below the set number. Finally, the user can set the detector trigger mode, i. e. internal or external.

Image acquisition settings can be adjusted on a GUI. Three types of image data can be saved: grayscale, ToF and interleaved. The grayscale setting returns the total number of counts collected within a frame; the ToF setting returns the ToF as time of the photon detection from the beginning of the gate per frame and finally the interleave setting saves the ToF data and interleaves it with the grayscale data at a rate indicated by the grayscale interleave ratio setting. The acquisition time is controlled by setting the number of frames.

The GUI displays in real-time the ToF and number of photon returns per pixel for the Gm-array. The grayscale array returns values of the photon counts per pixel in each frame; the ToF data array shows values of bins within the gate in which a photon count was recorded. For example, if a gate width of 500 ns is used with a bin width of 250 ps, then there will be 2000 bins.

The data was saved in a text format where each frame represented a 32 × 33 array. Each frame is separated by an empty line where the first row contains detector settings information.

The software does not produce live histograms and therefore there was no real-time view of a correlated target return available. Separate software was developed in LabVIEW which extracted raw data frame by frame for each of 1024 pixels; it generated and displayed a set of histograms allowing the user to monitor whether there were any correlated returns arriving from the target with the selected settings.

6.2.4 Data Analysis and Depth Profile Retrieval

The data was analysed by a program developed in LabVIEW which used the peak finder method based on least-squares fit to the data points as described in section 4.13.1.1. Once the peak has been found within a histogram, the time corresponding to that peak from the beginning of the gate, t_{GP}, was identified. The absolute range to the target was then calculated from the following

$$R = \frac{(mp + t_{GP} + t_{Del})c}{2} \qquad \textit{Eq. 6.1}$$

where m is the number of a gates prior to the gate in which the target return is located, p is the gate period of 8 μs corresponding to 1.2 km distance and t_{Del} is the delay between the laser pulse trigger and gate trigger. Google maps was used to find approximate

range to a target from which *m* is calculated [5]. For instance, if the target is located at a range of ~ 2.8 km then *m* = 2.

6.3 Experimental Setup and Alignment

The experimental setup of the transceiver is the same as the one used in evaluation of the system used in mode A (scanned single-element SPAD in a bi-static configuration) and is described in section 4.2 with three exceptions. The detector used in the arrangement is the Gm-array, lens L(b) is used to focus light onto the array and the scanning mirrors were set to an on-axis position (0 V) and remain static during data acquisition.

The system used an erbium-doped fibre laser operating at a wavelength of 1550 nm (see section 4.7), which generated 800 ps duration pulses at a repetition rate of 125 kHz (pulse energy of 4 µJ, 0.5 W total power). This laser power matched the power used for the bi-static single-element scanned system and was used for all measurements presented in this chapter.

The transmitter used in the setup is described in section 4.4 while its design and divergence measurement are described in section 4.4.1 and section 4.5 respectively. The transceiver bore-sighting procedure for this configuration is identical to that used in the bi-static single-scanned system and is described in section 4.12. In this case, however, the array provided the view of the fibre source mounted in the focal point of the parabolic mirror and thus scanning of the FoV was not necessary. The position of the array detector was adjusted such that the fibre source was located at the centre of a grayscale view window of the software.

6.4 Target Locations

The system was sited in a laboratory which provided access to an urban landscape with target sites at ranges of up to 10.5 km, at varying altitude along the line of sight. Figure 4.16 shows locations of targets used in the alignment and experiments as well as the location of Selex ES where the transceiver was located. The map was taken from Google Maps [5] from which approximate distances to the target locations were estimated. Those distances are as follows: Haymarket chimney: ~ 2.8 km, Napier University: ~ 4.2 km and Braids Hill: ~ 6.6 km.

6.5 Experimental Results

6.5.1 Haymarket Chimney

The Haymarket chimney was imaged over a range of ~ 2.8 km; a visible band photograph of the target and the approximate FoV of the image are shown in Figure 6.2. A delay between the gate trigger pulse and the laser pulse trigger was set on internal detector trigger and was equal to t_{Del} = 3132 ns. This ensured that photon returns were located in the centre of a 248 ns wide gate.

The data was acquired over 1024 pixels in a 32 × 32 array representing 8 cm spatial resolution at the target and with 30 k frames equivalent to 0.24 s acquisition time per frame. Raw plotted depth images of different viewpoints of the target were analysed using the least-squares fit peak finding technique (see section 4.13.1.1) and are shown in Figure 6.3 and Figure 6.4. The range to the target surface was obtained using least-squares fit to find the peak position (see section 4.13.1.1). In Figure 6.3 metal cross bar structure is evident which matches the structure shown in Figure 6.2. Figure 6.4(a) shows the target from a side view and Figure 6.4(b) shows a top view of the chimney in which its curvature can be seen.

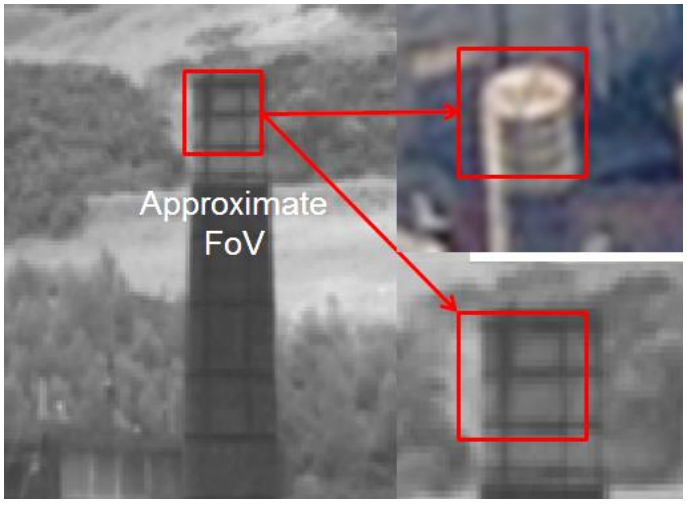

Figure 6.2. A visible-band, wide FoV photograph of the Haymarket chimney located ~ 2.8 km from the roof laboratory [5].

On the wide FoV image vertical and horizontal structure lines can be seen on the chimney. These lines can also be observed on scatterplots in Figure 6.4(a) and Figure 6.4(b) as low return regions and also as shallow dips in the chimney surface (not visible in the two-dimensional image). The scatterplot reveals that a slip-form technique was probably used for the construction of this tall industrial structure. This technique is

based on pouring concrete into special forms located within steel jack rods used as structural members and which are then extracted leaving characteristic vertical and horizontal imprints on the dry concrete [6].

From the analysis of raw data $x \approx 28.5$ cm (see Figure 6.4(c)) and arc width W (see Figure 4.22 in section 4.13.1) is approximately constant across the chimney height and is equal to $W \approx 1.39$ m. The constant value of W across the image suggests that the very top of the chimney is not tapered. From Eq. 4.13 (see section 4.13.1) the radius of curvature of the chimney is $r \approx 0.95$ m. The radius of curvature of the lower part of the chimney was calculated with the scanned single-element detector in section 4.13.1 and is on average equal to 0.95 m. This data compares very well with the results obtained with the Gm-array. It can be assumed that the scanning mirrors provide a scan step approximately equivalent to the pixel pitch of the Gm-array and confirms that the calibration of scanning mirrors was accurate.

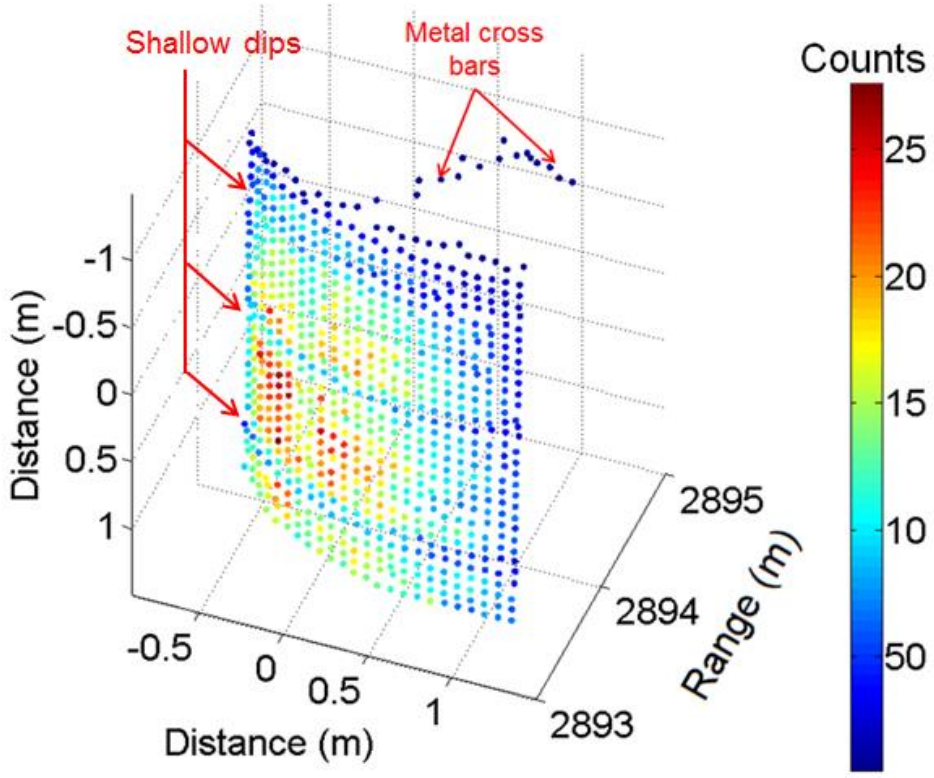

Figure 6.3. Scatterplot of the Haymarket chimney acquired with the Gm-array over a distance of ~ 2.8 km with pixel-to-pixel resolution of 7.84 cm and 0.24 s total acquisition time. Pixel colour represents the number of counts registered at a peak of a histogram at each scan point.

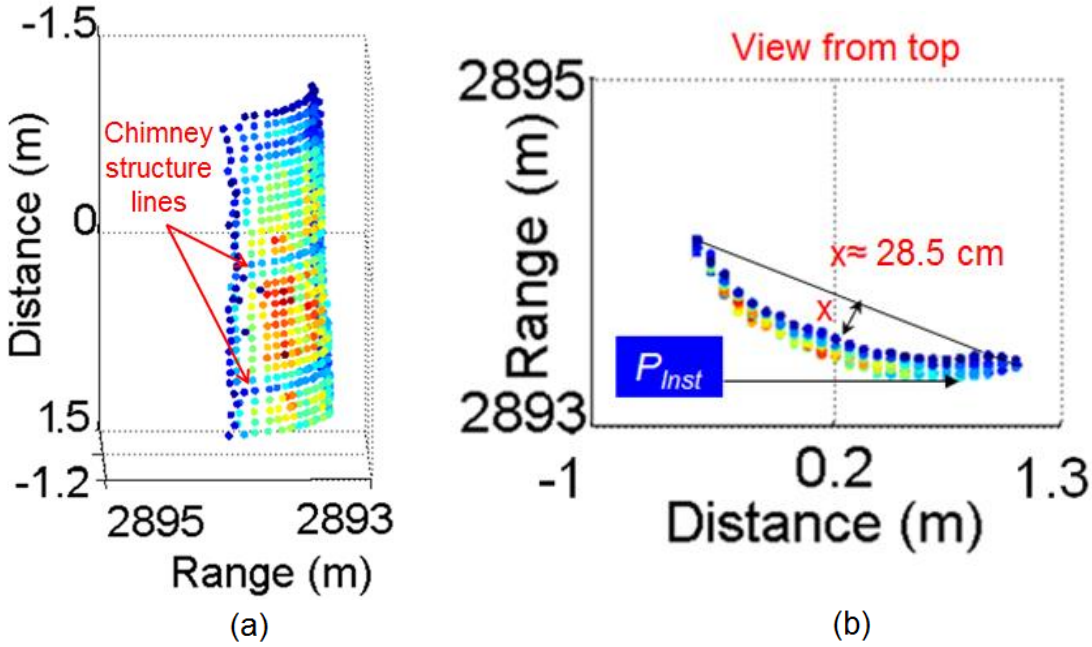

Figure 6.4. Scatterplots of the Haymarket chimney acquired with the Gm-array over a distance of ~ 2.8 km with pixel-to-pixel resolution of 7.84 cm and 0.24 s total acquisition time, where (a) is a side view and (b) is a top-view of the target.

6.5.2 Instrumental Response

The IRF was calculated for the pixel P_{Inst} (see Figure 6.4(b)) located in the region where the surface of the chimney is perpendicular to the optical axis of the transceiver. This ensures that the ToF is not smeared out by the shape of the chimney. The measured IRF is shown in Figure 6.5.

The shape of the IRF shows a typical behaviour of a system impulse function which is affected by the shape of the laser pulse, the jitter of the timing electronics and the jitter and slow diffusion tail of the detector. The effect of the electronics timing jitter is evident as a broadening of the histogram peak [7]. The FWHM of the IRF represents the system timing jitter Δt = 1 ns. The depth resolution Rs_{Depth} of the system was calculated from Eq. 4.40 (see section 4.16.1.1) and is equal to 15 cm.

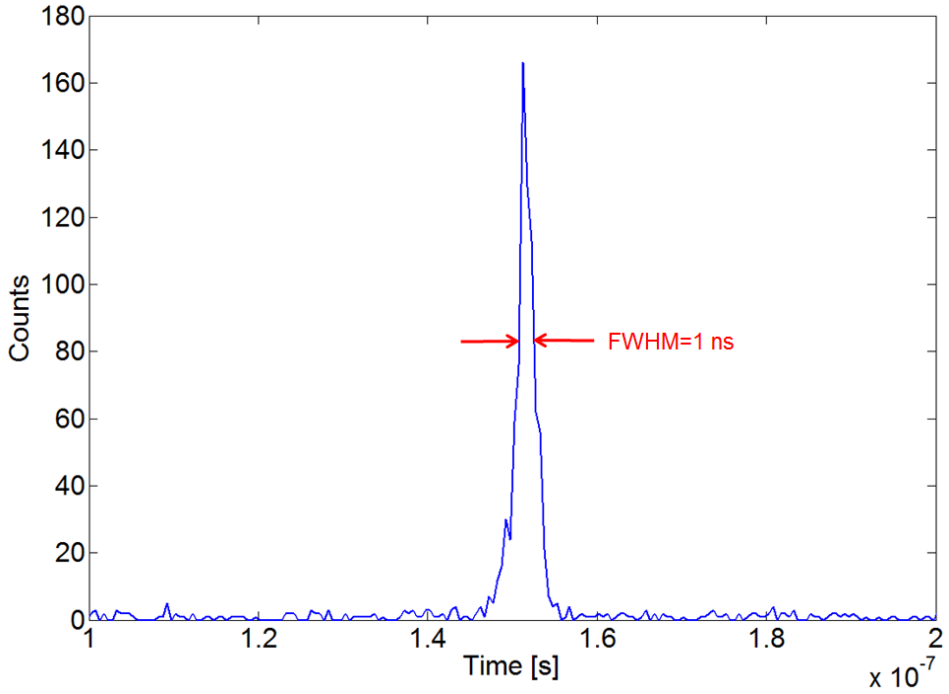

Figure 6.5. A plot of an instrumental response function. FWHM of the function was measured to be 1 ns which represents a depth resolution of approximately 15 cm.

6.5.3 Napier University Staircase

A wide FoV two-dimensional visible band image of an external staircase at Napier University located over a range of ~ 4.2 km is shown in Figure 6.6. A 32 × 32 scatterplot of the top view of the target is shown in Figure 6.7. The spatial resolution at this range is 11 cm. The data was acquired with 30 k frames equivalent to a total acquisition time of 0.24 s. The gate delay was set to 3900 ns, the gate width to 500 ns and the laser pulse energy was 4 µJ.

A line going through a pixel *P* on the image intersects two surfaces in the scene: surface *A* (the railing) and surface *B* (the wall). A histogram representing probability distribution of ToF for this pixel is shown in Figure 6.8. The position of peaks for the intersection points *A* and *B* was calculated using the least-squares fit, the range was calculated using Eq. 4.16 and was equal to 4124.4 m and 4125.5m respectively. Thus, the width of the stairs is 1.1 m. It can be noted from the histogram that the peak height significantly varies between the two points; this is because there are spaces between the individual bars of the railing which allow the laser beam to penetrate this structure and get transmitted onto the wall. The wall is solid and the FoV of the detector pixel is within the target size; these factors contribute to much higher level of returns recorded from this surface.

The image shown in Figure 6.7 was analysed with a peak threshold of 50 counts which allowed returns from stairs and the floor to be also captured.

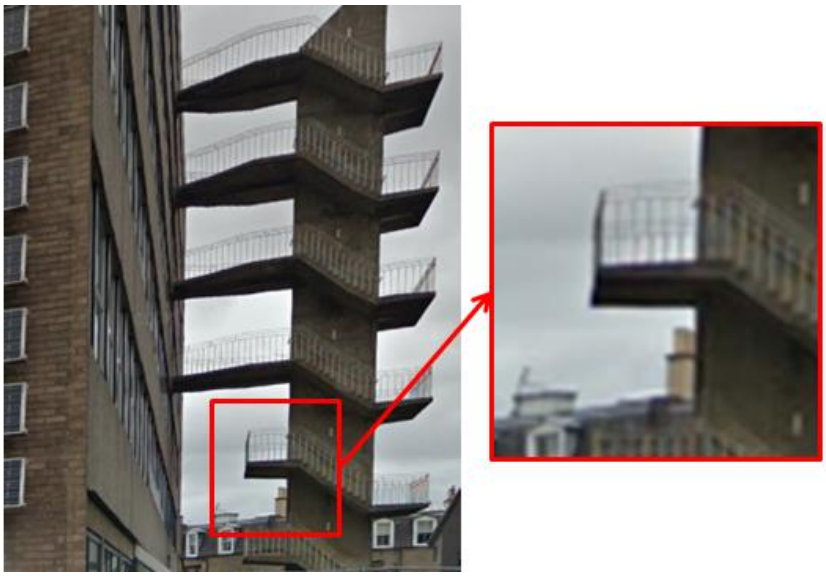

Figure 6.6. Wide FoV visible band image of the Napier University staircase.

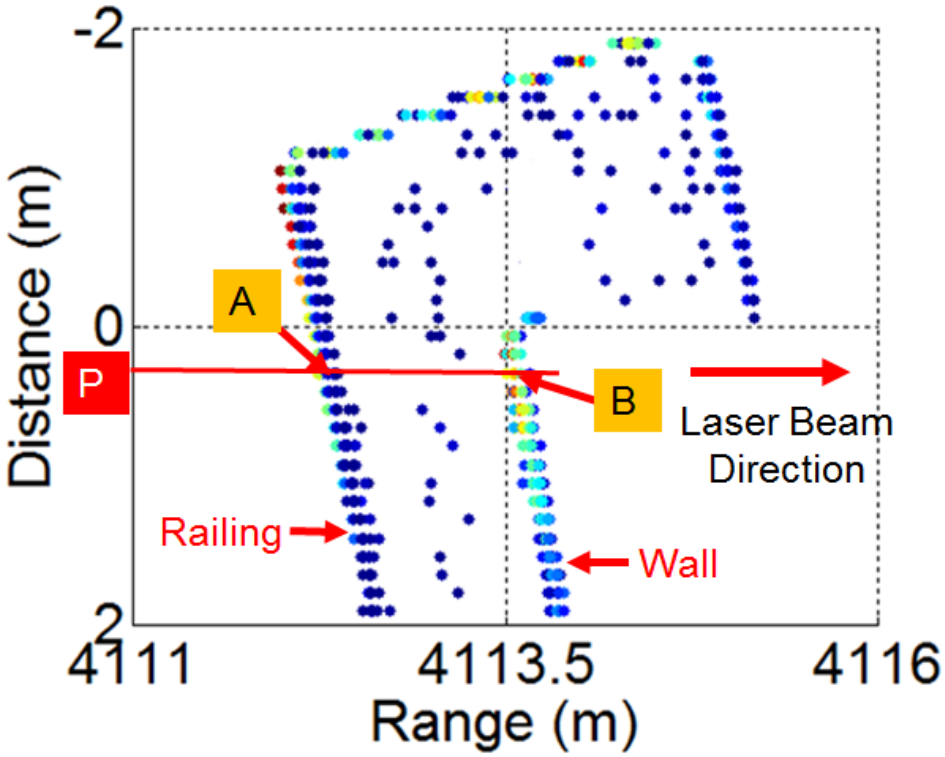

Figure 6.7. Top view of a 32 × 32 scatterplot of Napier University staircase acquired with a Gm-array over a range of ~ 4200 m with the total acquisition time of 0.24 s. A histogram of ToF probability distribution was generated for pixel P; points A and B indicate the location of two surfaces for this pixel.

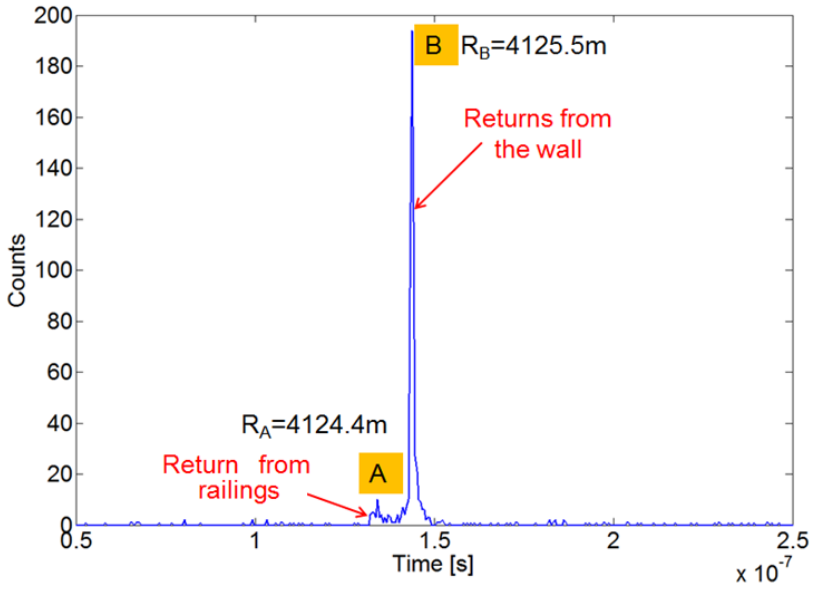

Figure 6.8. Histogram of ToF distribution for pixel P showing peak A and B which represent returns from the railing over a range of R_A = 4124.4 m and from the wall over a range of R_B = 4125.5 m respectively.

6.5.3.1 Spatial and Depth Resolution Considerations

To perform a direct comparison between the spatial and depth resolution of the scanned single-element configuration and the non-scanned Gm-array configuration a test similar to the one described in section 5.8.4 is required. The separation between the railings was used to obtain an absolute measurement of spatial and depth resolution. The spacing between the staircase railings, *d*, was measured and it is *d* = 20 cm (see Figure 6.9).

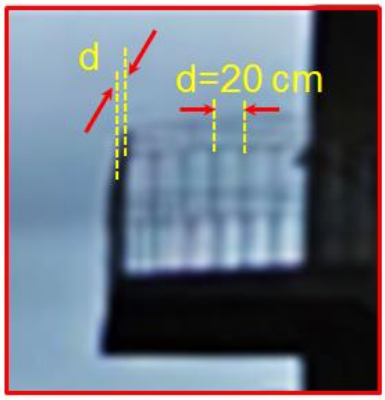

Figure 6.9. Visible-band image of the railings in the staircase; the distance between railings was measured to be d = 20 cm.

As seen in the scatterplot shown in Figure 6.10 the metal bars highlighted in areas *X1* and *X2* of the railing can be resolved which demonstrates the system's spatial resolution of 20 cm at ~ 4.2 km.

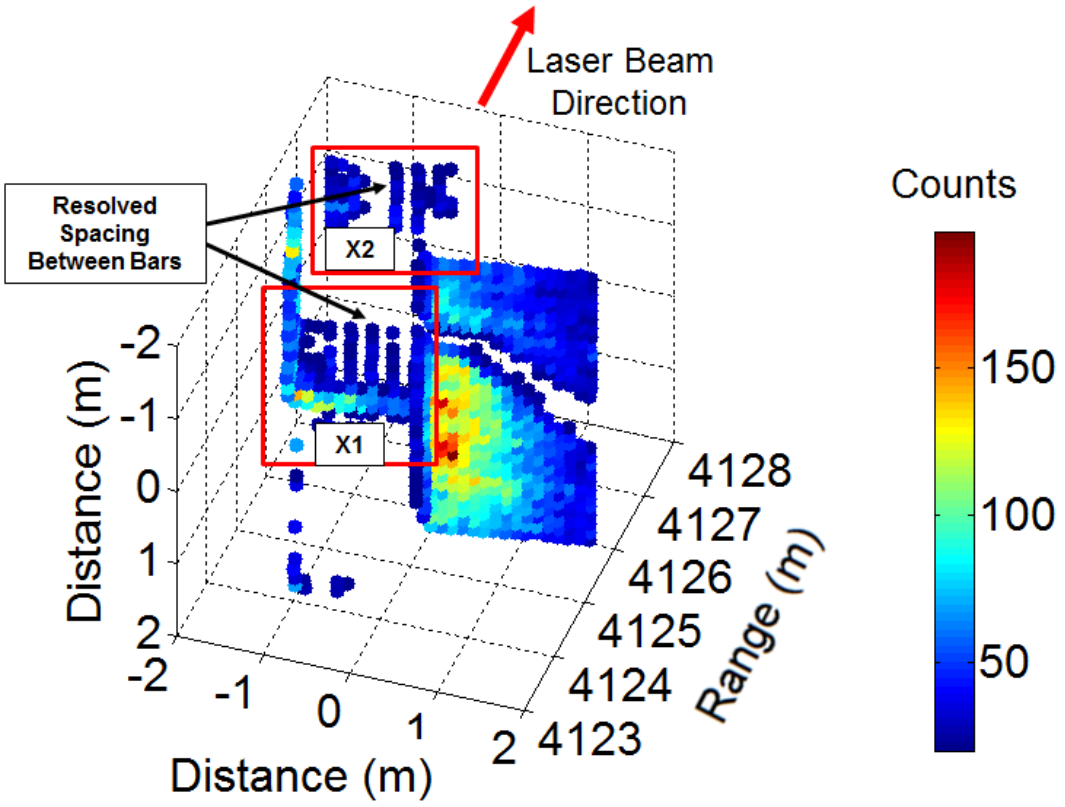

Figure 6.10. Intensity scatterplot of the staircase acquired with a Gm-detector over a range of ~ 4200 m with the total acquisition time of 0.24 s. Spacing between the railings is highlighted.

The image of this scene was also used to investigate depth resolution. As can be seen in Figure 6.11 the highlighted part of the railing is imaged in 7 steps due to the limit in the spatial resolution imposed by the number of the array pixels. The approximate length of that side of the railing is 3 m and, with the railing bar spacing of 20 cm, there should be ~ 16 of them. It is not possible to resolve each of them along the railing side because of the array pixel spacing. Nonetheless, the system demonstrates the capability of improved depth resolution in comparison to spatial resolution. Within a distance of 20 cm along the range there are multiple resolved points; the average number of the points for pixel spacing on the graph is approximately three. This implies that railings of range displacement of ~ 7 cm can still be resolved and demonstrates that depth resolution is < 30 cm and meets the specification defined in Chapter 3.

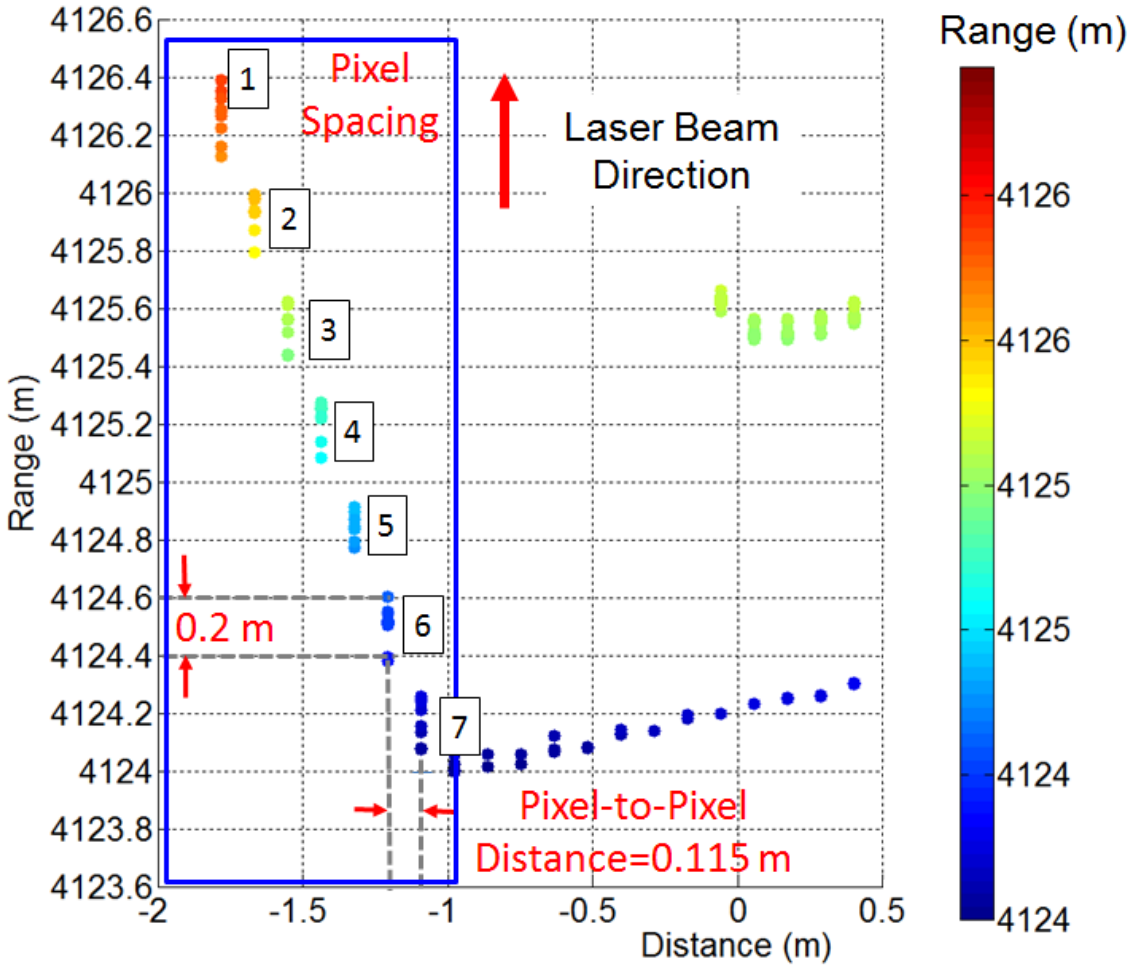

Figure 6.11. Intensity scatterplot of the right side of staircase (top view) acquired with a Gm-detector over a range of ~ 4200 m with the total acquisition time of 0.24 s.

6.5.4 Napier University Wall

The system was used to image a flat wall of a Napier University building over a range of ~ 4.4 km. A visible band wide FoV image of the target is shown in Figure 4.28, section 4.16.2. A 32 × 32 scatterplot of the target is shown in Figure 6.12, a pixel-to-pixel resolution at this range is 12 cm. The data was acquired with 30 k frames equivalent to a total acquisition time of 0.24 s. The camera was set to a gate delay of 4000 ns and gate width of 500 ns and the laser was operating with pulse energy of 4 µJ (0.5 W total power).

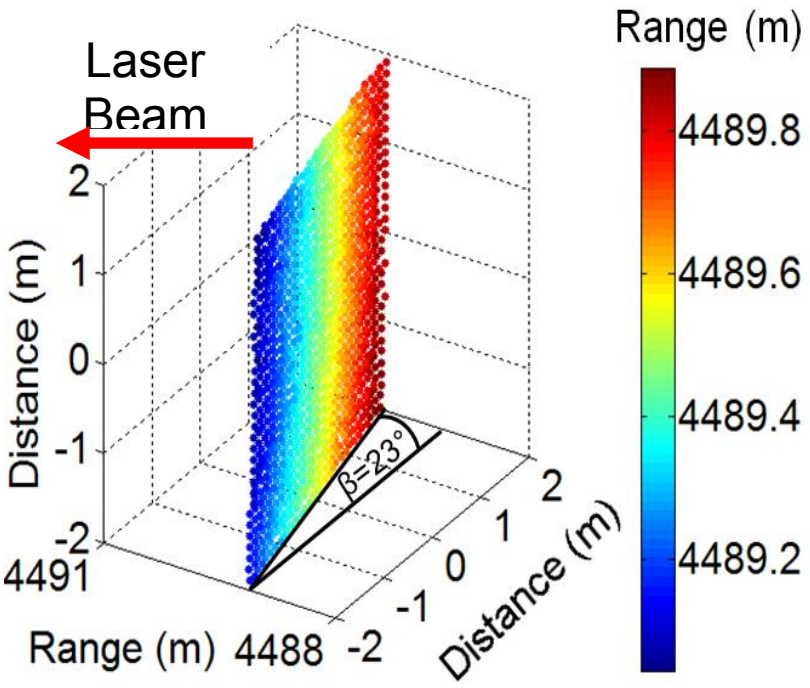

Figure 6.12. Front view of a 32 × 32 scatterplot of Napier University wall acquired with a Gm-detector over a range of ~ 4400 m with the total acquisition time of 0.24 s.

A linear fit to the top view of the data shown in Figure 6.13 was generated using a least-squares fit and is given by y = 0.435 x + 4489.4 (see section 4.16.2). From Eq. 4.42, for m = 0.435, the slope of the wall in respect to the line of sight is 23.5 °. This matches the estimation of the angle made for the scanned single-element SPAD configuration presented in section 4.16.2.

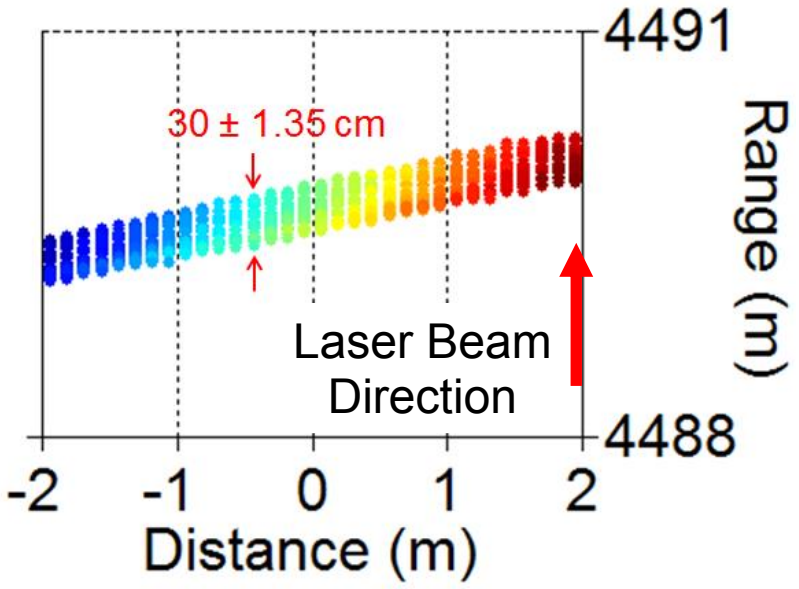

Figure 6.13. Top view of a 32 × 32 scatterplot of Napier University wall acquired with a Gm-array over a range of ~ 4400 m with the total acquisition time of 0.24 s.

The average width measured across the data points shown in Figure 6.13 is $\Delta w = 30 \pm 1.35$ cm. This suggests that the peak occurs within the FWHM of the IRF of 1 ns which equivalent to 15 cm and matches that measured with the scanned-single-element system in a bi-static configuration presented in section 4.16.2.

Figure 6.14 shows the distribution of peak photon counts across the image of the target. It resembles a Gaussian distribution of the illuminating beam along the line [*A*', *B*']. It should be noted from Figure 6.14 that there is ~ 2 m displacement between the centre of the transmitted laser beam and the centre of the scan indicating the optical axis of the system (angular misalignment of 0.172 mrad). This is an error in alignment and should have been corrected during the alignment process, ideally on a flat surface perpendicular to the line of sight. Similarly to the case presented for the scanned single-element configuration (as described in section 4.16.2) the consequence of this error is not severe because it was possible to detect a sufficient number of counts across the entire image required to build up a histogram and detect a peak.

The measured count rate for the average signal in column *A* (see Figure 6.14) was ~ 4.1 kcps which is higher than the theoretical estimate of 3.4 kcps (see Table 4.3, section 4.16). The count rate measured using the scanned single-element configuration in a bi-static mode which was measured for the same target with matching gate width of 500 ns and laser power of 0.5 W (see section 4.16.2) and is ~ 3 kcps. There is a discrepancy between the measured count rate for the two systems (array vs. single element in a bi-static configuration). However, the count rate measured with the non-scanned arrayed system and the single-element system (both configured in a bi-static mode) as well as the theoretical estimate of the count rate are in the similar ballpark. The differences between the two systems can be caused by scintillation effects which are random in nature and are difficult to predict (see Chapter 7 for details on scintillation). Also, although regions of similar levels of intensity projected on the wall for the two systems were chosen for analysis, the Gaussian beam is not identically centred on the FoV for both configurations and is off-centre from the axial position causing different levels of laser power across the scene. The model from which the theoretical estimate is calculated assumes a uniform intensity profile of the illuminating beam. In addition, the single-element detector, as opposed to the Gm-array, does have a hold-off time of 20 μs which has the effect of reducing the number of recorded counts as indicated by Eq. 4.10 (section 4.8). The expected count rate for the Gm-array was calculated from Eq. 4.6 which does not include the hold-off time limit on the count rate

[8]. The deviation between the theoretical count rate estimate and the value measured with the non-scanned mono-static system originate from limitations of the theoretical model which does not take into account the angle of incidence of the target to the optical axis of the system as well as the Gaussian intensity. Also, the reflectivity of the target as well as the properties of the target are unknown. Despite of these differences and approximations there is a reasonable agreement between the estimated count rate and the count rate recorded with the single-element configuration and the Gm-array configuration.

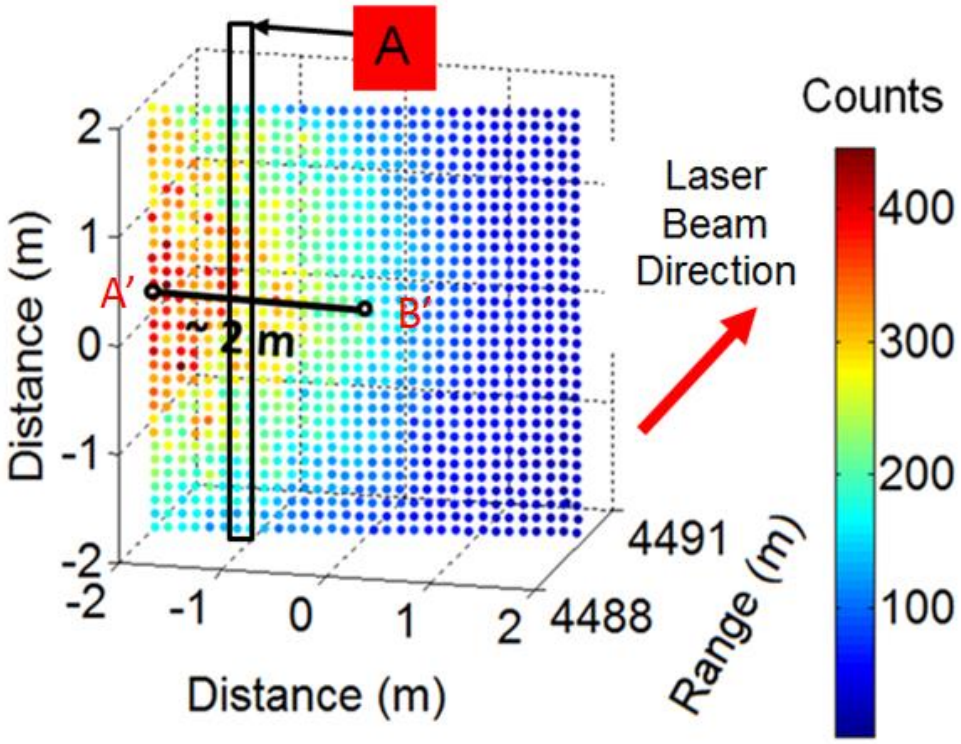

Figure 6.14. Top view of a 32 × 32 scatterplot of Napier University wall acquired with a Gm-detector over a range of ~ 4400 m with the total acquisition time of 0.24 s. Area A highlights a column from which the data is used for the count rate analysis.

6.5.5 Braids Hill Mast

A visible band wide FoV image of the Braids Hill mast is shown in Figure 6.15. The target was imaged over a range of ~ 6.6 km with a detector gate width of 500 ns and the gate delay set to 4500 ns.

Figure 6.15. Wide FoV visible band image of Braids Hill mast located at a range of ~ 6.6 km from the roof laboratory.

Multiple view 32 × 32 scatterplots of the target are shown in Figure 6.16(a) and Figure 6.16(b). The spatial resolution at this range is 18 cm. The plots demonstrate the ability of the system to resolve complex structure and detail in the target which is not easy to discern in the two-dimensional image, enabling recognition of multiple features of the target such as aerials and their spatial distribution. Figure 6.17 shows a plot of a side view of the mast which spreads across a depth of 2.2 m. Within this range as many as 8 spatially distributed surfaces can be distinguished showing that the system offers depth resolution of 28 cm over a range of 6.6 km. Dimensions of the image features are unknown; the number of pixels across which returns from the aerials were recorded vary from 3 – 1 (points *A*, *B* and *C* in Figure 6.16(a)). There is no signal cross-talk to the neighbouring pixel resulting from defocus which makes the structure appear wider than it really is. The structure *C* is focused to a single pixel which indicates that at 6.6 km the Airy disk is within the pixel area.

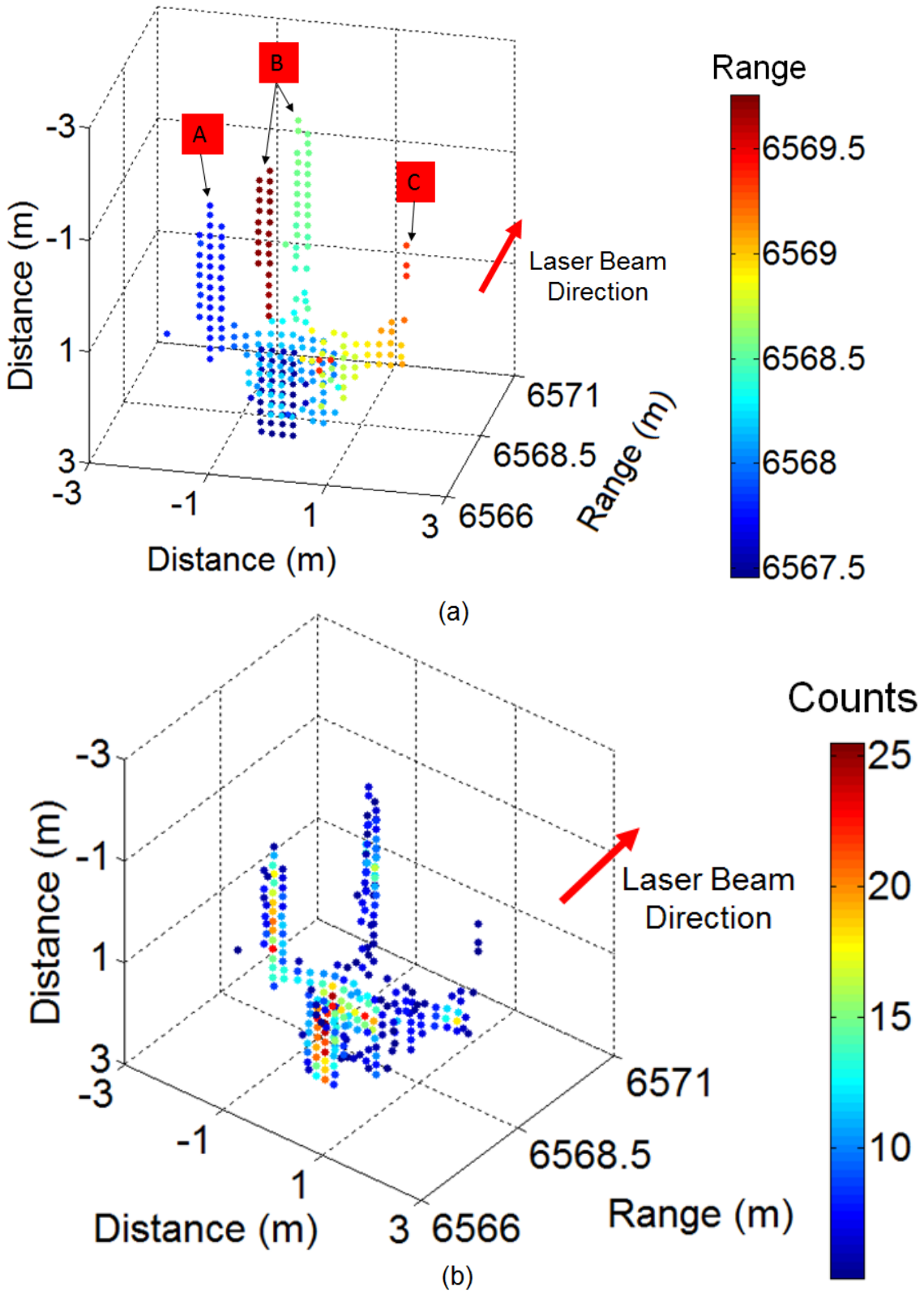

Figure 6.16. 32 × 32 scatterplots of Braids Hill mast acquired with a Gm-array over a range of ~ 6600 m with the total acquisition time of 0.24 s. (a) Is an oblique view of the target where the pixel colour represents range; in (b) the pixel colour represents the number of counts is a peak.

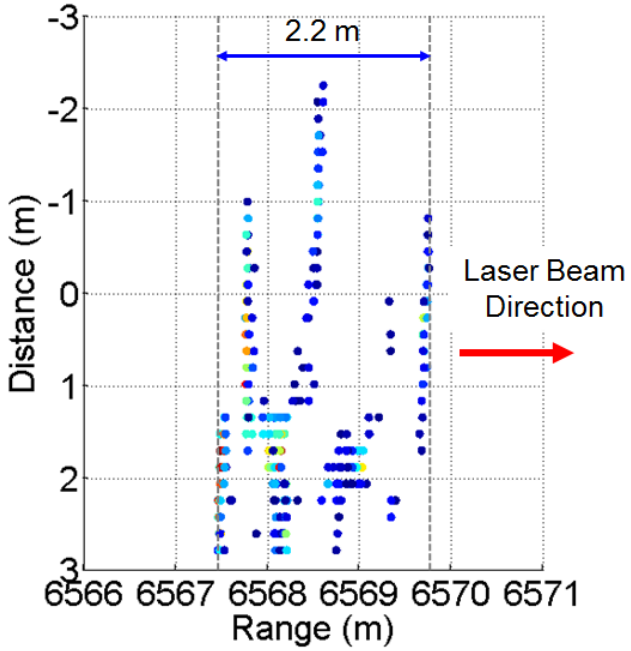

Figure 6.17. Side-view 32 × 32 scatterplots of Braids Hill mast acquired with a Gm-detector over a range of ~ 6600 m with the total acquisition time of 0.24 s.

6.5.6 Comparison of Single-Element Detector and Gm-Array Configurations

This section compares the performance of the system operating with the two detectors (single-element detector and the Gm-array) according to a set of criteria. In addition, a comparison between the single-element scanned system operating in a bi-static and in a mono-static mode is performed.

The scanned single-element configuration is compared against the non-scanned configuration based on three groups of criteria: system performance, physical parameters and cost. The performance criteria include: spatial and depth resolution, depth and spatial measurement accuracy, detection efficiency and its uniformity across the FoV, dark count rate, hold-off time, data acquisition time, data transfer and recording speed, pixel-to-pixel step control and FoV coverage. The physical criteria comprise system dimensions, its weight and number of components; these measures are used to evaluate ease of implementation into an airborne platform and a turret. Additional criterion on evaluating the design is the cost breakdown for the main components required to build and operate the system.

6.5.7 Comparison of Scanned Single-Element Detector and Non-Scanned Arrayed Detector Configurations

6.5.7.1 Performance Parameters Comparison

Table 6.1 shows system performance parameters for the single-element detector and for the Gm-array configuration. The primary comparison is performed based on the experimental system performance parameters which are mainly limited by the laser repetition rate of 125 kHz and its pulse width of 800 ps.

In the experimental setup both the single-element detector and the Gm-array operate at the repetition rate of 125 kHz. In case of the scanned system, the scanning mirrors cover a small fraction of the FoV at a time, which, for a FoV comprising 32 × 32 points, requires an acquisition time 1024 times longer than that required for the Gm-array. To record the same number of counts the single-element configuration requires acquisition time of ~ 4 min compared to 0.24 s required by the Gm-array. Therefore, the Gm-array provides three orders of magnitude faster acquisition time over the single-element scanned system when both detectors operate at a fixed gate repetition rate (125 kHz). Additionally, in the case of the mono-static single-element system the time required to save the data is 25 % longer than the time-tag acquisition due to the data transfer (see section 5.3.1). This would increase the total acquisition time to over 5 minutes.

The maximum gate repetition rate of the single-element detector is 1 MHz with the minimum gate hold-off time of 10 μs [2]. Figure 6.18 shows a plot of SPAD gate repetition rate vs. count rate for 10 μs hold-off time and 5 % photon return per pulse (from Eq. 4.10). This shows that the detector hold-off time limits the effective count rate to 1 MHz. Although the maximum gate repetition rate of the single-element detector is 133 MHz and it is significantly higher than the maximum frame rate of the Gm-array (186 kHz), the hold-off time prevents the device from operating at repetition rates close to the maximum. For hold-off times <10 μs the dark count rate increases above 80 kcps. The single-element SPAD operating at a repetition rate of 1 MHz can be approximately matched by five pixels of the array operating at its maximum repetition rate. This shows that the Gm-array can offer approximately 200 times faster acquisition times than the single-element SPAD which is limited by the hold-off time.

Parameter	Single-element Detector	Gm-Array
Depth resolution (min)	≤ 30 cm	≤ 30 cm
Spatial resolution (min)	30 cm at 10 km	20 cm at 4.4 km
Hold-off time (experimental)	20 µs	5.4 µs [2]
Hold-off time (minimum before dark counts < 80kcps)	10 µs	5.4 µs
SPAD dark counts rate	30 kHz [8]	35 kHz [3]
Detector timing jitter	100 ps	250 ps
Laser pulse width	800 ps	800 ps
Instrumental response FWHM	Bi-static setup – 0.93 ns, Mono-static setup – 0.85 ns	Bi-static setup: 1 ns, Mono-static setup: 0.95 ns
Detection efficiency and its uniformity across FoV	30 % average, no variation across FoV	22 % average, varies across FoV (6 % standard deviation)
Maximum gate repetition rate	133 MHz	186 kHz
Experimental gate repetition rate	125 kHz	125 kHz
Acquisition time for a 32 × 32 image (at the experimental gate repetition rate)	246 s	0.24 s
Scanner max rate.	2.86 kHz	N/A
Data read-out time and saving	25 % of time-tag acquisition time	3.85 µs min out of 5.5 µs hold-off during each frame
Accuracy of depth measurements	Given by Eq. 2.20	Given by Eq. 2.20
Accuracy of spatial measurements	Error in scanner positioning accuracy 4 %, 0.1 µrad for 28 µrad	Error in pixel positioning (data unavailable)
Pixel-to-pixel (array) or scan step size (single-element)	Adjustable. Minimum step size: ~ 17 ± 0.7 µrad in the object plane	Fixed pixel pitch: 28 µrad.
Maximum FoV coverage (at 10 km)	100 × 100 pixels, 30 cm per pixel, 30 × 30 m	32 × 32 pixels, 30 cm per pixel, 9.6 × 9.6 m

Table 6.1. Experimental system performance comparison between the single-element detector and Gm-array configuration.

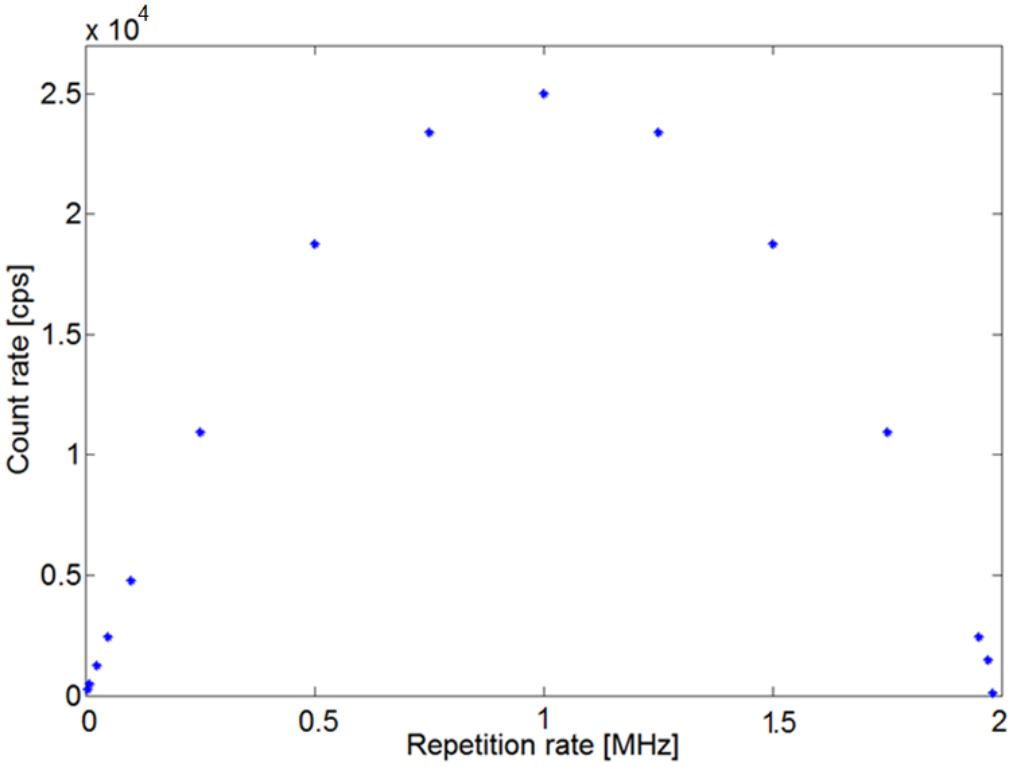

Figure 6.18. SPAD gate repetition rate vs. count rate with 1 µs hold-off time and 5 % photon return rate per pulse.

The single-element scanned configuration can provide < 30 cm spatial resolution at ~ 10 km (see section 5.8.4). The spatial resolution of the Gm-array in the transceiver is 20 cm at a range of 4.5 km. The IRF for both detectors is approximately 1 ns which indicates a comparable depth resolution of ~ 15 cm. In addition, when making a comparison between scatterplots of targets such as Haymarket chimney and the Napier University building generated with the scanned single-element and the Gm-array, both operating in a bi-static configuration, the images show a comparable degree of detail (see results presented in Chapter 4 and Chapter 6).

In the case of the Gm-array, a focal spot defocus can have a negative effect on spatial resolution as the defocused signal from one pixel will be detected by a neighbouring pixel making two spatially sparse targets appear as a continuous surface in the image. Therefore, ensuring that the system is focused at the range that provides required depth of field is critical in the implementation of arrays.

Tests performed with the system operating in the mono-static single-element configuration (see Chapter 5) show a high degree of target detail. This was achieved by the ability of the scanned configuration to adjust both the size and the number of scan steps which was impossible with the Gm-configuration. Increasing the number of steps beyond the diffraction limit of the system, called over-sampling, in principle, does not

improve the spatial resolution which is limited by the diameter of the Airy disk. However, it permits the spaces between the scan points to be filled, allowing for a continuous target surface coverage. Over-sampling can be easily implemented by the scanned configuration by increasing the number of scan points at an expense of acquisition time. The implementation of over-sampling with the Gm-configuration requires complex image processing techniques, such as spatial filters, to fill in the information between the spacing of the scan points which increases the time and cost of image processing. Additionally, the Gm-array limits the FoV to 32 × 32 pixels when compared to the scanned single-element system. Image mosaicing, or a large number of pixels in the array, are required for larger fields-of-view. The scanning system offers versatility in terms of the number of scan points and the scan step size; this is advantageous over the array as it permits imaging of larger scenes or imaging of targets with a smaller scan step.

Both, the single-element SPAD and the array offer comparable DCR and detection efficiency which are typically in the range of 30 kHz and 30 % respectively. The accuracy (standard deviation) of depth measurements in both cases is limited by the number of correlated counts recorded by the SPAD and by the detector timing jitter (see section 2.10.5). The single-element SPAD has a lower timing jitter than the array providing improved depth measurement accuracy for the same number of counts (see Eq. 2.20). The scan step accuracy for the single-element configuration depends on the accuracy of the scanner positioning which is 0.1 µrad for 28 µrad step size (0.36 %). The array eliminates this problem as scanning mirrors are not in use and the spatial data is acquired without any variation in the FoV.

6.5.7.2 Size and Weight and Number of Components Comparison

Table 6.2 shows comparison between size, weight and timing electronics components used for the scanned single-element detector configuration and the Gm-array configuration.

The dimensions of the breadboard and safety enclosure are identical for the two configurations (60 cm × 90 cm × 30 cm) which was imposed by the opto-mechanical design. The weight of the two systems is also similar (~ 97 kg). The number of electronic components required by the single-element configuration significantly exceeds that for the Gm-array configuration. This is mainly due to the larger number of

components required to control scanning mirrors in two dimensions. The Gm-array is assembled in a complete package containing all the necessary electronics required for timing and synchronisation. The total weight of timing electronics required to operate the scanned single-element detector configuration is ~ 18 kg whereas that required for the non-scanned arrayed detector configuration it is ~ 8 kg.

If the two systems were to be designed separately, the array configuration would eliminate the need for the scanning mirrors and the pair of the relay lenses, enabling a decrease in system's volume and weight. Nevertheless, larger pixel size of the arrayed detector (100 μm) than the 25 μm pixel size of the single-element SPAD requires the total focal length of the system to be four times larger than that for the single-element configuration. Long focal length systems require path folding mirrors and may increase the system's volume and weight. As indicated in section 3.3 a smaller pixel size in the array would be desired in order to decrease the focal length.

In order to implement the opto-electronic components into a turret of limited volume and an effective aperture of ~ 30 cm (see section 3.2) a compact system of small size and weight is needed. The system implementing the Gm-array offers advantages in terms of a lower number of components and lower weight than the non-scanned single-element configuration and is potentially more suitable for a compact and light-weight design.

Parameter	Single-element Configuration	Gm-Array Configuration
Dimensions of the breadboard and safety enclosure	60 cm × 90 cm × 30 cm	60 cm × 90 cm × 30 cm
Weight of the breadboard and safety enclosure	~ 97 kg	~ 97 kg
Timing electronics components	- SPAD driver and cables; - Board level pulse/delay generator BME02P; - Pulse splitter AVTECH; - PXI (PCI eXtensions for Instrumentation) – a PC based platform for measurement and automation systems) [9] which is used as a platform for the programmable FPGA used to control scanning mirrors; - NI FPGA board (scanner voltage i/o) [10]. - Connector block for interfacing input/output signals to plug in National Instruments (NI) data acquisition (DAQ) devices [11]; - Power supply for scanning mirrors; - Time interval analyser (GuideTech board) - Laser driver board; - Control PC.	- Sensor control board; - FPGA board and microcontrollers; - Interface board; - CameraLink cables; - Power supply for the Gm-detector; - Laser driver board; - Control PC.
Weight of the timing electronics	18 kg	8 kg

Table 6.2. Volume and weight comparison.

6.5.7.3 Cost Breakdown Comparison

Table 6.3 shows cost breakdown of main components for the single-element detector and the Gm-array configurations.

The cost of components was estimated based on current prices. The total estimated cost of the Gm-array configuration is approximately double that of the scanned single-

element configuration. It can be concluded that although the scanned configuration requires more components it is more cost effective. Analogue lidar systems operating over long ranges tend to require powerful laser sources; the cost of these sources can reach tens of thousands of pounds. Using single-photon technology minimises the cost of lasers as less powerful sources can be used over similar ranges. However, the high sensitivity of single-photon detectors and the complexity that is required to design and build them significantly increases their price when compared to standard analogue APD detectors which cost between £500 and £2000 [12].

Single-element Configuration	**Cost £**	**Gm-Array Configuration**	**Cost £**
MPD detector and module	20 k	Integrated camera array, timing electronics, CameraLink cables, control PC and software	100 k
Laser	5 k	Laser	5 k
CCD Camera	1 k	CCD Camera	1 k
Optical components	11 k	Optical components	7 k
Time interval analyser	5 k	-	-
Pulse/delay generator	1 k	-	-
Scanning mirrors	3.5 k	-	-
PXI	4.5 k		
FPGA card	2 k		
Connector block for interfacing i/o signals	0.5 k	-	-
Control PC	1 k	-	-
Total	54.5 k	Total	113 k

Table 6.3. Cost breakdown comparison.

6.5.8 Comparison Conclusions

The scanned single-element configuration offers advantages in terms of improved detector timing jitter and shorter bin width allowing higher depth resolution than the Gm-array configuration. In addition, the scanned configuration allows the scan step and the number of steps to be controlled which can be beneficial in imaging objects with

varying spatial and temporal features. The array configuration is advantageous in terms of acquisition time, allowing it to be two orders of magnitude lower than in the case of the single-element detector at kHz repetition rates. The single-element detector offers repetition rates in the range of hundred MHz, however long hold-off times reduce the effective repetition rate to 1 MHz. The single-element SPAD operating at a repetition rate of 1 MHz can be approximately matched by five pixels of the array operating at its maximum repetition rate (186 kHz). This shows that the Gm-array offers significantly faster acquisition times (approximately 200 times faster) than the single-element SPAD.

Advantages and drawbacks of the bi-static and mono-static configurations are discussed in section 2.3.2.1. The main benefit of the mono-static setup is the compactness that it offers. The main disadvantage is backscatter which may expose a single-photon detector to an excess level of laser energy and cause damage. Careful consideration of the detector response and protection mechanisms against photon saturation needs to be taken into account when designing a mono-static system.

The Gm-array can be purchased in a package with optimised and integrated timing electronics and supported by a user-friendly interface. The scanned single-element configuration incorporates scanning mirrors and relay lenses thus requiring a higher number of optical and electronic components. This increases the overall size and weight of the system and makes integration into an air platform more challenging.

The component cost breakdown for the two systems shows that the cost of the Gm-array configuration is double that of the scanned single-element system.

6.6 Acknowledgements

The system was bore-signted with the assistance of Dr. Philip Hiskett and Dr. Karen J. Gordon of Selex ES. The Gm-array data was acquired thanks to the assistance of Dr. Philip Hiskett.

6.7 Chapter Conclusions

This chapter presents the experimental results acquired with the Gm-array configuration operating in a bi-static mode.

Kilometre-range depth imaging using non-scanned Gm-array in bi-static configuration was demonstrated. An IRF was measured the FWHM of which was equivalent to depth resolution of 15 cm and matched that measured with the scanned single-element detector configuration in a bi-static mode. A staircase of the Napier University building was used to confirm spatial resolution of 20 cm at 4.4 km and depth resolution < 30 cm.

The system was used to image targets similar to those captured with the mono-static single-element configuration, such as Haymarket chimney and the Napier University wall. The radius of curvature of the chimney was measured to be $r \approx 0.95$ m and approximately matched the estimated radius of curvature of the lower part of the chimney measured with the single-element system. This demonstrated that the two systems provided a matching FoV per pixel. The average count rate for one column of the Napier University wall depth data was also compared between the Gm-array and the single-element configurations (both operating in a bi-static mode) as well as with the theoretical estimate of the count rate and was confirmed to be in the similar ballpark. Furthermore, imaging of a mast over a distance of 6.6 km was presented.

Finally, a comparison between the scanned single-element configuration and the Gm-array configuration was executed in terms of system performance parameters, physical parameters and cost. It was concluded that the Gm-array configuration is advantageous in terms of acquisition time and system compactness and could be easier to integrate into an airborne platform. The cost the Gm-array system is, however, double of that required to build a non-scanned single-element detector system. The use of the scanned single-element detector offers advantages in terms of lower detector jitter and shorter bin width proving higher depth resolution. It also allows the adjustment of the number and size of scan steps which can be beneficial when imaging targets with a large number of spatial and temporal features.

References

[1] M.A. Itzler, M. Entwistle, M. Owens, K. Patel, X. Jiang, K. Slomkowski, S. Rangwala, "*Geiger-Mode Avalanche Photodiode Focal Plane Arrays for 3D Lidar Imaging"*, Imaging and Appl. Opt., OSA Technical Digest (2011)

[2] M.A. Itzler, X. Jiang, M. Entwistle, K. Slomkowski, M. Owens, A. Tosi, F. Acerbi, F. Zappa, and S. Cova, *"Advances in InGaAsP-Based Avalanche Diode Single Photon Detectors*", J. Mod. Opt., 583–4, 174 – 200 (2011)

[3] M.A. Itzler, M. Entwistle, M. Owens, K. Patel, X. Jiang, K. Slomkowski, S. Rangwala, "*Comparison of 32 x 128 and 32 x 32 Geiger-Mode APD FPAs for Single-Photon 3D LADAR Imaging"*, Proc. SPIE, 8033, 8033G-1 (2011)

[4] http://www.princetonlightwave.com/images/pli_content/PLI%2032x32%20GmAPD%20Camera%20-%20ProdSum%20Rev%202.2.0.pdf

[5] https://www.google.co.uk/maps

[6] B. Binani, *"Slip Form Technique for High-Rise Structures (Chimneys)",* Constr. Industry Rev., 17-23 (2014)

[7] A. McCarthy, R.J. Collins, N.J. Krichel, V. Fernandez, A.M. Wallace. G.S. Buller, *"Long-Range Time-of-Flight Scanning Sensor Based on High-Speed Time-Correlated Single-Photon Counting*", Appl. Opt, 48, 32 (2009)

[8] A. Tosi, A. Della Frera, A. Bahgat Shehata and C. Scarcella, "*Fully Programmable Single-Photon Detection Module for InGaAs/InP Single Photon Avalanche Diodes with Clean and Sub-Nanosecond Gating Transitions"*, Rev. Sci. Instrum. 83, 013104 (2012)

[9] http://sine.ni.com/nips/cds/view/p/lang/en/nid/202013

[10] http://www.ni.com/rseries/

[11] http://sine.ni.com/nips/cds/view/p/lang/en/nid/1180

[12] http://voxtel-inc.com/products/laser-rangefinder-modules-and-devices/

Chapter 7

High-Speed Turbulence Measurements Using InGaAs/InP SPAD Detectors

7.1 Introduction

This chapter introduces the optical properties of Earth's atmosphere. It describes laser beam propagation through an optically turbulent atmosphere and introduces parameters used to characterise optical turbulence. Understanding the effect of turbulence on the performance of optical systems which rely on a long-range transmission and detection of electromagnetic radiation through the atmosphere is critical in the assessment of ToF lidar performance. This work experimentally determines parameters which characterise optical turbulence using a new approach utilising single-photon lidar. This data was obtained from sets of measurements performed over ranges of 5.6 km and 9.5 km. Both a single-element InGaAs/InP SPAD and a 32 × 32 array of InGaAs/InP SPADs were used in the experiments presented in this chapter. The results obtained were used to analyse the effect of background noise on the scintillation index, σ_I^2. Finally, this chapter introduces a comparative method of estimating the refractive index structure parameter, C_n^2.

7.2 The Earth's Atmosphere and its Effects on Active Imaging Systems

The Earth's atmosphere is a gaseous envelope that surrounds the planet, which contains a large number of different molecular species; primarily nitrogen, oxygen, carbon dioxide, nitrous oxide and water vapour. The composition, density and temperature of these gases vary as a function of latitude, longitude and altitude [1]. The atmosphere is in constant flux as a result of energetic stimulation from solar energy causing wind and turbulence. Although the atmosphere extends up to several hundred kilometres above the mean sea level; when photographed from space it resembles a thin blanket covering the Earth (see Figure 7.1 (a)) [1]. As early as the Renaissance the atmosphere was regarded as the "seat of volatile elements" [1]. During that time the Dutch mathematician, Christian Huygens, when observing the sun through a telescope compared its image to "boiling seas and belching mountains of fire" and noted that "it

is nothing but trembling motion of the vapour of our atmosphere which is likewise the cause of the stars twinkling" [2]. From the atmosphere's structure, chemical composition and physical properties, one can determine the resulting performance limits of systems which rely on propagation of electromagnetic radiation through the atmosphere.

7.2.1 Structure and Constituents of the Atmosphere

The atmosphere is divided into regions based mostly on temperature variations that can be described as a function of altitude (Figure 7.1(b)) [1] [3]. The *troposphere* is the lowest level of the atmosphere and this is the region in which the majority of weather occurs [4]. It extends from the surface of the Earth to an altitude of approximately 11 km and contains about 75 % of the entire atmospheric mass [3]. The *tropopause* is an isothermal layer extending up to 9 km above the troposphere where the air temperature remains constant [3].

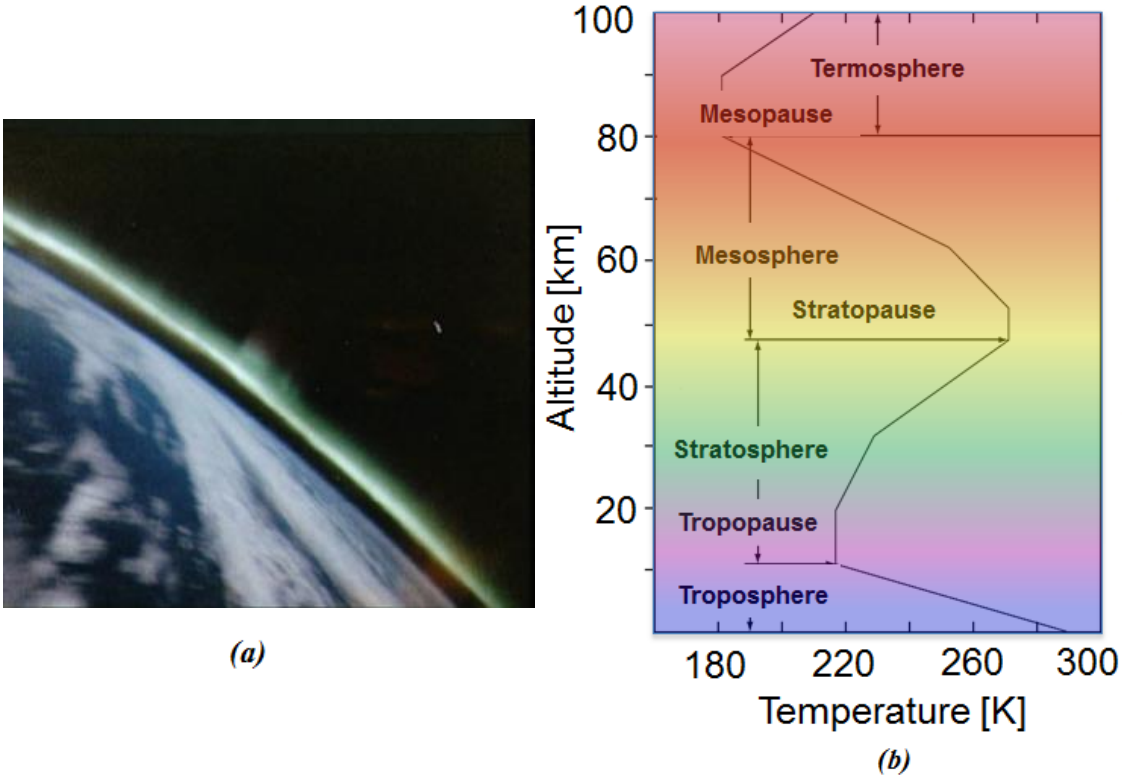

Figure 7.1. (a) Earth's atmosphere photographed from space during the space shuttle mission in 1991 (mission STS-039), (b) structure and temperature profile of the atmosphere [1].

The *stratosphere* is above the tropopause and extends from an altitude of about 20 km to 48 km [3]. It contains ozone gas, which absorbs ultraviolet light creating heat energy, resulting in a gradual increase of temperature in this layer [3]. The *stratopause*

is another isothermal layer above which the *mesosphere* is located [3]. The *mesospause* extends up to 90 km and is the coldest atmospheric layer [3]. *Karman line* is a commonly defined boundary between the atmosphere and the outer space and lies at an altitude of 100 km which represents a point where the atmosphere is too thin to support aeronautical flight. Nevertheless, the atmosphere does not abruptly end at a specific height, but becomes progressively thinner with altitude. The *termosphere* extends up to 900 km where the temperature increases to - 70 °C from a minimum of about - 85 °C in the mesopause [3].

Natural processes that occur in the atmosphere and industrial processes emit solid or liquid particles which remain suspended in the air. These particulates can be classified as fine (up to 2.5 μm) and coarse (2.5 μm to 10 μm) [5]. Fine particles include grains of mineral dust and water vapour [5]. Coarse particles comprise precipitation (water droplets and ice), sand, soil and pollen whipped up by atmospheric circulation [5].

7.2.2 Absorption, Scattering and Refraction

The atmosphere is a fluid that absorbs, scatters and refracts electromagnetic radiation. Optical absorption results from atomic and molecular transitions which convert photons into kinetic energy where the absorbed wavelength corresponds to the absorption band of a molecular species [1] [3]. The three gases that account for most absorption of electromagnetic radiation are: oxygen (O_2), carbon dioxide (CO_2) and water vapour (H_2O) [6]. Oxygen molecules absorb high-energy ultraviolet radiation, forming ozone molecules (O_3) as a result. Carbon dioxide absorbs mid- and far-infrared radiation. On the other hand, water vapour is several times more effective in absorbing radiation than all other atmospheric gases combined as its absorption can exceed 80 % in the region of the spectrum between 1.2 μm to 27 μm [6].

Scattering is caused by atmospheric molecules of oxygen and nitrogen and suspended particles such as fog, forest exudates, haze, dust, air pollutants and smoke [1] [6]. *Raleigh scattering* occurs when electromagnetic radiation interacts with particles that are small in comparison with the propagating wavelength, λ [3]. Rayleigh showed that the amount of scattering is inversely proportional to the fourth power of wavelength, λ^{-4}, and so blue light is scattered much more strongly than red photons and thus the sky appears blue. Figure 7.2(a), (b) and (c) illustrate the distinct scattering behaviours identified by Rayleigh. Scattering from large, irregular particles of dust and smoke

create a strong forward peak (Figure 7.2(a)). Nearly symmetric particles create no pronounced peaks (Figure 7.2(b)) while large water droplets generate a strong forward-scattered peak (Figure 7.2(c)) [6].

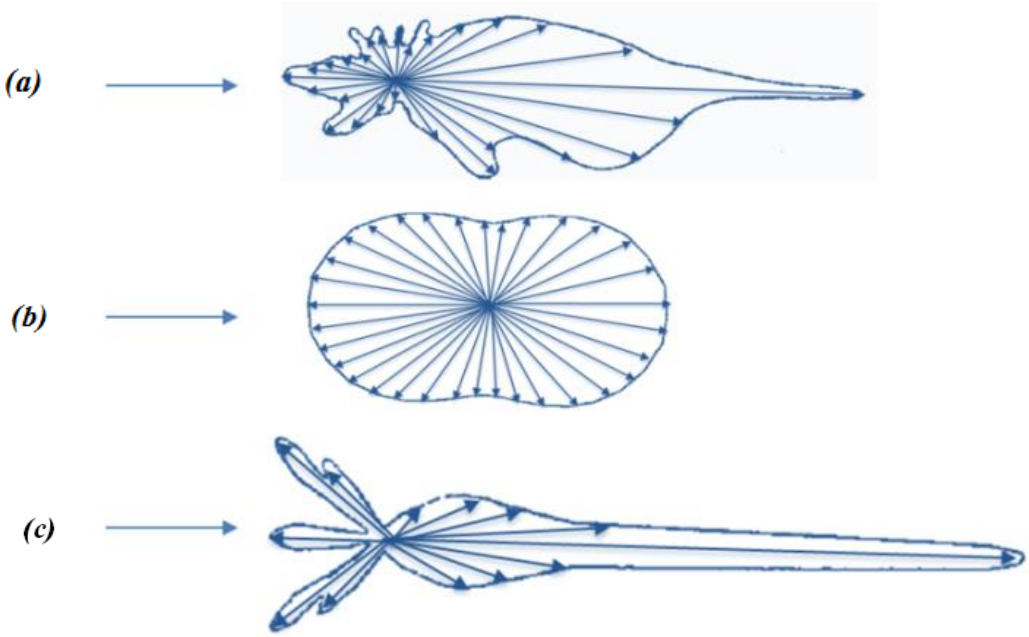

Figure 7.2. Atmospheric scattering behaviours for three types of particles. (a) Dust and smoke form irregular particles which generate a forward scattering peak. (b) Molecules of a regular shape which produce no pronounced peaks. (c) Large water droplets that create a strong forward scattering peak [6].

Mie scattering is generated by particles — such as pollen, smoke, water droplets and dust — with diameters roughly equivalent to the wavelength. *Nonselective scattering* occurs when particles are much larger that the wavelength of the scattered radiation and it is not wavelength dependent. It can be observed as a whitish or greyish haze and occurs equally for all wavelengths within the visible spectrum. Atmospheric scattering can be detrimental to remote sensing applications. For this reason, distance-ranging lidar avoids short wavelengths such as blue and ultraviolet [6].

Refraction refers to the bending of rays at the interface between two media through which the electromagnetic radiation is propagating. Refraction occurs as light passes through pockets of varying refractive index caused by temperature fluctuations, opacity and humidity. Those three effects lead to slight changes in density; since the atmosphere is in constant motion, the mixing of hot and cold air result in variations of refractive index [1].

7.2.3 Atmospheric Transmission Windows

The atmosphere transmits electromagnetic radiation within certain selective wavelength ranges. The wavelength ranges or wavebands that are transmitted are referred to as transmission windows and determine the wavelengths that can be effectively used in atmospheric and terrestrial sensing. Figure 7.3 shows a simplified diagram of these transmission windows measured as a function of opacity for the spectrum between 0.1 nm to 10 m [6].

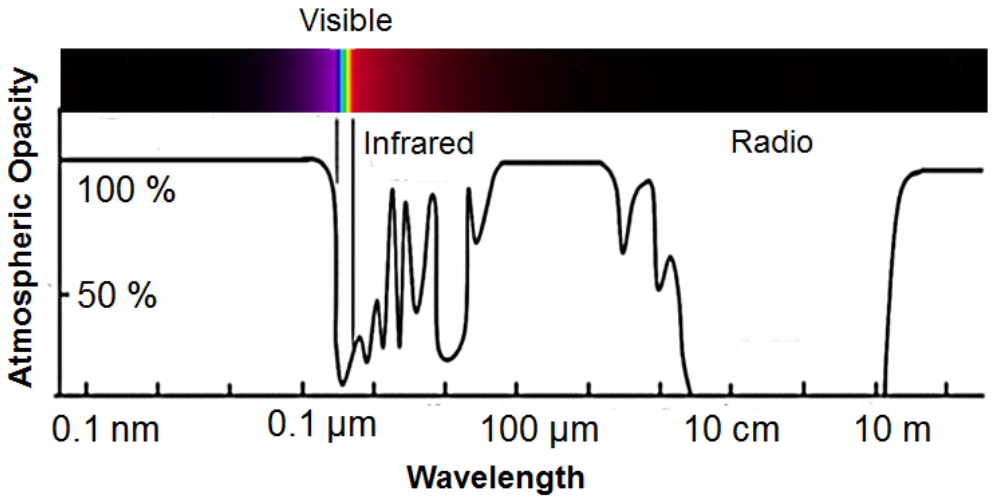

Figure 7.3. The opacity of the atmosphere at wavelength ranges between 0.1 nm to 10 m. The plot was reproduced from reference [6].

Opacity is a measure of attenuation of electromagnetic radiation propagating through a medium caused by absorption, scattering and refraction. In astronomy, opacity is defined by a mass attenuation coefficient, k_λ, at a particular wavelength, λ. If a beam of electromagnetic radiation of wavelength λ travels through a medium of opacity coefficient, k_λ, and mass density, ρ, the invacuo irradiance I_0 will be reduced with a distance s according to Beer's law [7]

$$I(s) = I_0 e^{-k_\lambda \rho s} \qquad \textit{Eq. 7.1}$$

where $I(s)$ is the irradiance of the beam after travelling distance s.

Transmittance, T, describes effectiveness of a medium in transmitting electromagnetic radiation such that the transmittance of 100 % corresponds to zero opacity, and is represented by the ratio between the irradiance transmitted through the medium, I, to invacuo irradiance, I_0, to [8]

$$T = \frac{I}{I_0} \qquad \textit{Eq. 7.2}$$

There are several atmospheric windows within the electromagnetic spectrum where opacity is < 50 % and they are listed in Table 7.1.

Designation	Wavelength range	Transmission band
Ultraviolet	0.330 - 0.390 µm	U
Visible (Blue)	0.391 - 0.490 µm	B
Visible (Green)	0.505 - 0.594 µm	V
Visible (Yellow/Orange)	0.590 – 0.660 µm	R
Near Infrared	0.780 – 1.020 µm	I
Short-Wavelength Infrared	1.100 – 1.400 µm	J
	1.475 – 1.825 µm	H
	2.000 – 2.400 µm	K
Mid-Wavelength Infrared	3.125 – 3.675 µm	L
	4.850 – 5.150 µm	M
Long-Wavelength Infrared	7.700 – 12.700 µm	N
Very Long-Wavelength Infrared	17.000 – 25.000 µm	Q
Radio-Wavelength	1 mm – 10 m	R

Table 7.1. Atmospheric windows for which opacity is < 50 % [1] [9].

7.2.1 Atmospheric Turbulence

Earth's atmosphere is a fundamentally changeable medium in which motion occurs primarily as a result of convection currents. Atmospheric convection occurs as a result of the transfer of solar energy to land and water areas in which the flow of air is continuously stimulated. As the air near the surface of the Earth is heated by the sun, it becomes less dense and rises above cooler air located at a higher level which then sinks to the ground layer. In turn, the cool air warms up and rises above the previously heated air [10]. This results in a cycle of air rising and sinking, which is referred to as turbulent transfer, and is illustrated in Figure 7.4 [6]. Approximately 25 % of the solar energy entering the atmosphere is either scattered or absorbed by particles in the atmosphere, while 30 % of it is reflected by clouds or by the Earth's surface [10]. The remaining portion of the solar energy is absorbed by the Earth's surface, which is

released in the form of heat to the ground-layer of the atmosphere before being dissipated into the upper layers of the atmosphere by convective currents [10]. The continuous heat-induced mixing of hot and cold air pockets due to convection currents and shear winds generate local density variations and thus refractive index irregularities.

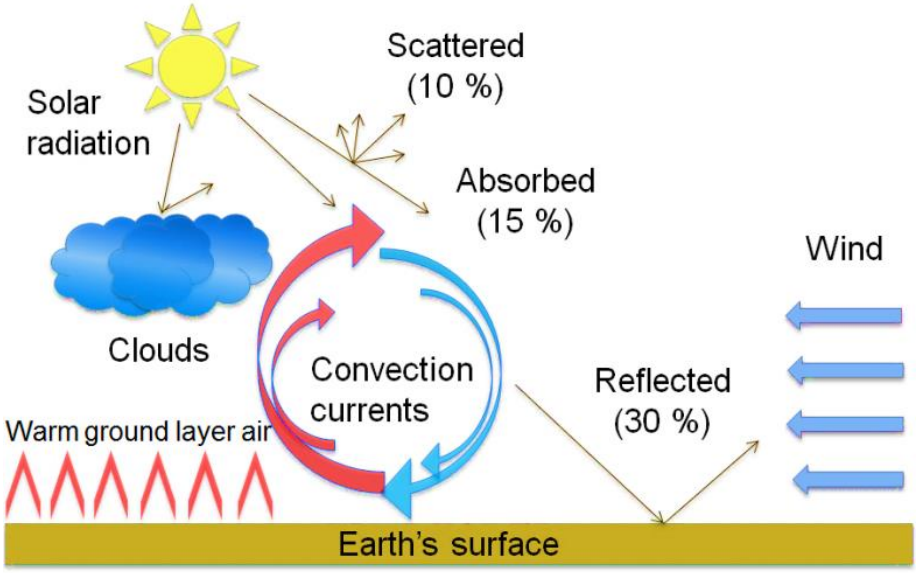

Figure 7.4. Illustration demonstrating the process of atmospheric heating by solar radiation [10].

7.2.2 Kolmogorov/Richardson Cascade Model

During the 1940's the Soviet mathematician, Andrey Kolmogorov, developed a model for how energy is transported from large scale vortices to small scale vortices [8]. Tatarskii applied Kolmogorov's model to solve the wave equation for propagation through regions of weak and random refractive index fluctuations. Tatarskii's model was then used by Fried who described turbulence in the form of Zernike polynomials. The combined result of Kolmogorov, Tatarskii and Fried formed the basis of current work in atmospheric optics [8]. The statistical approach to turbulence developed by Kolmogorov is based on Richardson's *energy cascade* model [3]. At high wind velocity, turbulent flow in the form of vortices or eddies develops, creating air pockets of varying temperature and density which are called atmospheric turbules. Turbulent motion of air is chaotic and can be represented by a set of turbules of various sizes, extending from small, l_0, called the *inner scale*, to large, L_0, called the *outer scale* and the difference defines the *inertial range* [3]. Typically, the parameter l_0 varies from several millimetres near the ground to several centimetres at altitude; it is therefore comparable with the laser beam width. The size of L_0 is usually of the order of 1 - 100 m [3]. Large turbules are broken down by the continuous stirring of the atmosphere

into increasingly smaller eddies until the energy is dissipated as heat, as illustrated in Figure 7.5 [10].

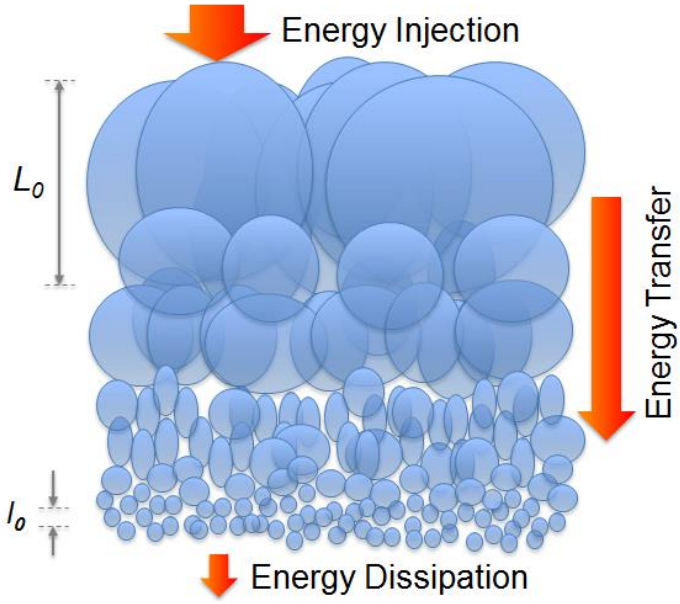

Figure 7.5. Kolmogorov/Richardson cascade model of energy transfer resulting from turbulence. Large eddies of size L_0 sequentially disintegrate to smaller eddies of size l_0 until the energy dissipates as heat. Illustration adapted from [3].

The molecules involved in a turbulent flow are subjected to two types of forces: viscous forces and inertial forces. The maximum size of turbules is limited by the Reynolds number, which is the ratio of the inertial force to the vicious force [8]. The viscous force, which is caused by inter-molecular forces between neighbouring particles, keeps the molecules involved in a turbulent motion together. In turn, the inertial force resulting from the gravitational pull accelerates particles towards the surface of the Earth in accordance to Newton's second law of motion. Large vortices tend to break up into smaller ones under the influence of inertial forces until viscous forces begin to dominate [3].

7.2.3 The Effect of Optical Turbulence on a Propagating Laser Beam

Optical turbulence is defined as changes in the refractive index that occur as a result of local variations in the air temperature [3] [10]. An optical wave propagating through a vacuum, which has a uniform index of refraction, can be represented by a plane or spherical wave [11]. However, the phase of a wave-front propagating through turbulent

atmosphere becomes distorted due to random refractive index fluctuations in the air [8]. As a result, an optical signal can be subjected to the deleterious effects of:

a) Beam wander: an angular deviation from the line-of-sight path causing the beam to miss the receiver and/or the target;

b) Fluctuations in the beam angle-of-arrival: this effect causes the image to "dance" in *x*, *y* direction along the focal plane;

c) Beam scintillation: an effect which results in fluctuations of the beam irradiance due to refractive index inhomogeneities [3].

The effect of optical turbulence on the propagating laser beam depends on the dominant scale size of the turbulent flow compared to the diameter of the beam. When the scale size of the turbulent flow along the beam path is smaller than the diameter of the laser beam, the effects of refraction and diffraction tend to dominate [12]. This results in beam distortion and intensity fluctuations known as scintillation and is illustrated schematically in Figure 7.6(a). If the scale is larger than the laser beam diameter, then the turbulent pockets of air tend to deflect the beam. As a result, the beam is deflected from its original direction, which is known as beam wander. This effect is illustrated schematically in Figure 7.6(b). Both effects can be observed simultaneously, depending on characteristics of the turbulence [12].

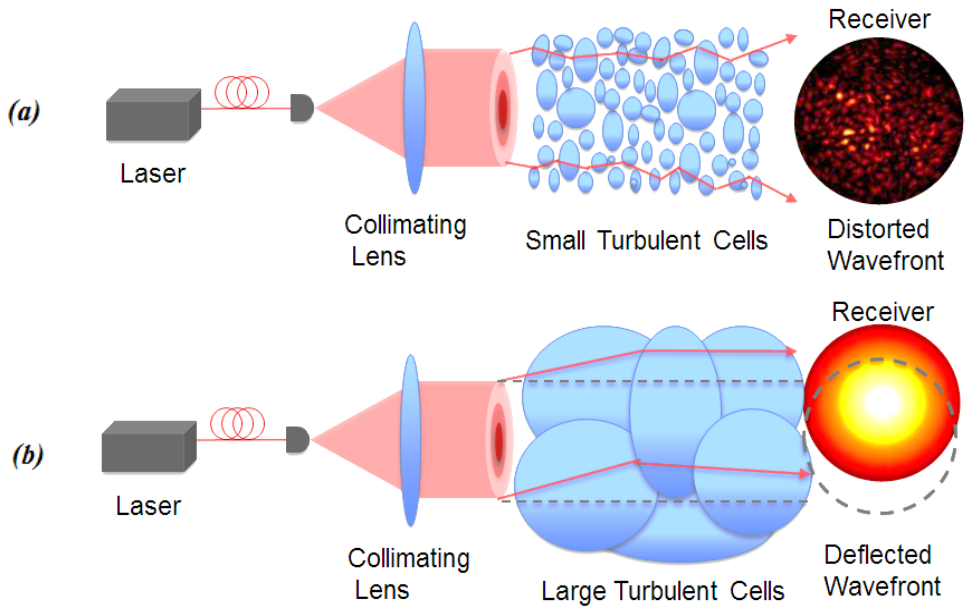

Figure 7.6. Effect of turbulence on the propagating laser beam where in (a) the beam diameter is larger in comparison to the scale size of the turbulent flow, as a result, the intensity of the beam and the beam diameter are altered; (b) the beam diameter is smaller in comparison to the scale size of the turbulent flow, as a result, the beam is deflected from its original position but its diameter is not altered [12].

In single-photon lidar measurements, intensity oscillations caused by turbulence have the potential to randomly increase the detector count rate which can contribute to pulse pile-up [13]. Additionally, turbulence can increase the diameter of the Airy disk to a value significantly higher than that predicted by optical design. This reduces the spatial resolution of the optical system and increases overall system losses. Additionally, variations in the angle-of-arrival can cause spatial and temporal image defects [8].

7.2.4 Parameters Characterising Optical Turbulence

A useful measure of the strength of the optical turbulence in the atmosphere can be derived from the inner scale, l_0, the outer scale, L_0, the structure parameter of refractive index fluctuations, C_n^2, and the scintillation index, σ_I^2. The latter two are strongly dependent on altitude [3]. A Gaussian beam can be viewed as being made up of a superposition of plane-wave components travelling at various angles to the direction of propagation as long as the plane wave components are traveling at angles $\theta \leq 0.5$ rad [14]. Gaussian wave components can diverge at cone angles of up to ≈ 30 ° before significant corrections to the plane wave approximation become necessary [14]. The maximum laser beam divergence used in experiments described in this thesis is 1.3 mrad, thus, in the treatment here, the lowest-order Gaussian mode (TEM_{00}) — represented by a plane wave under weak turbulence conditions where the scintillation index $\sigma_I^2 \leq 1$ — is considered [3].

The propagation of a monochromatic light through a random medium, when neglecting the effects of polarisation, is governed by the reduced wave equation [3]

$$\nabla^2 U(R) + k^2 n^2(R) U(R) = 0 \qquad \textit{Eq. 7.3}$$

where $U(R)$ represents the optical field of the wave at a position $R = x,y,z$, $n(R)$ is the refractive index at R and k is the optical wave number, $k = 2\pi/\lambda$, where λ is the operating wavelength [3]. The Rytov approximation can be applied to Eq. 7.3. The effect of the Rytov approximation is to introduce a linear perturbation into the phase of a wave-front as a result of random inhomogeneities along the propagation path [3]. The terms $\Psi_1(r, L)$ and $\Psi_2(r, L)$ denote first and second-order complex phase perturbations, respectively, which alter the mean optical field [3]

$$< U(r, L) >= U_0(r, L) < exp[\, \Psi_{1,2}(r, L)] > \qquad \textit{Eq. 7.4}$$

where L is the propagation path between the transmitter and receiver, r is the distance from the beam centre line in the transverse direction, $U_0(r, L)$ is a free Gaussian beam at the receiver, and $\Psi_{1,2}(r, L)$ is the total phase perturbation [3].

It can be shown that the mean field (Eq. 7.4) is given by [3]

$$< U(r,L) >= U_0(r,L)exp(-0.39C_n^2k^2L^{5/3}) \qquad \textit{Eq. 7.5}$$

where C_n^2 is the structure parameter of refractive index fluctuations [3]. C_n^2 is defined as the constant of proportionality in the index of refraction structure function $D_n(R)$, which can be expressed by

$$D_n(R) = \begin{cases} C_n^2 R^{2/3} & , l_0 \ll R \ll L_0 \\ C_n^2 l_0^{-4/3} R^2 & , R \ll l_0 \end{cases} \qquad \textit{Eq. 7.6}$$

where l_0 denotes the inner scale of turbulence and L_0 denotes the outer scale of turbulence [3].

7.2.4.1 Beam Wander

As illustrated in Figure 7.6(b), an optical beam propagating through large scale turbulence will experience random deflections from its original position [12]. A centroid of an instantaneous beam will randomly fluctuate in the plane of the optical aperture potentially causing losses to the detected optical signal. This type of laser beam fluctuations is called *beam wander*. Statistically, it can be described by the variance of the beam displacement [3].

7.2.4.2 Angle-of-Arrival and Refractive Index Structure Parameter

Fluctuations in the angle-of-arrival in the plane of the optical aperture result in the *image dancing* in the focal plane of the collecting optics. The magnitude of deflection of the focal spot and the size of active area of the collecting detector determine the scale of the signal loss. The angle-of-arrival depends on the phase shift across an aperture of a collecting lens and the path difference of the propagating beam, which is driven by the turbulence scale size. For a plane wave-front the variance in the angle-of-arrival, β^2, is given by [3]:

$$\left\langle \beta^2 \right\rangle = \begin{cases} 1.64C_n^2 L l_0 & , D \ll l_0 \\ 2.91C_n^2 L D^{-1/3} & , D \gg l_0 \end{cases} \qquad \textit{Eq. 7.7}$$

Where the angle brackets "< >" denote averaging over a time long compared to the timescale of the turbulence and *D* denotes diameter of the collecting aperture. This definition is independent of wavelength and is based on a theory of weak fluctuations [3].

When the diameter of the collecting telescope, *D*, is much larger than the inner scale of turbulence ($D >> l_0$) then the structure parameter of refractive index fluctuations, C_n^2, is given by [3]:

$$C_n^2 = \frac{< \beta^2 > D^{1/3}}{2.91\, L} \qquad \textit{Eq. 7.8}$$

where *L* is the propagation path between the transmitter and receiver.

7.2.4.3 Scintillation

Scintillation refers to random fluctuations in the beam intensity due to inner scale optical turbulence, l_0. This effect can occur even when the beam propagates through relatively short paths [3]. Temporal frequencies at which the intensity fluctuations are typically recorded at a fixed point within the beam vary between 0.1 - 1 kHz: a counting interval between 1 - 10 ms is required in order to effectively record effects of turbulence on photon counts [12]. The effect of scintillation on the TEM_{00} Gaussian beam profile has been simulated and is illustrated in Figure 7.7. The irradiance spikes can be observed in the scintillated irradiance profile: the maximum irradiance tends to be significantly higher than the corresponding values for the beam propagating through a vacuum [10].

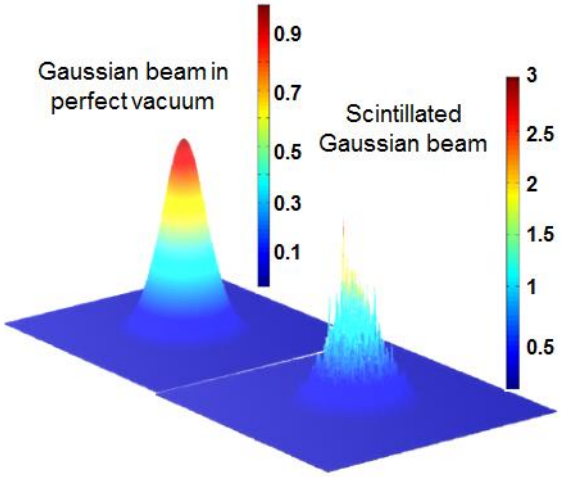

Figure 7.7. Gaussian beam irradiance pattern (TEM_{00}) in perfect vacuum and after propagating through a turbulent medium with a dominance of small scale optical turbulence resulting in scintillation. The figure is taken from reference [10]. Notice change in scale between two plots.

An important metric that quantifies irradiance fluctuations of the optical beam is the *scintillation index*, σ_I^2, which is a measure of the strength of optical turbulence. The scintillation index is defined as the normalised variance of irradiance fluctuations and is given by:

$$\sigma_I^2 = \frac{<I^2(t)>}{<I(t)>^2} - 1 \qquad \textit{Eq. 7.9}$$

where $<I(t)>$ represents normalised irradiance fluctuations at time t averaged over the acquisition period [3]. The irradiance $I(t)$ is the rate at which photon energy falls onto the surface of the optical receiver and is given by

$$I(t) = \frac{N_p E}{At} \qquad \textit{Eq. 7.10}$$

where N_p is the number of photons recorded by a detector, A is the area of the collecting telescope, t is the photon counting interval and E refers to the photon energy given by $E = hc/\lambda$, where h is the Planck constant, c is the speed of light and λ is wavelength of operation [15]. After substituting Eq. 7.10 to Eq. 7.9 the term E/At cancels out, therefore the scintillation index can be re-defined as

$$\sigma_1^2 = \frac{< {N_p}^2(t) >}{< N_p(t) >^2} - 1 \qquad \textit{Eq. 7.11}$$

A Gm-array is able to detect only one photon at a time during the detector gate period. This means that the intensity (photon flux) cannot be measured directly with photon counting. In determining the (nearly) instantaneous intensity $I(t)$ from a series of individual photon arrival times, it is necessary to average over a timescale which is very short compared to the coherence time of the turbulence. $<I(t)>$ is then found by averaging $I(t)$ over an extended time interval which is long compared to the coherence time. As noted earlier, the bandwidth for intensity fluctuations caused by turbulence is typically 0.1 – 1 kHz: in this case the coherence time is 1 – 10 ms.

Alternatively, the scintillation index can be estimated through evaluating the instantaneous photon rate, $R_p(t) \propto I(t)$ at a time t_1, by considering the time differences between adjacent photon events:

$$R_p(t_1) = \frac{1}{(t_2 - t_1)} \qquad \textit{Eq. 7.12}$$

where t_1 and t_2 are the arrival times of two consecutive detected photons. Thus, from Eq. 7.11 the scintillation index is:

$$\sigma_1^2 = \frac{< {R_p}^2(t) >}{< R_p(t) >^2} - 1 \qquad \textit{Eq. 7.13}$$

where $R_p(t)$ is a photon rate recorded at time t. In regimes of weak fluctuations (scintillation index $\sigma_I^2 \leq 1$), scintillation index, σ_I^2, is proportional to the Rytov variance for a plane wave [3], so that

$$\sigma_I^2 = 1.23 C_n^2 k^{7/6} L^{11/6} \qquad \textit{Eq. 7.14}$$

Weak optical turbulence is characterised by the condition $\sigma_I^2 < 1$, moderate turbulence by $\sigma_I^2 \approx 1$ and strong turbulence by $\sigma_I^2 >> 1$ [3]. Values of C_n^2 vary between 10^{-12} for strong turbulence, 10^{-13} for medium turbulence and 10^{-14} for weak turbulence [3].

7.2.5 Mitigation Methods

The effect of atmospheric turbulence on the performance of optical systems has been widely recognised since the 1950's. Since then, three major methods of turbulence mitigation have been proposed in astronomy: (1) post-processing techniques designed to mitigate the effect of turbulence on the quality of images, (2) adaptive optics techniques based on sensing the turbulence induced aberration and partially correcting for it in real time by means of deformable mirrors or spatial light modulators (SLMs), (3) hybrid techniques which combine elements of the post processing and adaptive optics [8].

Turbulence measurements using standard (analogue) lidar techniques have received some attention to date, but this has been primarily concerned with Satellite Laser Ranging (SLR) for inter-planetary applications [16]. The effects of turbulence on the performance of long-range imaging and communications systems incorporating SPADs have been studied theoretically and experimentally and has been reported in [17] [18] [19] and [20].

With the development of single-photon detector arrays new opportunities have emerged allowing capture of both the angle-of-arrival perturbations and irradiance fluctuations. An array of detectors offered an advantage over a single-element detector, as it allowed the simultaneous measurements of irradiance fluctuations and angle-of-arrival fluctuations. This technique can be used in an independent high-speed evaluation of parameters characterising optical turbulence using exactly the same set of data. This can prove useful in evaluating the validity of each method and can be potentially applied in real-time turbulence correcting algorithms.

7.3 Experimental Setup

A diagram of the imaging system used in the experiment is shown in Figure 7.8. The illumination was provided by a 1550 nm wavelength erbium-doped fibre laser which operated at a repetition rate of 125 kHz with pulse duration of 800 ps. The transceiver consisted of a Schmidt-Cassegrain telescope with a collecting aperture diameter, *D*, equal to 0.203 m. The optical system was designed to provide a diffraction-limited performance for either a 25 µm pixel diameter, single-element (SE) InGaAs/InP SPAD, or the Gm-array [21].

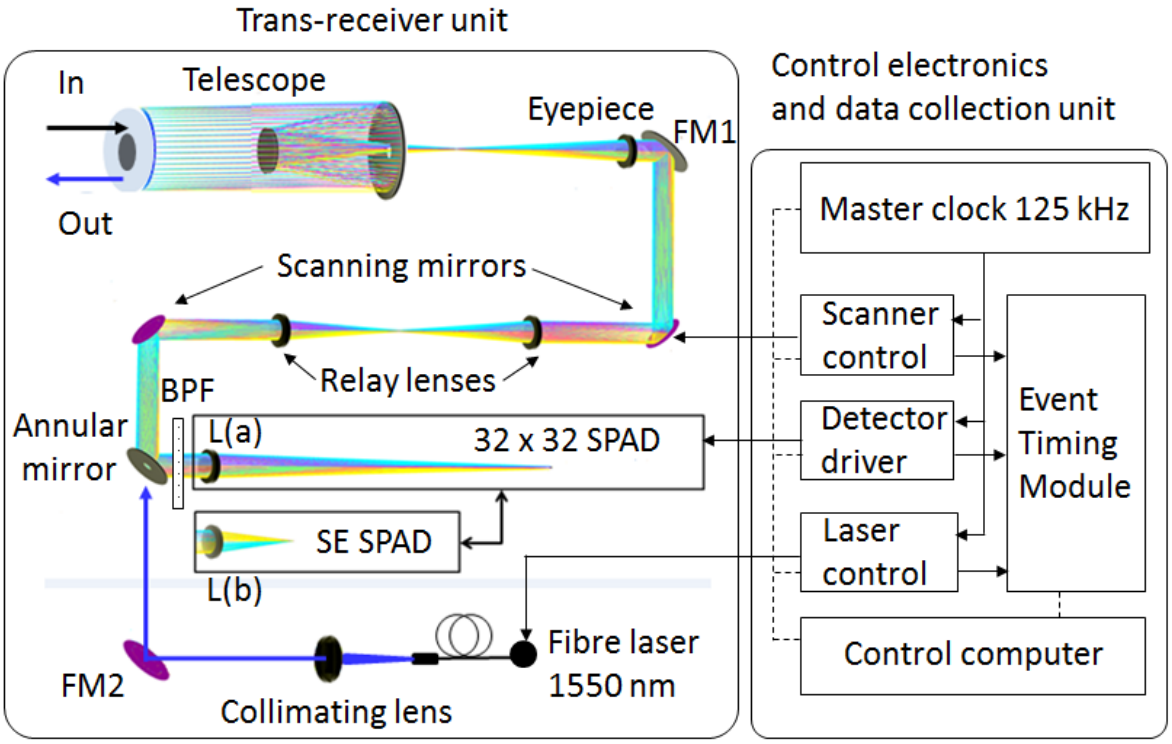

Figure 7.8. Diagram of the layout of the imaging system setup consisting of a transceiver unit, control electronics and data collection unit.

By incorporating an inter-changeable lens, *L(a, b)*, the system provided a matching pixel resolution of 28 µrad for both the single-element SPAD and for the Gm-array. For the measurements reported here, the transceiver was configured in a mono-static mode in which the laser beam was injected into the optical system through an aperture in an annular mirror, and transmitted to the target via a common transmit and receive channel.

The laser beam had a pulse energy of 80 nJ (average optical power of 10 mW) for the single-element SPAD and ~ 4 µJ (average optical power of 0.5 W) for the Gm-array.

Both detectors were gated with a 125 kHz synchronous signal activating them for a gate window of 10 ns (single-element SPAD) and 500 ns (array of SPADs) [21] [22].

The timing was controlled by a master clock which triggered the scanning mirrors, the laser and the SPAD detection gate. The event timing electronics collected time-stamps of each transmitted laser pulse and the events recorded by the detector. The data was recorded and processed by a control computer. To eliminate the detection of photon events caused by backscatter from internal components, a delay between the laser trigger pulse and the SPAD gate trigger was set to gate-off the detector at the expected return time of these unwanted back-reflections, whilst still efficiently detecting the photon return from the target.

For the measurements discussed in this chapter the single-element SPAD was set to an advanced mode of operation with 8.5 μs hold-off time, bias voltage of 3 V and 10 ns gate width. The Gm-array was operated with a sensitivity setting of 26, which provided 3.5 V bias voltage.

7.4 Experimental Results

The experimental data was acquired with both the single-element SPAD and the Gm-array (both configured in a mono-static mode) over ranges of 5.6 km and 9.5 km respectively. The target used in the single-element SPAD experiment was a 30 × 20 cm board covered with an acrylic, white micro-prismatic retro-reflective material. A retro-reflective corner-cube of 10 cm diameter was used with the Gm-array.

The transceiver system was positioned approximately 30 m above the ground in the roof laboratory at Selex ES, while both targets were mounted approximately 50 cm above the ground. The terrain was undulating, and the height of the beam along the beam trajectory varied from approximately 30 m to 100 m above the ground. The measurements were taken over a double-pass between the transceiver and the targets.

7.4.1 Turbulence Measurement Using a Single-Element InGaAs/InP SPAD

In the absence of dark and solar background counts, the uncertainty in photon-count measurement due to Poisson noise is proportional to the square root of the recorded number of counts (see Eq. 2.17). This suggests that by increasing the number of counts

in a counting interval, it is possible to decrease the ratio of standard deviation to mean count rate and improve the resolution of the measurement. As the timescale in which atmospheric structures evolve is typically between 0.1 - 1 kHz, a counting interval between 1 – 10 ms is required in order to effectively record the instantaneous value of the count rate.

For a pulse rate of 125 kHz only between 125 to 1,250 photons per interval of 1 ms and 10 ms respectively are available as an upper limit for a free-running SPAD. The minimum Poisson noise associated with the measurement is approximately $\sqrt{125}/125 \approx 9$ % for a 1 ms interval. The average number of photon counts recorded during the experiment was estimated to be between 1.68 to 15.08 photons per counting interval, yielding the Poisson noise between ~ 77 % to ~ 25 %. Figure 7.9 shows the relationship between the scintillation index (calculated from Eq. 7.11), the average number of counts and the interval during which the returns were counted.

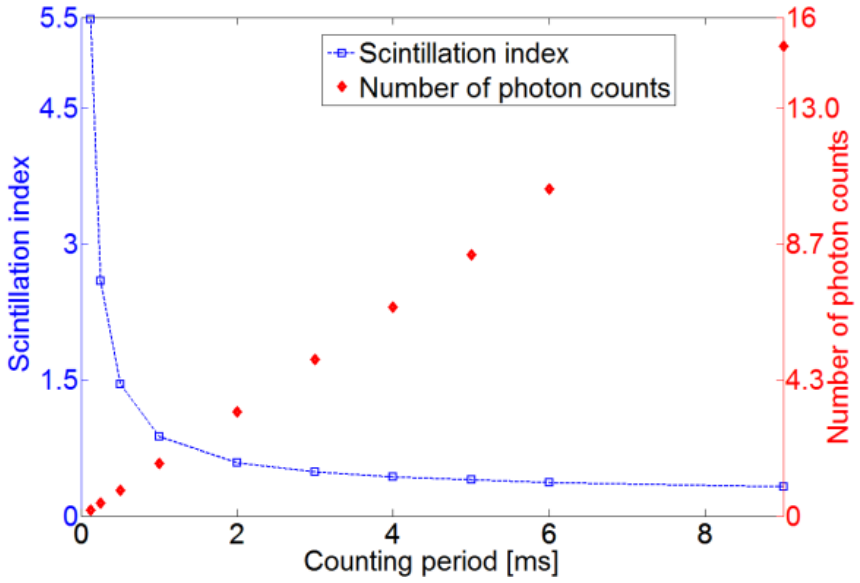

Figure 7.9. Plot showing the scintillation index, σ_I^2, and the average number of photon counts vs. counting interval recorded during the experiment.

This indicates that the scintillation index increases as the counting interval decreases. In turn, as the counting period decreases, the average number of photons per counting interval decreases. The small average number of photons recorded in such short measurement durations means that error due to Poisson statistics is relatively large, making scintillation measurements difficult to interpret.

To eliminate the problem with low average number of counts per counting interval an approach based on estimating the instantaneous photon rate was used. The scintillation

index was calculated from Eq. 7.13 for a 0.25 s duration over a 7.25 s acquisition time, which provided 29 estimations. Figure 7.10 shows a 0.37 s duration sample from the entire 7.25 s measurement window, exhibiting fluctuations of the photon count rate recorded by the SPAD and showing the effect of atmospheric scintillation on the signal.

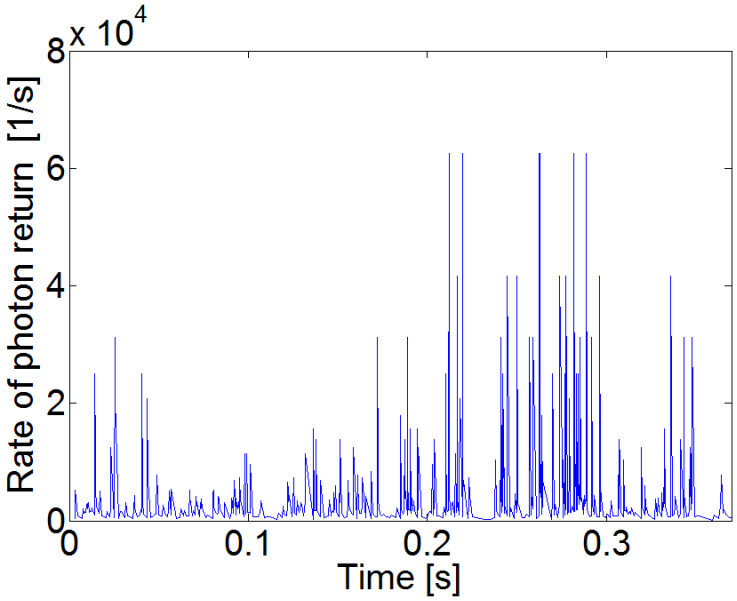

Figure 7.10. A 0.37 s acquisition window showing fluctuations of the photon return rate recorded by the single-element SPAD over 5.6 km. This data includes returns resulting from both the signal from the target and background noise.

The statistics of atmospheric scintillation tends to exhibit log-normal characteristics [23]. To establish whether the data has this distribution, a histogram of the photon rate distribution over a 7.25 s acquisition period was generated. Subsequently, a log-normal fit and a Poisson distribution of identical mean rate of 5900 [1/s] and identical number of photon count occurrences were matched to the distribution of photon rate. This is shown in Figure 7.11.

A continuous random variable X has a log-normal distribution if the random variable $Y = \log_e(X)$ is distributed log-normally with population mean μ_y and standard deviation σ_y [24]. The resulting probability density function, $f(x;\ \mu_y,\ \sigma_y)$, for a continuous random variable X, such that $0 \leq x < \infty$, is expressed by

$$f(x;\mu_y,\sigma_y) = \frac{1}{x\sqrt{2\pi\sigma_y}} \exp\left(-\frac{1}{2\sigma_y}(\log_e - \mu_y)^2\right) \qquad \textit{Eq. 7.15}$$

The mean, μ_x, and variance, σ_x^2, of the log-normal distribution are

$$\mu_x = \exp\left(\mu_y + \frac{\sigma_y^{\ 2}}{2}\right) \qquad \textit{Eq. 7.16}$$

and

$$\sigma_x^{\,2} = \exp\left(2\mu_y + \sigma_y^{\,2}\exp(\sigma_y - 1)\right) \qquad \textit{Eq. 7.17}$$

respectively [24] [25].

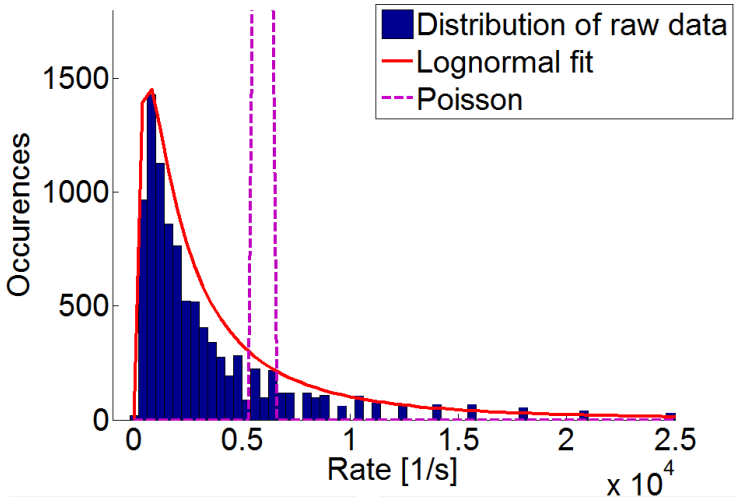

Figure 7.11. Distribution of photon rate occurrences recorded at the single-element SPAD over 7.25 s, a corresponding log-normal fit and a (partially shown) Poisson distribution of identical mean rate = 5900 [1/s] that would be recorded when turbulence is absent.

The histogram shown in Figure 7.11 represents a distribution of photon rate occurrences recorded by the single-element SPAD detector over 7.25 s and was generated in MatLab with 400 bins, 175 1/s width each [26]. The log-normal fit to the distribution was performed in MatLab using the "lognfit" function [27]. This function estimates μ_x and σ_x using the maximum likelihood estimate technique [27]. The maximum likelihood estimate technique derives an estimate of a population parameter that yields the largest probability of occurrence of the observed sample and is defined as follows [25] [28]. For an n sample of independent observations $x_1, x_2, \ldots, x_n$, of the random variables, $X_1, X_2, \ldots, X_n$, from a continuous population with probability density function, $f(x;\gamma)$, the maximum likelihood estimator, γ, is defined as that value of γ which maximises the likelihood function [25].

$$L(x_1, x_2, \ldots, x_n; \gamma) = \prod_{i=1}^{n} f(x_i, \gamma) \qquad \textit{Eq. 7.18}$$

The likelihood function, L, is the joint distribution of the random variables, $X_1, X_2, \ldots, X_n$ and represents the joint probability $P(X_1 = x_1, X_2 = x_1, \ldots, X_n = x_n \mid \gamma)$ of acquiring the observed values of the sample $x_1, x_2, \ldots, x_n$ given an appropriate value of the distribution parameter, γ [25].

By applying the "lognfit" function to the histogram data, the parameters of the best fit to the log-normal distribution were identified for both sets of data and their values are μ_{xSE} = 7.87 1/s and σ_{xSE} = 1.2 1/s. Log-normal curves for μ_{xSE}, σ_{xSE} were overlaid on the histogram in Figure 7.11.

The photon rate distribution cannot be described well by a Poisson distribution, but can be better approximated by a log-normal distribution [19]. The long tail and "skewness" of the distribution of photon rate recorded during the experiment shows a good match with the log-normal fit and therefore implies that the propagating light wave has been subjected to random and finite atmospheric perturbations. The Poisson distribution represents the result that would be observed when turbulence was absent.

The captured data consisted of photon returns from both the target and the background. To distinguish between photon returns from the target and the background, a histogram representing of photon arrival distribution over 7.25 s was generated and is shown in Figure 7.12.

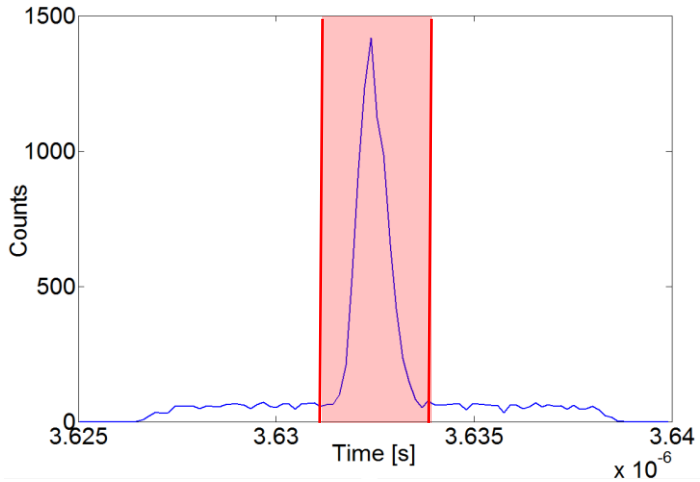

Figure 7.12. Histogram of photon counts recorded over a distance of 5.6 km with a single-element SPAD over 7.5 s acquisition time.

The peak corresponding to the return signal from the target is positioned within the shaded area, whereas photon counts outside of this region correspond to the background counts. The time of arrival recorded for each photon return outside of the peak region was converted to a count rate with respect to the acquisition time of 7.25 and is plotted in Figure 7.13. The photon rate due to the background counts was found to fluctuate in time around the average rate of 1700 [1/s].

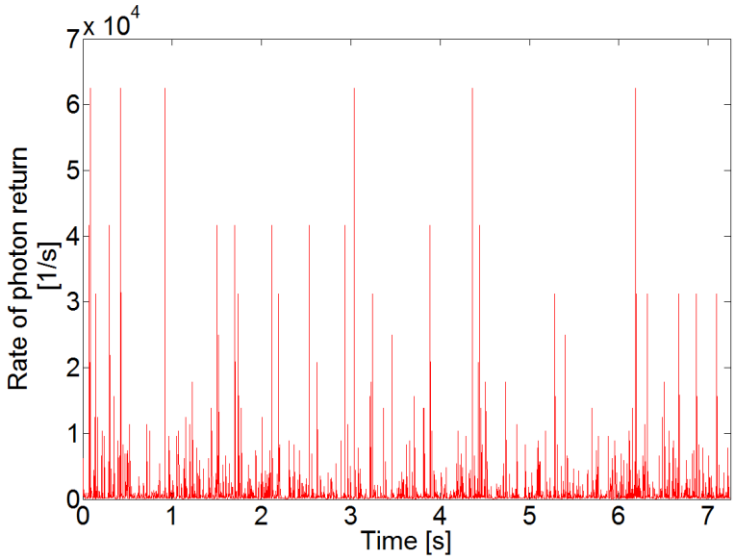

Figure 7.13. A 7.25 s acquisition window showing fluctuations of the photon return rate due to solar background and dark count noise recorded by the single-element SPAD. The average rate of photon counts due to background counts is 1700 [1/s].

The scintillation index was calculated from Eq. 7.11 in 29 steps for each 0.25 s for the background-uncorrected and background-corrected data. The signal counts were extracted from the data by subtracting the average background rate. From this, a plot of the measured scintillation index was obtained and is shown in Figure 7.14. The average scintillation index, before and after the background correction was σ_I^2 = 3.04 and σ_I^2 = 3.36 respectively. In both cases σ_I^2 is high and therefore the turbulence at the time of the measurement was strong.

The scintillation index, σ_I^2, for the background uncorrected data is on average 0.3 lower than the scintillation index, σ_I^2, calculated for the background corrected data. The increase in the scintillation index after the background noise correction suggests that the presence of background counts might have a "smoothing" effect on irradiance fluctuations.

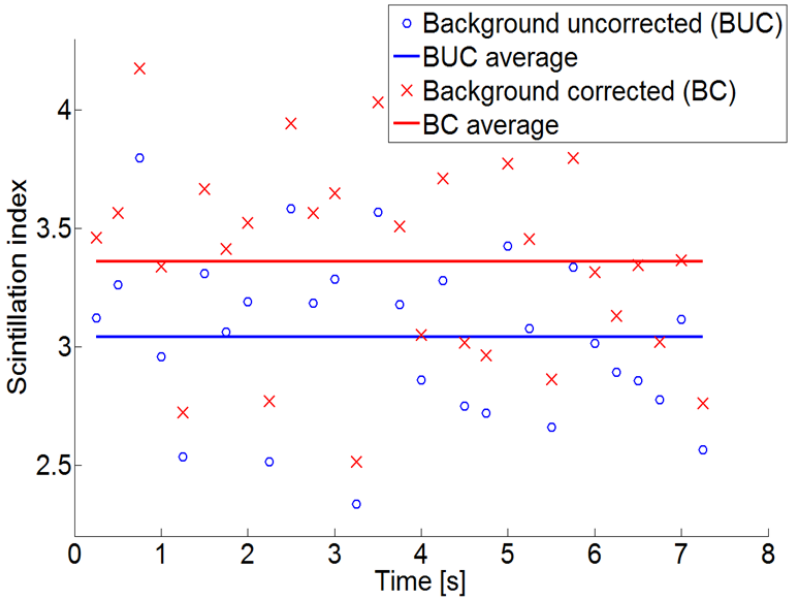

Figure 7.14. The plot shows scintillation index, σ_I^2, before and after background correction for multiple 0.25 s periods and then averaged over the entire acquisition time of 7.25 s. The data was acquired using a single-element SPAD detector.

7.4.2 Turbulence Measurement Using the Gm-Array of InGaAs/InP SPADs

When using a single-element SPAD, C_n^2 can be calculated by estimating the scintillation index using Eq. 7.11 or Eq. 7.13. However, as illustrated in Figure 7.15 imaging with the Gm-array has the advantage over imaging with a single-element SPAD in that it allows measurements of C_n^2 to be performed by means of two different approaches: that is by estimating the average variance of the angle-of-arrival $<\beta^2>$ (Eq. 7.8) and by measuring scintillation index from intensity fluctuations on the detector plane at each pixel of the array (Eq. 7.14). The outcome of C_n^2calculation performed using the two methods can be then compared.

The benefit of using the Gm-array is that it allows fluctuations of the optical wave reflected off the target to be analysed and visualised in three-dimensions. Figure 7.16 shows a series of accumulated images of the corner cube at range of 9.5 km with each image frame representing a number of photon counts for each of 1024 pixels of the detector summed over a 1 ms period.

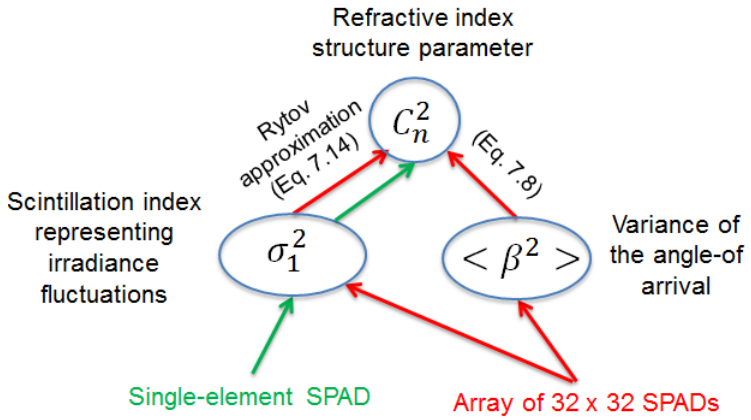

Figure 7.15. Illustration showing possible methods of C_n^2 calculation for a single-element SPAD detector and for the Gm-array.

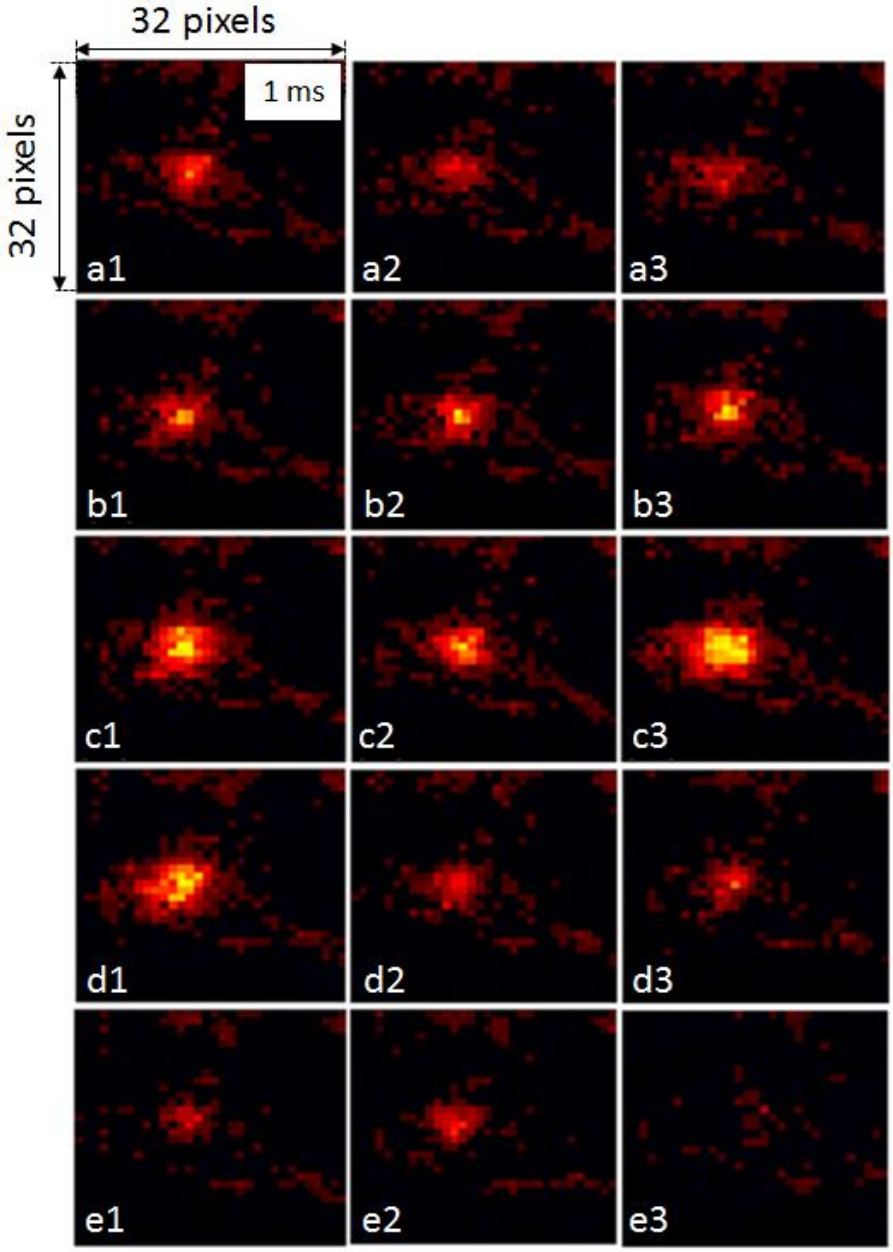

Figure 7.16. A series of images of the target taken with the Gm-array over a distance of 9.5 km. The sequence shows the variation in the position of the corner cube due to turbulence.

Figure 7.17 shows fluctuations of photon counts over a 6.75 s acquisition time recorded by an individual pixel of the detector array. The location of the chosen pixel corresponds to the average position of the intensity-weighted centroid within the 6.75 s acquisition time indicating the location of the image of the corner cube within the Gm-array. Figure 7.17 illustrates the effect of atmospheric scintillation on the signal and the Poisson noise distribution.

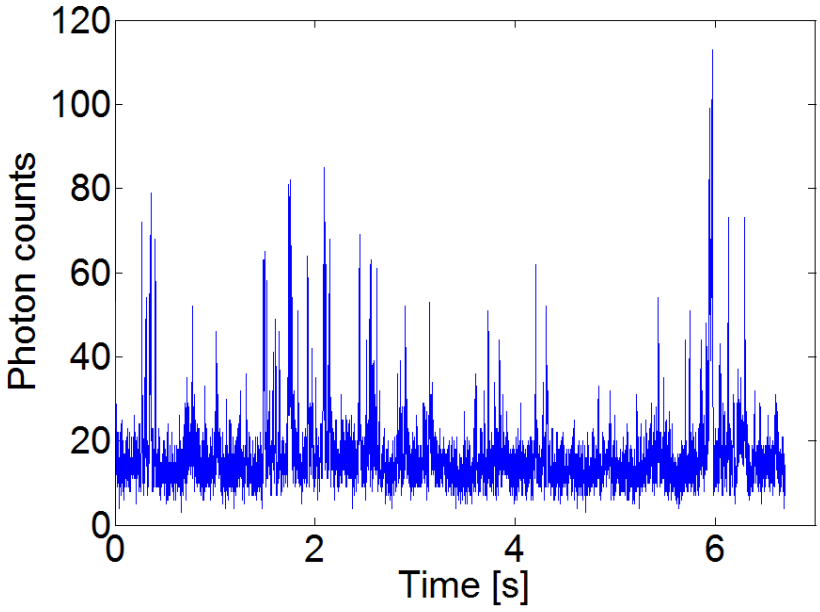

Figure 7.17. A 6.75 s duration acquisition window showing fluctuations of counts recorded by one pixel of the Gm-array.

Figure 7.18 shows a distribution of photon counts over 6.75 s for the same individual pixel generated in MatLab with 70 bins where 1 bin represents a width of 1 count and the Poisson distribution of the identical mean number of event occurrences and identical number of photon count occurrences. By applying the "lognfit" function (see section 7.4.1) to the histogram data, the parameters of the best fit to the log-normal distribution are $\mu_{xA} = 2.4852$ and $\sigma_{xA} = 0.4016$. The log-normal curve of the μ_{xA}, σ_{xA} was overlaid on the histogram shown in Figure 7.18.

The weaker the turbulence, the more the statistical distribution approaches the Poisson distribution. The plot shows that the distribution of data fits well within the log-normal curve; however, it not too dissimilar from a Poisson distribution, which indicates a weak level of turbulence present during the measurement.

The angle-of-arrival fluctuations of an optical wave in the plane of the receiver aperture cause "image dancing" in the focal plane of the detector [3]. The angle-of-arrival can be described in terms of the total beam shift across the image plane [3]. By averaging

the standard deviation of the beam position in Cartesian coordinates on the detector plane along *x* and *y* axis in each 0.25 s interval during the acquisition time, the mean variance in the angle of arrival $<\beta^2>$ was estimated. Subsequently, Eq. 7.8 was used to calculate the structure parameter of refractive index fluctuations, C_n^2.

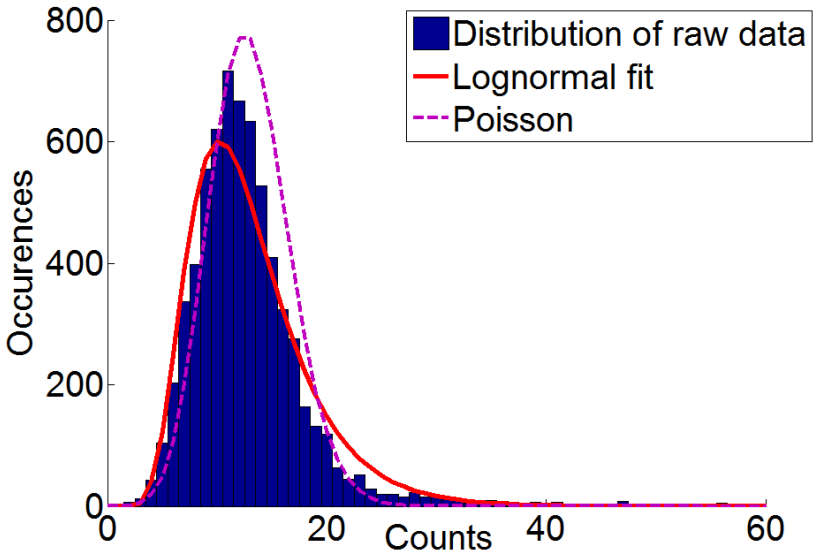

Figure 7.18. Distribution of photon counts over 6.75 s for a pixel position corresponding to the centroid, a log-normal fit and a Poisson distribution of the same mean number of counts = 13, that would be recorded when turbulence is absent.

The average variance in the angle-of-arrival $<\beta^2>$ in *x* and *y* was calculated using a "centroid" method. The "centroid" method is based on estimating the intensity-weighted centroid for the beam footprint of 32 × 32 pixels with an accuracy of ½ pixel, where the pixel intensity is defined by the number of photon counts recorded by a pixel in a 1 ms period. The intensity-weighted centroid is estimated by the means of geometric decomposition defined for coordinate *x* in Eq. 7.19 and for coordinate *y* in Eq. 7.20 [29].

$$x = \frac{\sum_1^i (x_i - 1/2) C_i}{\sum_1^i C_i} \qquad \textit{Eq. 7.19}$$

$$y = \frac{\sum_1^i (y_i - 1/2) C_i}{\sum_1^i C_i} \qquad \textit{Eq. 7.20}$$

where the parameter *i* represents the pixel value from 1 to 32 and *C* represents the number of photon counts recorded by a pixel.

Let us consider the example shown in Figure 7.19 in which an array of 5 × 5 pixels – each containing a number representing the number of counts – is used to calculate a central location of the target image using the "centroid" method.

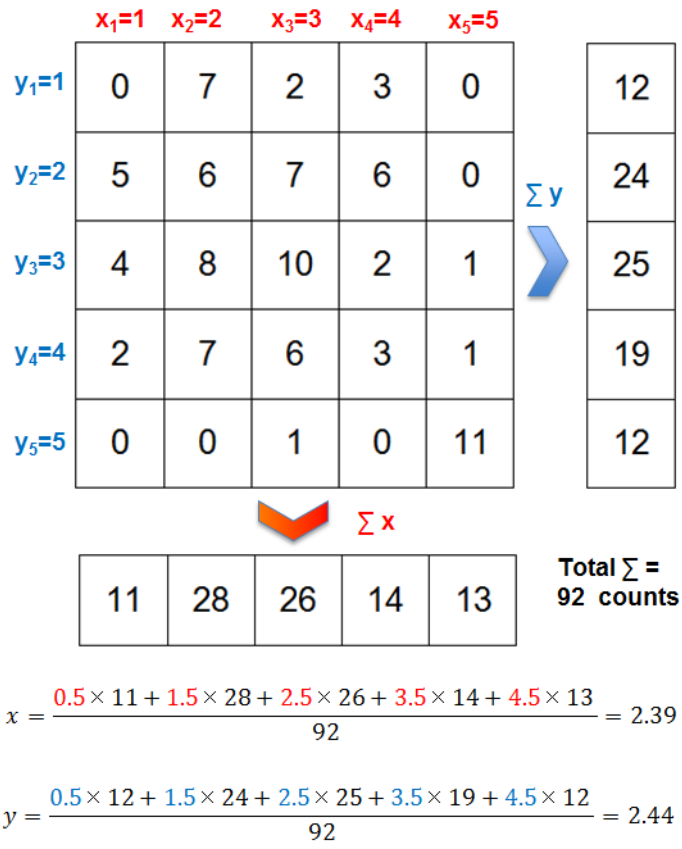

$$x = \frac{0.5 \times 11 + 1.5 \times 28 + 2.5 \times 26 + 3.5 \times 14 + 4.5 \times 13}{92} = 2.39$$

$$y = \frac{0.5 \times 12 + 1.5 \times 24 + 2.5 \times 25 + 3.5 \times 19 + 4.5 \times 12}{92} = 2.44$$

Figure 7.19. An array of 5 × 5 pixels, each containing a number representing the number of counts is used as an example to calculate a central location of the target image using the "centroid" method.

According to Eq. 7.19 and Eq. 7.20, each x and y coordinate is multiplied by the corresponding number of counts and summed over the entire array. Subsequently, it is divided by the total number of counts recorded by all 25 pixels of the array. The resulting position of the centroid within the array is $x = 2.39$, $y = 2.44$ which corresponds approximately to the centre of the array where the accumulation of large count values is located. It is necessary to convert the standard deviation of the angle-of-arrival expressed in Cartesian coordinates on the detector plane into radians. The width of the active area of each detector pixel on the array is equivalent to the spatial resolution of the optical system over the propagation distance. From the optical design, the angular resolution for each pixel side is ~ 28 µrad. For example, if the standard deviation in the angle of arrival is equal to 0.19 detector pixels, then by multiplying this value by the spatial resolution per pixel transfers the standard deviation of the angle-of-arrival in the image field of the optical system to the object field. In this example it is equal to ~ 4.75 cm. Calculating an arctangent of the 4.75 cm over the 9.52 km range will scale the standard deviation in the angle-of-arrival from centimetres to radians.

Table 7.2 (a), (b), and (c) shows an example of parameters for which the index of refraction structure parameter, C_n^2, was estimated. To demonstrate the extent to which the data varied throughout the acquisition period of 0.25 s, three specific data sets were chosen for which the standard deviation in the angle-of-arrival, β, and thus the C_n^2, and the back-calculated σ_I^2, were: (a) the lowest, (b) intermediate, (c) the greatest. It was observed that the standard deviation of the angle-of-arrival, β, varied from 1.6 μrad to 4.4 μrad.

(a)	**Centroid**	
Data set 1	*x*	*y*
Standard deviation of the angle-of-arrival β [rad]	1.7×10^{-6}	1.5×10^{-6}
Variance of the angle-of-arrival β^2 [rad^2]	3.1×10^{-12}	2.2×10^{-12}
Average variance of the angle-of-arrival β^2 [rad^2]	2.7×10^{-12}	
Index of refraction structure parameter C_n^2[m$^{-2/3}$]	**2.8×10^{-17}**	
Back-calculated scintillation index σ_I^2	**0.035**	
(b)	**Centroid**	
Data set 14	*x*	*y*
Standard deviation of the angle-of-arrival β [rad]	2.2×10^{-6}	4.3×10^{-6}
Variance of the angle-of-arrival β^2 [rad^2]	4.7×10^{-12}	1.9×10^{-11}
Average variance of the angle-of-arrival β^2 [rad^2]	1.2×10^{-11}	
Index of refraction structure parameter C_n^2[m$^{-2/3}$]	**1.2×10^{-16}**	
Back-calculated scintillation index σ_I^2	**0.154**	
(c)	**Centroid**	
Data set 27	*x*	*y*
Standard deviation of the angle-of-arrival β [rad]	2.6×10^{-6}	6.2×10^{-6}
Variance of the angle-of-arrival β^2 [rad^2]	6.8×10^{-12}	3.8×10^{-11}
Average variance of the angle-of-arrival β^2 [rad^2]	2.2×10^{-11}	
Index of refraction structure parameter C_n^2[m$^{-2/3}$]	**2.4×10^{-16}**	
Back-calculated scintillation index σ_I^2	**0.294**	

Table 7.2. Example results of C_n^2 and scintillation index, σ_I^2, calculation for three sets of data (a) data set 1, (b) data set 14 and (c) data set 27, 0.25 s each, measured with the Gm-array over a distance of 9.5 km.

The acquired results show that the standard deviation in the angle-of-arrival, β, on average represented approximately 13 % of the full diagonal FoV of an individual detector. This is equivalent to a lateral shift less than one detector pixel at the image plane of the optical system (~ 4 cm shift in the target location at a range of 9.5 km).

The calculated index of refraction structure parameter, C_n^2, indicates that the turbulence level was weak throughout the entire acquisition time. Without an independent

measurement of C_n^2 from a commercial scintillometer it has been concluded from general observations of the viewing conditions (15 ºC, cloudy with sunny intervals and with weak to moderate winds) that high levels of turbulence were not prevalent and that the method produces realistic results. The "centroid" method accounts for the distribution of light within an image and provides a reasonably accurate estimate of angular deviations caused by "image dancing".

The scintillation index, σ_I^2, for the array of detectors was calculated using Eq. 7.11 by averaging the number of photon counts in a 1 ms interval for the number of detector pixels located within the beam width determined by the "D4σ" parameter, which is the ISO11146 international standard definition for the beam width calculation [10]. According to this definition the beam width, *W*, of the Gaussian mode TEM_{00} is four times the value of the standard deviation, *σ*, of the horizontal (*x*) and vertical (*y*) marginal distribution and is expressed mathematically as:

$$W_x = 4\left(\frac{\sum_1^i (i-1/2-x)^2 C_i}{\sum_1^i C_i}\right)^{1/2} \qquad \textit{Eq. 7.21}$$

$$W_y = 4\left(\frac{\sum_1^i (i-1/2-y)^2 C_i}{\sum_1^i C_i}\right)^{1/2} \qquad \textit{Eq. 7.22}$$

where the parameter *i* represents the pixel value from 1 to 32, *C* represents the number of photon counts recorded by a pixel and *x* and *y* correspond to centroid coordinates defined in Eq. 7.19 and Eq. 7.20 [10]. On average, both W_x and W_y were approximately 12 detector pixels for a 1 ms period.

For the same set of data, the structure of refractive index parameter, C_n^2, was calculated from Eq. 7.14 by measuring the variance of the angle-of-arrival, *β*, in several 0.25 s periods. As shown in Figure 7.20 both, the C_n^2 calculated from fluctuations in the angle of arrival and the C_n^2 back-calculated from the scintillation index, vary from 5×10^{17} $m^{-2/3}$ to 3×10^{16} $m^{-2/3}$ within the acquisition time. The difference between values calculated using the two methods is plotted on the secondary axis in Figure 7.20 and shows that the maximum and minimum differences are: 3.1×10^{-19} $m^{-2/3}$ and 1.1×10^{-16} $m^{-2/3}$ respectively. The average difference is equal to 3.33×10^{-17} $m^{-2/3}$ with the standard deviation of 3.23×10^{-17} $m^{-2/3}$. The average difference between the two methods recorded across the 6.75 s acquisition time represents about 20 % of the average C_n^2 across acquisition time for the two methods. It can be concluded that the C_n^2 values calculated using the two different methods are well within the weak

turbulence level within the total acquisition time which justifies the use of Rytov approximation. This suggests that there is a sufficient degree of compatibility between the two methods of C_n^2 measurement; both methods allow for an accurate estimation of the regime within which the turbulence level is located.

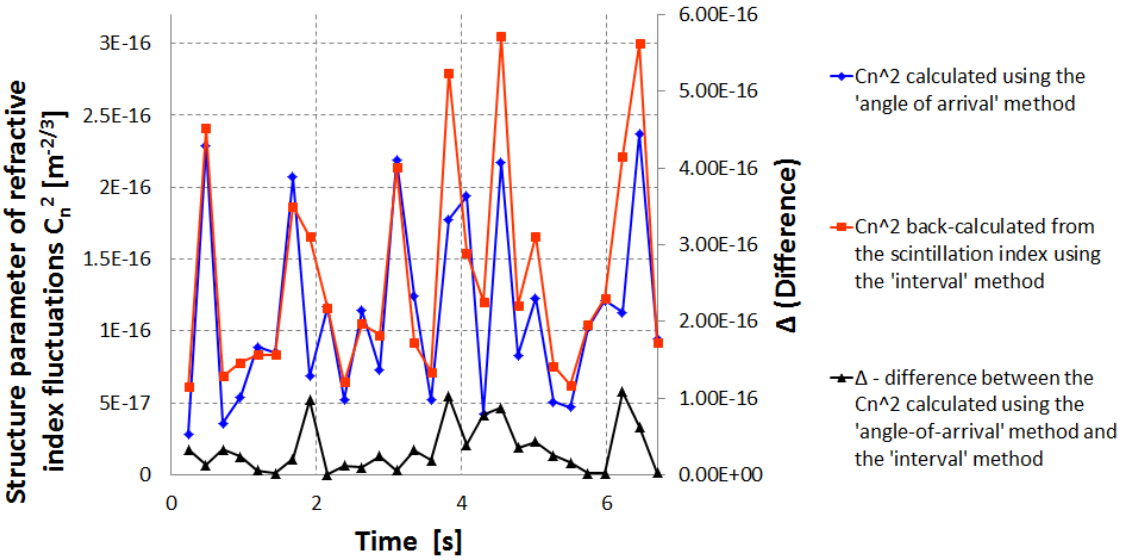

Figure 7.20. The structure parameter of refractive index fluctuations, Cn^2, was calculated from Eq. 7.8 for 6.75 s acquisition time of exactly the same set of data, by measuring the variance of the angle-of-arrival in each of the 0.25 s periods with 1 ms counting interval. The σ_I^2 was back-calculated from Eq. 7.14 for each of the 0.25 s intervals and plotted against the acquisition time.

It can be noted from Table 7.2 that there is a difference between the variance in the angle-of-arrival, β^2, along x and y axis for all three data sets. In this case, the x value refers to the direction perpendicular to the horizon while the y value indicates a direction parallel to it. The angle-of-arrival, β^2, was calculated for x and y across the 6.75 s acquisition window and plotted in Figure 7.21. On average the β_y^2 along the y axis is approximately twice of the β_x^2 along the x axis. This type of behaviour is expected when measuring turbulence. Since the air near the surface is heated by the sun, it becomes less dense and rises above the cool air located at a higher level. In turn, the cool air then warms up and rises which results in a cycle of air rising and sinking that occurs in the direction perpendicular to the horizon. The motion along the horizontal axis typically occurs at a much lower scale; it originates from cross-winds stirring the air across the horizon. The vertical motion of air masses tends to dominate in atmospheric turbulence, hence the factor of two difference between the β_y^2 and β_x^2.

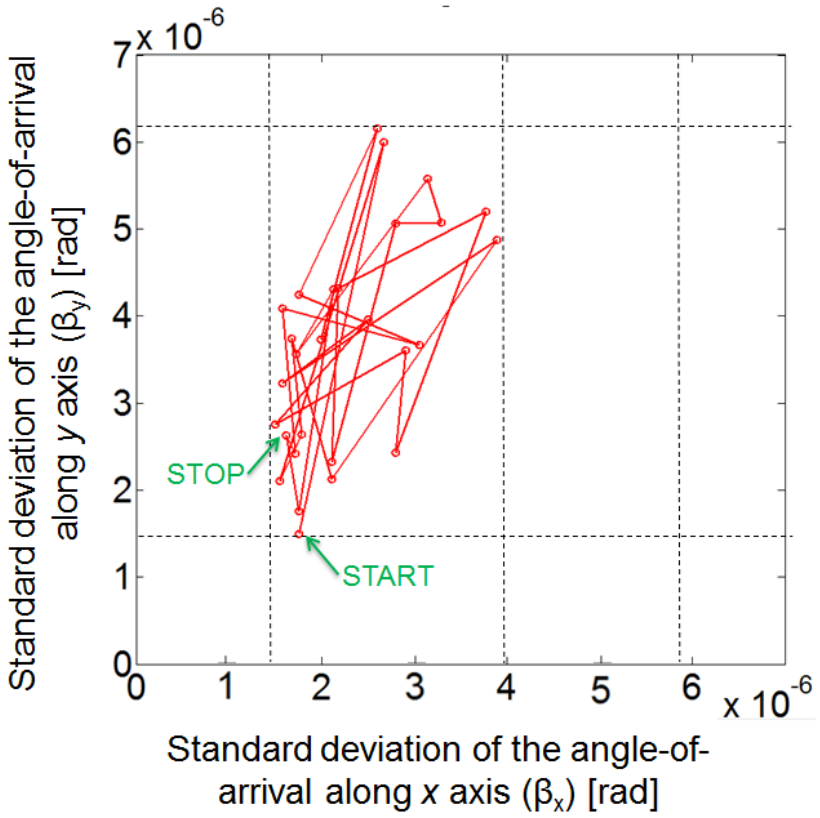

Figure 7.21. Graph showing standard deviation of the angle-of-arrival along the x axis (β_x) and along the x axis (β_y) that occurs over the 6.75 s acquisition time.

7.5 Acknowledgements

Field trials were performed with the assistance of apprentices Jamie Natta and Dillon Finesy of Selex ES. The Gm-array data was acquired with the assistance of Dr. Peter Sinclair, Ryan O'donnell and Roger Pilkington of Selex ES. The background information on the 4σ Gaussian beam diameter estimation was provided by Dr. Brian Flemming of Selex ES. Dr. Stephen Harding of Selex ES provided laser safety advice while Michael Dugan designed the window safety shield which was manufactured in the Selex ES workshop.

7.6 Conclusions

The statistical distribution of single-photon detection over a distance of 5.6 km and 9.5 km have been analysed using both a single-element SPAD and the Gm-array. The outcome of the scintillation index measurement with the single-element SPAD indicates that photon counts collected by the detector from the background have a "smoothing" effect on photon count fluctuations collected from the target and therefore the

scintillation index data without background correction is lower by 0.3 than the background corrected scintillation data.

Comparative measurements of C_n^2 measurement have also been performed with the Gm-array. This was achieved by the evaluation of irradiance fluctuations, σ_I^2 (by averaging fluctuations at the region of pixels located where the return from the target was located) and through measuring changes in angle-of-arrival fluctuations at the array. The two methods compare well. Therefore, comparable estimates of turbulence using the Gm-array with an independent analysis of beam position and intensity fluctuations have been shown.

Commonly available laser scintillometers based on analogue detection provide turbulence measurements averaged over integration times between 1 - 60 s in comparison to 0.25 s integration time demonstrated in this work [30] [31] [32]. Thus, Gm-detectors can provide a way of high-speed turbulence measurements with the flexibility of choosing the counting interval over which the data is to be averaged from 1 ms onwards. This can prove especially useful in some military tracking and surveillance imaging systems which require high accuracy measurements at high refresh rates.

In addition, it was shown that using an array of detectors allows monitoring of the angle-of-arrival, β^2, across x and y direction. This feature is not available with single-element detectors, or with scintillometers. The option of distinguishing between the dominant direction of the turbulent motion can be particularly useful in evaluating factors contributing to turbulence (convection vs. cross-winds). This can potentially be exploited in various studies on turbulence which can contribute to developing effective real-time turbulence mitigation mechanisms in active imaging.

References

[1] P. Lena, D. Rouan, F. Lebrun, F. Mignard, D. Pelat, "*Observational Astrophysics"*, Springer (2012),

[2] C. Huygens, "*The Celestial Worlds Discovered, or, Conjectures Concerning the Inhabitants, Plants and Productions of the Worlds of the Planets"*, James Knapton (1722)

[3] L.C. Andrews, R.L. Phillips, C.Y. Hopen, "*Laser Beam Scintillation with Applications"*, SPIE Press (2001)

[4] E. Martin, J. Daintith, "*Dictionary of Science"*, Oxford University Press (2005)

[5] C. Perino, "*Particulate Matter"*, Proc. of C.I.S.B Mini-Symposium (2010)

[6] B. Campbell, "*Introduction to Remote Sensing"*, The Guilford Press (2002)

[7] S.L. Shapiro, S.A. Teukolsky, "*Black Holes, White Dwarfs, and Neutron Stars"*, pp. 20-25, John Wiley & Sons (1983)

[8] M.C. Roggermann, B. Welsh, "*Imaging Through Turbulence"*, The CRC Press, Laser and Optical Science and Technology Series, 1-4, (1996)

[9] Committee on Developments in Detector Technologies; National Research Council, "*Seeing Photons: Progress and Limits of Visible and Infrared Sensor Arrays"*, The National Academy Press (2010)

[10] B.K. Flemming, *"Laser Energy Distribution in the Transient Regime",* Proc. of the International Laser Safety Conference, 11, 319 – 328, LIA (2013)

[11] J.C. Dainty, *Optical Effects of Atmospheric Turbulence,* in N. Ageorges and J.C. Dainty, "*Laser Guide Star Adaptive Optics for Astronomy"*, Kluwer Academic Publishers (2000)

[12] H. Weichel, "*Laser Beam Propagation in the Atmosphere"*, SPIE Press (1990)

[13] G.S. Buller, A.M. Wallace, *"Ranging and Three dimensional Imaging Using Time-Correlated Single-Photon Counting and Point-by-Point Acquisition",* IEEE J. Sel. Top. Quantum Electron., 13, 4 (2007)

[14] A.E. Siegman, *"Lasers",* University Science Books (1986)

[15] E. Hecht, "*Optics"*, Addison Wesley (2002)

[16] D. Dirkx, R. Noomen, I. Prochazka, S. Bauer, L.L.A. Vermeersen, "*Influence of Atmospheric Turbulence on Planetary Transceiver Laser Ranging",* Adv. Space Res., 54, 11, p. 2349-2370 (2014)

[17] M. Henriksson, L. Sjoqvist, "*Scintillation Index Measurement Using Time-Correlated Single-Photon Counting Laser Ladar"*, Opt. Eng., 53 (8) 081902 (2014)

[18] I. Capraro, A. Tomaello, A. Dall'Arche, F. Gerlin, R. Ursin, G. Vallone and P. Villoresi, "*Impact of Turbulence in Long-Range Quantum and Classical Communications*, PRL 109, 200502 (2012)

[19] P.W. Milonni, J.H. Carter, C.G. Peterson, R.J. Hughes, "*Effects of Propagation Through Atmospheric Turbulence on Photon Statistics"*, J. Opt. B: Quantum Semiclass. Opt. 6, 742-745 (2004)

[20] K.J. Gordon, P.A. Hiskett, R.A. Lamb, "*Advanced 3D Imaging Lidar Concepts for Long Range Sensing"*, Proc. SPIE, 91140G (2014)

[21] M.A. Itzler, X. Jiang, M. Entwistle, K. Slomkowski, M. Owens, A.Tosi, F. Acerbi, F. Zappa, and S. Cova, *"Advances in InGaAsP-based Avalanche Diode Single Photon Detectors",* J. Modern Opt., 58, 3–4, 174 – 200 (2011)

[22] A. Tosi, A. Della Frera, A. Bahgatv Shehata and C. Scarcella, "*Fully Programmable Single-Photon Detection Module for InGaAs/InP Single Photon Avalanche Diodes with Clean and Sub-nanosecond Gating Transitions"*, Rev. Sci. Instrum. 83, 013104 (2012)

[23] D. Dravins, L. Lindegren, E. Mezey, *"Atmospheric Intensity Scintillation of Stars. I. Statistical Distributions and Temporal Properties"*, Publications of the Astronomical Society of the Pacific, 109, 173-207 (1997)

[24] R.E. Walpole, R.H. Myers, S.L. Myers, K. Ye, "*Probability and Statistics for Engineers and Scientists"*, 9th Edition, Prentice and Hall (2013)

[25] B.K. Flemming, "*A Systems Study of Air-to-Ground Laser Operations: Statistical Modelling of Laser Energy Distribution in the Transient Regime"*, EngD Thesis, Heriot-Watt University (2014)

[26] http://uk.mathworks.com/help/matlab/ref/histogram.html

[27] http://uk.mathworks.com/help/stats/lognfit.html

[28] W. Feller, "*An Introduction to Probability Theory and its Applications: Volume I"*, Third Edition, John Wiley & Sons Inc. (1968)

[29] M.H. Protter, C.B. Morrey, "*Analytic Geometry"*, Addison Wesley (1970)

[30] http://www.scintec.com/english/CustomUpload/doc.pdf

[31] http://www.wittich.nl/NL/PDF/temperatuur-vocht/turbulentie/scintec_ scintillometer_sls.pdf

[32] http://www.kippzonen.com/Product/193/LAS-MkII-Scintillometer

Chapter 8
Conclusions

8.1 Summary and Conclusions

This thesis presented work on the optical design, tolerance analysis and performance evaluation of a re-configurable single-photon lidar system which can accommodate either a single-element SPAD detector operating in a scanning mode or a 32 × 32 Geiger-mode array operating in a non-scanning mode. Both the single-element and the array configurations can also be reconfigured to operate in a bi-static or mono-static transceiver setup. This is a bespoke design developed from a concept and includes custom-designed aspherical optics capable of delivering a diffraction limited performance for all configurations across all the FoV defined in the specification within a certain degree of mechanical and optical tolerances.

By incorporating an inter-changeable lens the system provides an identical pixel resolution for both configurations which permits performance comparisons to be conducted. The main parameters of the comparison included the acquisition time, spatial and depth resolution as well as size, weight and cost. This is the first time that such a comparison has been conducted and this lidar system is one of the earliest to assess the performance of a short wave infrared Gm-array. Both configurations incorporated InGaAs/InP SPAD detectors operational at a wavelength of 1550 nm. The main benefits of operating within the short-wave infra-red (SWIR) band included decreased solar background, lower atmospheric loss, improved covertness, as well as improved laser eye-safety thresholds.

The system used time-correlated single-photon counting to measure photon time-of-flight from which the range to a target was estimated and was used to reconstruct high-resolution three-dimensional images of various targets located at stand-off distances typicaly of the order of several kilometres. The system was configured to use the single-element detector in both bi-static and mono-static configurations as well as the Gm-array detector in a bi-static configuration.

Measurements and analysis performed with the single-element scanned system operating in the bi-static configuration were described in Chapter 3. This included the

theoretical modelling of the system losses which was evaluated against real-life measurements. The instrumental response function (IRF) of the system was measured and three-dimensional images demonstrating imaging through a semi-transparent sheet of netting were presented. The chapter presented results which demonstrated the ability of the system to produce three-dimensional images of targets at ranges from 2.8 km to 4.2 km at a spatial resolution of 8 cm and 12 cm respectively.

Chapter 5 described experimental results collected with the lidar system operating with the scanned single-element detector in a mono-static configuration. Details of the transmitter design, timing electronics, the alignment and the mitigation of backscatter by gating of the detector were described. The surface-to-surface depth resolution test was enhanced using a least-squares fit peak finder applied to the data which was cross-correlated with the normalised IRF. Depth images of different types of objects such as buildings, a pylon, foliage and terrain acquired over distances between 800 m and 10.5 km were presented using an average laser power of as little as 10 mW which is within the class I laser operation. The 10.5 km is the longest range over which imaging with this type of a lidar has been reported in the scientific literature. In addition, image mosaicking of an object with 100 × 235 scan points was demonstrated.

Chapter 6 described experimental results acquired with the lidar system operating with the Gm-array in a bi-static configuration. The scope, main features and specifications of the array were presented together with data acquisition, analysis and depth profile retrieval. An IRF was measured and scatterplots of targets such as a chimney, a staircase and a mast acquired over ranges of 2.8 km, 4.2 km and 6.6 km respectively were also presented. These demonstrated the ability of the bi-static array system to acquire long-range three-dimensional images of complex structures. This chapter also presented a comparison between the single-element detector configuration and the Gm-array configuration.

Chapter 7 introduced the underlying background on the properties of the Earth's atmosphere. It described laser beam propagation through an optically turbulent atmosphere and introduced parameters used to characterise optical turbulence. This experimentally determined the parameters which characterise optical turbulence with a new approach using single-photon lidar data obtained from sets of measurements performed over ranges of 5.6 km and 9.5 km. The single-element detector and the Gm-array were both used in the experiments and this was the first report of the measurement

of atmospheric turbulence using a Gm-array. The results obtained were implemented to analyse the effect of background noise on the scintillation index, σ_I^2. Finally, a comparative method of calculating the refractive index structure parameter, C_n^2 was introduced. This new approach may point the way towards the measurement of near real-time turbulence which may help the development of turbulence algorithms for active imaging.

To conclude, the research presented in this thesis has demonstrated a high resolution three-dimensional imaging lidar that was used to analyse various objects over ranges of several kilometres. It has shown that long range data acquisition is feasible in a practical apparatus and that the three-dimensional point clouds and images generated can provide clear feature extraction and object recognition even through turbulence. Elements of this research are now being developed further by Selex ES as part of their product strategy for future airborne targeting sensors.

8.2 Summary of the Comparison Between the Single-Element Detector and the Gm-Array

Table 8.1 shows the comparison parameters between the scanned single-element system operating in a mono-static configuration and the non-scanned array system operating in a bi-static configuration which are based on the experimental setup used in this thesis.

The single-element system was configured mono-statically in which the transmitted laser beam was parallel to the optical axis of the receiver. In this configuration the laser beam used the scanning mirrors to illuminate a specific region of interest which was co-aligned with the FoV of the detector pixel. Operating in a mono-static configuration is optimal for scanned single-element systems because it takes advantage of the scanning mirrors and eliminates the need for high-power laser beams required in bi-static systems where the entire area of interest must be flood-illuminated. In the experimental setup of the mono-static single-element configuration the laser beam divergence was ~ 4.5 times larger than the angular resolution of the detector pixel. Ideally the beam divergence should match the pixel angular resolution however, this was not possible due to various reasons explained in detail in section 5.4.1. Therefore, the area of the laser beam was approximately twenty times larger than the area of the field-of-view (FoV) of the single-element detector. The total average laser power of the transmitted beam was 10 mW

which provided 0.5 mW per FoV that represented a single detector pixel (assuming a uniform laser beam distribution).

The array detector was set up in a bi-static configuration. In this configuration the laser beam was transmitted along a separate channel to the receiver where the entire region of interest representing 32 × 32 pixels was flood-illuminated. This is the optimal configuration for the array detector; as data from multiple pixels is collected simultaneously, much higher laser power is required to illuminate the entire area of the FoV. The total average laser power used in this case was 500 mW which provided 0.4 mW per detector pixel.

Although the total average laser power used in the bi-static array configuration (500 mW) is significantly higher that required for the single-element mono-static configuration (10 mW), the single-element system provides nearly identical power per FoV representing one detector pixel. The array configuration requires laser class IV operation as opposed class I operation for the single-element configuration. The extended non-ocular hazard distance (*ENOHD*) (see section 4.6) for the single-element system is zero, as it is for all class I lasers, whereas it is ~ 2 km for the array system. Class IV laser operation and long *ENOHD* has some serious laser safety implications and requires complex and lengthy risk assessment and approval procedures. This suggests that, from the laser-safety point of view, the mono-static single-element configuration is much easier to be implemented in field trials.

During the experiments presented in this thesis both the single-element and the array configurations operated at the laser and detector gate repetition rate of 125 kHz. With the nearly identical laser power per FoV of the pixel the array configuration provided 1024 times faster acquisition times to acquire a similar number of photon counts over identical ranges and targets. Therefore, although the single-element system required much lower average power levels to acquire similar number of counts per pixel its acquisition times were three orders of magnitude slower due to the need for two-dimensional scanning.

	Single-Element	**32 × 32 Array**
Configuration	Mono-static (laser beam divergence is 4.5 times larger than the angular resolution of the detector pixel)	Bi-static (laser beam flood-fills all of the 32 × 32 pixels of the array)
Total average laser power	10 mW	500 mW
Average laser power per FOV representing one detector pixel (assuming uniform laser beam distribution)	0.5 mW per FoV of one detector pixel	0.4 mW per FoV of one detector pixel
Laser safety implications	Class I laser (straightforward to approve)	Class IV laser (requires a complex and lengthy laser risk assessment and approval procedures)
Extended non-ocular hazard distance	0 metre	~ 2 km
Laser and detector gate repetition rate	125 kHz	125 kHz
Acquisition time for a 32 × 32 pixel image	246 s	0.24 s
Laser pulse duration	800 ps	800 ps
Detector timing jitter	100 ps	250 ps
FWHM of instrumental response function	~ 1 ns	~ 1 ns
Depth resolution	15 cm	15 cm
Depth resolution limited by	Laser pulse duration	Laser pulse duration
Spatial resolution at 10 km	~ 30 cm	~ 30 cm
Pixel spacing	~ 30 cm	~ 30 cm
Maximum Field of View at 10 km	100 × 100 pixels (30 × 30 metres)	32 × 32 pixels (9.6 × 9.6 metres)
Weight	18 kg	8 kg
Cost	~ £50 k	~ £100 k

Table 8.1. Main parameters of the comparison between the scanned mono-static single-element detector system and the arrayed detector system operating in a bi-static mode based on the experimental setup presented in this thesis.

Although the single-element detector has a shorter timing jitter than the Gm-array (100 ps vs. 250 ps) the limit on the instrumental response function (IRF) and thus depth resolution for both detector configurations is imposed by the long laser pulse duration of 800 ps. The instrumental response function was measured to be ~ 1 ns for both configurations which imposes a limit on depth resolution of ~ 15 cm.

The spatial resolution was equal to ~ 30 cm at 10 km for both configurations. The pixel spacing for the single-element detector configuration was set to match the spacing for each pixel in the detector array.

The Gm-array configuration allows data collection from a maximum number of 32 × 32 pixels which, for a 30 cm spatial resolution per pixel, limits the total FoV to 9.6 × 9.6 metres at 10 km. The single-element scanned configuration allows the adjustment in the number of scan steps to up to 100 × 100 pixels (above this number clipping from aperture can be observed). For a 30 cm spatial resolution per pixel this provides the maximum FoV of 30 × 30 metres at 10 km. The single-element therefore allows imaging of larger objects with a high degree of target detail.

The number of electronic components required to build the single-element configuration exceeds that for the Gm-array configuration. This is due to the larger number of components required to control scanning mirrors in two dimensions. The Gm-array is assembled in a complete package containing all the necessary electronics required for timing and synchronisation. The total weight of timing electronics required to operate the scanned single-element detector configuration is ~ 18 kg whereas that required for the non-scanned arrayed detector configuration it is ~ 8 kg. However, it is likely that in some applications, use of a 32 × 32 Gm array will require additional scanning, hence this saving in system mass cannot be achieved. The cost of the array configuration was double of that required to build the single-element configuration.

The mono-static setup of the single-element offers compactness at an expense of backscatter which may expose a single-photon detector to an excess level of laser energy and cause detector saturation. The bi-static setup of the array configuration is more bulky as it requires two separate channels for the transmitter and receiver, and will suffer from parallax, and angular adjustment may be required as the target range is altered.

The repetition rate of the laser restricts the gate repetition rate of a detector. In the experimental setup a laser with a repetition rate of 125 kHz was used which limited the repetition rate of both detectors to 125 kHz. However, if a laser operating at a faster repetition rate was available then, this would allow the repetition rate of the single-element detector to be significantly increased. The maximum gate repetition rate of the single-element detector quoted by the manufacturer is 133 MHz and the minimum hold-off time before the dark count rate (DCR) increases above 80 kcps is 10 μs. It can be shown from Eq. 4.10 that the hold-off time limits the effective repetition rate to 1 MHz, 1.8 MHz, 5 MHz and 50 MHz for photon return rates per pulse of 5 %, 3 %, 1 % and 0.1 % respectively. In these scenarios, 5, 10, 27 and 270 pixels of the Gm-array operating at its maximum repetition rate of 186 kHz could match the count rate of the single-element detector. Therefore, the array is faster than the single-element detector by a factor of 200, 100, 40, 4 for a photon return rate of 5 %, 3 %, 1 % and 0.1 % respectively. This suggests that the single-element detector may be a more obvious choice in scenarios where photon return rates per pulse are low, i.e. when operating ranges are very long, or when the target signature is particularly low. Furthermore, in order to get only a factor of four advantage in the acquisition time by using the array over the single-element detector at a photon return rate of 0.1%, the laser power would need to be 50 times greater which necessarily leads to significant laser safety and electrical power consumption issues. In addition, the monostatic system described illustrates a less than ideal overlap of the laser excitation spot with the detected FoV, leading to higher powers than necessary in an optimised system. Therefore, in an optimised monostatic single-element system operating at a photon return rate of 0.1% of the repetition rate, the improvement factor in using an array is only a factor of four compared to the factor of 1000 more optical power required. Hence, for a photon sparse situation (i.e. photon return rate < 1 %), the monostatic single-element detector is the better option. With higher return levels, the Gm-array detector used in the thesis is generally the best option. These comparisons can only be made with the detector options available during the EngD project, however the later introduction of the asynchronously addressed array [1] will mean the system selection would be much more favoured towards the array detector configuration.

To conclude, the outcome of the comparison shows that the array detector configuration may be advantageous in terms of compactness and may be easier to be integrated into an airborne platform due to decreased mass resulting from no requirement for two-

dimensional scanning. However, in cases where use of a 32 × 32 Gm-array will require additional scanning, the mass of the array configuration will be similar to that of the single-element configuration. At short operating ranges where the photon return rate per pulse is high (~ 5 %), the array can provide an improvement in the acquisition time by a factor of 200 over the single-element detector. The single-element detector however, can operate at significantly higher operating rates (up to 50 MHz) when the photon return rate per pulse is low (0.1 %) and will be a better choice when operating ranges are very long. Although the array may provide improved compactness and faster acquisition times in some circumstances, the cost of the array is double that required to build a single-element system and requires significantly higher average laser power levels. In addition, if a laser of short pulse duration time is used, the single-element configuration has the potential to provide improved depth resolution over the array due to the smaller timing jitter.

The choice between the array and the single-element detector is not straightforward and requires a careful consideration of multiple factors. There are cases where the use of the single-element configuration will have significant advantages over the use of the array (i.e. when long operating ranges, wide FoV, high depth resolution and low laser power levels are required). The array would in turn be advantageous in cases where narrow FoV and lower spatial resolution are sufficient; where lower system mass is required and where high cost and laser safety are not an issue.

8.3 Improvements and Future Work

Following from this work there are several areas of improvement and further investigation such as opto-mechanical design, detector improvements, theoretical modelling, testing, signal processing, integration, improvement of performance parameters and hyperspectral imaging that are suggested.

8.3.1 Opto-Mechanical Design

Future performance optimisation of the optical design includes increased spatial resolution by incorporating a telescope of 30 cm aperture diameter that fits into a Titan turret (see Figure 3.1). This would still meet the limits of the turret aperture while allowing the spatial resolution to increase to 20 cm from 30 cm at 10 km for a 20 cm diameter (see Figure 3.3 in section 3.3). In addition, the extended FoV with diffraction-

limited performance for up to 300 × 300 pixels (pixel-to-pixel step size of 30 cm at 10 km) would enable swaths of 90 m × 90 m to be imaged over 10 km facilitating imaging of larger targets without the need for complex image processing.

Commercial telescopes are typically coated with a visible-band coating which in the current design contributes to ~ 15 % signal loss. In a future design it would be desirable to incorporate a telescope with a 1550 nm coating to minimise the loss and back-reflections from the internal structures of the telescope. This is especially important is the case of the mono-static configuration.

The volume of the lidar system described in this thesis significantly exceeds requirements for sensors that are incorporated into airborne platforms. For implementation into an airborne platform system both volume and weight need to be reduced. This can be achieved by eliminating the need for scanning mirrors which is possible with Gm-arrays. However, in the case of a single-element configuration, scanning systems are essential. Implementing dual-axis scanning components would eliminate the requirement for a second scanning component and relay optics and thus minimise the volume and weight of the system. This can be achieved by dual-axis galvo-scanning mirrors [2]. Micro-electro-mechanical systems (MEMS), membrane deformable mirrors, spatial light modulators (SLMs) and liquid crystal polarization gratings could potentially be incorporated assuming that their speed of operation is in the range of kHz [3] [4] [5] [6].

8.3.1 Detector Improvements

8.3.1.1 Larger Array Formats and Improved Performance

The pixel diameter of commercially available Gm-arrays is expected to be reduced to 30 – 40 μm in 2018/2019 and in 2022 it is expected be further reduced to 17 μm [7]. In addition, the array format is expected to increase to 128 ×128 and 64 × 64 in 2016 and to 256 × 256 in 2018/2019. As discussed in section 3.3 smaller pixel diameters would allow a reduction in the system's focal length, decreasing systems volume and improving system's implementation into airborne platforms. Larger array formats can have a two-fold effect on the future progress: larger number of pixels increases the FoV enabling recognition of larger targets or allow smaller targets to be imaged at higher spatial resolution. The expected improvements in detector pixel performance include

lower timing jitter, higher photon detection efficiency, lower dark count rate and lower reset time. These factors would contribute to higher spatial and depth resolution as well as faster acquisition times from extended targets.

8.3.1.2 Other Types of Detectors

Cadmium mercury telluride (CMT) semiconductor avalanche photo-diodes (APDs) have been in use since 1960's [8]. Recent research into expanding their application into single-photon detection conducted at Selex ES shows promising results.

A composition-tunable bandgap of CMT APDs allow wavelength tunability across short-wave infrared (SWIR: 1 – 3 μm), mid-wave infrared (MWIR: 3 – 5 μm), long-wave infrared (LWIR: 8 –14 μm) and very long-wave infrared (VLWIR: 14 –30 μm). It was shown that the performance of CMT APDs can be optimised across wide range of infrared wavelengths and temperatures [8].

There are large pixel CMT arrays available (up to 1032 × 1280) with a pixel pitch of 17 μm [9] and high frame acquisition rates of ~ 20 MHz [10]. CMT can be grown with very high quality resulting in low dark count rate (DCR) and low probability of afterpulsing. A near-ideal single-carrier cascade avalanche results in almost "noiseless" gain in the pixel providing high photon detection efficiency (~ 70 %) when compared to InGaAs/InP APDs.

Further progress in this area would enable single-photon imaging at wide FoV and high repetition rates at wavelengths spanning across SWIR and VLWIR from one focal plane and camera. Multiple-band fused imager would aid recovery of useful target information and significantly improve target identification.

8.3.2 Theoretical Modelling

The current theoretical model discussed in section 4.14 used to estimate count rate is restricted to Lambertian targets, a corner cube retro-reflector and to a target angle perpendicular to the optical axis. The model also ignores the effect of solar background, weather conditions and the position of the sun along the horizon. Thus, developing a model which takes into the account the Gaussian intensity distribution of the illuminating beam and which can operate for an expanded set of targets (such as foliage

and tower-like structures) and which includes modification of target surface angles and solar background, would be useful.

A model calibration is required for targets listed above. In particular, a spectralon [11], which exhibits highly Lambertian behaviour can be implemented to prove validity of the model for a Lambertian target in respect to known target reflectance at a wavelength of 1550 nm.

8.3.3 Testing

The scope of testing can be improved by performing high resolution, high frame acquisition speed (milliseconds) imaging enabling identification of:

- People and vehicles under camouflage in one three-dimensional frame;
- Moving targets, such as vehicles and people.

Results on turbulence measurements presented in Chapter 7 would greatly benefit from an independent measurement using a scintillometer. A simultaneous data acquisition across shorter ranges using both, Gm-array and a scintillometer can be used to validate single-photon detection as a viable tool for turbulence measurement.

8.3.4 Image Processing

Although the peak finding algorithms described in this thesis have been shown to be effective in many cases, they fail when the returns have amplitudes that are significantly lower than the level of background counts, or in the case when peaks are so closely separated that the estimation merges two returns into one. Reversible Jump Markov Chain Monte Carlo (RJMCMC) is a data processing technique that has demonstrated improvement in surface-to-surface resolution of closely separated targets [12][13]. First-photon technique introduced in [14] based on an approach described in [15] can produce depth images with 1 detected photon per pixel and was reported to significantly reduce acquisition times [16]. Other methods, such as Bayesian approaches [17] of processing sparse photon depth data have shown good image reconstruction at much less than one average photon per pixel. In single-photon imaging target scene is represented by a three-dimensional matrix of range inputs and thus, various matrix completion methods can be applied to retrieve missing target information and allow target reconstruction [18][19].

Implementing these techniques can be computationally intensive, however, it would allow for improvement in depth resolution and target recognition with short acquisition times.

8.3.5 Improvement of Performance Parameters

Duration of the laser pulse used in the setup is 800 ps and represents the main factor limiting IRF and thus depth resolution. Although complex processing algorithms can be used to minimise the effect of the IRF, using lasers of shorter pulse durations would be of benefit to resolving closely spaced surfaces. Currently, the commercially available lasers operating at a wavelength of 1550 nm offer pulse widths in the range of tens picoseconds and power of tens of pJ per pulse at MHz repetition rates. Such low power is not sufficient for long range imaging using the Gm-array where the FoV is flood-illuminated. Progress in laser technology would allow improvement in depth resolution acquired by Gm-arrays over long ranges.

8.3.6 Integration

In the current setup the components such as the detector, the laser, scanning mirrors and time-interval analyser are controlled from separate platforms. Integrating these in a single platform with a user-friendly interface would greatly improve the effectiveness of the operation of the system. In addition, by enabling the three-dimensional data to be processed and displayed in real time would create a fully integrated package suitable for airborne platforms.

8.3.7 Hyperspectral Imaging

Hyperspectral sensor systems generate an additional dimension by increased spectral resolution. Significant spectral differences exist between camouflaged targets and the background in the infrared region. Studies have shown that multispectral infrared sensors offer significant detection improvement over single-band detection [20]. Increasing the ability of the lidar system to provide multiple-wavelength imaging would widen the scope and functionality of photon-counting allowing simultaneous multi-channel data acquisition [21].

References

[1] J. Frechette, P.J. Grossmann, D.E. Busacker, G.J. Jordy, E.K. Duerr, K.A. McIntosh, D.C. Oakley, R.J. Bailey, A.C. Ruff, M.A. Brattain, J.E. Funk, J.G. MacDonald, S. Verghese, *"Readout Circuitry for Continuous High-Rate Photon Detection with Arrays of InP Geiger-Mode Avalanche Photodiodes",* Proc. SPIE, 8375 (2012)

[2] https://www.thorlabs.com/newgrouppage9.cfm?objectgroup_id=6057

[3] http://www.ipms.fraunhofer.de/en/applications/mems-scanners.html

[4] http://www.okotech.com/ao-systems-with-membrane-mirrors

[5] http://www.laser2000.co.uk/optics_&_optomechanics.php?Category=219

[6] J. Kim, M.N. Miskiewicz, S. Serati, M.J. Escuti, *"Demonstration of Large-Angle Nonmechanical Beam Steering Based on Liquid Crystal Polymer Polarization Gratings",* Proc. SPIE, 8052, 80520T (2011)

[7] M.A. Itzler, *"Geiger-mode APD Cameras for LADAR Imaging",* Oral Presentation, Heriot-Watt University, October (2013)

[8] A. Rogalski, *"HgCdTe Infrared Detector Material: History, Status and Outlook"*, Rep. Prog. Phys. 68, 2267-2336 (2005)

[9] http://www.qi3.co.uk/wp-content/uploads/2010/05/06-Keith-Barnes.ppt.pdf

[10] http://www.eso.org/~gfinger/toulouse_2011/WELLER%20SELEX%20GALILEO_CNES_work shop_67Dec_IS2_HW_finalx.pdf

[11] https://www.labsphere.com/labsphere-products-solutions/materials-coatings-2/targets-standards/diffuse-reflectance-standards/diffuse-reflectance-standards/

[12] G.S. Buller, A.M. Wallace, *"Ranging and Three-Dimensional Imaging Using Time-Correlated Single-Photon Counting and Point-by-Point Acquisition",* IEEE J. Sel. Top. Quantum Electron., 13, 4 (2007)

[13] S. Hernandez-Marin, A.M. Wallace and G.J. Gibson, "*Multi-Layered 3D LiDAR Image Construction Using Spatial Models in a Bayesian Framework"*, IEEE Trans. Pattern anal. Mach. Intell., 30(6), pp.1028-1040 (2008)

[14] D. Shin, A. Kirmani, V.K. Goyal, J.H. Shapiro, *"Computational 3D Reflectivity Imaging with High Photon Efficiency",* Proc. IEEE Int. Conf. Image Process. Paris, France (1995)

[15] A. Kirmani, D. Venkatraman, D. Shin, A. Colaco, F.N.C. Wong, J.H. Shapiro, V.K. Goyal, *"First-Photon Imaging",* Science, 343, 6166, 58-61 (2014)

[16] D. Shin, A. Kirmani, U.K. Goyal, J.H. Shapiro, " Photon-Efficient Computational 3D and Reflectivity Imaging with Single-Photon Detectors", Opt. Express, 24, 1873-1888 (2016)

[17] Y. Altmann, X. Ren, A. McCarthy, G.S. Buller, S. McLaughlin, *"Collaborative Single Target Detection for Depth Imaging From Sparse single-Photon Data"*, arXiv:1601.06149v1 [physics.ins-det] (2016)

[18] S. Lu, X. Ren, F. Liu, *"Depth Enhancement via Low-Rank Matrix Completion",* IEEE Conf. Comput. Vis. Pattern Recognit., 1063-6919 (2014)

[19] K. Fragkiadaki, M. Salas, P. Arbrlaz, J. Malik, *"Grouping-Based Low-Rank Trajectory Matrix Completion and 3D Reconstruction",* Proc. of Adv. in Neural Inf. and Inf. Processing Sys., 55-63 (201)

[20] G. Wong, R.A. Pilkington, A.R. Harvey, *"Achromatixation of Wollaston Polarizing Beam Splitters",* Opt. Lett., 36, 1332 – 1334 (2011)

[21] G.S. Buller, R.D. Harkins, A. McCarthy, P.A. Hiskett, G.R. MacKinnon, G.R. Smith, R. Sung, A.M. Wallace, R.A. Lamb, K.D. Ridley, J.G. Rarity, "*Multiple Wavelength Time-of-Flight Sensor Based on Time-Correlated Single-Photon Counting"*, Rev. Sci. Instrum.,76, 083112 (2005)